

**The Dynamic Behavior of a Concentrated Composite Fluid Containing  
Non-Brownian Glass Fibers in Rheometrical Flows**

Aaron Paul Rust Eberle

Dissertation submitted to the faculty of  
Virginia Polytechnic Institute and State University  
in partial fulfillment of the requirements for the degree of

DOCTOR OF PHILOSOPHY

in

Chemical Engineering

Dr. Donald G. Baird, Co-Chairman

Dr. Peter Wapperom, Co-Chairman

Dr. John Walz

Dr. Richey Davis

July 8<sup>th</sup>, 2008

Blacksburg, VA

Keywords: short glass fiber, composite fluid, glass fiber suspension, fiber orientation,  
transient rheology

# **The Dynamic Behavior of a Concentrated Composite Fluid Containing Non-Brownian Glass Fibers in Rheometrical Flows**

Aaron Paul Rust Eberle

(ABSTRACT)

With this research, we work towards the overall objective of being able to accurately simulate fiber orientation in complex flow geometries of composite fluids of industrial significance. The focus of this work is to understand the rheological behavior of these materials and its connection to fiber orientation as determined in simple shear flow. The work includes the development of a novel approach to characterizing the transient rheology; an experimental study of the relationship between the stress growth functions in startup of flow and the fiber orientation; a critical assessment of the limitations of current fiber suspension theory; and an approach to determining unambiguous model parameters by fitting.

A key difference between the rheological studies performed in this work and others is the use of a cone-and-plate device combined with “donut” shaped samples (CP-D) to prevent boundary effects on the measurement. The conventional method for obtaining transient rheological data is to use parallel disk (PP) geometry set at a gap where the measurements are independent of disk spacing. However, this work suggests that the inhomogeneous velocity gradient imposed by the PP geometry induces excessive fiber-fiber contact contributing to exaggerated measurements of the stress growth functions.

An experimental study of the transient rheological behavior of a 30 wt% short glass fiber-filled polybutylene terephthalate was performed using the CP-D. Stress growth measurements during startup of flow were performed in combination with direct measurement of the fiber orientation to determine the relationship between the transient rheology and the fiber microstructure. The well defined fiber orientation and rheological experiments allowed for a quantitative assessment of current fiber suspension theory. Comparison between the experimental fiber orientation and predictions based on Jeffery's equation and the Folgar-Tucker model show that the fiber orientation evolves much slower than predicted. In addition, the addition of a "slip" term improved the agreement between the predictions and experimental results. Predictions using the Lipscomb model coupled with the Folgar-Tucker model, with slip, were fit to the transient stresses to determine the feasibility of fitting unambiguous model parameters for a specific composite fluid. Model parameters determined by fitting at  $\dot{\gamma} = 6 \text{ s}^{-1}$  allowed for reasonable predictions of the transient stresses in flow reversal experiments at all the shear rates tested.

## Acknowledgments

The author wishes to express his thanks to both Professors Donald G. Baird and Peter Wapperom for their support and guidance that resulted in the completion of this work. In addition, the author would like to thank his committee members Dr. John Walz and Dr. Richey Davis for their insightful comments and suggestions during progression of this work.

The author would also like to acknowledge the following people:

- His grandparents Paul and Geraldine Rust, for supplying a sheltered environment and helping him make sense of the most difficult questions in life.
- His mother Kay Rust, for forcing her son to pursue a secondary education which then led to a love of science and understanding.
- His wife Rosa Duarte, for her love, understanding and continuous support.
- His uncle Dr. Jon Rust, for never doubting his abilities, challenging him and showing him how to live without inhibition and yet exhibit qualities such as honor and integrity.
- His sister Rachel Eberle, for being the most concrete person he has ever known.
- His father Dean Eberle, for inadvertently helping to mold his person and character.
- His aunt Dr. Jane Rust, for adding an additional perspective to his thoughts.
- Dr. Eric Scribber, for helping him develop his niche and style of teaching.
- His friend and research associate Gregorio Vélez-García for his patience and hard work and never ending list of ideas.
- All current and past members of the Polymer Processing Lab that he had the opportunity to serve with: Eric Scribber, Quang Nyguen, Matt Wilding, Gregorio Vélez-García, Brent Cunningham, Chris Seay, David Litchfield, Chris McGrady, Myoungbae Lee, Desmond VanHouton and last but in no way shape or form least Wade DePolo.
- Those members of the Chemical Engineering department staff who have made this work easier: Diane Cannaday, Chris Moore, Riley Chan, Amanda Kelly and Michael Vaught.
- High school teachers Kenneth Way, Glenn Hall, Blair Wood and Professors Eldred Chimowitz, Ben Ebenhack and Paule D'Alessandris for their inspiration through teaching.

## Original Contributions

The following are considered to be significant original contributions of this research:

- A novel approach to characterizing the transient rheological behavior of polymer melts containing short glass fibers was established. Donut shaped samples in combination with a cone-and-plate fixture lead to accurate measurements of the transient stresses.
- It was determined that the initial fiber orientation of parallel disk and cone-and-plate samples were closer to a planar orientation than a random orientation. This has a significant impact on the understanding of the stress growth behavior as measured by the rotational rheometer, the determination of unambiguous model parameters by fitting and accurate model predictions.
- A clearer understanding of the relationship between the stress response to deformation and the associated fiber microstructure of a short glass fiber filled composite fluid in simple shear flow.
- A method for determining unique model parameters for fiber suspension theory by fitting to the stress growth functions in startup of flow experiments was determined.

## **Format of Dissertation**

This dissertation is written in journal format. Chapters 3, 4, and 5 are self contained papers that are to be submitted for journal publication. Each paper separately describes the experiments, results and discussion, and conclusions relative to each chapter. With the exception of chapter 2, the review of literature, the figures and tables are presented after the reference section of each chapter.

# Table of Contents

<b>1.0 Introduction</b> .....	2
1.1. Rheology.....	2
1.2. Modeling .....	4
1.3. Research Objectives .....	6
1.4. References .....	7
<b>2.0 Literature Review</b> .....	9
2.1. Glass Fiber Composites.....	10
2.1.1. Glass Fiber Structure.....	10
2.1.2. Surface Modifications.....	12
2.1.3. Suspension Morphology.....	13
2.1.4. Suspension Preparation.....	14
2.1.5. Orientation Analysis.....	15
2.2. Rheology of Non-Newtonian Fluids Containing Glass Fibers.....	18
2.2.1. Abstract.....	19
2.2.2. Background.....	20
2.2.2.1. Classifying Glass Fiber Suspensions by Concentration.....	20
2.2.2.2. Classifying Glass Fiber Suspensions by Length.....	22
2.2.2.3. Rheometry: Flow Field and Boundary Effects.....	24
2.2.2.4. Impact of Brownian Motion and Sedimentation.....	30
2.2.3. Shear Rheology.....	33
2.2.3.1. Steady Shear Flow.....	33
2.2.3.2. Small-Amplitude Oscillatory Shear Flow.....	46

2.2.3.3. Transient Shear Flow.....	55
2.2.3.3.1. Startup of Shear Flow.....	55
2.2.3.3.2. Cessation of Steady Shear Flow.....	62
2.2.3.3.3. Interrupted Shear Flow.....	63
2.2.3.3.4. Creep.....	70
2.2.4. Extensional Rheology .....	71
2.2.4.1. Tensile Extension.....	72
2.2.4.2. Biaxial Extension.....	77
2.2.4.3. Planar Extension.....	78
2.2.5. Flow Phenomena.....	79
2.2.5.1. Weissenberg Effect.....	79
2.2.5.2. Entrance Pressure Loss.....	79
2.2.5.3. Extrudate Swell.....	80
2.2.6. Summary on the Rheology of Fiber Suspensions.....	81
2.3. Modeling.....	84
2.3.1. Motion of Rigid Fibers.....	85
2.3.1.1. Dilute Suspension.....	86
2.3.1.1.1. Single Fiber.....	86
2.3.1.1.2. Multiple Fibers.....	92
2.3.1.2. Semidilute Suspension.....	97
2.3.1.3. Concentrated Suspension.....	97
2.3.1.4. Closure Approximations.....	99
2.3.2. Stress.....	105

2.3.2.1. Newtonian Suspending Medium.....	106
2.3.2.1.1. Dilute.....	106
2.3.2.1.2. Semidilute.....	108
2.3.2.1.3. Concentrated.....	110
2.3.2.2. Non-Newtonian Suspending Medium.....	110
2.3.2.2.1. Generalized Newtonian Fluid.....	110
2.3.2.2.2. Viscoelastic Matrices.....	111
2.3.2.3. Closure Approximations.....	115
2.3.3. Flexible Fibers.....	116
2.3.4. Summary and Discussion.....	119
2.4. References.....	123

### **3.0 Obtaining Reliable Transient Rheological Data on Concentrated Short Fiber**

<b>Suspensions Using a Rotational Rheometer.....</b>	<b>132</b>
3.1. Abstract.....	133
3.2. Introduction.....	134
3.3. Theory.....	137
3.4. Experimental.....	141
3.4.1. Materials.....	141
3.4.2. Rheological Measurements.....	142
3.4.3. Measurement of Fiber Orientation.....	144
3.5. Results and Discussion.....	146
3.5.1. Experimental.....	146
3.5.2. Model Predictions.....	152

3.6. Conclusions.....	154
3.7. Acknowledgements.....	155
3.8. References.....	156
<b>4.0 Fiber Orientation Kinetics of a Concentrated Short Glass Fiber Suspension in</b>	
<b>Startup of Simple Shear Flow.....</b>	<b>172</b>
4.1. Abstract.....	173
4.2. Introduction.....	174
4.3. Theory.....	177
4.4. Experimental.....	182
4.4.1. Materials.....	182
4.4.2. Rheological Measurements.....	183
4.4.3. Measurement of Fiber Orientation.....	185
4.5. Results and Discussion.....	187
4.5.1. Experimental.....	187
4.5.2. Simulations.....	191
4.6. Conclusions.....	198
4.7. Acknowledgments.....	199
4.8. References.....	200
<b>5.0 Using Transient Rheology to Determine Material Parameters in Fiber</b>	
<b>Suspension Theory.....</b>	<b>217</b>
5.1. Abstract.....	218
5.2. Introduction.....	219
5.3. Theory.....	222

5.3.1. Orientation Tensors.....	222
5.3.2. Orientation Evolution Equation.....	222
5.3.3. Stress Equation.....	225
5.4. Experimental.....	228
5.4.1. Materials.....	228
5.4.2. Rheological Measurements.....	229
5.4.3. Measurement of Fiber Orientation.....	231
5.5. Results and Discussion.....	233
5.5.1. Rheology.....	233
5.5.2. Model Predictions.....	237
5.6. Conclusions.....	241
5.7. Acknowledgments.....	242
5.8. References.....	243
<b>6.0 Recommendations.....</b>	<b>259</b>
6.1. Material Considerations.....	259
6.2. Rheological Characterization.....	261
6.3. Modeling.....	263
<b>Appendix A. Rheological Data.....</b>	<b>264</b>
<b>Appendix B. Fiber Orientation Analysis and Data.....</b>	<b>307</b>
<b>Appendix C. Numerical Method: Matlab Code.....</b>	<b>321</b>
<b>Appendix D. Nomenclature.....</b>	<b>351</b>

## List of Figures

### Chapter 2.0

Figure 2.1. Fiber orientation angles  $\theta$  and  $\varphi$ , determined from the elliptical projection.<sup>8</sup> .....17

Figure 2.2. Effect of gap height, in a torsional PPR, on the shear stress growth coefficient in startup of shear flow for a glass fiber-filled polypropylene (PP),  $\phi = 0.0354$ , the fiber length was not given.<sup>44</sup> .....26

Figure 2.3. Shear viscosity vs. shear rate (filled symbols) and the dynamic viscosity vs. frequency (unfilled symbols) for short glass fibers ( $a_r = 24.3$ ) in a Newtonian suspending medium of various fiber concentration,  $\phi = 0$  ( $\blacksquare$ ,  $\square$ ), 0.05 semidilute ( $\bullet$ ,  $\circ$ ), 0.08 concentrated ( $\blacklozenge$ ,  $\lozenge$ ). All measurements were performed on a torsional PPR.<sup>59</sup> .....35

Figure 2.4. Reduced shear viscosity vs. shear rate for various concentrations of glass fiber ( $a_r \sim 20$ ) suspended in polybutene (PB, a Newtonian fluid) and a Boger fluid (B). The fiber volume fractions are  $\phi = 0.0158$ , 0.0327, and 0.0706 termed SD-1, SD-2 (semidilute régime) and C (concentrated régime), respectively. All measurements were performed on torsional PPR with gap-to-fiber length ratio greater than 3.<sup>45</sup> .....36

Figure 2.5. Shear viscosity vs. shear rate. (a) Two short glass fiber-filled polypropylene (PP) suspensions ( $\phi = 0.038$ ,  $a_r \sim 30$ , semidilute régime and  $\phi = 0.132$ ,  $a_r = 21.4$ , concentrated régime) and the neat suspending medium. The rheological experiments were performed on a PPR.<sup>11</sup> (b) Short glass fiber-filled high-density polyethylene HDPE ( $\phi = 0.136$ ,  $a_r = 30$ , concentrated régime) and the neat suspending medium.<sup>47</sup> The rheological experiments were performed with various rheometers as indicated in the figure legend.....38

Figure 2.6. Shear viscosity vs. shear rate for glass fiber suspensions of various fiber length in a low viscosity non-Newtonian fluid with constant glass fiber concentration ( $\phi = 0.02$ ). The various suspensions have mono-disperse fiber lengths,  $L = 0.5$ , 1.0, 1.5, and 2.0 mm, and corresponding aspect ratios,  $a_r = 31.25$ , 62.5, 93.75, and 125 respectively. The shortest glass fiber suspension related to the semidilute régime, the rest were concentrated. Rheological experiments were performed with a concentric cylinder rheometer.<sup>32</sup> .....40

Figure 2.7.  $N_I$  vs. shear rate. All measurements were performed on a torsional CPR. (a) Various glass fiber suspensions containing a constant fiber content ( $\phi = 0.044$ ,  $a_r = 276$ ) but different Newtonian suspending medium viscosities ( $\Delta$  14,  $\square$  16,  $\circ$  120 Pa\*s). (b) Two glass fiber suspensions of constant fiber concentration ( $\phi \sim 0.00046$ ) and Newtonian suspending medium with various fiber aspect ratio ( $a_r = \diamond$  276,  $\square$  552).<sup>60</sup> .....43

Figure 2.8.  $N_1$ - $N_2$  vs. shear rate for various concentrations of short glass fiber ( $a_r \sim 20$ ) suspended in polybutene (PB) and a Boger fluid (B). The fiber volume fractions are  $\phi = 0.0158, 0.0327,$  and  $0.0706$  termed SD-1, SD-2 (semidilute régime) and C (concentrated régime) respectively. All tests were performed on a torsional PPR with gap-to-fiber length ratio greater than 3.<sup>45</sup> .....44

Figure 2.9.  $N_1$  and  $N_1$ - $N_2$  vs. shear rate for a short glass fiber-filled HDPE ( $a_r = 157.5$  for  $\phi = 0.084$  and  $a_r = 78.7$  for  $\phi = 0.196$ ). The filled symbols represent  $N_1$  and the unfilled symbols  $N_1$ - $N_2$ .  $N_1$  and  $N_1$ - $N_2$  were obtained using a CPR and PPR, respectively.<sup>76</sup> .....45

Figure 2.10.  $|\eta^*|$  in small-amplitude ( $\gamma_0 = 0.15$ ) oscillatory shear for a short glass fiber-filled polybutylene terephthalate ( $\phi = 0.1766, a_r \sim 21.4,$  concentrated régime). All measurements, denoted by run 1-6, were performed on the same sample in a torsional PPR with a gap of  $\sim 2$  mm.<sup>77</sup> .....49

Figure 2.11.  $|\eta^*|$  vs. frequency for a long glass fiber-filled polypropylene ( $\phi = 0.132, a_r \sim 1071$  or  $L = 15$  mm, concentrated régime) at various strain amplitudes  $\gamma_0$ . All tests were performed on a torsional PPR with a gap of 1 mm.<sup>78</sup> .....50

Figure 2.12. The effects of pre-shear on  $|\eta^*_r|$  vs. frequency for a short glass fiber-filled polypropylene ( $\phi = 0.124, a_r \sim 21.4,$  concentrated régime). In this case  $|\eta^*_r|$  is the pre-sheared sample normalized by the no pre-shear sample values. All measurements were performed on a PPR.<sup>11</sup> .....52

Figure 2.13. The storage modulus vs. frequency: (a) for two short glass fiber-filled polypropylene suspensions ( $\phi = 0.038, a_r \sim 30,$  semidilute régime and  $\phi = 0.132, a_r = 21.4,$  concentrated régime) and the neat suspending medium;<sup>11</sup> (b) for a short glass fiber-filled polypropylene ( $a_r = 85$  and  $35$  for  $\phi = 0.017$  and  $0.0763$  respectively, the aspect ratio for the other concentrations was not given) of various concentrations of fiber.<sup>69</sup> Both measurements were performed on a PPR.....53

Figure 2.14 Transient specific viscosity ( $\eta_{sp} = \eta_r - 1$ ), normalized by the glass fiber volume fraction, vs. time, normalized by the period of oscillation T. Tests were performed on a dilute suspension of rigid aluminum coated Nylon fibers of varying concentration and constant aspect ratio,  $a_r = 5.2,$  in a Newtonian suspending medium. The rods were initially aligned parallel to the direction of velocity gradient with the used of an electric field. All tests were performed on a torsional CPR, at  $\dot{\gamma} = 2.51 \text{ s}^{-1}$ .<sup>86</sup> .....56

Figure 2.15.  $\sigma^+$  vs. strain. All tests were performed on a CPR. (a) Polystyrene-acrylonitrile (SAN, estimated density  $\approx 1.4 \text{ g/cm}^3$ ) containing short glass fibers ( $a_r = 22$ ) of varying concentrations (concentrated régime) and one sample containing glass beads denoted by (o) with diameter of 3-5  $\mu\text{m}$ . Experiments were performed at a shear rate of  $0.2 \text{ s}^{-1}$ . (b) Polyamid-6 (Nylon-6) containing short glass fibers of constant concentration ( $\phi = 0.1507$ ) and varying aspect ratio. The smallest aspect ratio sample was in the semidilute régime, and the rest were concentrated. The experiments were performed at  $\dot{\gamma} = 0.1 \text{ s}^{-1}$  that was interrupted at  $\gamma \sim 7$ .<sup>47</sup> .....59

Figure 2.16.  $\eta^+$  vs. strain for interrupted stress growth tests. All tests were performed on a torsional PPR with gap-to-fiber length ratio greater than 3:1. The clockwise (CW) and counter clockwise (CCW) notation is to give the reader context of the shear direction in a torsional rheometer. The flow reversal was applied immediately to the sample. (a) Short glass fiber-filled polybutene PB (fiber content:  $\phi = 0.0706$ ,  $a_r \sim 20$ , concentrated) suspension at  $\dot{\gamma} = 5 \text{ s}^{-1}$ .<sup>45</sup> (b) Neat and short glass fiber-filled polypropylene PP (fiber content:  $\phi = 0.115$ ,  $a_r \sim 20$ , concentrated), denoted in the figure as -gf, at  $\dot{\gamma} = 0.1 \text{ s}^{-1}$ .<sup>84</sup> .....67

Figure 2.17.  $N_1^+ - N_2^+$  plotted vs. strain. All tests were performed on torsional PPR with gap-to-fiber length ratio greater than 3:1. The clockwise (CW) and counter clockwise (CCW) notation denotes the direction of plate rotation. The flow reversal was applied immediately to the sample. (a) Short glass fiber-filled polybutene PB (fiber content:  $\phi = 0.0706$ ,  $a_r \sim 20$ , concentrated) suspension at  $\dot{\gamma} = 5 \text{ s}^{-1}$ .<sup>45</sup> (b) Neat and short glass fiber-filled polypropylene PP (fiber content:  $\phi = 0.115$ ,  $a_r \sim 20$ , concentrated), denoted in the figure as -gf, at  $\dot{\gamma} = 0.1 \text{ s}^{-1}$ .<sup>84</sup> .....69

Figure 2.18. Strain vs. time for a short glass fiber-filled ( $a_r = 25$ ,  $\phi = 0.124$ , concentrated) polypropylene subject to a shear stress of 400 Pa; experiments were performed on a torsional PPR.<sup>89</sup> .....70

Figure 2.19. Tensile stress growth function vs. strain,  $\varepsilon = L/L_o$ , for a short glass fiber filled high-density polyethylene HDPE (fiber content:  $\phi = 0.1358$ ,  $a_r \sim 30$ , concentrated) with various initial fiber orientations. The samples were prepared from compression molded and injection molded plates. Experiments were performed at a strain rate of  $0.1 \text{ s}^{-1}$  on a Meissner type extensional rheometer.<sup>47</sup> .....74

Figure 2.20. Tensile stress growth coefficient vs. time. Experiments in both graphs were completed on an in-house built fiber extensional rheometer. (a) Neat polystyrene at various strain rates. (b) Short glass fiber-filled polystyrene (fiber content:  $\phi = 0.0872$ ,  $a_r \sim 140$ , concentrated) at various strain rates.<sup>76</sup> .....76

Figure 2.21. Biaxial stress growth coefficient normalized by six times the shear stress growth coefficient vs. biaxial strain for a neat maleic anhydride modified polypropylene (MAH-g-PP) and four fiber-filled suspensions of various fiber content. Three of the glass fiber filled samples were composed of a similar MAH modified PP suspending medium as the neat fluid denoted PP/GF-2S (fiber content:  $\phi = 0.0763$ ,  $a_r \sim 24.4$ ), PP/GF-2L (fiber content:  $\phi = 0.0763$ ,  $a_r \sim 36.4$ ), PP/GF-4 (fiber content:  $\phi = 0.1805$ ,  $a_r \sim 28.4$ ) and one glass fiber filled sample was composed of an unmodified PP suspending medium denoted as PP/GF-2AS (fiber content:  $\phi = 0.0763$ ,  $a_r \sim 50$ ). All samples were all in the concentrated régime. Experiments were performed at a biaxial strain rate of  $\sim 0.04 \text{ s}^{-1}$  .....77

Figure 2.22. Unit vector  $\mathbf{u}$  describing the orientation state of a rod in spherical coordinates.....86

Figure 2.23. Polar and azimuthal angles defining the orientation of an ellipsoidal particle in simple shear flow as predicted by the analytical solution to the Jeffery's equation of motion, Eqs. (2.23) and (2.24). The solution is for an ellipsoid with  $a_r = 5$  with initial conditions of  $\varphi_o = 175^\circ$ ,  $\theta_o = 45^\circ$ . Graph is reproduced from Brabosa and Bibbo<sup>104</sup> .....89

Figure 2.24. Evolution of orientation in the azimuthal direction for a nylon fiber in a Newtonian suspending medium,  $a_{re} = 27.5$ , subject to simple shear flow,  $\dot{\gamma} = 0.26 \text{ s}^{-1}$ . Graph is reproduced from Moses et. al.<sup>111</sup> .....90

Figure 2.25. Evolution of orientation for an ellipsoidal particle with infinitely large  $a_r$  subject to simple shear flow as predicted by Eqs. (2.27) and (2.28). Predictions were subject to the initial conditions  $\varphi_o = 175^\circ$ ,  $\theta_o = 20, 45, 60$ , and  $90^\circ$ .<sup>104</sup> .....91

Figure 2.26. Motion of a flexible fiber from an initial distorted configuration as predicted by Eqs. (2.68) and (2.69). The fiber configuration is plotted for various  $\gamma$ . The numbers in the legend relate to the various strains with 0 representing the initial fiber orientation.<sup>159</sup> .....116

### Chapter 3.0

Figure 3.1. Unit vector  $\mathbf{u}$  describing the orientation state of a rigid fiber in spherical coordinates.....160

Figure 3.2. Schematic drawing and cross-sectional profile of the donut sample.....161

Figure 3.3. Representative drawing of the cross-sectional profile of a parallel pate and donut sample. The confocal laser microscopy images were taken for the parallel plate sample at a distance of 4.0, 7.0, and 10.0 mm from the outer edge denoted by PP-1, PP-2, PP-3 respectively. Similarly, the images were taken for the donut sample at a distance of 4.0, 6.25, and 8.5 mm from the outer edge denoted by PD-1, PD-2, PD-3.....162

Figure 3.4. The effect of the PP geometry gap height on the stress growth behavior of PBT-30 in startup of flow experiments at  $\dot{\gamma} = 1 \text{ s}^{-1}$ . (a)  $\eta^+$  vs. strain and (b)  $N_1^+ - N_2^+$  vs. strain. The various data points relate to measurements performed at different gap heights in millimeters.....163

Figure 3.5. The stress growth behavior of the neat PBT measured using the 50 mm CP geometry with an unmodified sample and with the donut sample, CP and CP-D, respectively. Measurements were performed at  $\dot{\gamma} = 1 \text{ s}^{-1}$ .....164

Figure 3.6.  $\eta^+$  vs. strain as a function of concentration at  $\dot{\gamma} = \dot{\gamma}_R = 1 \text{ s}^{-1}$ . (a) Measurements performed using the PP geometry. The symbols (x), ( $\Delta$ ), (-), (o), ( $\diamond$ ) and ( $\square$ ) represent fiber wt% 4.07, 8.42, 15, 20, 25 and 30. The symbol ( $\blacksquare$ ) represents  $\eta^+$  of PBT-30 measured using the CP- D for comparison. (b) Measurements performed using the CP-D. The symbols (x), ( $\blacktriangle$ ), (-), ( $\bullet$ ), ( $\blacklozenge$ ) and ( $\blacksquare$ ) represent fiber wt% 4.07, 8.42, 15, 20, 25 and 30. The symbol ( $\square$ ) represents the stress growth of PBT-30 measured using the PP geometry for comparison. The line shows the neat PBT for comparison in both graphs.....165

Figure 3.7.  $N_1^+$  and  $N_1^+ - N_2^+$  vs. strain at  $\dot{\gamma} = \dot{\gamma}_R = 1 \text{ s}^{-1}$ . (a) Measurements performed using the PP geometry. The symbols (x), ( $\Delta$ ), (-), (o), ( $\diamond$ ) and ( $\square$ ) represent fiber wt% 4.07, 8.42, 15, 20, 25 and 30. The symbol ( $\blacksquare$ ) represents the  $N_1^+$  of PBT-30 measured using the CP-D for comparison. (b) Measurements performed using the CP-D. The symbols (x), ( $\blacktriangle$ ), (-), ( $\bullet$ ), ( $\blacklozenge$ ) and ( $\blacksquare$ ) represent fiber wt% 4.07, 8.42, 15, 20, 25 and 30. The line shows the neat PBT for comparison in both graphs.....166

Figure 3.8. Stress growth in startup of flow measurements for PBT-30 at  $\dot{\gamma} = \dot{\gamma}_R = 1 \text{ s}^{-1}$ . (a)  $\eta^+$  and (b)  $N_1^+ - N_2^+$ ,  $N_1^+$  vs. strain. For both graphs PP, CP and CP-D refers to measurements performed using PP geometry, CP geometry with the unmodified sample and the CP geometry with the donut sample, respectively.....167

Figure 3.9. Stress growth in startup of flow measurements for PBT-30 at  $\dot{\gamma} = \dot{\gamma}_R = 4 \text{ s}^{-1}$ . (a)  $\eta^+$  and (b)  $N_1^+ - N_2^+$ ,  $N_1^+$  vs. strain. For both graphs PP and CP-D refers to measurements performed using PP geometry and the CP geometry with the donut sample respectively.....168

Figure 3.10. Spherical angles  $\theta$  and  $\varphi$  representing the reorientation of a fiber subject to simple shear flow vs. time as predicted by Eqs. (3.4) and (3.5) for various shear rates,  $\dot{\gamma} = 1, 0.2, 0.1 \text{ s}^{-1}$ . The initial conditions were  $\varphi_o = 175^\circ$ ,  $\theta_o = 60^\circ$ .....169

Figure 3.11. Effect of initial conditions on model fit to stress growth data for PBT-30 measured using the CP-D at  $\dot{\gamma} = 1 \text{ s}^{-1}$ . Predictions were made using Eqs. (3.6), (3.8) and (3.9). Model parameters, fit to  $\eta^+$ , using the experimentally determined initial conditions were  $N = 104$  and  $C_1 = 0.00001$ , and for the random  $N = 14$ ,  $C_1 = 0.0004$ .....170

Figure 3.12. Experimental data for PBT-30 and model predictions of the stress growth functions for a homogeneous and inhomogeneous velocity gradient denoted by CP and PP, respectively, at  $\dot{\gamma} = \dot{\gamma}_R = 1 \text{ s}^{-1}$ . (a) Experimental and predicted  $\eta^+$  vs. strain.  $\eta^+$  is calculated for CP and PP using Eqs. (3.8) and (3.10) respectively. (b) Experimental and predicted  $N_1^+$ ,  $N_1^+ - N_2^+$  and vs. strain.  $N_1^+$ ,  $N_1^+ - N_2^+$  were calculated for CP and PP using Eqs. (3.9) and (3.11) respectively. For all predictions  $\eta_s = 372 \text{ Pa}\cdot\text{s}$ ,  $C_1 = 0.00001$  and  $N$  is shown in the legend.....171

#### Chapter 4.0

Figure 4.1. Unit vector  $\mathbf{u}$  describing the orientation state of a rod in spherical coordinates.....203

Figure 4.2. Schematic drawing and cross-sectional profile of the donut sample.....204

Figure 4.3. Schematic drawing of the polished and imaged planes perpendicular to the neutral,  $x_3$ , and flow,  $x_1$ , directions. The  $x_2 - x_3$  plane images were taken of the sample at a distance of 4.0, 6.25, and 8.5 mm from the outer edge denoted by PD-1, PD-2, PD-3. For the  $x_1 - x_2$  plane, images were taken in one location denoted by PD-4. In all locations images were taken through the entire height of the sample.....205

Figure 4.4. Stress growth behavior of PBT and PBT containing various concentrations of short glass fiber at  $\dot{\gamma} = 1 \text{ s}^{-1}$ . (a) Shear stress growth coefficient,  $\eta^+$ , (b) first normal stress growth,  $N_1^+$ , vs. strain. The numbers in the legend relate to the wt% of glass fiber.....206

Figure 4.5.  $\sigma^+$  and  $N_1^+$  vs. strain,  $\gamma$ , for PBT-30 in interrupted flow experiments at  $\dot{\gamma} = 1 \text{ s}^{-1}$ . (a) Two interrupted experiments were performed on two different samples. In one experiment the flow was removed for 50 s and in the other experiment flow was removed for 200 s. (b) An interrupted flow experiment where a fresh sample was subject to flow at  $\dot{\gamma} = 1 \text{ s}^{-1}$  for 10 s, the flow was removed for 20 s, then the flow was applied.....207

Figure 4.6. (a) Elliptical “footprint” of fiber cross section where  $M$  is the major axis and  $m$  is the minor axis. (b) Two possible unit vectors,  $\mathbf{u}$ , along the backbone of the fiber and depiction of the positive angle  $\theta$ .....208

Figure 4.7. Comparison of predictions of Jeffery’s equation with and without the IBOF closure approximation. The dashed line represents Jeffery’s with the use of the IBOF closure, Eq. (4.4), and the solid line represents the predictions without the use of a closure approximation using Eq. (4.4). For the predictions random initial conditions were used at a  $\dot{\gamma} = 1 \text{ s}^{-1}$ .....209

Figure 4.8. Effect of the slip constant,  $\alpha$ , and the Folgar-Tucker constant,  $C_1$ , on the predictions of the  $A_{11}$  component at  $\dot{\gamma} = 1 \text{ s}^{-1}$ . In the figures Jeffery's represents Eq. (4.3). F-T represents Eqs. (4.5), Jeffery's + slip represents Eq. (4.6) with  $C_1 = 0$ , and F-T + slip represents Eq. (4.6). Decreasing  $\alpha$  refers to values  $\alpha = 0.75, 0.5$  and  $0.25$ , and increasing  $C_1$  refers to values of  $C_1 = 0.001, 0.005$  and  $0.01$ .....210

Figure 4.9. Non-physical oscillations in  $A_{11}$  and  $A_{33}$  as predicted by Jeffery's Eq. (4.3) using the IBOF closure approximation with experimentally determined initial conditions at  $\dot{\gamma} = 1 \text{ s}^{-1}$ . The dashed line represents Jeffery's and the solid line represent the stabilized Jeffery's, Jeff-S, with the Folgar-Tucker constant with small  $C_1 = 0.00015$ .....211

Figure 4.10. Experimental and predicted fiber orientation represented through the  $A_{ii}$  components in startup of simple shear flow at  $\dot{\gamma} = 1 \text{ s}^{-1}$ . The dashed line represents the Jeff-S model and the solid the F-T model with a  $C_1 = 0.006$ . (a) the  $A_{11}$  component, (b) the  $A_{22}$  and  $A_{33}$  components vs. strain.....212

Figure 4.11. Linear fit of the last three data points (strains 50, 100, 200) of the  $A_{11}$  and  $A_{33}$  components.....213

Figure 4.12. Experimental and predicted fiber orientation represented through the  $A_{ii}$  components in startup of simple shear flow at  $\dot{\gamma} = 1 \text{ s}^{-1}$ . The dashed line represents the Jeff-S + slip model and the solid line the F-T + slip model with a  $C_1 = 0.006$ . (a) the  $A_{11}$  component, (b) the  $A_{22}$  and  $A_{33}$  components vs. strain.....214

Figure 4.13. Experimental and predicted fiber orientation represented through the  $A_{12}$  component in startup of simple shear flow at  $\dot{\gamma} = 1 \text{ s}^{-1}$ . The dashed line represents the Jeff-S + slip model and the solid the F-T + slip model with a  $C_1 = 0.006$ . Predictions were performed starting at a strain of 0 and 7 shown as Pred. IC  $\gamma = 0$  and Pred. IC  $\gamma = 7$ , respectively, in the figure.....215

Figure 4.14. Experimental and predicted stress growth functions in startup of simple shear flow at  $\dot{\gamma} = 1 \text{ s}^{-1}$ . The dashed line represents the Jeff-S + slip model and the solid the F-T + slip model with a  $C_1 = 0.006$  for fiber orientation.  $\eta^+$  and  $N_1^+$  were produced by means of Eqs. (4.10) and (4.11), respectively. (a)  $\eta^+$ , (b)  $N_1^+$  vs. strain.....216

## Chapter 5.0

Figure 5.1. Schematic drawing and cross-sectional profile of the donut sample.....248

Figure 5.2. Schematic drawing of the polished and imaged planes perpendicular to the neutral,  $x_3$ , and flow,  $x_1$ , directions. The  $x_2 - x_3$  plane images were taken of the sample at a distance of 4.0, 6.25, and 8.5 mm from the outer edge denoted by PD-1, PD-2, PD-3. For the  $x_1 - x_2$  plane, images were taken in one location denoted by PD-4. In all locations images were taken through the entire height of the sample cross-sections.....249

Figure 5.3. The linear viscoelastic behavior of the neat PBT, and the Carreau-Yasuda model fit to the magnitude of the complex viscosity. Carreau-Yasuda parameters can be found in Table 5.1.....250

Figure 5.4.  $N_1$  as a function of fiber volume fraction at  $\dot{\gamma} = 1 \text{ s}^{-1}$ .....251

Figure 5.5. Shear stress growth coefficient,  $\eta^+$ , as a function of shear rate  $\dot{\gamma} = 1-10 \text{ s}^{-1}$ . (a)  $\eta^+$  (b)  $\eta^+/\eta$  where  $\eta$  is the quasi-steady state viscosity taken at 200 strain units. The numbers in the legend relate to the different shear rates.....252

Figure 5.6. First normal stress difference growth function,  $N_1^+$ , normalized by the shear rate,  $\dot{\gamma}$ , as a function of shear rate  $\dot{\gamma} = 1-10 \text{ s}^{-1}$ . The numbers in the legend relate to the different shear rates.....253

Figure 5.7. Shear stress growth coefficient,  $\eta^+$ , in flow reversal following startup of flow as a function of shear rate  $\dot{\gamma} = 1-10 \text{ s}^{-1}$ . (a)  $\eta^+$  (b)  $\eta^+/\eta$  where  $\eta$  is the quasi-steady state viscosity taken at 200 strain units. The numbers in the legend relate to the different shear rates. 6-CW relates to the stress growth behavior in the clockwise direction (CW) previous to the flow reversal in the counter clockwise direction (CCW).....254

Figure 5.8. First normal stress difference growth function,  $N_1^+$ , normalized by the shear rate,  $\dot{\gamma}$ , in flow reversal following startup of flow as a function of shear rate  $\dot{\gamma} = 1-10 \text{ s}^{-1}$ . The numbers in the legend relate to the different shear rates. 6-CW relates to the stress growth behavior in the clockwise direction (CW) previous to the flow reversal in the counter clockwise direction (CCW).....255

Figure 5.9. Experimental results and model predictions of the stress growth functions in (a) startup of flow, (b) flow reversal following startup of flow at  $\dot{\gamma} = 6 \text{ s}^{-1}$ . Model parameters can be found in Tables 5.1 and 5.2.....256

Figure 5.10. Experimental results and model predictions of the stress growth functions in flow reversal following startup of flow. (a) The shear stress growth coefficient,  $\eta^+$ , and (b) the first normal stress growth function,  $N_1^+$ . Model parameters can be found in Tables 5.1 and 5.2.....257

Figure 5.11. Experimental and predicted fiber orientation represented through the  $A_{ii}$  components in startup of simple shear flow at  $\dot{\gamma} = 1 \text{ s}^{-1}$ . The lines represent the model predictions of Eq. (5.7). Model parameters can be found in Table 5.2.....258

## List of Tables

### *Chapter 2.0*

Table 2.1. Comparison of physical and mechanical properties for E-glass <sup>4</sup> , carbon <sup>5</sup> , and Kevlar 29 <sup>6</sup> fibers.....	12
---	----

### *Chapter 3.0*

Table 3.1. The initial fiber orientation represented through the components of the orientation order parameter tensor, $\mathbf{A}$ . The components of $\mathbf{A}$ were found to be reproducible to $A_{ij} \pm 8\%$ .....	159
--	-----

### *Chapter 5.0*

Table 5.1. Carreau-Yasuda model parameters for neat PBT.....	246
Table 5.2. Suspension theory fit and calculated model parameters.....	247

## **1.0 Introduction**

## 1.0 Introduction

Parts made from short glass fiber composites are typically manufactured using injection or compression molding where the composite melt is forced into a mold cavity which results in the formation of a layered fiber microstructure.<sup>4</sup> Depending on the complexity of the part and the mold filling process, local variations can arise in the fiber orientation distribution which can severely affect the properties. As a result it is desired to accurately predict fiber orientation as a function of mold design and composite rheological properties. Hence, the rheological behavior of these materials and its connection to fiber orientation as determined in simple shear flow is of significant relevance to the development of constitutive relations that can accurately predict fiber orientation in complex flow situations.

## 1.1 Rheology

The rheological behavior of suspensions containing short glass fibers is complex because it not only depends on the suspending medium but the fiber and its orientation. The dynamic behavior of the fiber is dependent on the degree interaction, i.e. hydrodynamic and/or direct contact. As a result it is common to classify fiber suspensions into three concentration régimes based on excluded volume defined through the fiber volume fraction,  $\phi$ , and aspect ratio,  $a_r$ , of the fiber: dilute ( $\phi \ll a_r^{-2}$ ), semidilute ( $a_r^{-2} \ll \phi \ll a_r^{-1}$ ) and concentrated ( $\phi > a_r^{-1}$ ).<sup>5</sup> Typically, the aspect ratio of short glass fibers lie in the range  $15 < a_r < 100$  and composites of industrial interest

typically have fiber concentrations  $\phi > 0.1$  which places the materials of interest for this work in the concentrated régime.<sup>4</sup>

Characterizing the rheological behavior of composite melts containing glass fibers has proven to be a formidable task. To prevent wall effects on the dynamic behavior of the fiber, Blankeney<sup>3</sup> suggested that the rheometer gap be greater than three times the fiber length,  $L$ . In rotational rheometers cone-and-plate (CP) fixtures impose a homogeneous velocity gradient but the gap height varies linearly from the center ( $\sim 50 \mu\text{m}$ ) to the plate rim. At the center of the plates where the rheometer gap is small compared to the fiber length, excessive fiber boundary interaction can cause a suppression of the transient behavior.<sup>4</sup> As a result, it is common practice for researchers to use the parallel disk (PP) geometry in rotational rheometers to perform the rheological measurements as it allows for a certain amount of gap control. However, in the PP fixtures the tangential velocity at any point on the moving plate is a function of the radial position.<sup>5</sup> This results in an inhomogeneous velocity gradient. Both experimental<sup>6,7</sup> and theoretical<sup>8</sup> results have shown that for dilute and semidilute suspensions of fibers where external forces, inter-particle contact and hydrodynamic forces are neglected, the rate of change of the particle orientation is a function of the velocity gradient.<sup>6</sup> For concentrated suspensions where the inter-particle spacing can be on the order of the fiber diameter, we believe that the inhomogeneous velocity gradient may induce excessive fiber contact resulting in a misleading measurement of the suspensions stress response to deformation.

Many researchers have studied the experimental stress growth behavior of non-dilute suspensions of short glass fibers. A good summary of some of these works can be found in Laun<sup>9</sup>, Ganani and Powell,<sup>10</sup> Powell,<sup>11</sup> Zirnsak et al.,<sup>12</sup> Sepehr et al.,<sup>13</sup> and Eberle et

al.<sup>14</sup> From these works it can be shown that in general, as the concentration and/or aspect ratio of the fiber increases, the overshoot behavior of the shear stress growth coefficient,  $\eta^+$ , and first normal stress difference growth function,  $N_1^+$ , increases. The overshoot is attributed to a reorientation of the fibers as they try to establish an orientation along the fluid streamlines which is the orientation of least resistance to flow.

In semidilute suspensions, the period of fiber rotation orientation has been directly linked to shear stress oscillations which can dampen over time as a result of several interactions including boundary, particle-particle, hydrodynamic, or slight aspect ratio variations.<sup>7</sup> As the stress approaches a steady state, a pseudo-equilibrium fiber orientation state is reached, which, after a short period of time, may slowly change with time.<sup>8</sup> In concentrated suspensions the distance between fibers is on the order of the fiber diameter or less, and particle simulations show that under dynamic conditions fiber-fiber contact can severely affect the fiber motion.<sup>10, 11</sup> To our knowledge the dynamic behavior of fibers in a concentrated suspension has not been studied. As a result, conclusions based on the relationship between the stress growth behavior and the fiber orientation has relied heavily on theory.

## **1.2 Modeling**

The first theoretical frame work that is easily extendable to fibers is the work of Jeffery.<sup>17</sup> Jeffery showed that the motion of a single ellipsoidal particle suspended in a Newtonian fluid in a Stokes flow field will rotate around the vorticity axis. In a spherical coordinate system, the period required for a rotation of  $\pi$  radians in the direction of the

zenith angle,  $\theta$ , has been termed a Jeffery orbit and is a function of the particle aspect ratio,  $a_r$ .<sup>18</sup> Blunt ended particles such as rigid rods or fibers follow a similar behavior that one can predict using Jeffery's equation by defining an equivalent aspect ratio. For a dilute suspension of Nylon fibers in a Newtonian suspending medium, Moses et al.<sup>9</sup> showed that the fiber rotation followed Jeffery orbits when the fiber center of mass was greater than the fiber length from the boundaries.

The most common approach to simulating the fiber orientation in complex flow simulations, such as in injection mold filling, is to use the F-T model for fiber orientation in combination with a theory for the hydrodynamic extra stress contribution from the fiber, such as the Dinh and Armstrong theory. Though the simulations do qualitatively predict the shape of the microstructure patterns, they fail quantitatively.<sup>16</sup> To improve on the simulations, Huynh<sup>17</sup> introduced a strain reduction factor to the F-T model, termed the SRF model, using the argument that the fibers move in clusters and experience less strain than the bulk. Simulations using the SRF model resulted in more accurate predictions but the strain reduction factor was fit to experimentally determined fiber orientation data which is time intensive to determine. Also, the suspension theory used to predict fiber orientation in complex flows fails to predict the rheological behavior of the suspensions.

Sepehr et al.<sup>18, 19</sup> found they were only able to predict the stress growth behavior of a non-dilute short glass fiber suspension when the material parameters were fit to the rheological measurements and a slip parameter (similar to the strain reduction factor) was added to the F-T equation. This suggests that the theoretically determined material parameters are highly inaccurate and could be a large source of error in the complex flow

simulations. We do note, however, that the stress growth experiments used in the comparison were performed in a rotational rheometer with parallel disk geometry in which there is a varying shear rate from the center of the plates to the rim. Also, in the predictions of Sepehr et al.<sup>18, 19</sup> the initial fiber orientation was assumed random. However, this work shows that the initial orientation in rotational rheometer samples is closer to a planar orientation which can have a large impact on the transient predictions.

### **1.3 Research Objectives**

The goal this work is to understand the rheological behavior of short glass fiber filled polymeric fluids and its connection to fiber orientation as determined in simple shear flow. In addition, we wish to establish a model that can accurately predict the stress response to deformation and fiber orientation in well defined flows. The three objectives required to accomplish these goals are stated below:

1. Develop a rheological scheme where the measurements are unaffected by the rheometer geometry.
2. Experimentally characterize the evolution of fiber orientation during startup of flow and characterize the transient rheology of a concentrated short glass fiber composite fluid.
3. Assess the performance of current fiber suspension theories for orientation and stress and determine a method for obtaining unambiguous model parameters.

## 1.4 References

1. Advani, S. G., E. M. Sozer, *Process Modeling in Composites Manufacturing*. **2003**.
2. De, S. K., J. R. White, *Short fibre-polymer composites*. **1996**.
3. Guo, R., J. Azaiez, C. Bellehumeur, Rheology of fiber filled polymer melts: Role of fiber-fiber interactions and polymer-fiber coupling. *Polymer Engineering and Science* **2005**, 385-399.
4. Advani, S. G.; Sozer, E. M., *Process Modeling in Composites Manufacturing*. Marcel Dekker Inc.: New York, 2003.
5. Doi, M.; Edwards, S. F., *The Theory of Polymer Dynamics*. Oxford University Press: New York, 1988.
6. Blankeney, W. R., Viscosity of suspensions of straight rigid rods. *J. Colloid Interface Sci.* **1966**, 22, (4), 324.
7. Utracki, L. A., *Two-Phase Polymer Systems*. Oxford University Press: New York, 1991; p 277-331.
8. Bird, R. B.; Armstrong, R. C.; Hassager, O., *Dynamics of Polymeric Liquids*. John Wiley & Sons, Inc.: New York, 1987; Vol. 1.
9. Moses, K. B.; Advani, S. G.; Reinhardt, A., Investigation of fiber motion near solid boundaries in simple shear flow. *Rheol. Acta* **2001**, 40, 296-306.
10. Iso, Y.; Koch, D. L.; Cohen, C., Orientation in simple shear flow of semi-dilute fiber suspensions. 1. Weakly elastic fluids. *J. Non-Newt. Fluid Mech.* **1996**, 62, (2-3), 115-134.
11. Barbosa, S. E.; Bibbo, M. A., Fiber motion and the rheology of suspensions with uniform fiber orientation. *J. Poly. Sci., Part: B, Polym. Phys.* **2000**, 38, 1788-1799.
12. Eberle, A. P. R.; Baird, D.; Wapperom, P., Rheology of non-Newtonian fluids containing glass fibers: A review of experimental literature. *Ind. Eng. Chem. Res.* **2008**, 47, (10), 3470-3488.
13. Petrich, M. P.; Koch, D. L.; Cohen, C., An experimental determination of the stress-microstructure relationship in semi-concentrated fiber suspensions. *J. Non-Newt. Fluid Mech.* **2000**, 95, 101-133.
14. Ivanov, Y.; VanDeVen, T. G. M.; Mason, S. G., Damped oscillations in the viscosity of suspensions of rigid rods. I. Monomodal suspensions. *J. Rheol.* **1982**, 26, (2), 213-230.
15. Tseng, S.; Osswald, T. A., Predicting shrinkage and warpage of fiber-reinforced composite parts. *Poly. Comp.* **1994**, 15, 270-277.
16. Sepehr, M.; Ausias, G.; Carreau, P. J., Rheological properties of short fiber filled polypropylene in transient shear flow. *J. Non-Newt. Fluid Mech.* **2004**, 123, 19-32.
17. Jeffery, G. B., The motion of ellipsoidal particles immersed in a viscous fluid. *Proc. R. Soc. Lond. A* **1922**, 102, 161-179.
18. Larson, R. G., *The Structure and Rheology of Complex Fluids*. Oxford University Press: New York, 1999.
19. Batchelor, G. K., The stress generated in a non-dilute suspension of elongated particles by pure straining motion. *J. Fluid Mech.* **1971**, 46, 813-829.
20. Petrich, M. P.; Koch, D. L., Interactions between contacting fibers. *Phys. Fluids* **1998**, 10, 2111-2113.

21. Sundararajakumar, R. R.; Koch, D. L., Structure and properties of sheared fiber suspensions with mechanical contacts. *J. Non-Newt. Fluid Mech.* **1997**, 73, (3), 205-239.
22. Sepehr, M.; Carreau, P. J.; Moan, M.; Ausias, G., Rheological properties of short fiber model suspensions. *J. Rheol.* **2004**, 48, (5), 1023-1048.
23. Brenner, H., Rheology of a dilute suspension of axisymmetric Brownian particles. *Int. J. Multiphase Flow* **1974**, 1, 195-341.
24. Hinch, E. J.; Leal, L. G., The effect of Brownian motion on the rheological properties of a suspension of non-spherical particles. *J. Fluid Mech.* **1972**, 52, 683-712.
25. Darlington, M. W., G. R. Smith, Voiding in glass fibre reinforced thermoplastics mouldings. *Polymer* **1975**, 16, 495-462.

## **2.0 Literature Review**

### **Preface**

This chapter provides the review of literature relevant to this research. The first section, § 2.1, is a review of glass fiber composites in general. This is followed by a review of the rheological behavior of glass fiber composite fluids, in § 2.2, which is a major focus of this review. § 2.2 is a self containing paper, with the exception of the references, which can be found at the end of the chapter, and was submitted and accepted to a special addition issue of Industrial & Engineering Chemistry Research in honor of E. Bruce Nauman Festschrift. The last section, § 2.3, relates to modeling the rheological behavior of glass fiber suspensions.

## **2.0 Literature Review**

### **2.1 Glass Fiber Composites**

The rheological behavior of glass fiber composite melts can be significantly affected by the characteristics of the glass fiber. This includes the fiber length, aspect ratio, orientation, distribution, and degree of interaction of the fiber surface with the polymer melt. The following section focuses on these ideas to set the stage for the review on rheology. In subsections § 2.1.1 and § 2.1.2 glass fiber in general, and the use of surface treatments to increase the interaction between the fiber surface and matrix is discussed. This is followed by a review of the suspension morphology in § 2.1.3 which is generated during mixing of the polymer and glass fiber, and processing of the composite melt which is discussed in § 2.1.4. Lastly, we review the techniques used to characterize the fiber orientation in § 2.1.5.

#### **2.1.1 Glass Fiber Structure**

Natural glass has been in existence since the formation of the earth, birthed from volcanoes spewing molten rock, lightning strikes and impacts from meteors. The technology to melt and form glass has been around since roughly 3500 BC.<sup>1</sup> There are many obvious reasons why glass has been such an important and useful material. Probably the largest reason is the natural abundance of components that form glass found in nature, with the earth's crust containing roughly 30 wt% of silicon, the major component of glass. Glass fibers have been produced since the 1940s and roughly a

decade thereafter glass fiber composites found applications in the automotive industry in composite materials.<sup>2</sup>

Glass, in general, can be divided into two groups, oxides (which include compounds with oxygen atoms) and non-oxides. Each group contains many subsets that differ in chemical structure which effect strength, melt temperature and cost. 90% of all commercially produced glass is “oxide/soda-lime” that inherits its name from the chemical make up of 72% Si, 13% Na<sub>2</sub>O (from soda ash), 11% CaO (from limestone) and roughly 4% minor ingredients. For composite filler purposes, E-glass, or electrical grade glass, has become the standard which has a typical nominal composition of 54% SiO<sub>2</sub>, 14% AlO<sub>3</sub>, 22% CaO and MgO, 10% B<sub>2</sub>O<sub>3</sub>, and 2% Na<sub>2</sub>O and K<sub>2</sub>O by weight. Originally, E-glass was developed for wire insulation purposes, and later was found to have excellent process and fiber forming characteristics. E-glass fibers generally elongate uniformly during the fiber spinning process leaving a round cross section and a smooth surface. Fiber diameters for composites can range from 5-20 μm, and lengths from 0.1 mm to a continuous fiber strand, before processing or pelletization. The use of relatively small diameter fibers in composites is a result of desired large surface area to weight ratio resulting in a large interfacial interaction between the fiber and matrix. Other positive characteristics of glass fiber are low production cost, high strength, high stiffness, non-flammable, and chemically resistant. Table 2.1 lists the density as well as the tensile strength and Young’s modulus for E-glass in comparison to carbon fiber, and Kevlar 29. The disadvantages to E-glass fibers are they have a relatively low modulus compared to other higher performance fibers (Table 2.1), are self abrasive, have a low fatigue resistance, and can suffer hydrolytic degradation.<sup>3</sup>

**Table 2.1** Comparison of physical and mechanical properties for E-glass<sup>4</sup>, carbon<sup>5</sup>, and Kevlar 29<sup>6</sup> fibers.

	Density (g/cm <sup>3</sup> )	Tensile Strength (MPa)	Youngs Modulus (GPa)
E-glass	2.55	1450	72.4
Carbon	1.76	3840	220
Kevlar 29	1.44	3409	103

### 2.1.2 Surface Modifications

The surface of a glass fiber is typically modified for two reasons: to minimize the self-destructive abrasive contact between the fibers and to increase the fiber-matrix interaction of the melt and adhesive strength of the composite. The use of “sizing” as a surface treatment has become an industrial standard and addresses both the abrasive contact and surface interaction. Sizing is a functional coating that acts as an abrasive barrier that is tailored to transfer stress from the matrix to the fiber reinforcement.<sup>4</sup> Though manufacturers are reticent about revealing the complete chemical formulation, typically sizing consists of a water-based mixture containing a lubricant, film forming agent and a coupling agent that is applied in the form of a solution or aqueous emulsion. This creates a polymeric film on the fiber surface, of which, epoxy and poly(vinyl acetate) are common forms.<sup>5</sup> Coupling agents increase surface interaction and promote adhesion between the fiber and the polymeric matrix.<sup>6</sup> This is typically accomplished by molecules containing a silane group with an aliphatic branch or tail such as methacryloxypropyltrimethoxysilane (MPS) or phenyltriethoxysilane (PTS).<sup>7, 8</sup> The silane group is hydrolyzed at the glass surface to form silanols which form hydrogen bonds with the hydroxyl groups on the glass surface. Upon drying, a condensation

polymerization occurs to form a polysiloxane ring on the glass fiber surface.<sup>9</sup> With the siloxane section of the molecule preferentially bonded to the inorganic glass surface a favorable and robust interaction between the aliphatic section and the polymer matrix is accomplished.

Plasma polymerization can be used to further improve the surface adhesion between the matrix and the fiber surface.<sup>4</sup> In this process Ar, H<sub>2</sub>, O<sub>2</sub>, CO<sub>2</sub>, NH<sub>3</sub> or air plasma at the fiber surface is used to initiate chemical and physical reactions altering surface properties and morphology. This generates a more favorable surface for the coupling agent to bond.<sup>10</sup>

### **2.1.3 Suspension Morphology**

Generally speaking, the degree of dispersion, the length and orientation distribution of the glass fibers within a matrix defines the morphological state of the composite. The degree of dispersion and fiber length distribution is dependant on the method used to compound the fiber with the polymer and then process the composite into its desired form.<sup>7</sup> The orientation distribution is primarily dependant on the flow history.<sup>8</sup> Speaking in terms of mechanical properties of a final consolidated composite, the most desirable morphology is a uniformly dispersed composite with high fiber alignment in the direction of mechanical interest while retaining fiber length.<sup>2,9</sup> In reality, most composites contain a distribution of orientations and fiber lengths induced by geometry and shear stress during the compounding and/or the processing step of part fabrication. In most composites the volume fraction of filler is highly controlled, though some concentration

gradient may occur during part fabrication typically induced by mold geometry.<sup>10</sup> To fully understand the morphology it is imperative to define the methods used for composite preparation.

#### **2.1.4 Suspension Preparation**

The most common and economical method to incorporate glass fibers into a polymer is direct melt compounding, generally accomplished with an extruder.<sup>9</sup> Other methods include similar approaches to that used for wire coating on continuous glass fiber bundles, in situ polymerization and batch mixing.<sup>9</sup> Compounding results in a high degree of degradation to fiber length<sup>11</sup>, but as stated by Bader and Bowyer<sup>12</sup> there is little advantage in developing techniques to retain fiber length and integrity in a pelletized form, unless improvements are made in preventing degradation in the processing step of part fabrication.

Melt compounding is accomplished by dry blending glass fibers of specific length with the desired thermoplastic matrix which is fed directly into an extruder.<sup>2</sup> The mixing occurs as both components are fed by the screw through the barrel. The extrudate can then be directly injected into a mold for part fabrication purposes or passed through a capillary die and pelletized.<sup>13</sup> As previously mentioned the preservation of fiber integrity and length is an issue. The loss of fiber length can be minimized partially with screw design by increasing the flight depth and by isolating machine parameters that have the greatest effect on fiber length.<sup>14</sup>

Large weight percent, long fiber composites are typically formed by a process termed pultrusion. Pultrusion is similar to the technique used in wire coating, in which a bundle of parallel continuous fibers are forced through a heated die and encapsulated by a polymer sheath. The continuous strand can then be cut or pelletized to the desired length. Pultrusion yields composites in a pellet form with a narrow fiber length distribution, but the fibers are generally concentrated at the center of the pellet resulting in inadequate dispersion and imperfect wetting of the fibers by the polymer.<sup>9</sup> The pellets are then processed, typically in an extruder where mechanical degradation becomes a repeating issue. Surprisingly, long glass fiber composites tend to maintain their length distribution better than the short glass fiber samples in conventional processing equipment.<sup>13</sup>

In-situ polymerization can yield composites of varying orientation from isotropic to collimated, where the fibers are completely wetted by the matrix material.<sup>9</sup> This method represents an improvement in dispersion and wetting of the fibers compared to direct melt compounding of dry fibers with polymer. However, in situ polymerization is typically not economically feasible for large scale production. Currently this method is used to apply functional coatings as described in the previous section.

### **2.1.5 Orientation Analysis**

The measurement of fiber orientation within a suspension in its molten or consolidated state is a more complex task, especially since the orientation can vary considerably through the thickness of the sample. Current methods used to quantify the orientation include transmission optical microscopy<sup>7</sup>, contact microradiography<sup>15</sup>,

scanning acoustic microscopy<sup>16</sup>, scanning electron microscopy<sup>17</sup>, nuclear magnetic resonance (NMR) imaging<sup>18</sup>, x-ray tomographical imaging,<sup>19</sup> and reflection microscopy.<sup>20</sup> Many of these techniques offer different strengths, but have similar weaknesses dealing with image resolution, and sample size that can be effectively quantified. Transmission optical microscopy, contact microradiography and scanning acoustic microscopy only provide two dimensional images, typically with poor resolution.<sup>21</sup> An automated approach has yet to be developed that incorporates the imaging ability of scanning electron microscopy, NMR imaging, and x-ray tomography<sup>8</sup> which reduces the sample size that can be measured. Reflection microscopy has become the most popular and widely used method. Though it is not clear who or when the ideas for this method were developed, it is known that its foundation stems from simple geometric analysis of ellipsoids and was directly used to quantify fiber orientation by Darlington and McGinley<sup>15</sup> as early as 1975. This method suffered from the same insufficiencies in being able to process large sample sections to acquire accurate orientation distributions until the advent of economical, high-speed, image analysis systems.<sup>22, 23</sup>

In reflection microscopy a section of the sample is cut, often normal to the flow direction encapsulated in an epoxy resin and polished to a smooth surface. The epoxy prevents the degradation of the fibers at the edges of the ellipses. Contrast between the matrix and the fiber is produced by oxygen plasma etching; this process creates a rough surface around the glass fibers which appear dark in reflected light.<sup>8</sup> The three dimensional orientation of the individual fibers is then calculated from the ellipse that occurs where the fibers intersect the section plane.

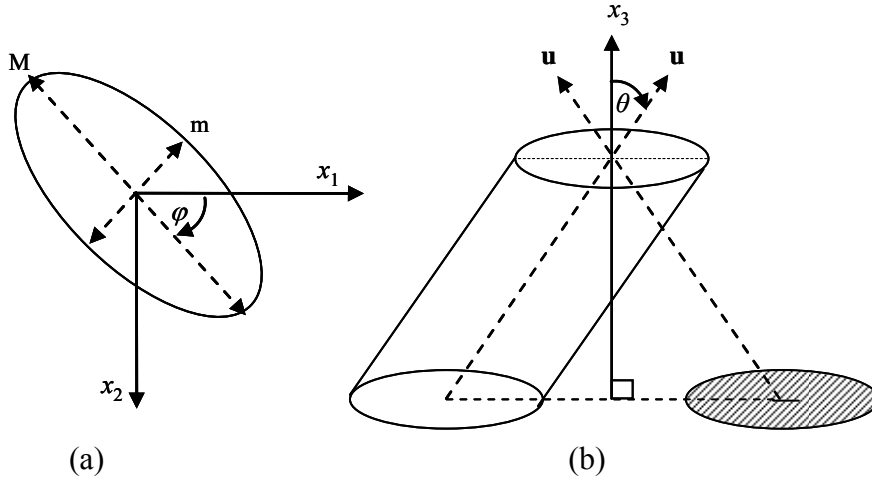


**Figure 2.1.** Fiber orientation angles  $\theta$  and  $\varphi$ , determined from the elliptical projection.<sup>8</sup>

The orientation of each fiber can be described using a unit vector,  $\mathbf{u}$ , along the backbone of fiber. The zenith and azimuthal angles  $\theta$ ,  $\varphi$  defining the components of  $\mathbf{u}$  for a each fiber can be calculated based on the ratio of the minor and major axis and is dependant on which plane is being processed, Eq. (2.1); the other angle can be measured directly from the image.<sup>24</sup> Figure 2.1 (a) depicts the elliptical foot print in the  $x_1 - x_2$  plane and the angle  $\varphi$  measured directly from the image.

$$\cos \theta|_{1-2} = \frac{m}{M}, \quad \cos \varphi|_{2-3} = \frac{m}{M} \quad (2.1)$$

The subscript 1-2 or 2-3 refers to the plane being processed. The limitation of calculating the angle based on Eq. (2.1) is that the calculated angle is always between 0 and  $\pi$  causing an inherent ambiguity. For example, in the  $x_1 - x_2$  plane it is impossible to distinguish between a fiber that is oriented  $(\theta_1, \varphi_1)$  and  $(\pi - \theta_1, \varphi_1)$  because their cross

sections are identical. Figure 2.1 (b) depicts two possible unit vectors  $\mathbf{u}$  for the same elliptical footprint.

Other limitations of this method include many assumptions that have to be made about the distribution of fiber lengths and fiber orientations to be able to apply certain correction factors for counting bias.<sup>25, 26</sup> Also, the technique is limited to short glass fiber composites due to increased and incalculable errors associated with fibers that are not perfectly straight.<sup>21</sup> In the case of long glass fibers, no dedicated assessment protocol has been identified in literature.<sup>14</sup> Techniques such as x-ray tomography have the ability to capture the 3D spatial distribution, but currently there is no analysis software capable of quantifying the orientation.

## **2.2 Rheology of Non-Newtonian Fluids Containing Glass Fibers**

The following is a review of the experimental literature pertaining to the rheological behavior of non-Newtonian fluids containing glass fibers. Before reviewing the rheology it is imperative to have a basic understanding of glass fiber suspensions, the rheometers used to characterize them and any extra forces that can lead to mechanisms for changes in the fiber microstructure. For this reason in subsection § 2.2.2 we classify fiber suspensions by their concentration and length. This is followed by a review of the different rheometers and rheometer geometries used to characterize glass fiber suspensions including a discussion of their strengths and weaknesses with respect to obtaining accurate measurements of rheological material functions. Lastly, we discuss and estimate the contribution of Brownian motion and gravity (relating to particle

sedimentation) to changes in fiber orientation within the suspension. This is followed by a critical review of the rheological behavior including both shear (in subsection § 2.2.3) and shear-free flows (in subsection § 2.2.4) after which we discuss flow phenomena such as the Weissenberg effect and extrudate swell in subsection § 2.2.5. The review concludes with a summary of the findings in subsection § 2.2.6.

### **2.2.1 Abstract**

The objective of this review is to elucidate the rheological behavior of glass fiber suspensions whose suspending mediums are non-Newtonian fluids. In particular, this review focuses on determining the impact of fiber concentration, aspect ratio, orientation distribution, interaction with the suspending medium and suspending medium viscoelasticity on the rheology of glass fiber composite fluids. The presence of glass fiber can induce a yield-like behavior causing shear thinning to occur at reduced shear rates. Glass fiber can impede the elastic properties of the suspending medium but enhance the first normal stress function. Large stress overshoots in both the shear and normal stress growth functions are observed which are associated with changes in fiber orientation. Upon cessation of flow, stress relaxation follows that of the suspending medium but fibers retain their orientation. The presence of glass fiber can induce extension rate thinning and suppress the strain thickening behavior of the suspending medium.

## 2.2.2 Background

### 2.2.2.1 Classifying Glass Fiber Suspensions by Concentration

As discussed later, the dynamic behavior of fiber suspensions is highly dependent on the concentration and length of the fibers within the suspension. For this reason we define three concentration régimes based on the degree of particle interaction and fiber excluded volume, as dilute, semidilute, and concentrated. Following the theory of Doi and Edwards<sup>27</sup>, we consider a suspension of  $n$  fibers per unit volume, of equal length  $L$ , diameter  $D$  and corresponding aspect ratio  $a_r = L/d$ . The fiber concentration described through the volume fraction  $\phi$  is defined as

$$\phi = \frac{\pi n L D^2}{4} = \frac{\pi n L^3}{4 a_r^2} \quad (2.2)$$

For comparison purposes, subsequently we will report the volume fraction limits associated with the three concentration régimes for a test fiber of  $D = 15 \mu\text{m}$  and  $L = 1.5 \text{ mm}$  with corresponding  $a_r = 100$ .

**(a) Dilute Régime.** The dilute régime is described as one having a sufficiently low concentration of fibers in which a fiber is free to rotate without interference from contact with other fibers. Furthermore, it is assumed there is no hydrodynamic interaction. Theoretically, this occurs when the average distance between the center of mass of two rods is greater than  $L$ . Therefore, a perfectly disperse suspension must obey the constraint  $n < 1/L^3$  to be considered dilute. This can be related to the fiber aspect ratio

and volume fraction by  $4\phi < \pi a_r^{-2}$  which is roughly  $\phi < a_r^{-2}$ . A dilute suspension containing our test fiber would be subject to the constraint  $\phi < 0.0001$ .

**(b) Semidilute Régime.** The semidilute régime is such that hydrodynamic interaction, as a result of the relatively close proximity between fibers, is the predominant phenomena and some physical contact between fibers is present. However, the suspension orientation state is not subject to geometric constraints, i.e. can be completely random. Interaction between fibers is achieved when  $n > 1/L^3$  but when the mean spacing between fibers,  $S_m$ , is on the order of the diameter of the fiber, physical contact between rods becomes an increasingly significant phenomena; therefore the upper limit is subject to the constraint  $S_m \gg D$ .<sup>28</sup> The mean spacing between fibers is a function of the orientation state of the rods within the suspension. For a random orientation state the mean spacing is estimated as  $S_m \cong 1/(nL^2)$  and for a suspension whose fibers are completely aligned the mean spacing is of the order  $S_m \cong (nL)^{-1/2}$ .<sup>29, 30</sup> This leads to two upper limits:  $n \ll 1/(DL^2)$  for random and  $n \ll 1/(D^2L)$  for aligned orientation. This can be related to the fiber aspect ratio and volume fraction by  $\phi \ll (\pi/4)a_r^{-1}$  which is roughly  $\phi \ll a_r^{-1}$  and  $\phi \ll \pi/4$  respectively. A randomly oriented, semidilute suspension containing our test fiber would be subject to the constraints  $0.0001 < \phi < 0.01$ .

**(c) Concentrated Régime.** The concentrated régime is where  $n \geq 1/(DL^2)$  or  $\phi \geq a_r^{-1}$ . In this range the dynamic properties of the rods can be severely affected by fiber-fiber interactions and can lead to solid-like behavior.<sup>28</sup> Above some critical concentration  $\phi^*$ , rod-like molecules will preferentially align and become nematic. Doi and Edwards estimated the critical concentration to be  $\phi^* \cong 4a_r^{-1}$  and Flory<sup>31</sup> estimated  $\phi^* \cong 12.5a_r^{-1}$ . It is not clear whether fibers within a suspension will also preferentially align but it seems

reasonable, for rigid fibers, that geometric constraints would cause this to occur. A concentrated suspension containing our test fiber would be subject to the constraint  $\phi > 0.01$  and the critical concentration for alignment, following Doi and Edwards, would be  $\phi^* \cong 0.04$ . As a note, glass fiber composites of industrial interest typically have fiber concentrations of  $\phi > 0.1$ .

### 2.2.2.2 Classifying Glass Fiber Suspensions by Length

In suspensions containing a distribution of fiber lengths the two most common averaging techniques used are the number average ( $L_n$ ) and weight average ( $L_w$ ) defined as

$$L_n = \frac{\sum_i n_i L_i}{\sum_i n_i} \quad (2.3)$$

$$L_w = \frac{\sum_i n_i L_i^2}{\sum_i n_i L_i} \quad (2.4)$$

The majority of the literature refers to the number average when calculating  $a_r$  and in defining the concentration régime of interest and will be used for this review unless otherwise specified.

Huq and Azaiez<sup>32</sup> compared the steady shear viscosity of mono-disperse and poly-disperse suspensions and found that of the standard fiber length averages  $L_w$  gave the best

representation, but was still inaccurate at representing the effect of fiber length on the shear viscosity. Their study suggested that the following average, termed here as  $L_{HA-avg}$ , was more appropriate and is defined as

$$L_{HA-avg}^2 = \frac{\sum_i n_i L_i^3}{\sum_i n_i L_i} \quad (2.5)$$

The authors state that this average is only valid for the dilute and semidilute concentration régime.

In general, the fiber length of glass fiber suspensions is divided into two classes: short and long. Exactly what determines a fiber to be categorized as short or long is somewhat ambiguous, but usually short glass fiber suspensions contain fibers that are assumed to remain rigid during flow. Conversely, long glass fibers are ones that flex while the fluid is deformed. Kumar et al.<sup>33</sup> state that short glass fiber composites contain glass fibers with  $a_r < 100$ . Little work has been done to mathematically establish boundaries that separate short from long glass fiber suspensions. However, Forgacs and Mason<sup>34</sup> developed an equation to estimate the critical extra stress,  $\tau_{critical}$ , at which the shear-induced axial compression can cause a rotating fiber to buckle:

$$\tau_{critical} \cong \frac{E_f [\ln(2a_r) - 1.75]}{2a_r^4} \quad (2.6)$$

where  $E_f$  is the flexural or bending modulus of the fiber. The authors found the equation to be in reasonably good agreement with experimental results for nylon, dacron and rayon fibers with diameters of 12.2, 7.8 and 3.5  $\mu\text{m}$  respectively, and various lengths resulting in aspect ratios ranging from 170-310. As an estimate this same approach can be applied to glass fiber. For glass fibers with  $a_r = 20, 60, 100$  and 600 the critical shear stress, using Eq. (2.6), is calculated to be  $\tau_{critical} = 4.4*10^5, 8.5*10^3, 1.3*10^3$  and 1.5 (Pa) respectively, assuming  $E_f \approx 73 \text{ GPa}$ .<sup>35</sup> Defining a dilute fiber suspension as short or long depends on the shear stress seen by the fiber within the fluid. In more concentrated suspensions direct contact forces can lead to other mechanisms for fibers to bend but the complexity of the problem makes it difficult establish a relationship for a  $\tau_{critical}$  which is a function of concentration or number of fiber contact points. Regardless, in low shear stress flow fields (i.e. low shear rate rheometrical flows) fibers with  $a_r < \sim 100$  typically can be classified as short fibers. In high shear stress flow fields (i.e. injection molding) fibers with  $a_r < \sim 40$  typically can be classified as short fibers.

### **2.2.2.3 Rheometry: Flow Field and Boundary Effects**

Many different shear rheometers have been used to characterize the rheology of fiber suspensions. The most commonly used for polymer melt suspensions are torsional and capillary rheometers and, in a few instances, sliding plate rheometers.<sup>36</sup> Also, for low viscosity suspensions concentric cylinder<sup>32, 37</sup>, falling ball<sup>38</sup>, and Couette<sup>39</sup> viscometers have been used. It is of importance to note that the type of rheometer used to characterize a fluid containing relatively large particles when compared to the rheometer flow field

dimensions may influence the rheology. This can occur through boundary interactions, flow field complications associated with curvilinear streamlines and particle migration during testing. Subsequently, we review the strengths and weaknesses of the different rheometers used to characterize glass fiber suspensions. First, we look at torsional and sliding plate shear rheometers followed by pressure driven flow capillary rheometers.

**(a) Torsional Rheometers.** Torsional rheometers are commonly used to characterize the low shear rate rheology of glass fiber suspensions. Traditionally, this type of rheometer utilizes cone-and-plate (CPR) or parallel-plate (PPR) fixtures with small gaps (CPR  $\sim$  .05 mm, PPR  $\sim$  0.5-2 mm) and plate diameters ranging from 25 – 75 mm. In general CPRs provide a homogeneous shear field but allow for no gap control and can impart a flow history on the sample as it is *squeezed* to proper gap dimensions. PPRs allow a certain amount of gap control but the shear rate varies from the center of the plate to the outer edge resulting in an inhomogeneous shear field. Because the rate of fiber rotation is dependent on the shear rate, an inhomogeneous shear field could result in increased fiber-fiber interaction during transient changes in the fiber microstructure. However, this issue has not been addressed in literature.

Boundary interactions can occur when the rheometer gap is small compared to the characteristic length of the filler.<sup>40</sup> For a fiber, the characteristic length can significantly change depending on its orientation. For instance, a fiber whose orientation is in the shear direction has a characteristic length that is equal to the length of the fiber, while a fiber that is aligned in the flow direction has a characteristic length equal to the diameter of the fiber.<sup>40</sup> Glass fibers in composite fluids of industrial interest typically have a diameter on the order of 10  $\mu\text{m}$  with the majority between 13-16  $\mu\text{m}$  and average lengths

which range from roughly 0.1-12.5 mm and in some cases exceed 25 mm. To minimize fiber-boundary interaction Blankeney<sup>37</sup>, and Attanasio et.al.<sup>41</sup> suggested that the sample thickness should be greater than three times the characteristic length of the filler. Mondy et al.<sup>42</sup> calculated that for a non-spherical particle to maintain its periodic rotation - mathematically described by Jeffery<sup>43</sup> and termed “Jeffery orbit”- the distance between the boundaries must be greater than four times the characteristic length of the particle.

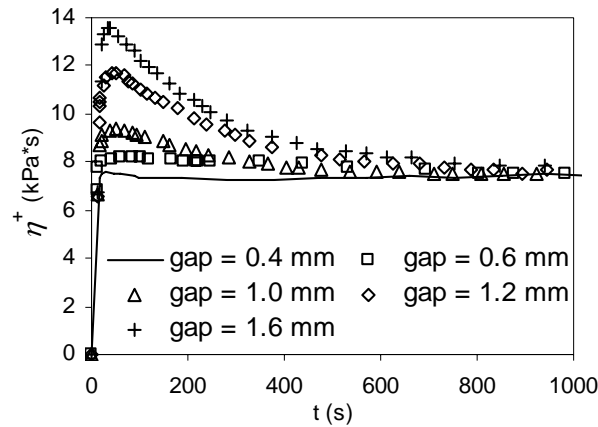


**Figure 2.2.** Effect of gap height, in a torsional PPR, on the shear stress growth coefficient in startup of shear flow for a glass fiber-filled polypropylene (PP),  $\phi = 0.0354$ , the fiber length was not given.<sup>44</sup>

Boundary interactions are most probable in the case of a fiber tumbling in the shear plane. The effect of boundary interaction can be seen in Fig. 2.2. Figure 2.2 is a plot of the shear stress growth coefficient in startup of shear flow for a glass fiber-filled polypropylene (PP) with increasing gap in a PPR; the length of the fiber was not given.<sup>44</sup> The shear stress growth coefficient is clearly dependent on the gap height in the initial startup region; the magnitude of the overshoot is greater for experiments performed with a larger rheometer gap. However, the steady-state value is unaffected by gap height. This is believed to be a result of the boundaries interfering with fiber end-over-end

rotation during startup of shear flow for a sample whose initial fiber orientation is not aligned in the flow direction. Sepehr et al.<sup>45</sup> found minimal gap height dependence above a gap height of 1.4 mm in a PPR for a suspension containing glass fibers with an average length of 0.26 mm.

In the case of torsional shear devices the presence of curvilinear streamlines may also lead to inaccuracies in rheological measurements of glass fiber suspensions. When a suspension is deformed the fibers try to establish an orientation of least resistance to flow, aligned parallel to the streamlines. Rigid fibers, however, can never fully align themselves with the curvilinear streamlines. Although there is no recorded quantification of this factor it must be taken into consideration in the accuracy of the rheological measurements in torsional devices, especially in the case of suspensions containing long fibers.

**(b) Sliding Plate Rheometers.** In an attempt to reduce the error associated with torsional rheometers Owen et al.,<sup>46</sup> Laun,<sup>47</sup> and Ericsson et al.<sup>36</sup> employed a sliding plate rheometer that generates a rectilinear flow field. No indication was given on the ability to perform transient experiments where fiber tumbling and boundary interaction could be an issue. However, theoretically, very large gaps can be employed which could reduce error associated with fiber-boundary interactions. As a note, no estimations were made about error reduction associated with this flow geometry compared to torsional rheometers but it is believed that this type of rheometer represents an improvement in obtaining accurate rheological measurements.<sup>36</sup> One disadvantage to using a sliding plate rheometer is the maximum strain one can achieve is limited and is dependent on rheometer design.

**(c) Capillary Rheometers.** Capillary rheometers have traditionally been used to investigate the deformation behavior of fiber suspensions at high shear rates. In this case the suspension is forced through an abrupt contraction and the pressure drop is measured across the contraction and capillary length. Studies have shown that particle migration can occur away from the channel wall across streamlines, in laminar flow, due to small inertia and wall effects termed “*tubular pinch*”. Experimentally, this was first observed by Segré and Silberberg<sup>48, 49</sup> for a dilute suspension of neutrally buoyant spheres in flow through a pipe. As a result of the particle migration the authors found a maximum concentration at a radial position from the centerline to pipe radius ratio ( $r/R$ ) of 0.6. Koh et. al.<sup>50</sup> discovered similar results in which a concentration maximum was found near the center in a rectangular channel for a concentrated suspension. Conversely, Wu<sup>51</sup> reported the opposite behavior for a short glass fiber-filled polyethylene terephthalate (PET) where he found the concentration of fiber to deplete near the relative radial position  $r/R = 0.63$  and accumulate near the surface and axis. Mondy et. al.<sup>52</sup> studied suspensions of rods in a Newtonian suspending medium and found shear-induced particle migration to occur out of higher-shear-rate regions of flow until the shear rate gradients are balanced by concentration gradients. The rate at which migration occurs was found to increase with increasing rod volume but be independent of rod aspect ratio. Becraft and Metzner<sup>53</sup> found no large scale fiber migration but did find local variations in concentration. The degree of particle migration in glass fiber suspensions is unclear. However, if migration does occur away from the boundaries, the regions of highest shear rates, close to the capillary wall, could contain a far less concentration of fibers which results in a stress response similar to the pure matrix.<sup>54</sup>

**(d) Summary of Rheometers.** The rheological response of a suspension can be influenced by the rheometer used to characterize it.<sup>36</sup> The influences are a result of boundary interactions, flow field complications associated with curvilinear streamlines and possibly particle migration. Fiber-boundary interactions are most prevalent in the case of a fiber tumbling in the shear plane, as can be found in the startup of shear flow experiments, when the rheometer gap height is roughly the same size or smaller than the characteristic length of the fiber.<sup>40</sup> In this case the transient stress response can be masked by the boundaries interfering with fiber rotation as depicted in Fig. 2.2. Flow field geometry complications can occur in torsional rheometers or in any case where the rheometer flow field streamlines are curvilinear and significantly differ from the geometry of the particle. Inhomogeneous shear, as in PPRs, could potential result in a greater degree of fiber-fiber interaction, of which, the effects on the rheology have not been investigated. Particle migration can possibly occur in the case of abrupt contractions in pressure driven flow rheometers (as in capillary rheometers). This behavior can result in a stress response similar to the matrix, masking the presence of the fiber.<sup>51</sup>

The statements above outline possible sources of error associated with typical melt rheometers used to characterize the rheological behavior of fiber suspensions. However, these rheometers have been widely used by researchers to characterize the rheology of fiber suspensions due to their availability and temperature control capabilities useful for polymer melts. As a result it is difficult to quantitatively asses the rheological behavior of glass fiber suspensions, especially long glass fiber suspensions, but the published rheological measurements still allow for qualitative relations to be made. Ideally, any

rheological measurement should be performed in a “sufficiently large” device so that the boundary and flow field effects are minimized.<sup>40</sup>

#### 2.2.2.4 Impact of Brownian Motion and Sedimentation

Subsequently, we discuss Brownian motion and sedimentation with the intent of clarifying the contributing forces that can lead to either dynamic or static changes in fiber orientation and position.

**(a) Brownian Motion.** Brownian motion refers to the random movement of a sufficiently small particle suspended in a fluid. The movement of the particle is a result of a random number of impacts, of various strength, from random directions by molecules of the suspending fluid. Therefore, the effects of Brownian motion are only seen in systems where the particles are small enough to be affected by the bombardment of molecules. In a system of sufficiently small rods where Brownian motion effects are present (i.e. liquid crystalline molecules), the rods exhibit two kinds of Brownian motion, translational and rotational. Translational Brownian motion is the random motion of a position vector indicating the center of mass of the rod and rotational Brownian motion is the random motion of the unit vector around the center of mass.<sup>27</sup>

The most common way to determine if a particle is affected by Brownian motion is to calculate the Péclet number (Pé). The Péclet number is defined as the dimensionless ratio of the shear rate,  $\dot{\gamma}$ , to the rotational diffusion constant,  $D_r$ . The rotational diffusion constant represents the rate at which a particle changes its orientation with respect to rotational Brownian motion.  $D_r$  is defined as

$$D_r = \frac{k_B T}{\xi_r} \quad (2.7)$$

where  $k_B$  is Boltzmann's constant,  $T$  is the temperature in Kelvin and  $\xi_r$  is the rotational friction constant. For a cylinder of  $a_r > 3$  the rotational friction constant is given by

$$\xi_r = \frac{\pi \eta_s L^3}{3 [\ln(a_r) - \alpha_c]} \quad (2.8)$$

where  $\eta_s$  is the viscosity of the suspending medium and  $\alpha_c$  is a correction factor. Calculations based on the point force approximation give  $\alpha_c = 0.8$  as a good estimate.<sup>55</sup> At small  $Pe$ , Brownian effects are significant and can dominate the rod motion leading to particle orientations, under static conditions, that are close to random. Conversely, at high  $Pe$  the effects of Brownian motion are insignificant and hydrodynamic forces dominate particle motion. For comparison purposes, a thermotropic copolyester liquid crystalline polymer commercial name Vectra A900 (copolyester of 27 mole % 2-hydroxy-6-naphthoic acid and 73 mole % hydroxybenzoic acid) has a  $D_r \sim 12.2 \text{ s}^{-1}$  at its melt temperature of 283°C, while a short glass fiber ( $L = 0.5 \text{ mm}$ ,  $d = 15 \text{ }\mu\text{m}$ ) in a viscous suspending medium ( $\eta_s = 1,000 \text{ Pa}\cdot\text{s}$  at 200 C) has a  $D_r \sim 10^{-13} \text{ s}^{-1}$ . Larson<sup>56</sup> makes the statement that a particle whose longest dimension exceeds  $\sim 10 \text{ }\mu\text{m}$  can be considered non-Brownian.

**(b) Sedimentation.** To support discussion later in the review it is of interest to estimate the effect that gravity has on a fiber within a fluid not subjected to deformation.

Chaouche and Koch<sup>57</sup> proposed an expression to estimate the relative time scale for sedimentation,  $t_s$ , the time required for a fiber parallel to the vertical direction to sediment over its length, as

$$t_s = \frac{8\eta_s L}{\Delta\rho g D^2 [\ln(2a_r) - 0.72]} \quad (2.9)$$

where  $\Delta\rho$  difference between the densities of the suspending medium and the particle and  $g$  is the acceleration due to gravity. The sedimentation time scale for our test fiber ( $D = 15 \mu\text{m}$  and  $L = 1.5 \text{ mm}$ ,  $\rho = 2.617 \text{ g/cm}^3$ ) in a fluid of  $\eta_s = 100 \text{ Pa}\cdot\text{s}$  ( $\rho = 0.9 \text{ g/cm}^3$ ) using this approach is calculated to be  $t_s \sim 19 \text{ hr}$ . As a comparison, the sedimentation time scale for a similar suspension with  $\eta_s = 10 \text{ Pa}\cdot\text{s}$  and fiber  $L = 0.15 \text{ mm}$  is estimated to be  $t_s \sim 0.4 \text{ hr}$ . This time increases with fiber length and is proportional to the viscosity of the suspending medium. Obviously, this basic estimation does not take into account fiber-fiber interactions that would also act to increase the sedimentation time. In glass fiber suspensions of very small fibers in low viscosity fluids gravity could potentially effect fiber position and orientation under static conditions. However, it is typically assumed that gravity has no effect on fibers in polymer melts.

## 2.2.3 Shear Rheology

### 2.2.3.1 Steady Shear Flow

In the case of simple shear flow, as found in rheometrical flows, the fluid velocity occurs in one direction only ( $v_1 = \dot{\gamma} x_2$ ,  $v_2 = v_3 = 0$ ) and the shear rate is assumed to be constant within the rheometer gap. With these assumptions and following the official nomenclature for material functions of viscoelastic fluids<sup>58</sup>, the non-Newtonian fluid shear viscosity  $\eta$ , can be defined through the shear stress as

$$\eta = \sigma / \dot{\gamma} \quad (2.10)$$

In the same manner, the first and second normal stress functions,  $N_1$  and  $N_2$  respectively, are defined as

$$N_1 = \sigma_{11} - \sigma_{22} \quad (2.11)$$

$$N_2 = \sigma_{22} - \sigma_{33} \quad (2.12)$$

In addition, we refer to  $N_1 - N_2$  as the normal stress function difference. The subsequent review of literature pertaining to the shear rheology of glass fiber suspensions begins with the shear viscosity followed by a review of first and second normal stress functions.

**(a) Shear Viscosity.** The addition of glass fiber to either a Newtonian or non-Newtonian fluid enhances the shear viscosity when compared to the neat suspending medium, especially at low shear rates. The degree to which the shear viscosity is affected is a function of the fiber concentration, aspect ratio, and orientation distribution.<sup>40</sup> In the subsequent section, the effect that fiber concentration and aspect ratio have on Newtonian fluids is outlined first, as a basis for comparison to glass fiber suspensions in non-Newtonian fluids. We then review the effects of fiber concentration, aspect ratio, and shear history (i.e. orientation distribution) on shear viscosity of non-Newtonian fluids. Finally we consider the temperature dependence of the shear viscosity.

In general for suspensions of glass fibers in Newtonian fluids, in the dilute and semidilute fiber concentration régime, the shear viscosity has a linear dependence with fiber concentration, that increases with aspect ratio.<sup>59</sup> A deviation from this general trend was found by Milliken et al.<sup>38</sup> when they performed experiments on a suspension of short glass fibers ( $a_r = 19.8$ ) in a Newtonian suspending using a falling ball viscometer. Their results suggested that the shear viscosity dependence on the volume fraction of fibers changes from a linear correlation for dilute suspensions to a cubic dependence on volume fraction at the transition between dilute and semidilute concentrations. As a note, the aspect ratio was not varied in the experiment.

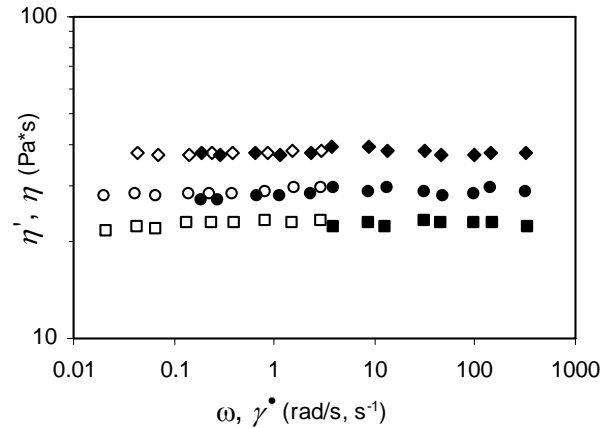


**Figure 2.3.** Shear viscosity vs. shear rate (filled symbols) and the dynamic viscosity vs. frequency (unfilled symbols) for short glass fibers ( $a_r = 24.3$ ) in a Newtonian suspending medium of various fiber concentration,  $\phi = 0$  (■, □), 0.05 semidilute (●, ○), 0.08 concentrated (◆, ◇). All measurements were performed on a torsional PPR.<sup>59</sup>

The presence of fiber has been shown to induce shear thinning characteristics in Newtonian fluids, the degree of which is dependent on the concentration and aspect ratio of the fiber. At low concentrations and small aspect ratios, in the dilute to semidilute concentration régimes, fiber suspensions in Newtonian suspending mediums show little to no dependence on shear rate, as shown in Fig. 2.3 (filled symbols). Fig. 2.3 is an example of the shear viscosity vs. shear rate for a Newtonian fluid containing various fiber concentrations of  $\phi = 0$ , 0.05 (semidilute), and 0.08 (concentrated). The unfilled symbols represent the real component of the complex viscosity vs. frequency and will be commented on in a later subsection. In this case, the presence of glass fiber enhances the magnitude of the shear viscosity, but it remains fairly constant over the complete range of shear rates tested. However, for suspensions containing higher concentrations, especially with large aspect ratio fibers the shear thinning behavior can be significant. Ganani and Powell<sup>59</sup> reviewed much of the literature in the area of glass fibers suspended in Newtonian fluids and found that for suspensions containing fibers with aspect ratios in

the range of 35-45 a weak shear thinning behavior was noticed at low shear rates, followed by a Newtonian plateau at  $\dot{\gamma} > 10 \text{ s}^{-1}$ . For  $a_r > 100$ , the authors found a strong shear rate dependence that was seen over a shear rate range of  $0.1 - 100 \text{ s}^{-1}$ . The shear thinning behavior of non-dilute suspensions of glass fibers in a Newtonian fluid is explained by the destruction of transient network structures of fibers at increasing shear rates.<sup>60</sup>

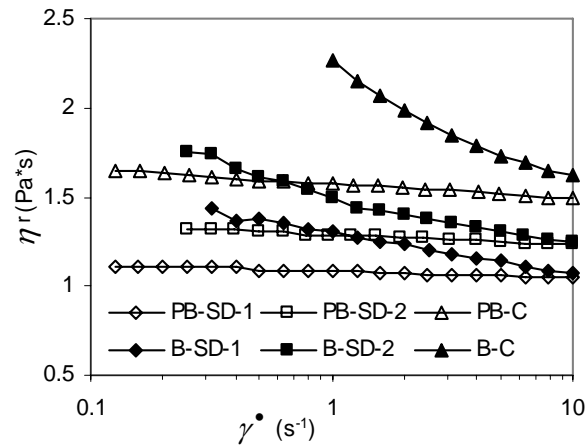
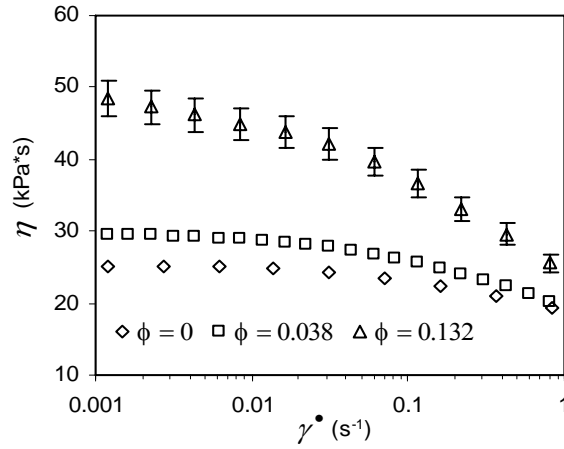


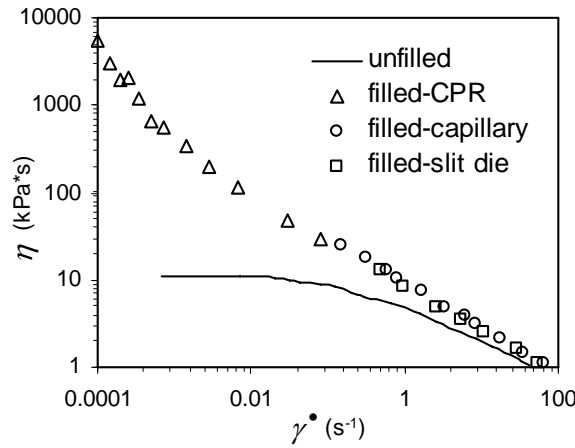
**Figure 2.4.** Reduced shear viscosity vs. shear rate for various concentrations of glass fiber ( $a_r \sim 20$ ) suspended in polybutene (PB, a Newtonian fluid) and a Boger fluid (B). The fiber volume fractions are  $\phi = 0.0158$ ,  $0.0327$ , and  $0.0706$  termed SD-1, SD-2 (semidilute régime) and C (concentrated régime), respectively. All measurements were performed on torsional PPR with gap-to-fiber length ratio greater than 3.<sup>45</sup>

The effect of glass fiber on the shear viscosity significantly changes with the viscoelastic nature of the suspending medium. This behavior can be seen in Fig. 2.4 for two model suspensions containing short glass fibers of  $a_r \sim 20$ : a polybutene (PB) suspension (roughly a Newtonian fluid) and a Boger fluid suspension (a fluid that exhibits elastic behavior but has little shear rate dependence). Similar to the suspensions in a purely Newtonian fluid, the reduced shear viscosity of the PB suspension increases in

a linear manner with the fiber volume fraction. The reduced shear viscosity refers to the fiber suspension viscosity normalized by the viscosity of the suspending medium at constant temperature, pressure and shear rate,  $\eta_r \equiv \eta / \eta_s$ . Also, while it is difficult to detect, the authors state that the suspension exhibits a slight shear thinning behavior that was not present in the neat PB.<sup>45</sup> At similar fiber concentrations the fiber-filled Boger fluid exhibits an increasing yield-like behavior and greatly enhanced shear thinning characteristics. Interestingly, the Boger fluid is 91.0 mass % the same composition of the Newtonian fluid, with 0.6 mass % of a high MW polyisobutene, and 8.4 mass % kerosene. The polyisobutene is the source of the elastic properties and apparently lead to the enhanced effect of the fibers. It is thought that this behavior is a result of increased fiber-fiber interaction through a pseudo network formed by adsorption of the high molecular weight chains onto the glass fibers.<sup>45</sup> This interaction is increased and the effects enhanced by the use of surface treatments to the glass fiber.<sup>54, 61, 62</sup> However, due to the lack of published data, it is still unclear how fiber surface treatments exactly effect the rheology other than enhancing the interaction between the suspending medium and fibers.



(a)



(b)

**Figure 2.5.** Shear viscosity vs. shear rate. (a) Two short glass fiber-filled polypropylene (PP) suspensions ( $\phi = 0.038$ ,  $a_r \sim 30$ , semidilute régime and  $\phi = 0.132$ ,  $a_r = 21.4$ , concentrated régime) and the neat suspending medium. The rheological experiments were performed on a PPR.<sup>11</sup> (b) Short glass fiber-filled high-density polyethylene HDPE ( $\phi = 0.136$ ,  $a_r = 30$ , concentrated régime) and the neat suspending medium.<sup>47</sup> The rheological experiments were performed with various rheometers as indicated in the figure legend.

The presence of glass fiber appears to have an even greater influence on the shear viscosity of suspensions whose suspending mediums are high molecular weight polymer melts, especially at low shear rates ( $\dot{\gamma} < \sim 10 \text{ s}^{-1}$ ).<sup>40, 45, 59, 63, 64</sup> This increases the difficulty in empirically delineating the dependence of the shear viscosity on fiber concentration and aspect ratio. In general, the shear viscosity of suspensions containing a

low concentration of low aspect ratio fiber (in the dilute and semidilute régime) usually approach a Newtonian plateau at low shear rates, and in many instances show little change from the behavior of the neat matrix.<sup>44</sup> The shear viscosity of suspensions containing a high concentration of fiber or fiber with a large aspect ratio (in the concentrated régime), exhibit a more pronounced behavior. At low shear rates the shear viscosity can exhibit a Newtonian plateau as shown in Fig. 2.5 (a) or rise in an unbounded manner and exhibit yield-like characteristics as shown in Fig. 2.5 (b). At high shear rates, shear thinning can occur at a reduced shear rate which can result in a shear viscosity similar to that of the neat suspending medium. Fig. 2.5 (a) shows the shear viscosity vs. shear rate for two short glass fiber-filled polypropylene (PP) suspensions at various concentrations and the neat suspending medium. The shear viscosity of the two suspensions ( $\phi = 0.038$ ,  $a_r \sim 30$ , semidilute régime and  $\phi = 0.132$ ,  $a_r = 21.4$  concentrated régime) appear to reach a Newtonian plateau at low shear rates, within the range of error. However, the increased fiber concentration causes the onset of shear thinning to occur at a lower shear rate. At high shear rates, the shear viscosity merges onto that of the neat matrix. Fig. 2.5 (b) shows the shear viscosity vs. shear rate of a short glass fiber-filled high-density polyethylene (HDPE) suspension ( $\phi = 0.136$ ,  $a_r = 30$ , concentrated régime) and the neat suspending medium.<sup>47</sup> In this case, the glass fiber suspension exhibits a yield-like behavior, and shows a shear thinning response over the whole shear rate range. This behavior is typical of a highly concentrated suspension of glass fibers in a non-Newtonian fluid, though deviations from this behavior do occur. Guo et al.<sup>65</sup> reported no yield-like behavior for a polymer suspension containing up to  $\phi = 0.384$  of short glass fiber in a linear low-density polyethylene with a melt flow index of 3.3. The authors do

not discuss the use of surface treatments on the glass which could affect the interaction with the matrix nor give possible explanation of why no yield-like behavior was observed.

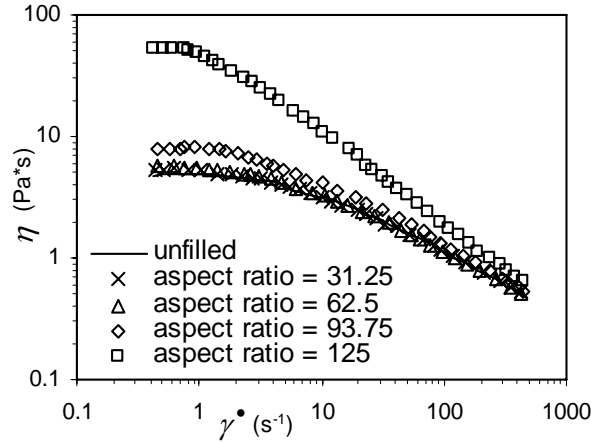


**Figure 2.6.** Shear viscosity vs. shear rate for glass fiber suspensions of various fiber length in a low viscosity non-Newtonian fluid with constant glass fiber concentration ( $\phi = 0.02$ ). The various suspensions have mono-disperse fiber lengths,  $L = 0.5, 1.0, 1.5,$  and  $2.0$  mm, and corresponding aspect ratios,  $a_r = 31.25, 62.5, 93.75,$  and  $125$  respectively. The shortest glass fiber suspension related to the semidilute régime, the rest were concentrated. Rheological experiments were performed with a concentric cylinder rheometer.<sup>32</sup>

The shear viscosity is also highly dependent on fiber length which we describe through the aspect ratio. In general, higher aspect ratio fibers have a stronger contribution to the suspension shear viscosity, as seen in Fig. 2.6. Figure 2.6 shows the shear viscosity vs. shear rate of a suspension of 3 wt% polyethylene oxide in water with  $\phi = 0.02$  of glass fiber of various mono-disperse aspect ratios. The suspension with the smallest aspect ratio relates to the semidilute régime and the others are just above the concentrated régime boundary. The shear viscosity for the suspensions with the shortest aspect ratio show little deviation from the neat matrix, but the highest aspect ratio suspension shows a marked increase. Similar to other highly concentrated suspensions,

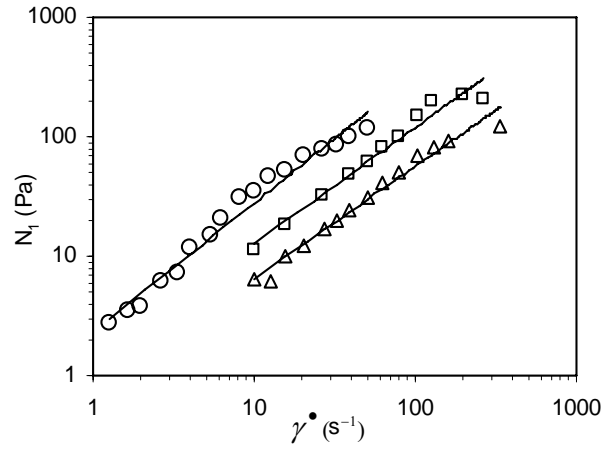
whose shear viscosities deviate considerably from their neat counter parts, the suspension with the greatest aspect ratio exhibited shear thinning behavior at lower shear rates. Deviations from this general trend are scarce but can occur at very large fiber aspect ratios. Ericsson et al.<sup>36</sup> found little effect of fiber aspect ratio between values of  $a_r = 1050$  and  $2100$  for a suspension tested in a sliding plate rheometer. This was attributed to the inability of the long fiber to rotate out of plane and the fibers behaving more as continuous strands than as individual fibers.

The more pronounced effect of fibers on shear viscosity at low shear rates and decreased effects at high shear rates is a reflection of changes in the suspension's microstructure.<sup>44</sup> It is speculated that changes in the fiber orientation distribution in a suspension during flow are irreversible and lead to shear history dependent rheology.<sup>44</sup> It is also speculated that a higher shear rate will impart a higher degree of fiber orientation in the flow direction.<sup>47</sup> As a result, a sample that is pre-sheared may not exhibit the same shear viscosity compared to a sample that has not been sheared or has an isotropic fiber orientation distribution.<sup>66</sup>

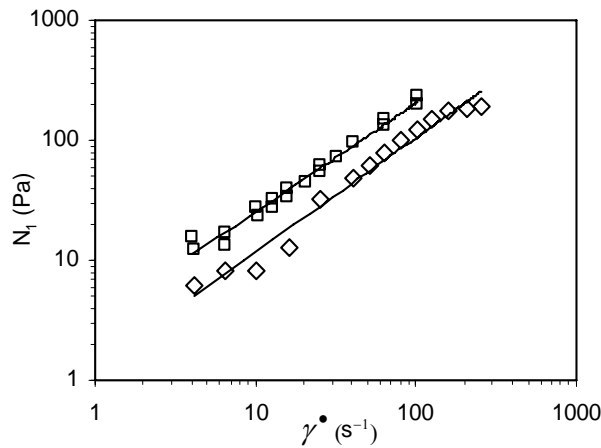
The presence of fiber has little to no influence on the temperature dependence of the shear viscosity.<sup>11, 47</sup> As with all liquids, the viscosity function of polymers and polymer suspensions decreases with increasing temperature.<sup>67</sup> However, the shape of the shear viscosity curve remains constant, even in the case of fiber suspensions where no zero shear viscosity is present.<sup>47</sup> Because of this, a master curve can be formulated using shift factors (time-temperature superposition), that for most polymeric fluids, follow an Arrhenius type temperature dependence.<sup>68</sup> The shift factors for fiber-filled non-Newtonian fluids are similar or the same as that of the neat suspending medium.

Though published information was limited, there was evidence by Greene and Wilkes<sup>69</sup> that glass fibers could reduce the molecular weight of the suspending medium in an amount proportional to the concentration of fibers. The authors found this phenomenon to be evident in both polycarbonate and nylon materials, but had no influence on a polypropylene matrix. This behavior was attributed to mechanical degradation by the fibers, but no discussion was given to hydrolysis or thermal degradation as mechanisms for molecular weight reduction.

**(b) First and Second Normal Stress Function.** The first and second normal stress functions ( $N_1$  and  $N_2$ ) and the difference between them ( $N_1-N_2$ ), defined by Eqs. (2.11) and (2.12), are typically limited to viscoelastic fluids. For unfilled Newtonian fluids both  $N_1$  and  $N_2$  are equal to zero. However, glass fiber suspensions with Newtonian suspending mediums can exhibit significant values of  $N_1$  and the presence of glass fiber can enhance  $N_1$  in viscoelastic fluids. The magnitude of the normal stress functions is dependent on the concentration and aspect ratio of the fiber and the elastic behavior of the matrix.<sup>40</sup> We first review the effect of fiber concentration and aspect ratio on the normal stress functions in Newtonian suspending mediums for comparison purposes. This is followed by a review of the effect that the glass fiber concentration and aspect ratio have on the normal stress functions in non-Newtonian suspending mediums.



(a)



(b)

**Figure 2.7.**  $N_1$  vs. shear rate. All measurements were performed on a torsional CPR. (a) Various glass fiber suspensions containing a constant fiber content ( $\phi = 0.044$ ,  $a_r = 276$ ) but different Newtonian suspending medium viscosities ( $\Delta$  14,  $\square$  16,  $\circ$  120 Pa.s). (b) Two glass fiber suspensions of constant fiber concentration ( $\phi \sim 0.00046$ ) and Newtonian suspending medium with various fiber aspect ratio ( $a_r = \diamond$  276,  $\square$  552).<sup>60</sup>

Many workers have published non-zero values of  $N_1$  and  $N_1 - N_2$  for non-dilute glass fiber suspensions<sup>45, 60, 70, 71</sup> and other high aspect ratio filler suspensions<sup>72, 73</sup> with Newtonian suspending mediums.  $N_1$  is found to be dependent on the viscosity of the suspending medium, and the concentration and aspect ratio of the fiber. In general,  $N_1$  depends linearly on shear rate and by comparing  $N_1$  to  $N_1 - N_2$  it is typically found that  $N_2$  is negligible ( $-N_2 < 10\%$  of  $N_1$ ).<sup>60</sup> Fig. 2.7 (a) and (b) show  $N_1$  vs.  $\dot{\gamma}$  as a function of the

viscosity of the Newtonian suspending medium and aspect ratio of the fiber, respectively; Fig. 2.8 (PB suspension) depicts the concentration dependence. In all three cases, increasing the suspending medium viscosity or the fiber aspect ratio and concentration increased the magnitude of  $N_I$  but the slope of  $N_I$  vs.  $\dot{\gamma}$  stayed roughly at unity.

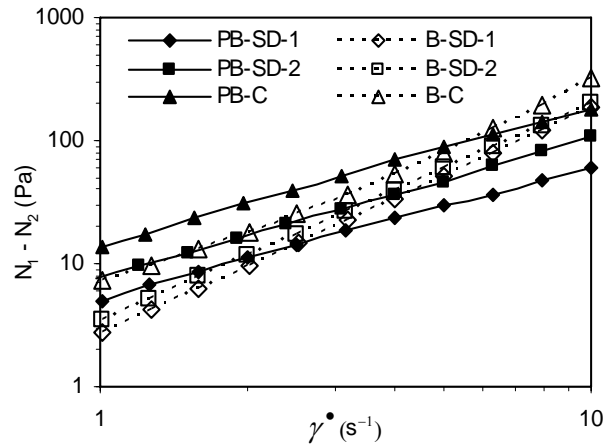


**Figure 2.8.**  $N_I-N_2$  vs. shear rate for various concentrations of short glass fiber ( $a_r \sim 20$ ) suspended in polybutene (PB) and a Boger fluid (B). The fiber volume fractions are  $\phi = 0.0158, 0.0327,$  and  $0.0706$  termed SD-1, SD-2 (semidilute régime) and C (concentrated régime) respectively. All tests were performed on a torsional PPR with gap-to-fiber length ratio greater than 3.<sup>45</sup>

In general,  $N_I$  for fiber suspensions in non-Newtonian fluids follow a similar shear rate dependence as their unfilled counter part at some enhanced value, but in some cases can exhibit a plateau at low shear rates or merge onto the matrix value at high shear rates.<sup>44</sup> The enhanced values of  $N_I$  and  $N_I-N_2$  are believed to be the result of fiber-fiber interactions within the suspension.<sup>45</sup> In addition, fiber interaction can result in imperfect alignment of the fibers in the flow direction.<sup>74</sup> Current theories for fiber suspensions in Newtonian fluids have shown that normal stresses arise when the fiber orientation has a component out of the plane of shear.<sup>75</sup> This behavior can be seen in Fig. 2.8 for a short

glass fiber filled PB and Boger fluid. Fig. 2.8 is a graph of  $N_1-N_2$  vs.  $\dot{\gamma}$  for short glass fiber suspensions of constant  $a_r \sim 20$  with  $\phi = 0.05, 0.1$  and  $0.2$ . An interesting observation when comparing the PB (Newtonian-like) and Boger (viscoelastic) fluid suspensions is the PB suspension exhibits a more pronounced dependence of  $N_1-N_2$  on fiber concentration than the Boger fluid suspension. This behavior agrees with the work of Iso et al.<sup>63, 64</sup>, who compared the end-over-end fiber rotation of a dilute suspension of fibers suspended in a Newtonian and non-Newtonian fluid under simple shear flow conditions. Their experimental results suggest that the elastic nature of non-Newtonian fluids can compete with the fiber-fiber interactions. This same phenomenon is speculated to be the cause of higher values of  $N_1-N_2$  for the PB suspension at low shear rates compared to the values for the Boger fluid suspension.

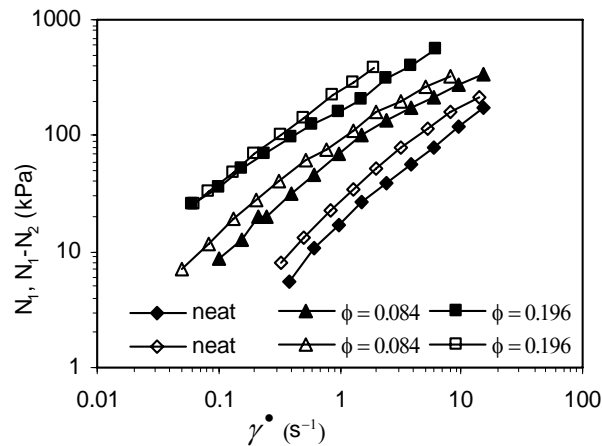


**Figure 2.9.**  $N_1$  and  $N_1-N_2$  vs. shear rate for a short glass fiber-filled HDPE ( $a_r = 157.5$  for  $\phi = 0.084$  and  $a_r = 78.7$  for  $\phi = 0.196$ ). The filled symbols represent  $N_1$  and the unfilled symbols  $N_1-N_2$ .  $N_1$  and  $N_1-N_2$  were obtained using a CPR and PPR, respectively.<sup>76</sup>

$N_2$  in non-Newtonian fluid suspensions is not negligible. This can easily be seen in Fig. 2.9 which is a graph of  $N_1$  and  $N_1-N_2$  vs. shear rate for two short glass fiber-filled

HDPE suspensions of different fiber content.<sup>76</sup> The presence of fiber enhances both  $N_1$  and  $N_1-N_2$  alluding to non-negligible values of  $N_2$ . However, it is currently difficult to conclude on any effect that glass fiber might have on  $N_2$  due to the limited published data.

In general, the presence of glass fiber enhances  $N_1$  exhibited by non-Newtonian fluids. The most significant effect to the normal stresses is seen in the concentrated régime. The existence of non-negligible values of  $N_1$  in glass fiber suspensions in Newtonian suspending mediums suggests that the enhanced normal stresses are a result of fiber interactions and not an enhancement to the elasticity of the suspending medium. Conversely, the presence of glass fiber seems to suppress the normal stresses resulting from the elasticity of suspending medium.

### 2.2.3.2 Small-Amplitude Oscillatory Shear Flow

We now consider the linear viscoelastic behavior of glass fiber-filled non-Newtonian fluids in small-amplitude oscillatory simple shear flow. These experiments involve the measurement of the unsteady response of a fluid when subject to sinusoidal deformations. The complex viscosity and complex modulus are defined as

$$\eta^*(\omega) = \eta' - i\eta'' \quad (2.13)$$

$$G^*(\omega) = G' + iG'' \quad (2.14)$$

respectively, where  $\eta'$ ,  $G'$  are the real and  $\eta''$ ,  $G''$  are the imaginary components. The phase angle  $\delta$  is as  $\tan(\delta) = G''/G'$ . Subsequently, we review the literature pertaining to the linear viscoelastic properties of glass fiber suspensions in non-Newtonian suspending mediums. As an introduction to each section, a brief review is given of fiber suspensions in Newtonian suspending mediums for comparison purposes. As a note, for the following section pertaining to the small-amplitude oscillatory shear flow, it can be assumed that the initial fiber orientation of the samples is random unless otherwise specified.

**(a) Complex Shear Viscosity.** There is a limited amount of published work relating to the complex viscosity of fiber-filled Newtonian fluids. The data that is published suggests only the real or viscous component of the complex viscosity exists. For short glass fiber-filled Newtonian fluids, in the semidilute and concentrated régime, Ganani and Powell<sup>59</sup> found the dynamic viscosity,  $\eta'$ , to be in good agreement with shear viscosity which can be seen in Fig. 2.3. The authors also found  $\eta'$  to remain fairly constant over a frequency range of .06-7.5 rad/s, the magnitude of which increased with fiber concentration. This behavior is similar to unfilled Newtonian fluids where the shear stress oscillates in phase with the shear rate. This suggests that though Newtonian suspensions can exhibit normal stresses, the presence of the fiber does not induce elasticity in Newtonian fluids at small strain amplitudes.

The addition of fibers to a non-Newtonian fluid increases the magnitude of the complex viscosity,  $|\eta^*|$ ; the degree of which is dependent on the concentration, aspect ratio and orientation distribution of the fiber.<sup>11, 65</sup> The dependence of  $|\eta^*|$  on glass fiber concentration and aspect ratio is not obvious. Many authors have published data that

suggests that the addition of glass fiber has little effect on  $|\eta^*|$  when compared to the matrix material in the dilute and semidilute régime.<sup>11, 65, 77</sup> Guo et al.<sup>65</sup> suggested that a small amount of fiber was not sufficient to cause deviations from the properties of the neat matrix in small-amplitude oscillatory shear flow. However, in the concentrated régime the effects are more significant. Similar to the shear viscosity behavior at low shear rates,  $|\eta^*|$  can exhibit an enhanced Newtonian plateau<sup>11, 65</sup> or rise in an unbound manner at low frequencies.<sup>69, 77, 78</sup> At high frequencies,  $|\eta^*|$  can begin to merge onto that of the matrix<sup>69</sup> or follow a similar shear thinning curve of the matrix at a constant enhance value.<sup>11, 65</sup>

$|\eta^*|$  increasingly deviates from the shear viscosity at increasing fiber concentrations for both Newtonian and non-Newtonian fiber suspensions.<sup>38, 65, 77, 79</sup> This suggests that the Cox-Merz relationship<sup>80</sup> does not hold for glass fiber-filled systems. The Cox-Merz rule is an empiricism that states that  $|\eta^*|$  is equal to the shear viscosity at corresponding values of frequency and shear rate:

$$\eta(\dot{\gamma}) = \left| \eta^*(\omega) \right|_{\omega=\dot{\gamma}} \quad (2.15)$$

Deviations from the Cox-Merz rule are typically explained by shear induced fiber orientation changes that are more prevalent in steady shear deformation than in oscillatory shear.

It is speculated that small-amplitude oscillatory shear in the linear strain region is too weak to induce fiber reorientation of the same magnitude as in steady shear flow.<sup>65</sup>  $|\eta^*|$  for a randomly oriented fiber suspension is greater than that of an aligned suspension.<sup>11</sup>

For this reason,  $|\eta^*|$  of a sample with isotropic fiber orientation is typically larger than values of the shear viscosity under the same conditions and corresponding shear rates.<sup>38, 77, 79</sup> A discrepancy from this trend has been published by Guo et al.<sup>65</sup>, where at low frequencies the authors found  $|\eta^*|$  to be lower than the steady shear viscosity at corresponding frequencies and shear rates while the opposite occurred at high frequencies and shear rates for a short glass fiber-filled linear low-density polyethylene (LLDPE). However, no discussion was given about the initial fiber orientation in the samples.

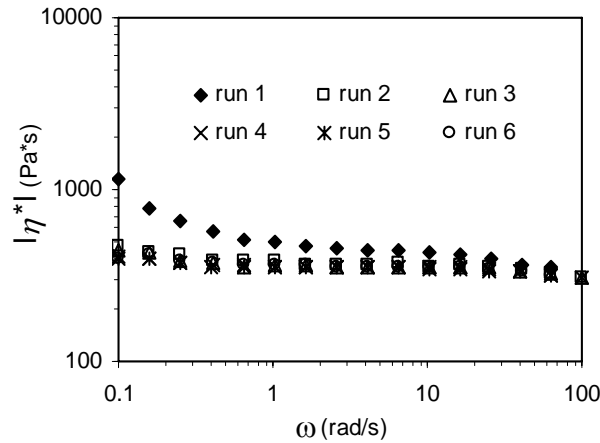


**Figure 2.10.**  $|\eta^*|$  in small-amplitude ( $\gamma_o = 0.15$ ) oscillatory shear for a short glass fiber-filled polybutylene terephthalate ( $\phi = 0.1766$ ,  $a_r \sim 21.4$ , concentrated régime). All measurements, denoted by run 1-6, were performed on the same sample in a torsional PPR with a gap of  $\sim 2$  mm.<sup>77</sup>

Work by Kim and Song<sup>77</sup> suggests that some orientational changes do occur in dynamic oscillatory tests. They authors noticed that  $|\eta^*|$ , for a short glass fiber-filled ( $\phi = 0.1766$ ,  $a_r \sim 21.4$ , concentrated régime) polybutylene terephthalate (exhibits little shear rate dependence) suspension, changed after repeated dynamic oscillatory tests on the same sample, denoted as run 1-6 in Fig. 2.10. A sample with isotropic fiber orientation at low frequencies exhibited a yield-like behavior. After repeated tests on the same sample

a Newtonian plateau developed. This suggests that the small-amplitude shear oscillations can induce orientation in the flow direction and that the micro-structure of the fiber is a possible contributor to the yield-behavior. As a note, no comparisons were made between  $|\eta^*|$  and the steady shear viscosity for the suspension or the neat matrix.

Glass fiber suspensions in non-Newtonian fluids show a strain amplitude dependence in the dynamic functions that markedly increases with concentration and aspect ratio. Mutel and Kamal<sup>81</sup> found that the addition of short glass fibers to a PP caused a strain amplitude dependence for all concentrations tested, 10-40 wt% ( $\phi = 0.0354 - 0.1805$ ), with increasing strain amplitude dependence for increasing concentration. As a note, the neat PP suspending medium exhibited linear strain dependence through a range of 5-50 strain%. Kim and Song<sup>77</sup> found that as the strain amplitude was increased for a short glass fiber suspension, while staying in the linear strain amplitude region of the suspending medium,  $|\eta^*|$  at constant frequency decreased. This was attributed to larger strains increasing the average orientation of the fibers along the flow direction.

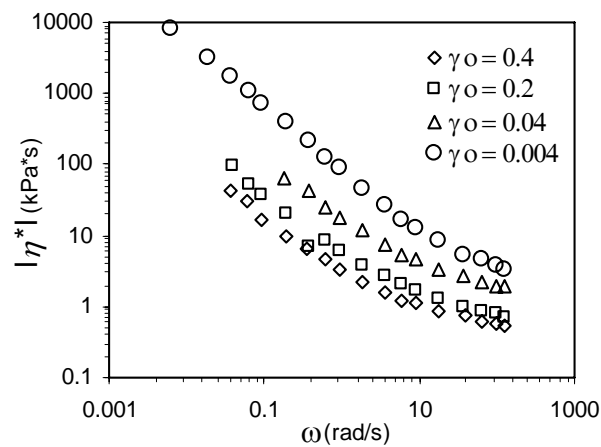


**Figure 2.11.**  $|\eta^*|$  vs. frequency for a long glass fiber-filled polypropylene ( $\phi = 0.132$ ,  $a_r \sim 1071$  or  $L = 15$  mm, concentrated régime) at various strain amplitudes  $\gamma_0$ . All tests were performed on a torsional PPR with a gap of 1mm.<sup>78</sup>

In some cases, typically with suspensions containing high glass fiber concentration and aspect ratio (relating to the concentrated régime), the dependence of  $|\eta^*|$  on the strain amplitude can be seen through the complete range tested, even at very low strain amplitude. The non-linear behavior at very small strain amplitudes is indicative of a yield stress and can be seen in Fig. 2.11, for a long glass fiber-filled polypropylene ( $\phi = 0.132$ ,  $a_r \sim 1071$  or  $L = 15$  mm, concentrated régime).<sup>78</sup> For this suspension  $|\eta^*|$  drastically decreases with increasing strain amplitude, even at small strains between 0.004 and 0.04 strain.

The source of the yield-like behavior exhibited by some glass fiber suspensions at high concentrations or large aspect ratios in the concentrated régime remains to be established. The two most plausible hypotheses are the formation of a pseudo-network between the fibers and the matrix macromolecules<sup>45</sup>, and high fiber-fiber interaction in samples with isotropic fiber orientation.<sup>77</sup> The lack of published data with regards to fiber surface treatments and their effect on the matrix-fiber interaction as well as the initial fiber orientation of published rheological data make it impossible to delineate the cause of the yield-like behavior.

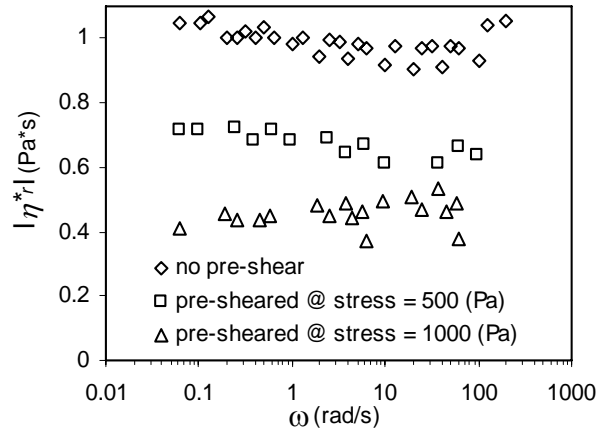
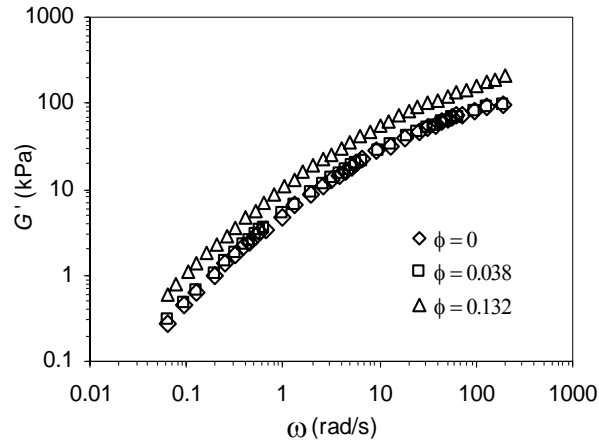


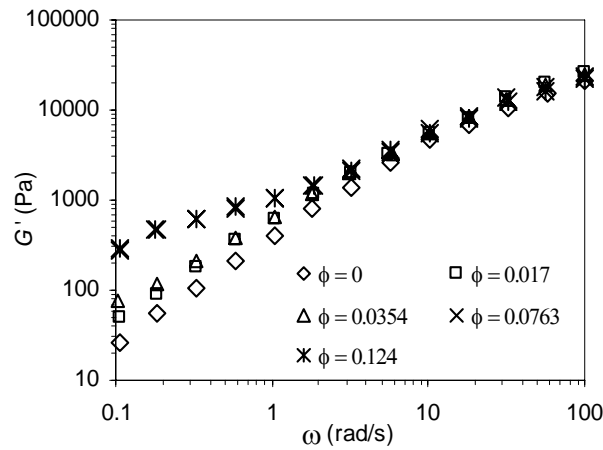
**Figure 2.12.** The effects of pre-shear on  $|\eta_r^*|$  vs. frequency for a short glass fiber-filled polypropylene ( $\phi = 0.124$ ,  $a_r \sim 21.4$ , concentrated régime). In this case  $|\eta_r^*|$  is the pre-sheared sample normalized by the no pre-shear sample values. All measurements were performed on a PPR.<sup>11</sup>

Similar to the shear viscosity, the initial orientation of the sample can have an effect on  $|\eta^*|$ . A sample whose initial orientation is random will exhibit a larger  $|\eta^*|$  than a sample whose fiber is oriented in the flow direction. Mobuchon et al.<sup>11</sup> reported over a 50% reduction in  $|\eta^*|$  after pre-shearing a concentrated short glass fiber-filled polypropylene ( $\phi = 0.124$ ,  $a_r \sim 21.4$ , concentrated régime), Fig. 2.12. The reduction in  $|\eta^*|$  was attributed to the pre-shear aligning the fibers flow direction; the greater the pre-shear stress the greater the overall fiber alignment.

**(b) Complex Shear Modulus.** There is little published data on the complex modulus or corresponding moduli of glass fiber suspensions in Newtonian fluids. Specifically, only one paper pertaining to the dynamic response of a fiber-filled purely Newtonian fluid was found. Ganani and Powell<sup>59</sup> reported that glass fiber suspensions in Newtonian fluids showed no significant values for the storage modulus  $G'$ , or no elastic behavior.



(a)



(b)

**Figure 2.13.** The storage modulus vs. frequency: (a) for two short glass fiber-filled polypropylene suspensions ( $\phi = 0.038$ ,  $a_r \sim 30$ , semidilute régime and  $\phi = 0.132$ ,  $a_r = 21.4$ , concentrated régime) and the neat suspending medium;<sup>11</sup> (b) for a short glass fiber-filled polypropylene ( $a_r = 85$  and  $35$  for  $\phi = 0.017$  and  $0.0763$  respectively, the aspect ratio for the other concentrations was not given) of various concentrations of fiber.<sup>69</sup> Both measurements were performed on a PPR.

For fiber suspensions in non-Newtonian fluids, the storage and loss modulus ( $G'$  and  $G''$ ) typically show little deviation from the neat matrix at low concentrations and small aspect ratios of fiber in the dilute and semidilute régimes. At high concentrations and sufficiently large aspect ratios, relating to the concentrated régime, two general trends become apparent. First, both the storage and loss moduli may increase in magnitude but

follow the same general curve of the matrix. This trend can be seen for the storage modulus in Fig. 2.13 (a). Second, a more pronounced enhancement at low frequencies ( $\omega < \sim 10$  rad/s) that becomes more apparent with increasing concentration and aspect ratio. At high frequencies ( $\omega > \sim 10$  rad/s) the moduli typically merge onto the value exhibited by the matrix. This trend can be seen for  $G'$  in Fig. 2.13 (b). In the second case, the low frequency plateau or “tail” is indicative of a yield-like behavior and often corresponds with a  $|\eta^*|$  that does not exhibit a Newtonian plateau.<sup>69, 82</sup> The high frequency merger between the matrix and suspension moduli is typically attributed to the evolution of the fiber orientation distribution. However, no comparative studies of repeated runs or pre-shearing are reported to confirm the effect of fiber orientation on the dynamic moduli.<sup>69,</sup>

83

In all the published results that were reviewed regarding the dynamic moduli of non-Newtonian suspensions, the loss modulus was of greater magnitude than the storage modulus.<sup>11, 65, 69, 82, 83</sup> In the referenced work where the behavior of the neat resin was given for comparison purposes, the matrix also followed this trend of  $G'' > G'$ . Though the dynamic moduli can change slightly with fiber concentration and aspect ratio, the ratio of the storage and loss modulus typically remains constant.

**(c) Phase Angle.** For glass fiber suspensions in both Newtonian and non-Newtonian fluids the phase angle is independent of fiber content, and typically equal to that exhibited by the suspending fluid.<sup>70</sup> Mobuchon et al.<sup>11</sup> found the phase angle to be independent of fiber content and fiber orientation and equal to that of the matrix over a frequency range of 0.1-100 rad/s for a short glass fiber-filled polypropylene. Slight deviations from this behavior do occur. Guo et al.<sup>65</sup> found that at low frequencies ( $\omega =$

0.135-1.351 rad/s)  $\tan(\delta)$  decreased with fiber volume fraction but at higher frequencies (up to 277 rad/s)  $\tan(\delta)$  remained constant with increasing fiber concentration. Similar results were published by Greene and Wilkes<sup>69</sup> for a short and long fiber-filled polypropylene.

### **2.2.3.3 Transient Shear Flow**

We now consider the nonlinear viscoelastic behavior of glass fiber-filled non-Newtonian fluids in shear. The following review will include the most commonly reported experiments: stress growth upon inception of steady shear flow, stress relaxation after cessation of steady shear flow, interrupted stress growth and strain upon inception of constant stress. As an introduction to each section, a brief review is given to fiber suspensions in Newtonian suspending mediums for comparison purposes.

#### **2.2.3.3.1 Startup of Shear Flow**

In startup of shear flow a sample is at rest and in equilibrium when  $t < 0$ . At  $t \geq 0$  the sample is deformed at a constant deformation rate while the shear stress growth function  $\sigma^+$  or corresponding shear stress growth coefficient  $\eta^+$  and the normal stress growth functions  $N_1^+$  and  $N_2^+$  are measured as a function of time and shear rate. Subsequently, we begin with a review of  $\sigma^+$  behavior followed by the normal stress growth functions of glass fiber filled non-Newtonian fluids.

(a) **Shear Stress Growth.**  $\sigma^+$ , often reported in terms of  $\eta^+$ , gives insight into the nonlinear viscoelastic behavior of glass fiber suspensions and the temporal evolution of the fibers' orientation distribution. The addition of glass fiber to a Newtonian or non-Newtonian fluid has a dramatic effect on  $\sigma^+$  in startup of shear flow; the most profound effect being a relatively large overshoot. Initial orientation distribution, concentration and aspect ratio of the fiber, viscoelastic nature of the matrix, and the shear rate all influence the magnitude of the overshoot as well as the length of time for a steady-state to be reached.<sup>84</sup> This is speculated to be directly related to the evolving microstructure of the glass fibers within the suspension. Because the unsteady shear flow material functions are dependent on an evolving microstructure, they seem to be more affected by the presence of fiber than the steady shear flow material functions.<sup>85</sup>

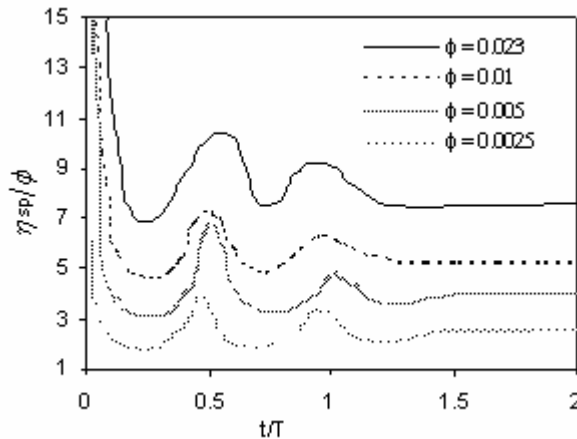
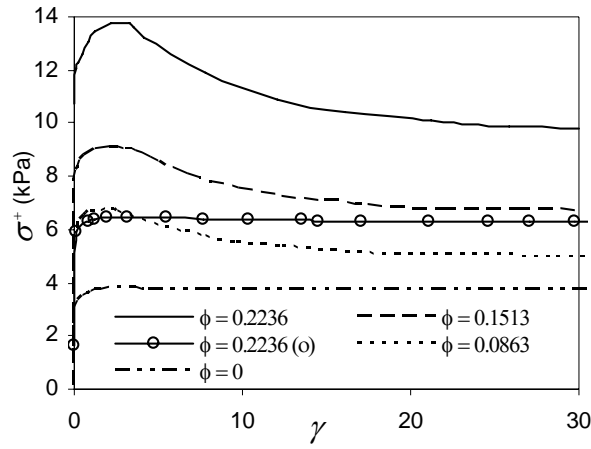


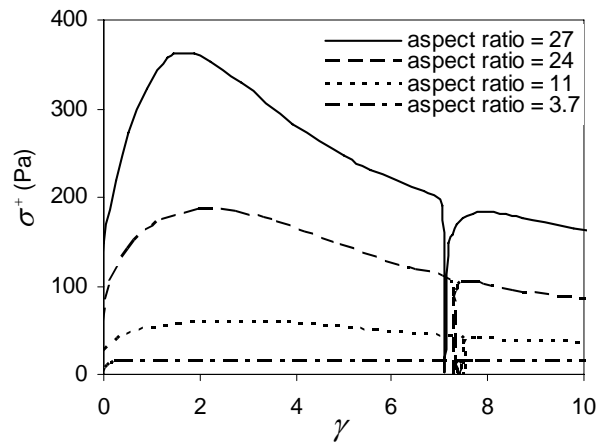
**Figure 2.14** Transient specific viscosity ( $\eta_{sp} = \eta_r - 1$ ), normalized by the glass fiber volume fraction, vs. time, normalized by the period of oscillation  $T$ . Tests were performed on a dilute suspension of rigid aluminum coated Nylon fibers of varying concentration and constant aspect ratio,  $a_r = 5.2$ , in a Newtonian suspending medium. The rods were initially aligned parallel to the direction of velocity gradient with the use of an electric field. All tests were performed on a torsional CPR, at  $\dot{\gamma} = 2.51 \text{ s}^{-1}$ .<sup>86</sup>

The transient response to deformation of a suspension is highly dependent on the Newtonian or non-Newtonian behavior of the suspending medium.<sup>47</sup> Rods in a dilute suspension whose suspending medium is a Newtonian fluid will rotate around a vorticity axis unless acted upon by another force. Mathematically described by Jeffery<sup>43</sup>, this phenomenon gives rise to an oscillating stress response that is dependent on the orientation state of the particle. In a theoretically perfect system, the period of oscillation would stay constant, but in all experimental cases the amplitude of  $\sigma^+$  decayed with time. This behavior is shown in Fig. 2.14 for a dilute suspension of glass fibers in a Newtonian fluid by way of the oscillating specific viscosity  $\eta_{sp}/\phi$ , normalized by the glass fiber concentration, vs. time, normalized by the period of fiber rotation. The decay of the stress oscillation can be a result of several interactions including boundary, particle-particle, hydrodynamic or slight aspect ratio variations.<sup>87</sup> For non-dilute suspensions in a Newtonian fluid, fiber-fiber and fiber-hydrodynamic interactions prevent or retard periodic fiber rotation and typically a pseudo-equilibrium orientation state is reached, which, after a short period of time, may slowly change with time.<sup>85</sup> Iso et al.<sup>63, 64</sup> performed many experiments on dilute and semidilute suspensions of weakly and highly elastic fluids. The authors found that the addition of a small concentration of elastic polymer lead to a competition between the spiraling toward the vorticity axis (Jeffery orbit) and the randomization of the fiber orientation due to hydrodynamic interactions. In highly elastic fluids, the authors found that the polymer stress acted to confine the fiber orientation to the flow direction. In both cases the behavior was attributed to the elastic stresses competing with hydrodynamic forces.

Ganani and Powell<sup>59</sup> performed startup of shear flow experiments on fiber suspensions in Newtonian fluids in the concentrated régime ( $\phi = 0.08$ ,  $a_r = 24.3$ , tests performed on a CPR). They found that the suspensions exhibit stress shear growth functions similar to viscoelastic suspensions. Upon flow, a sample that started with a random orientation state would exhibit a peak in the stress overshoot of roughly 25% greater than the steady-state value. The overshoot maximum occurred at a strain of roughly 5, and completely decayed by a strain of roughly 15.



(a)



(b)

**Figure 2.15.**  $\sigma^+$  vs. strain. All tests were performed on a CPR. (a) Polystyrene-acrylonitrile (SAN, estimated density  $\approx 1.4 \text{ g/cm}^3$ ) containing short glass fibers ( $a_r = 22$ ) of varying concentrations (concentrated régime) and one sample containing glass beads denoted by (o) with diameter of  $3\text{-}5 \mu\text{m}$ . Experiments were performed at a shear rate of  $0.2 \text{ s}^{-1}$ . (b) Polyamid-6 (Nylon-6) containing short glass fibers of constant concentration ( $\phi = 0.1507$ ) and varying aspect ratio. The smallest aspect ratio sample was in the semidilute régime, and the rest were concentrated. The experiments were performed at  $\dot{\gamma} = 0.1 \text{ s}^{-1}$  that was interrupted at  $\gamma \sim 7$ .<sup>47</sup>

Unlike glass fiber suspensions in Newtonian fluids,  $\sigma^+$  of suspensions in non-Newtonian fluids does not oscillate at very dilute fiber concentrations and small aspect ratios, but rises to a peak that decays to a steady-state (stress overshoot) or simply rises to a steady-state value.<sup>63, 64</sup> The effect of glass fiber on  $\sigma^+$  is primarily quantified by the

magnitude of stress overshoot. Increasing fiber concentration and/or fiber aspect ratio increases the overshoot and the time needed to reach steady-state in a similar manner. Fig. 2.15 (a) is a graph of  $\sigma^+$  vs. strain for a polystyrene-acrylonitrile (SAN, estimated density  $\approx 1.4 \text{ g/cm}^3$ ) containing short glass fibers ( $a_r = 22$ ) of varying concentrations (all in the concentrated régime) and one sample containing glass beads with diameters between 3-5  $\mu\text{m}$ . It is interesting to note the effect of glass spheres on the rheology in comparison to glass fibers at similar concentrations, in Fig. 2.15 (a). First, the suspension containing glass spheres does not exhibit any visible shear stress overshoot but does enhance the steady state stress by roughly 50%. Second, the presence of glass fiber enhanced the steady state shear stress of the suspending medium by roughly 80% more than does the presence of glass spheres. This suggests that the stress overshoot is a result of the evolving fiber orientation and that the glass fibers are restricted from completely aligning in the flow direction. Fig. 2.15 (b) is a graph of  $\sigma^+$  vs. strain for a polyamid-6 (Nylon-6) containing short glass fibers of constant concentration ( $\phi = 0.1507$ ) and varying aspect ratio. The smallest aspect ratio sample was in the semidilute régime, and the rest were in the concentrated régime. The experiment was interrupted at a strain  $\gamma \sim 7$ , the results of which will be discussed later in the appropriate section. Similar to increasing the fiber concentration, increasing the fiber aspect ratio increased the magnitude of the stress overshoot and the steady-state stress.

The overshoot in Newtonian and non-Newtonian suspensions is speculated to be a result of an evolving microstructure, where, upon flow the fibers orient themselves towards the flow direction. A sample whose initial fiber orientation is aligned parallel to the direction of velocity gradient will exhibit the greatest overshoot. In contrast, a sample

whose initial fiber orientation is parallel to the flow direction will exhibit the lowest overshoot, with a randomly oriented sample falling between these two ideal cases.<sup>47</sup> Ramazani et al.<sup>85</sup> showed that pre-shearing a sample before the stress growth experiments removed the initial overshoot exhibited by randomly oriented fiber suspensions. The peak of the shear stress overshoot scales with strain at varying shear rates and typically occurs between 2-10 strain units. Current theory suggests that the peak in the shear stress overshoot corresponds to an average fiber orientation of 45° with respect to the flow direction.<sup>47, 85</sup> However, no thorough experimental analysis to confirm the orientation distribution that coincides with a specific stress response has been reported. A steady-state in the stresses can be reached if ample time is given for a suspensions' fiber orientation to reach a steady-state at that given shear rate, which typically occurs at 50-100 strain units.<sup>44</sup>

There is an insufficient amount of comparable data to delineate the effect of matrix viscosity and elasticity on  $\sigma^+$  of glass fiber suspensions in non-Newtonian fluids. However, upon reviewing the current published transient data it would appear that the magnitude of the initial overshoot increases with increasing matrix elasticity, interfacial matrix-fiber interaction and viscosity; with the viscosity being a secondary factor to the matrix elasticity and matrix-fiber interaction.<sup>45, 54, 61</sup> A simple experiment, that to our knowledge has not been reported with respect to stress growth functions, would be to run startup of shear flow tests on similar samples at various temperatures, effectively changing the viscosity of the suspending medium. This would help elucidate the effect of suspending medium viscosity on the stress overshoot and corresponding evolution of the fiber orientation.

**(b) First and Second Normal Stress Growth Functions.** The published rheological data pertaining to the normal stress growth functions of glass fiber suspensions in Newtonian fluids is limited. However, the response of suspensions whose suspending mediums are Newtonian-like (i.e. polybutene) suggests that the presence of fiber does induce normal stresses that exhibit transient behavior. For suspensions whose suspending mediums are non-Newtonian, similar to  $\sigma^+$ , the magnitude of the  $N_1^+$  or  $N_1^+ - N_2^+$  overshoot increases with increasing concentration, aspect ratio, and shear rate.<sup>47, 84</sup> The peak of the overshoot can be as large as an order of magnitude greater than the steady-state value and typically occurs at a greater strain than the shear stress overshoot.<sup>45, 84, 85</sup> The overshoot scales with strain at various shear rates.

#### 2.2.3.3.1.2 Cessation of Steady Shear Flow

The stress relaxation experiment is defined so that a sample at  $t < 0$  is subject to steady shear flow and at steady state. At  $t \geq 0$  the flow is stopped and the shear stress decay function  $\sigma^-$ , and the normal stress decay functions  $N_1^-$  and  $N_2^-$  are measured as a function of time and shear rate. Subsequently, we begin with a review of the shear stress decay function behavior followed by the normal stress decay functions of glass fiber filled non-Newtonian fluids.

**(a) Shear Stress Decay.** In Newtonian suspensions the presence of fiber has little effect on shear stress decay function behavior.<sup>88</sup> Likewise, with non-Newtonian suspensions it is typically stated that the presence of the fibers has a negligible influence on the relaxation dynamics of a suspension when compared to the neat matrix.<sup>45, 47, 84</sup>

Laun<sup>47</sup> showed that an increase in fiber concentration had negligible effect on the time needed for half the steady-state stress to relax which was concluded from the data plotted in Fig. 2.15 (a) for a polystyrene-acrylonitrile (SAN) containing short glass fibers ( $a_f = 22$ ) of varying concentrations (all in the concentrated régime).

**(b) Normal Stress Decay.** Similar to the normal stress growth functions, there is little data pertaining to the normal stress decay function of glass fiber suspensions in Newtonian fluids. However, the response of suspensions whose suspending mediums are Newtonian-like (i.e. polybutene) suggests that the presence of fiber has little effect on the relaxation behavior.<sup>45</sup> The same is true for non-Newtonian suspensions. Similar to the stress relaxation, it is typically stated that the presence of fiber has little impact on the relaxation behavior of the normal stress differences.<sup>47, 84</sup> Laun<sup>47</sup> found no difference in the time for  $N_1^- - N_2^-$  to relax to half its steady state value, for concentrations between 0 and 35wt% ( $\phi \sim 0-0.2236$ ) of short glass fiber in SAN.

### 2.2.3.3.3 Interrupted Shear Flow

Interrupted stress growth experiments are designed such that a sample is deformed at a constant shear rate for a specific time, after which the flow is stopped. Then the flow is turned back on, either immediately or after a pre-determined period of time, in the same flow direction or the reverse direction (flow reversal tests). Because the initial response of a suspension is exactly the same as described in the preceding sections, we will focus our discussion on the stress growth behavior of the suspension after the flow is reapplied to the suspension.

The effect of fiber concentration and aspect ratio on interrupted experiments is similar in nature to the stress growth and relaxation experiments reviewed in the preceding sections. The following section on interrupted stress growth is meant to further the reader's understanding of how various flow conditions and shear histories can have an effect on the rheological behavior. The review begins with the interrupted shear stress growth behavior of Newtonian and non-Newtonian suspensions followed by the behavior of the shear stress in flow reversal. Then we review the normal stress differences with the same format.

**(a) Shear Stress Growth.** We first consider the case of a glass fiber suspension in a Newtonian fluid that has been subject to an interrupted shear flow experiment where the flow is reapplied in the same direction as the initial flow. Ganani and Powell<sup>88</sup> showed for a semidilute short glass fiber-filled Newtonian fluid ( $\phi = 0.08$ ,  $a_r = 24.3$ , tests performed on a CPR) that when the flow was reapplied after a wait period of one minute the shear stress rose immediately to the steady-state value. However, when the sample was allowed to rest for a greater period of time  $\sim 10$  minutes, the overshoot reappeared with similar magnitude to the first deformation. The behavior was attributed to particle sedimentation, altering the steady-state fiber orientation distribution resulting in a change in the fibers orientation distribution when the flow was reapplied. This hypothesis can be supported with the use of Eq. (2.9) that estimates the time scale for sedimentation of the fibers and is found to be  $\sim 10$  min, assuming a low suspending medium viscosity of  $\eta_s \sim 2$  Pa.s and a fluid density of  $1 \text{ g/cm}^3$ .

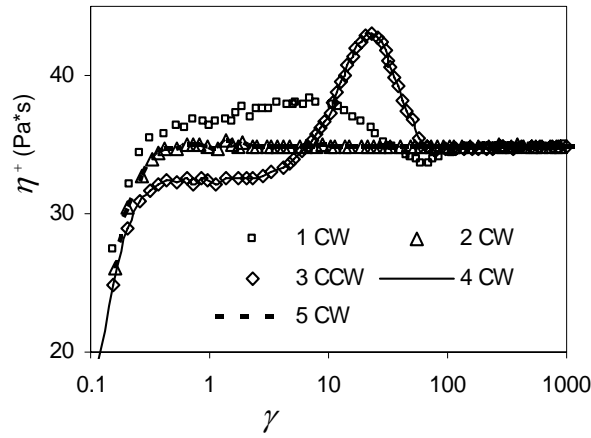
The shear stress response to flow reversal tests, for the same suspension described in the paragraph above, was slightly different. Only a one minute rest time after the flow

was removed from the sample was needed for an overshoot of similar magnitude to the initial overshoot to appear in the reverse direction. Again, this was attributed to particle sedimentation. However, no comment was made on why the suspension assumed a new orientation distribution after only one minute in the reverse direction while it took  $\sim 10$  minutes of rest for the overshoot to reappear in the same flow direction.

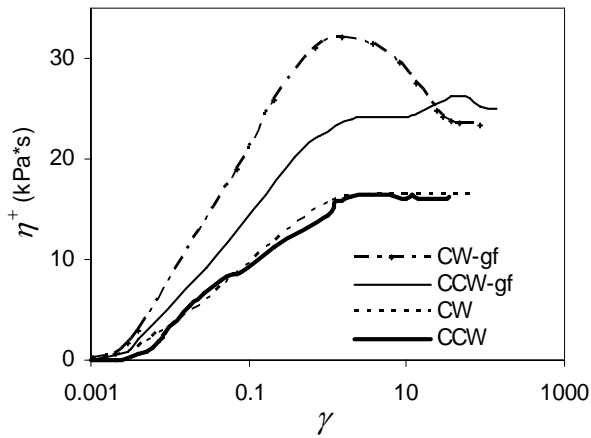
We now consider the shear stress response to interrupted flow of non-Newtonian fluids containing glass fibers. Fig. 2.15 (b) is a typical example where after the sample is subject to startup of shear flow, the flow is stopped and then immediately reapplied in the same direction. As expected  $\sigma^+$  momentarily relaxes as the flow is interrupted and then returns to the previous value.<sup>47</sup> The lack of an overshoot peak on resumption of flow was attributed to the lack of any recovery of orientation and structure during the period of no flow. This is a typical response for viscoelastic fluids where sedimentation and Brownian motion are not contributing factors even after very long interruptions of flow, though deviations from this behavior do occur.<sup>44</sup> For example, when an overshoot reappears during interrupted tests with long interruption times between flow in the same direction. There is debate on the cause of this phenomenon, but one common factor between the suspensions that exhibited this response was they had low viscosity suspending mediums which suggests the possibility of particle sedimentation altering flow induced fiber orientation at least slightly during quiescent rest periods.<sup>60</sup> However, Sepehr et al.<sup>45</sup> explained this behavior exhibited by a Boger fluid suspension by the elastic recoil of the macromolecules altering the fiber orientation during stress relaxation.

$\sigma^+$  in flow reversal experiments, when the flow is re-applied in the opposite direction as the initial deformation, exhibits a slightly more complex behavior. When  $\sigma^+$  is plotted

vs.  $\ln(\dot{\gamma})$  it is first seen to rise to a pseudo plateau which is explained in the following way. In concentrated suspensions the fibers orient in the flow direction and form a “crystalline” structure of least resistance to flow. When the flow is reversed the aligned microstructure has a low resistance to flow until it tilts over in the new flow direction to form its mirror image. The reverse overshoot is a result of the reverse tumbling of the fibers, even if the fibers were mostly aligned prior to flow reversal. The peak of the reverse overshoot occurs at an increased strain compared to the first overshoot and increases with concentration and aspect ratio and the overshoot peak scales with strain.<sup>45, 59</sup> Interestingly, Sepehr et al.<sup>45</sup> found that the magnitude of the reverse overshoot in Newtonian and non-Newtonian suspensions decreases with increasing  $\dot{\gamma}$ , but no explanation to why was given by the authors. One possible explanation is based on the idea that that higher shear rates impart a higher degree of fiber orientation at steady state.<sup>65, 66</sup> As a result, fewer fibers are subject to tilt or reverse tumbling during flow reversal at higher shear rates effectively reducing the magnitude of the reverse overshoot.



(a)



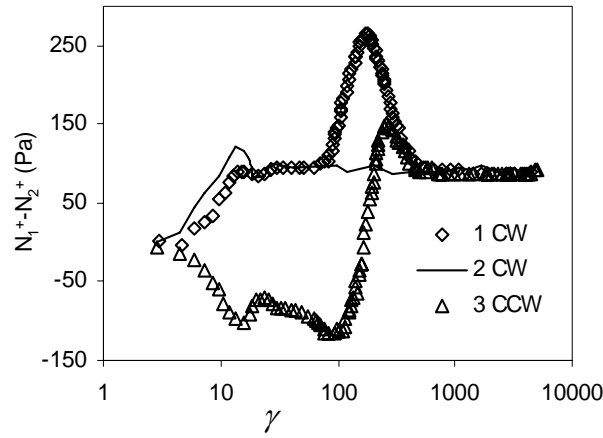
(b)

**Figure 2.16.**  $\eta^+$  vs. strain for interrupted stress growth tests. All tests were performed on a torsional PPR with gap-to-fiber length ratio greater than 3:1. The clockwise (CW) and counter clockwise (CCW) notation is to give the reader context of the shear direction in a torsional rheometer. The flow reversal was applied immediately to the sample. (a) Short glass fiber-filled polybutene PB (fiber content:  $\phi = 0.0706$ ,  $a_r \sim 20$ , concentrated) suspension at  $\dot{\gamma} = 5 \text{ s}^{-1}$ .<sup>45</sup> (b) Neat and short glass fiber-filled polypropylene PP (fiber content:  $\phi = 0.115$ ,  $a_r \sim 20$ , concentrated), denoted in the figure as -gf, at  $\dot{\gamma} = 0.1 \text{ s}^{-1}$ .<sup>84</sup>

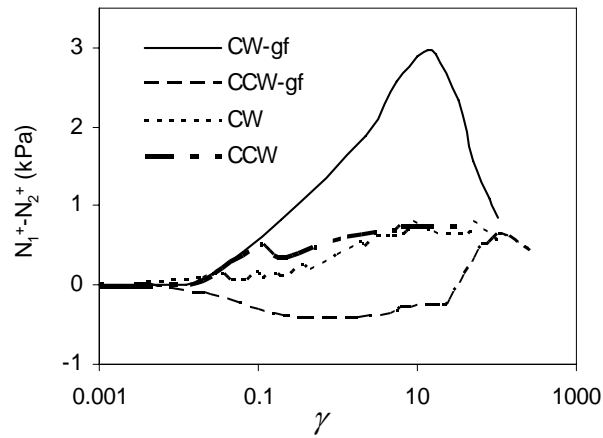
Results of the flow reversal test can be seen in Fig. 2.16 (a) and (b) for a short glass fiber-filled polybutene (glass content:  $\phi = 0.0706$ ,  $a_r \sim 20$ ) and a short glass fiber-filled polypropylene (fiber content:  $\phi = 0.115$ ,  $a_r \sim 21$ ), respectively. For the polybutene suspension, the weak initial overshoot compared to the reverse overshoot is most likely due to orientation distribution of fiber generated during sample loading into the

rheometer. An interesting observation is that the reverse overshoot for the polybutene (Newtonian-like) suspension is greater in magnitude than the first overshoot, as seen in Fig. 2.16 (a), but for the polypropylene (non-Newtonian) suspension the second overshoot is smaller, as seen in Fig. 2.16 (b). It is difficult to draw a precise conclusion from comparing these two graphs as the tests were performed at different shear rates, but a possible explanation for this behavior can be established through the work of Iso et al.<sup>63</sup>,<sup>64</sup> He found that the elastic nature of non-Newtonian fluids stabilizes fiber rotation. This could result in a greater number of fibers tumbling  $180^\circ$  in the Newtonian suspensions when compared to the non-Newtonian suspensions.

**(b) Interrupted Normal Stress Growth Function.** We now consider  $N_1^+$  in interrupted flow and flow reversal experiments. For a short glass fiber-filled polybutene (PB) suspension starting with an isotropic fiber orientation, Sepehr et al.<sup>45</sup> found that  $N_1^+ - N_2^+$ , on a  $N_1^+ - N_2^+$  vs.  $\ln(\gamma)$  plot to initially rise to a plateau equal to that of the steady-state value before exhibiting a large overshoot. The peak of the initial overshoot occurred at a strain of roughly 100, Fig. 2.17 (a). In Fig. 2.17 (a), 1<sup>st</sup> CW is the initial deformation in the clockwise direction starting from a random fiber orientation. 2<sup>nd</sup> CW is an intermittent deformation in the same clockwise direction. As expected during the 2<sup>nd</sup> CW the overshoot is no longer present. However, in the 3<sup>rd</sup> deformation in the CCW (counter clockwise) direction the normal stress initially takes on a negative value before rising to an overshoot corresponding to a similar strain seen in the first overshoot.



(a)



(b)

**Figure 2.17.**  $N_1^+ - N_2^+$  plotted vs. strain. All tests were performed on torsional PPR with gap-to-fiber length ratio greater than 3:1. The clockwise (CW) and counter clockwise (CCW) notation denotes the direction of plate rotation. The flow reversal was applied immediately to the sample. (a) Short glass fiber-filled polybutene PB (fiber content:  $\phi = 0.0706$ ,  $a_r \sim 20$ , concentrated) suspension at  $\dot{\gamma} = 5 \text{ s}^{-1}$ .<sup>45</sup> (b) Neat and short glass fiber-filled polypropylene PP (fiber content:  $\phi = 0.115$ ,  $a_r \sim 20$ , concentrated), denoted in the figure as -gf, at  $\dot{\gamma} = 0.1 \text{ s}^{-1}$ .<sup>84</sup>

Suspensions whose matrix have elastic properties and exhibit a large degree of shear rate dependence have been shown to behave similarly to the previously described polybutene suspension.<sup>45, 84, 85</sup> In Fig. 2.17 (b)  $N_1^+ - N_2^+$  is shown for a short glass fiber-filled polypropylene, PP30, and the neat polypropylene, PP0, for comparison.<sup>84</sup> Starting from an isotropic fiber orientation, the sample exhibits a large overshoot but does not

have the initial plateau exhibited by the polybutene suspension. However, it does exhibit the negative  $N_1^+ - N_2^+$  when the flow is reversed. The authors hypothesize that the cause of the negative normal stress differences is due to non-affine deformation similar to liquid-crystalline polymers.<sup>84</sup>

#### 2.2.3.3.4 Creep

In creep experiments a sample is subject to a constant stress and the strain is recorded. The following is a review of literature pertaining to this experiment with regard to non-Newtonian suspensions as no experimental data was found with regard to Newtonian suspensions.

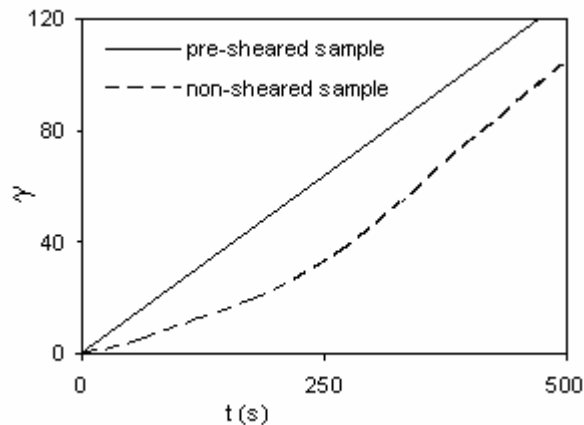


**Figure 2.18.** Strain vs. time for a short glass fiber-filled ( $a_r = 25$ ,  $\phi = 0.124$ , concentrated) polypropylene subject to a shear stress of 400 Pa; experiments were performed on a torsional PPR.<sup>89</sup>

Using a sliding plate rheometer Laun<sup>47</sup> studied the creep behavior of a short glass fiber-filled LDPE ( $a_r = 31$ ,  $\phi = 0.131$ ) with different initial fiber orientations of random,

in the shear plane and parallel to the direction of velocity gradient. He found that fibers oriented in the flow direction exhibited the least resistance. Interestingly, the slope of the creep curve for fibers oriented in the shear plane but perpendicular to the flow was only slightly lower. The highest resistance was found in samples whose fiber orientation was parallel to the direction of velocity gradient. The resistance to flow of a randomly oriented sample was found to lie between these two ideal cases. The effect of fiber orientation on the creep behavior of a short glass fiber-filled polypropylene ( $a_r = 25$ ,  $\phi = 0.124$ ) subject to a shear stress of 400 Pa can be seen in Fig. 2.18. The pre-sheared sample exhibits a greater slope, lower creep viscosity, than the non-sheared sample at short times while at  $t > 250$  (s) they seem to become equal. This is attributed to the fibers aligning themselves in the flow direction.

#### 2.2.4 Extensional Rheology

In the case where  $\dot{\epsilon}$  is the largest principle strain rate two general extensional flow viscosities  $\eta_1^+$ ,  $\eta_2^+$  can be defined as follows:

$$\eta_1^+ = \frac{\sigma_{11} - \sigma_{33}}{2(2+m)\dot{\epsilon}}; \quad \eta_2^+ = \frac{\sigma_{22} - \sigma_{33}}{2(1+2m)\dot{\epsilon}} \quad (2.16)$$

where every possible extensional flow corresponds to some value for  $m$  between -0.5 and +1.0.<sup>90</sup> The extensional flows of interest in this review are tensile, biaxial and planar corresponding to values for  $m = -1/2$ , 1 and 0 respectively. We define the elongational stress growth coefficient for tensile, biaxial and planar elongation as  $\eta_E^+ = \eta_1^+$ ,  $\eta_B^+ = \eta_1^+$

=  $\eta_2^+$ , and  $\eta_P^+ = \eta_1^+$  respectively. The steady state extensional viscosity ( $\eta_E$ ,  $\eta_B$ , and  $\eta_P$ ) denotes the value of the elongational stress growth coefficient when a steady state has been reached in the normal stresses.

The majority of the published work relating to the rheological behavior of glass fiber suspensions has been concerned with shear flows, primarily for two reasons. First, shear flows can dominate the kinematics in extrusion and other processing flow fields. However, in the frontal region of mold filling and in converging or diverging flow situations extensional behavior is important. Second, obtaining reliable and reproducible experimental data in extension is difficult as a result of non-uniform elongation of the sample. Subsequently, we review the limited literature pertaining to the shear-free flow rheological behavior of glass fiber suspensions in tensile, biaxial, and planar elongation respectively.

#### **2.2.4.1 Tensile Extension**

The tensile viscosity of glass fiber suspensions in Newtonian fluids is enhanced by the presence of glass fiber but is typically reported to be independent of the strain rate.<sup>60</sup> The degree of the tensile viscosity enhancement is a function of both concentration and aspect ratio and can be more than an order of magnitude greater than the tensile viscosity of the suspending medium. Even more interesting is the ratio of the tensile viscosity to the shear viscosity, termed the Trouton ratio. For Newtonian fluids and non-Newtonian fluids that tend toward linear viscoelastic behavior at small strain and shear rates the ratio is typically equal to three. Mewis and Metzner<sup>91</sup> found a constant tensile viscosity, that

exhibited no strain thickening behavior, for glass fiber suspensions of various fiber aspect ratios ( $a_r = 280-1260$ ) in a Newtonian fluid that was between one and two orders of magnitude greater than the shear viscosity. Weinberger and Goddard<sup>92</sup> found that the extensional kinematics caused quick fiber alignment resulting in a constant tensile viscosity that was roughly 26 times greater than the shear viscosity.

The shear-free flow behavior of glass fiber suspensions in non-Newtonian fluids is more interesting. The tensile viscosity increases with increasing fiber concentration and aspect ratio, but the fibers induce a strain rate thinning behavior. Using a Rheometrics Elongational Rheometer (RER), Kamal et al.<sup>93</sup> reported tensile viscosity data for a glass fiber-filled polypropylene with varying concentration (fiber content:  $\phi = 0-0.1805$ ,  $a_r = 150$ ) at strain rates of  $0.003-0.6 \text{ s}^{-1}$ . The authors found that the tensile viscosity increased with an increase in fiber concentration, but decreased with increasing strain rate. As a note, the neat polypropylene matrix exhibited an increasing tensile viscosity with increasing strain rate. The strain rate thinning behavior was believed to be a result of an induced shear flow between the filler particles, which increase with fiber concentration. Similar results have been published by Chan et al.<sup>76</sup> for short glass fibers in high-density polyethylene HDPE and Creasy and Advani<sup>94</sup> for a long discontinuous carbon fiber-filled poly-ether-ketone. Both studies were performed on an elongational rheometer that was built “in-lab”.

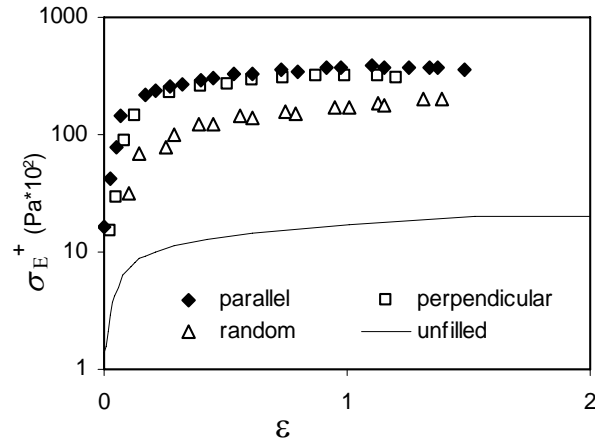
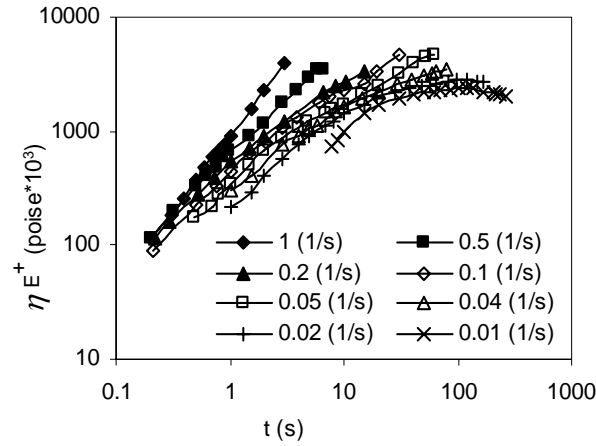


**Figure 2.19.** Tensile stress growth function vs. strain,  $\epsilon = L/L_0$ , for a short glass fiber filled high-density polyethylene HDPE (fiber content:  $\phi = 0.1358$ ,  $a_r \sim 30$ , concentrated) with various initial fiber orientations. The samples were prepared from compression molded and injection molded plates. Experiments were performed at a strain rate of  $0.1 \text{ s}^{-1}$  on a Meissner type extensional rheometer.<sup>47</sup>

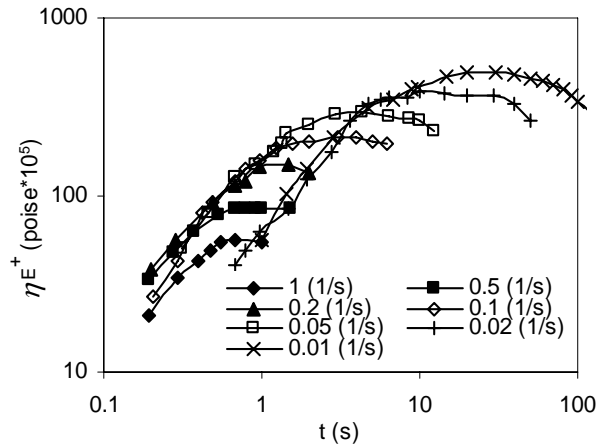
Similar to glass fiber-filled Newtonian fluids, glass fiber-filled non-Newtonian fluids can exhibit tensile stresses over an order of magnitude greater than that exhibited by the suspending medium. Laun<sup>47</sup> found the tensile viscosity for a short glass fiber-filled HDPE (fiber content:  $\phi = 0.1358$ , aspect ratio  $\sim 30$ ) to be 46 times greater than the neat suspending medium (tests were performed on a Meissner type elongational rheometer). Using the same HDPE suspension Laun compared the extensional behavior of samples with different initial fiber orientations of parallel and perpendicular to the direction of elongation and random, Fig. 2.19. The shape of the tensile stress growth function was similar to the neat suspending medium for all samples but the sample whose fibers were aligned parallel to the direction of elongation exhibited the greatest tensile stress values, even after a steady state was reached.

Some researchers have attempted to approximate the tensile viscosity. Using both the approximation by Binding<sup>95</sup> and by Cogswell<sup>96</sup>, Thomasset et al.<sup>78</sup> calculated the

apparent tensile viscosity from the pressure loss in a conical capillary entrance. The authors found that both methods gave similar results. For a long glass fiber-filled polypropylene (fiber content:  $\phi = 0.076-0.18$ ,  $a_r = 714-1428$  pre-extrusion), the tensile viscosity increased with fiber concentration and aspect ratio. However, the shape of the curve remained constant and followed the shear thinning behavior exhibited by the shear viscosity. This was expected as the Bagley corrections were found to be independent of shear rate. Also, the Trouton ratio increased with fiber concentration and aspect ratio from six for the neat resin to 23 for the highest concentration suspension.



(a)



(b)

**Figure 2.20.** Tensile stress growth coefficient vs. time. Experiments in both graphs were completed on an in-house built fiber extensional rheometer. (a) Neat polystyrene at various strain rates. (b) Short glass fiber-filled polystyrene (fiber content:  $\phi = 0.0872$ ,  $a_r \sim 140$ , concentrated) at various strain rates.<sup>76</sup>

Most transient extensional rheology studies for non-Newtonian suspensions focus on the effect fibers have on the time-dependent tensile stress growth coefficient, or the biaxial stress growth coefficient plotted vs. time or Hencky strain.<sup>93, 94, 97, 98</sup> These tests suggest that the presence of fibers suppresses the strain thickening behavior of the suspending medium.<sup>97</sup> The tensile stress growth coefficient can be seen in Fig. 2.20 for a neat polystyrene (PS), Fig. 2.20 (a), and a short glass fiber-filled PS (fiber content:  $\phi =$

0.091) Fig. 2.20 (b). The fiber-filled suspension, when compared to the neat resin, seems to suppress the strain thickening characteristics of the melt.

### 2.2.4.2 Biaxial Extension

The literature pertaining to biaxial extension of glass fiber suspension is limited. However, the published data that was found suggests a similar trend to that seen in tensile extension; the presence of glass fiber enhances the biaxial viscosity but suppresses the biaxial strain thickening characteristics of the suspending medium.

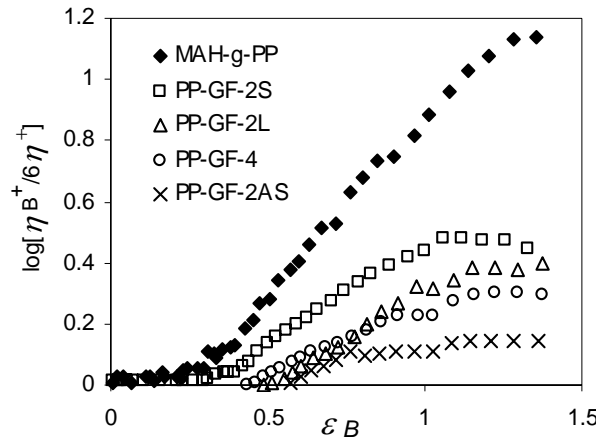


**Figure 2.21.** Biaxial stress growth coefficient normalized by six times the shear stress growth coefficient vs. biaxial strain for a neat maleic anhydride modified polypropylene (MAH-g-PP) and four fiber-filled suspensions of various fiber content. Three of the glass fiber filled samples were composed of a similar MAH modified PP suspending medium as the neat fluid denoted PP/GF-2S (fiber content:  $\phi = 0.0763$ ,  $a_r \sim 24.4$ ), PP/GF-2L (fiber content:  $\phi = 0.0763$ ,  $a_r \sim 36.4$ ), PP/GF-4 (fiber content:  $\phi = 0.1805$ ,  $a_r \sim 28.4$ ) and one glass fiber filled sample was composed of an unmodified PP suspending medium denoted as PP/GF-2AS (fiber content:  $\phi = 0.0763$ ,  $a_r \sim 50$ ). All samples were all in the concentrated régime. Experiments were performed at a biaxial strain rate of  $\sim 0.04 \text{ s}^{-1}$ .<sup>97</sup>

The effect of glass fiber on the biaxial strain thickening can be seen in Fig. 2.21. Figure 2.21 depicts the biaxial stress growth coefficient normalized by six times the shear stress growth coefficient of the corresponding fluid vs. biaxial strain for a neat maleic anhydride modified polypropylene (MAH-PP) and four short glass fiber-filled MAH-PP samples. The ratio of the biaxial viscosity to the shear viscosity is six in the linear viscoelastic region. The neat MAH-PP showed the greatest strain hardening effects which decreased with increasing fiber concentration and aspect ratio of fiber. The weakest strain thickening occurred in the glass fiber suspension which had no MAH modification. This suggests that the interaction between the fiber and the matrix influences the strain hardening behavior.

#### **2.2.4.3 Planar Extension**

No literature pertaining to the direct measurement of glass fiber suspensions in planar elongation was found. However, Mobuchon et al.<sup>11</sup> developed a novel on-line slit rheometer attached to an injection molder to study shear rheology and apparent  $\eta_p$  of glass fiber suspensions under injection molding conditions. The apparent  $\eta_p$  was found by measuring the pressure drop over the planer converging die region combined with the Binding<sup>95</sup> and Cogswell<sup>96</sup> approximations. Using this approach a short glass fiber-filled polypropylene exhibited a Trouton ratio of around 40 for low extension rates ( $0.2 \text{ s}^{-1}$ ) that decreased to roughly 4 at high extension rates ( $200 \text{ s}^{-1}$ ). The authors found that an increase in concentration ( $\phi = 0.035\text{-}0.124$ ) had little effect on the  $\eta_p$  when compared to the neat suspending medium.

## 2.2.5 Flow Phenomena

### 2.2.5.1 Weissenberg Effect

When a rotating rod comes in contact with a viscoelastic fluid the meniscus will climb the rod. This effect is known as the Weissenberg effect and is typically attributed to normal stresses within a fluid. Because normal stresses must be present, homogeneous Newtonian fluids do not exhibit this behavior. However many authors have observed rod climbing by fiber-filled Newtonian fluid suspensions that exhibit little elastic behavior through a measure of  $G'$  but exhibit normal stresses.<sup>39, 60, 76, 91</sup> Chan et al.<sup>76</sup> explained this behavior by the shear flow of the suspending medium between the fibers inducing a tensile stress which act along the streamlines creating a normal force. Others attributed normal forces and hence, rod-climbing, to fiber-fiber interactions.<sup>60</sup>

### 2.2.5.2 Entrance Pressure Loss

The entrance pressure loss through a contraction is of interest to many researchers, primary because it has been suggested that it is related to the elongational viscosity of a fluid. Both the entrance and exit pressure loss increases with fiber concentration and aspect ratio.<sup>47, 65, 78</sup> Guo et al.<sup>65</sup> found the exit pressure drop to increase with fiber concentration up to  $\phi = 0.3$ . The authors also reported that increasing fiber aspect ratio had a more pronounced effect on the exit pressure drop than the shear and complex

viscosities. Laun<sup>47</sup> found that the entrance pressure loss increased with the addition of fibers and was independent of melt temperature, i.e. viscosity for both a low-density and high-density polyethylene (LDPE:  $\phi = 0.131$ ,  $a_r \sim 31$ ; HDPE:  $\phi = 0.136$ ,  $a_r \sim 30$ ). Thomasset et al.<sup>78</sup> found similar results for long glass fiber suspensions that were independent of capillary diameter. The increase in pressure loss at the entrance and exit is attributed to the random fiber orientation in the barrel of the capillary rheometer rotating to align in the flow direction at the capillary entrance. However, there are no studies that investigate the effect of fiber orientation within the barrel of the capillary and its possible effects on the steady shear material functions or entrance pressure.

### 2.2.5.3 Extrudate Swell

Extrudate swell is a processing phenomenon that can occur during the extrusion process through any die geometry.<sup>53</sup> For viscoelastic fluids, extrudate swell is thought to be associated with the elastic component or normal stresses within the fluid and most empirical equations that attempt to predict the amount of extrudate swell as a function of shear rate, have a non-zero  $N_1$  component.<sup>68</sup> The presence of fibers significantly reduces the amount of extrudate swell, compared to the neat matrix and introduces gross surface irregularities, especially at low shear rates.<sup>53</sup> Becraft and Metzner<sup>53</sup> found that for glass fiber-filled polypropylene suspensions (fiber content:  $\phi = 0.0369, 0.187$  and  $a_r \sim 64, 27$  respectively), filaments that were extruded below a shear rate of  $\sim 115 \text{ s}^{-1}$  (shear rate is below that associated with melt fracture) had irregular diameters and a “fuzzy” surface. The fuzzy surface appearance was a result of fibers protruding from the surface of the

filament. It was hypothesized that the somewhat flexible fibers traveled through the capillary in a bent position. The fibers closest to the surface were then able to “spring out” after exiting the die. Kalaprasad et al.<sup>54</sup> found a 20% reduction of die swell when short glass fibers were added to a low-density polyethylene. Similar results for diameter and surface irregularities have been published by Wu<sup>51</sup>, Crowson et al.<sup>99</sup>, and Knuttson and White<sup>100</sup>. The apparent contradiction between the increased normal stress differences but decreased extrudate swell is unclear.

### **2.2.6 Summary on the Rheology of Fiber Suspensions**

Careful consideration should be taken by any perspective researcher to the rheometric device used to characterize glass fiber suspensions as the geometry may influence the results. In addition, it would be invaluable for researchers to either pre-condition or experimentally determine the initial orientation distribution of suspension samples. This would aid in delineating the effects of the fiber on the rheology, especially with respect to experiments associated with the linear and non-linear viscoelasticity in shear and non-linear viscoelasticity in extension.

Adding fibers to either a Newtonian or non-Newtonian fluid can have a dramatic effect on both the shear and shear-free flow rheological behavior of that fluid. The extent and magnitude of the effect is a function of the fiber's orientation distribution, concentration, aspect ratio, suspending medium's viscoelastic properties and interaction with the suspending medium. The effect of the glass fiber on the rheology is greatest in the case of an evolving microstructure. This is a direct result of a change in the

characteristic length of a fiber depending on its orientation relative to the direction of flow.

Some of the interesting effects that glass fibers can have on the steady shear flow rheology are increased yield-like behavior and the onset of shear thinning occurring at lower shear rates. Both of these behaviors appear more frequently at fiber concentrations and aspect ratio relating to the concentrated régime. The source of the yield-like behavior is still inconclusive and needs to be further investigated. It is possibly a manifestation of one or both of the two most persuasive hypotheses. The first, being yield behavior is a result of dynamic fiber-fiber interaction. The second, yield behavior is due to long range networks formed by polymer-fiber entanglements.<sup>45, 97</sup> The discrepancies between glass fiber suspension that exhibit and do not exhibit a yield-like behavior could be a result of the variables in initial fiber orientation and how they are loaded into the rheometer and/or the degree of interaction with the suspending medium. The onset of shear thinning of a suspension at lower shear rates compared to the neat matrix is believed to be the result of an orientation distribution that is shear rate dependent.

The effect that glass fiber has on the elastic properties of Newtonian and non-Newtonian fluids is slightly ambiguous. The presence of normal stress differences in Newtonian suspensions and enhanced normal stress differences in non-Newtonian suspensions suggests that the presence of fiber enhances the elastic properties. However, if one takes the magnitude of the storage modulus as a measure of elasticity, then the absence of the storage modulus in Newtonian suspensions and the relatively unaffected storage modulus in non-Newtonian suspensions suggests that the presence of fiber has no

effect on the elasticity. Further evidence in support of this statement can be found in the relaxation spectrum of a suspension. Many authors have shown that the presence of fiber has little effect on the short relaxation times of a fluid. This is another indication that the elasticity is unaffected by the fiber. Also, the presence of fiber has been shown to decrease the extrudate swell. Work accomplished by Iso et al.<sup>63,64</sup> and Sepehr et al.<sup>45</sup> has shown that the presence of fiber impedes the elasticity of viscoelastic fluids. The reviewed literature seems to suggest that the presence of the fiber acts to retard the elastic behavior of viscoelastic fluids and the enhanced normal stresses are a result of direct interaction between fibers.

Interrupted, unsteady shear flow experiments have led to the hypothesis that the evolution of the orientation distribution is specific to the kinematics of the flow and is irreversible.<sup>44</sup> A suspension whose initial fiber orientation is isotropic will exhibit a stress overshoot believed to be a result of the fibers rotating toward the flow direction. Ignoring the possible phenomena of quiescent orientation changes, the overshoot will only reappear if the sample is deformed in the opposite direction, and then at a delayed strain compared to the initial overshoot. Also, an initial normal stress difference overshoot typically occurs at a larger strain than the shear stress. Direct measurements of fiber orientation correlating to various rheological measurements would be invaluable in proving conclusive statements on fiber orientation effects on the unsteady shear flow rheology.

In extensional flow, the presence of fiber greatly enhances the steady-state tensile viscosity resulting in a Trouton ratio that can be an order of magnitude greater than the value three in the linear viscoelastic limit, and induces a large extension rate thinning

behavior in non-Newtonian suspensions. The fiber also seems to suppress the strain thickening characteristics of the suspending medium. This is believed to be a result of induced shearing forces between fibers in extensional flow, dominating the kinematics.

### **2.3 Modeling**

The theoretical work on modeling fiber suspensions has been the subject of a considerable number of published works that have spanned roughly ninety years.<sup>101</sup> Through that time the majority of the theoretical work has dealt with dilute fiber suspensions in Newtonian suspending mediums. Still, some work has attempted to deal with the increased complexities associated with more concentrated systems where particle-particle interaction and increased hydrodynamics forces are significant and a few have tried to capture the behavior of more complex non-Newtonian suspending medium suspensions.

The following will be a review of literature pertaining to both theoretical and empirical approaches to modeling glass fiber suspensions. The focus of this review will be on the current approaches to modeling rheology and microstructure of fibers suspended in non-Newtonian fluids, but because the majority of these approaches are based on the theories developed for Newtonian suspensions we will also review the development of these theories. For a complete review of the predictions for fiber-filled Newtonian fluid suspension theories the reader is referred to Petrie<sup>102</sup> and Zirnsak.<sup>60</sup> As a note, for the review of literature pertaining to modeling the rheology of fiber suspensions we will synonymously refer to fibers as rods as this is common practice in theoretical

work. First, we will look at the motion of rigid fibers (§ 2.3.1). This includes both single and multiple fiber dynamics for all concentrations, and closure approximations. From the evolution of rod orientation, the contribution to the total extra stress can be calculated and is also reviewed in § 2.3.2 for both Newtonian and non-Newtonian fluids, for dilute and non-dilute suspensions. After which we consider flexible fibers § 2.3.3, and conclude the review with a summary and discussion of findings in § 2.3.4.

### **2.3.1 Motion of Rigid Fibers**

The two most common approaches modeling a suspension containing a large number of rods are: mathematically describe the motion and contribution to the extra stress of each rod within the suspension or model the suspension as one containing a large number of rods whose orientation is described by a probability distribution function where the contribution to the extra stress is taken as an average based on the orientation distribution. Predictions based on the first approach are as accurate as the theory and numerical methods used in the simulation. While predictions based on the second approach include error as a result of assumptions about particle distribution and the use of closure approximations to simplify the equations to a form that is computationally efficient. Both approaches begin with the theoretical development with respect to the motion of a single rod and is where we begin this subsection. This is followed by the development of a distribution of particles, followed by the hydrodynamic contribution of the fibers to the extra stress. Finally, we discuss the various closure approximations used in modeling a distribution of particles.

### 2.3.1.1 Dilute Suspension

#### 2.3.1.1.1 Single Fiber

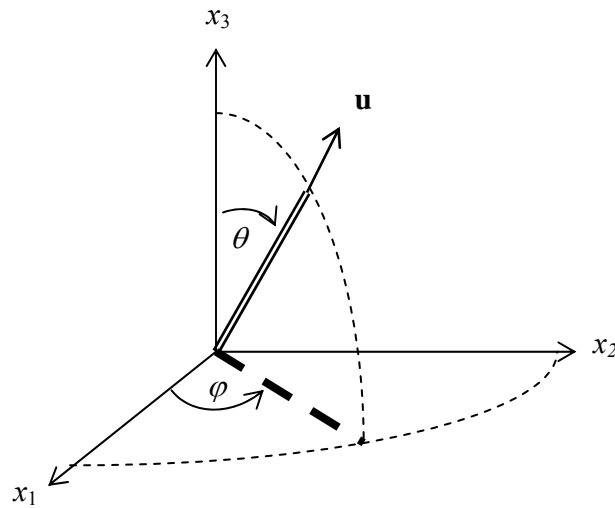


**Figure 2.22.** Unit vector  $\mathbf{u}$  describing the orientation state of a rod in spherical coordinates.

The orientation of a single fiber can be described with a unit vector  $\mathbf{u}$  along the fiber axis as shown in Fig. 2.22. In Fig. 2.22,  $\varphi$  is the azimuthal angle and  $\theta$  is the zenith angle. The components of  $\mathbf{u}$  can be mathematically described in spherical coordinates by Eqs. (2.17)-(2.19). Also, when discussing simple shear flow ( $v_1 = \dot{\gamma}y$  and  $v_2 = v_3 = 0$ ) we define  $x_1$  as the flow direction,  $x_2$  as the direction of velocity gradient, and  $x_3$  as the neutral direction.

$$u_1 = \sin \theta \cos \varphi \quad (2.17)$$

$$u_2 = \sin \theta \sin \varphi \quad (2.18)$$

$$u_3 = \cos \theta \quad (2.19)$$

The first theoretical work that is easily extendable to rigid rods is the work of Jeffery<sup>43</sup>. Jeffery extended Einstein's<sup>103</sup> approach to solving the equations of motion for the flow of a Newtonian fluid around a spherical particle to that of a neutrally buoyant ellipsoidal particle in the absence of Brownian motion. Following Jeffery's analysis, in spherical coordinates, the rotation of an ellipsoid subject to simple shear flow is governed by the following differential equations:

$$\frac{\partial \varphi}{\partial t} = \frac{\dot{\gamma}}{a_r^2 + 1} (a_r^2 \cos^2 \varphi + \sin^2 \varphi) \quad (2.20)$$

$$\frac{\partial \theta}{\partial t} = \lambda \frac{\dot{\gamma}}{4} \sin 2\theta \sin 2\varphi \quad (2.21)$$

where  $\lambda$  is a constant describing the ellipticity of the particle, given by:

$$\lambda = \left( \frac{a_r^2 - 1}{a_r^2 + 1} \right) \quad (2.22)$$

The analytical solutions to the system of differential Eqs. (2.20) and (2.21) are:

$$\tan \varphi = a_r \tan \left( \frac{\dot{\gamma} t}{a_r + a_r^{-1}} + k \right), \quad \tan k = \left( \frac{1}{a_r \tan \varphi_o} \right) \quad (2.23)$$

$$\tan \theta = \frac{C a_r}{\sqrt{a_r^2 \sin^2 \varphi + \cos^2 \varphi}}, \quad C = \frac{\tan \theta_o}{\sqrt{a_r^2 \sin^2 k + \cos^2 k}} \quad (2.24)$$

where  $C$  and  $k$  are constants that may be obtained from initial orientation of the ellipsoid,  $\varphi_o$  and  $\theta_o$ . Both  $\varphi(t)$  and  $\theta(t)$  are functions of time and are periodic resulting in a three dimensional orientation that never reaches a steady state under dynamic conditions termed a Jeffery orbit. The relative time lapse during rotation is dependant on the particle's initial orientation, aspect ratio and shear rate seen by the particle. High  $a_r$  particles spend the majority of time aligned parallel to the direction of flow.<sup>102</sup> The period of rotation,  $T$ , required for a rotation of  $2\pi$  about the particle center of mass is:

$$T = \frac{2\pi}{\dot{\gamma}} \left( a_r + \frac{1}{a_r} \right) \quad (2.25)$$

Predictions for the analytical solution to Jeffery's analysis that clearly show the periodicity of the particles orientation can be seen in Fig. 2.23. Fig. 2.23 is a graphical representation of Eqs. (2.23) and (2.24) for an ellipsoidal particle with an  $a_r = 5$  and initial orientation conditions  $\varphi_o = 175^\circ$  and  $\theta_o = 45^\circ$ .

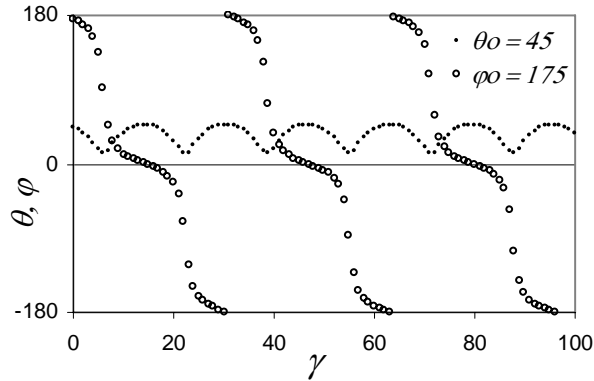


**Figure 2.23.** Polar and azimuthal angles defining the orientation of an ellipsoidal particle in simple shear flow as predicted by the analytical solution to the Jeffery's equation of motion, Eqs. (2.23) and (2.24). The solution is for an ellipsoid with  $a_r = 5$  with initial conditions of  $\varphi_o = 175^\circ$ ,  $\theta_o = 45^\circ$ . Graph is reproduced from Barbosa and Bibbo<sup>104</sup>.

The above analysis pertains to ellipsoidal particles but the theory can be extended to non-ellipsoidal particles by using an effective aspect ratio ( $a_{re}$ ).<sup>105</sup> The effective aspect ratio can be determined by comparing the rate of rotation and  $a_r$  of a particle. Work has been done both theoretically<sup>106, 107</sup> and empirically<sup>39, 108</sup> to establish relations between the particle shape and  $a_{re}$ . Cox<sup>106</sup> found  $a_{re}$  for blunt ended bodies to be represented by,

$$a_{re} = \frac{1.24a_r}{(\ln a_r)^{1/2}} \quad (2.26)$$

This work suggests that for blunt ended particles  $a_{re} < a_r$  and, therefore, have a slower period of rotation than particles with a rounded end. The exception is particles with  $a_r < 4.8$ , in which case Eq. (2.26) predicts  $a_{re} > a_r$ .

Experimentally, Jeffery orbits have been observed in various systems containing high aspect ratio particles.<sup>63, 109-111</sup> The transient shear response of a dilute suspension of rigid rods in a Newtonian suspending medium under simple shear flow conditions will rotate

around a vorticity axis unless acted upon by another force, i.e. direct contact and/or hydrodynamic interactions between other particles or boundaries.<sup>40</sup> This behavior can be seen in Fig. 2.24 for a single nylon fiber,  $a_{re} = 27.5$ , suspended in a Newtonian fluid subject to simple shear flow. Though the predictions using Jeffery's equation seem to agree well with experimental results, the authors state the model tends to over predict the rate of fiber orientation as determined experimentally.<sup>111</sup>

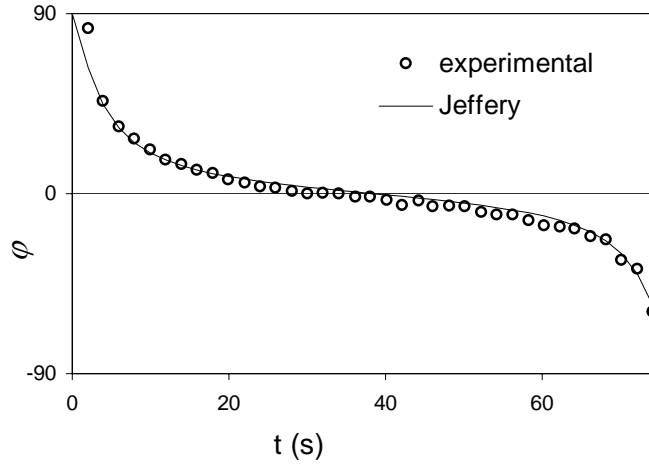


**Figure 2.24.** Evolution of orientation in the azimuthal direction for a nylon fiber in a Newtonian suspending medium,  $a_{re} = 27.5$ , subject to simple shear flow,  $\dot{\gamma} = 0.26 \text{ s}^{-1}$ . Graph is reproduced from Moses et. al.<sup>111</sup>

In the limit that  $a_r \rightarrow \infty$ ,  $\lambda \rightarrow 1$  and the solution to Eqs. (2.23) and (2.24) can be simplified to functions of strain,  $\gamma = \dot{\gamma}t$ , as,

$$\tan \theta = \tan \theta_o \sqrt{\gamma^2 \sin^2 \varphi_o + 2\gamma \sin \varphi_o \cos \varphi_o + 1} \quad (2.27)$$

$$\tan \varphi = \frac{1}{\cot \varphi_o + \gamma} \quad (2.28)$$

In this case the solution is no longer periodic, or simply, the period of rotation is infinite. As a result, a particle will rotate from its initial orientation toward the flow direction but never completely align or continually oscillate. This can be seen in Fig. 2.25 which graphically depicts the solutions to Eqs. (2.27) and (2.28) for various initial conditions.

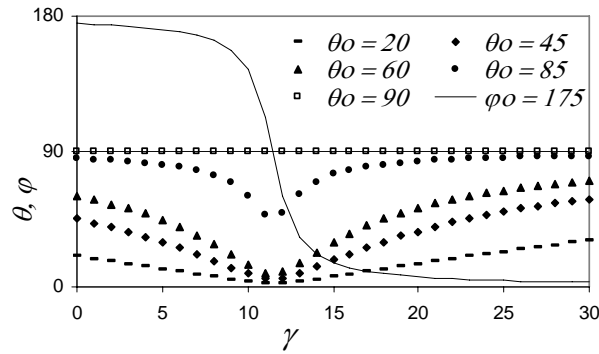


**Figure 2.25.** Evolution of orientation for an ellipsoidal particle with infinitely large  $a_r$  subject to simple shear flow as predicted by Eqs. (2.27) and (2.28). Predictions were subject to the initial conditions  $\varphi_o = 175^\circ$ ,  $\theta_o = 20, 45, 60,$  and  $90^\circ$ .<sup>104</sup>

For a more in-depth discussion of the motion of a fiber predicted by Jeffery's analysis, the reader is referred to Barbosa and Bibbó<sup>104</sup>.

Equations (2.20) and (2.21) can be generalized for any flow field in terms of  $\mathbf{u}$  as:<sup>112-</sup>

114

$$\dot{\mathbf{u}} = \frac{D\mathbf{u}}{Dt} = \mathbf{W} \cdot \mathbf{u} + \lambda [\mathbf{D} \cdot \mathbf{u} - \mathbf{u}(\mathbf{u} \cdot \mathbf{D} \cdot \mathbf{u})] \quad (2.29)$$

where  $\dot{\mathbf{u}}$  is the substantial time derivative of the unit vector  $\mathbf{u}$ ,  $\mathbf{W} = [(\nabla \mathbf{v})^t - \nabla \mathbf{v}]/2$  is the vorticity and  $\mathbf{D} = [\nabla \mathbf{v} + (\nabla \mathbf{v})^t]/2$  is the rate of strain tensor and  $\nabla \mathbf{v} = \partial v_j / \partial x_i$ . Because the

particles are assumed rigid and inextensible,  $\mathbf{u} \cdot (\mathbf{u} \cdot \mathbf{D} \cdot \mathbf{u})$  is subtracted, which is the term associated with stretch along the primary axis of a flexible particle or molecule. Eq. (2.29) can be simplified further, in limiting case that  $\lambda \rightarrow 1$  and by noting the quantity  $(\mathbf{u} \cdot \mathbf{W} \cdot \mathbf{u})$  is zero due to the antisymmetric nature of  $\mathbf{W}$ , as<sup>75, 102</sup>

$$\dot{\mathbf{u}} = \nabla \mathbf{v} \cdot \mathbf{u} - \mathbf{u} (\mathbf{u} \cdot \nabla \mathbf{v} \cdot \mathbf{u}) \quad (2.30)$$

### 2.3.1.1.2 Multiple Fibers

We now consider the case of an ideal suspension, which consists of a large number of rods that are identical in size and shape and whose concentration is spatially uniform. To predict the motion of such a suspension, using Eqs. (2.29) or (2.30), one would have to track the movement of each fiber from its initial condition resulting in an overwhelming amount of computational effort. Fortunately the fiber orientation state can be easily represented using a distribution function,  $\psi(\theta, \varphi, t)$ , that describes the probability of a rod at time  $t$  being in the range  $\theta, \varphi$  to  $\theta + d\theta, \varphi + d\varphi$ . In certain cases it is convenient to represent the distribution function in terms of the unit vector  $\mathbf{u}$  as  $\psi(\mathbf{u}, t)$ . The distribution function is normalized so that the integral over the unit sphere is equal to unity:

$$\int_0^{2\pi} \int_0^\pi \psi(\theta, \varphi, t) \sin \theta d\theta d\varphi = \int \psi(\mathbf{u}, t) d\mathbf{u} = 1 \quad (2.31)$$

$\psi(\mathbf{u}, t)$  must also be symmetric, i.e.  $\psi(\mathbf{u}) = \psi(-\mathbf{u})$ . This is a result of rod symmetry in that a rod whose orientation is  $\mathbf{u}$  is indistinguishable from one whose orientation is  $-\mathbf{u}$ .<sup>102</sup> Finally the distribution function must be able to describe the evolution of fiber orientation under dynamic conditions, termed the continuity condition.<sup>75</sup> To satisfy this condition one must employ a convection-diffusion type of equation. The equation used by Doi<sup>115</sup> and commonly referred to by others is the Smoluchowski equation or a modified Fokker-Planck equation<sup>116</sup>. The Smoluchowski equation is a macroscopic description of a multi-particle system. For a suspension of non-interacting rods subject to an external flow field and neglecting Brownian motion the Smoluchowski equation can be written in the simple form:

$$\frac{D\psi}{Dt} = -\frac{\partial}{\partial \mathbf{u}} \cdot (\dot{\mathbf{u}}\psi) \quad (2.32)$$

Eq. (2.32) is valid for any  $\dot{\mathbf{u}}$ . For dilute suspensions we can substitute Eq.(2.30) into Eq. (2.32):

$$\frac{D\psi}{Dt} = -\frac{\partial}{\partial \mathbf{u}} \cdot [(\nabla \mathbf{v} \cdot \mathbf{u})\psi - \mathbf{u}(\mathbf{u} \cdot \nabla \mathbf{v} \cdot \mathbf{u})\psi] \quad (2.33)$$

Using  $\psi(\mathbf{u}, t)$  to describe the orientation state of a suspension is complete, resulting in a clear description of the suspension microstructure and can be solved for any flow field. However, using the distribution function for predicting the particle orientation in complex flows is cumbersome because the amount of information computed is so large.<sup>74</sup>

For this reason, most theoretical work has been formulated around having to calculate the distribution function explicitly. Typically, this is accomplished by using a set of orientation tensors. Using the distribution function, an infinite number of even-order tensors can be formulated that define an averaged orientational state of the system, often referred to as structure tensors. The structure tensors of interest with respect to modeling fiber suspensions are the second- and fourth-order tensors defined as:

$$\mathbf{A}(t) = \int \mathbf{u}\mathbf{u} \psi(\mathbf{u}, t) d\mathbf{u} \quad (2.34)$$

$$\mathbf{A}_4(t) = \int \mathbf{u}\mathbf{u}\mathbf{u}\mathbf{u} \psi(\mathbf{u}, t) d\mathbf{u} \quad (2.35)$$

The trace of  $\mathbf{A}$  is always equal to 1 and for a completely random orientation state  $\mathbf{A} = 1/3 \mathbf{I}$ , where  $\mathbf{I}$  is the unity tensor. In the limit that all the fibers are perfectly aligned in the  $x_1$  direction the only non-zero component is  $A_{11} = 1$ . The fourth-order tensor arises in the theoretical analysis for both the particle motion and in calculating the contribution of the hydrodynamic interaction of the rods to the extra stress. For a more complete description of orientation tensors and their use in representing fiber suspensions the reader is referred to Advani and Tucker.<sup>74</sup> In some theoretical formulations the deviatoric form of the orientation order parameter tensor is used and is given by:

$$\mathbf{S}(t) = \int \left( \mathbf{u}\mathbf{u} - \frac{1}{3} \mathbf{I} \right) \psi(\mathbf{u}, t) d\mathbf{u} \quad (2.36)$$

There are two approaches to obtain an evolution equation in a form containing  $\mathbf{A}$ . The first approach developed by Lipscomb<sup>117, 118</sup>, following suggestions by Evans,<sup>119</sup> showed that the Fokker-Planck equation, Eq. (2.32), can be eliminated from the above analysis in the absence of Brownian motion with knowledge of the initial orientation distribution, as follows,

$$\mathbf{A} = \int \frac{(\Delta \cdot \mathbf{u})(\Delta \cdot \mathbf{u})}{(\Delta^t \cdot \Delta : \mathbf{u}\mathbf{u})} \psi(\mathbf{u}, 0) d\mathbf{u} \quad (2.37)$$

$$\mathbf{A}_4 = \int \frac{(\Delta \cdot \mathbf{u})(\Delta \cdot \mathbf{u})(\Delta \cdot \mathbf{u})(\Delta \cdot \mathbf{u})}{(\Delta^t \cdot \Delta : \mathbf{u}\mathbf{u})^2} \psi(\mathbf{u}, 0) d\mathbf{u} \quad (2.38)$$

where,

$$\Delta = E_{ij}^{-1} = \left( \frac{\partial x_j}{\partial x_i^o} \right)^{-1} \quad (2.39)$$

and,  $E_{ij}$  is the deformation gradient. Under certain conditions the distribution function is known, such as for static conditions and when the rods are completely random:

$$\psi_{random}(\mathbf{u}) = \frac{1}{4} \pi \quad (2.40)$$

At steady-state when the fibers are oriented in the direction  $\mathbf{u}_f$ :

$$\psi_{ss}(\mathbf{u}) = \delta(\mathbf{u} - \mathbf{u}_f) \quad (2.41)$$

where  $\delta$  is the Dirac delta function. Starting from a completely random state, defined by Eq. (2.40), Dinh and Armstrong<sup>75</sup> showed that the solution for the distribution function is:

$$\psi(\mathbf{u}, t) = \frac{1}{4\pi} (\Delta \cdot \Delta^t : \mathbf{u}\mathbf{u})^{-\frac{3}{2}} \quad (2.42)$$

When the distribution function is unknown or  $\dot{\mathbf{u}}$  does not have the simple form of Eq. (2.29) one must take the material derivative of Eq. (2.34) and substitute in the governing equation for  $\psi$  and  $\dot{\mathbf{u}}$ , Eq. (2.32), on the right hand side. Integration by parts, with some simplification, leads to,

$$\frac{D\mathbf{A}}{Dt} = \mathbf{A} \cdot \nabla \mathbf{v} + \lambda \left[ (\mathbf{A} \cdot \nabla \mathbf{v})^t - 2\mathbf{D} : \mathbf{A}_4 \right] \quad (2.43)$$

Eq. (2.43) is also commonly written in the form,<sup>74</sup>

$$\frac{D\mathbf{A}}{Dt} = (\mathbf{W} \cdot \mathbf{A} - \mathbf{A} \cdot \mathbf{W}) + \lambda (\mathbf{D} \cdot \mathbf{A} + \mathbf{A} \cdot \mathbf{D} - 2\mathbf{D} : \mathbf{A}_4) \quad (2.44)$$

### 2.3.1.2 Semidilute Suspension

In semidilute suspensions, the period of fiber rotation has been directly linked to shear stress oscillations which can dampen over time as a result of several interactions including boundary, particle-particle, and hydrodynamic, or slight aspect ratio variations.<sup>86</sup> As the stress approaches a steady state, a pseudo-equilibrium fiber orientation state is reached, which, after a short period of time, may slowly change with time.<sup>63</sup> In theories for semidilute suspensions Jeffery's equation for the fiber orientation is used with the assumption that the fiber is infinitely long, or  $\lambda = 1$ , in which case,<sup>30</sup>

$$\frac{D\mathbf{A}}{Dt} = (\mathbf{W} \cdot \mathbf{A} - \mathbf{A} \cdot \mathbf{W}) + (\mathbf{D} \cdot \mathbf{A} + \mathbf{A} \cdot \mathbf{D} - 2\mathbf{D} : \mathbf{A}_4) \quad (2.45)$$

### 2.3.1.3 Concentrated Suspension

In the first attempts at simulating the fiber orientation of concentrated suspensions in mold filling, Jeffery's equation for infinitely long fibers, Eq. (2.45), was used.<sup>120</sup> Comparison between fiber orientation measurements of injection molded parts and simulation results suggested Jeffery's equation over predicts the degree of alignment and the shear strain needed to align the fibers. As a result Folgar and Tucker<sup>121</sup> modified Jeffery's theory to include a phenomenological term that prevents full alignment of fiber orientation, termed the Folgar-Tucker model (F-T). The Folgar-Tucker (F-T) model can be written in terms of  $\mathbf{A}$  as follows:<sup>74</sup>

$$\frac{D\mathbf{A}}{Dt} = (\mathbf{W} \cdot \mathbf{A} - \mathbf{A} \cdot \mathbf{W}) + (\mathbf{D} \cdot \mathbf{A} + \mathbf{A} \cdot \mathbf{D} - 2\mathbf{D} : \mathbf{A}_4) + 2C_1 \dot{\gamma} (\mathbf{I} - 3\mathbf{A}) \quad (2.46)$$

where  $C_1$  is a phenomenological parameter. The last term on the right hand side of the equation is very similar to the isotropic diffusivity term in theories for Brownian rods.<sup>27</sup> The F-T model allows for the control of the steady state fiber orientation through the magnitude of  $C_1$  but the rate of fiber reorientation is still dominated by the flow field for case of small  $C_1$ , which is typically in the range of 0.016 - 0.0001.<sup>122</sup> Currently there is no theoretical approach to calculate the interaction coefficient,  $C_1$ , in the F-T model and as a result it is typically determined by fitting predictions to experimental results which can be very time intensive to produce.<sup>123</sup> Bay<sup>122</sup> developed an empirical expression for concentrated suspensions that is a function of the fiber volume fraction and aspect ratio as,

$$C_1 = 0.0184 \exp(-0.7148 \phi a_r) \quad (2.47)$$

Equation (2.47) predicts that  $C_1$  decreases for increasing  $\phi a_r$ , an effect known as screening. Phan-Thien et al.<sup>124</sup> proposed a model in which  $C_1$  increases with increasing  $\phi a_r$  as,

$$C_1 = M [1.0 - \exp(-N \phi a_r)] \quad (2.48)$$

where  $M$  and  $N$  are fit parameters which they found to be,  $M = 0.03$ ,  $N = 0.224$ .

The F-T model improves the predictions of the steady state fiber orientation but has little effect on the strain at which the steady state orientation occurs. In an attempt to control the rate of fiber reorientation, Huynh<sup>125</sup> and Sepehr et al.<sup>84</sup> both included a term to reduce the rate of fiber orientation termed the strain reduction factor by Huynh and the slip coefficient by Sepehr. The slip coefficient can be added to the F-T model as follows,

$$\frac{D\mathbf{A}}{Dt} = \alpha [(\mathbf{W} \cdot \mathbf{A} - \mathbf{A} \cdot \mathbf{W}) + (\mathbf{D} \cdot \mathbf{A} + \mathbf{A} \cdot \mathbf{D} - 2\mathbf{D} : \mathbf{A}_4) + 2C_l \dot{\gamma} (\mathbf{I} - 3\mathbf{A})] \quad (2.49)$$

where the slip coefficient,  $\alpha$ , is some value between 0-1.

Model predictions of fiber orientation using the strain reduction factor in combination with the F-T model showed excellent predictions of the fiber orientation compared to the experimental results in injection molded plaques. However, the addition of the slip or strain reduction factor to the equations governing fiber motion results in a loss of objectivity of the equation. This can affect the results when the coordinate frame is translated, rotated or give different results when solved in different coordinate frames as might be required in complex flow simulations of mold filling. However, the physical aspects of the predictions, in the case of simple shear flow, are still acceptable.

### 2.3.1.4 Closure Approximations

In the above analysis relating to Eqs. (2.44)-(2.49) the theoretical description is still as general and accurate as the Smoluchowski equation but is not of a closed form with respect to  $\mathbf{A}$  because of the fourth-order tensor. The fourth-order tensor has been the

subject of much research because in order to complete the analysis one must use a closure or decoupling approximation to express the fourth-order tensor in terms of the second-order tensor. Various closure approximations have been suggested and will be discussed subsequently.

Appropriately described through its name, a closure approximation is some function which approximates a higher order orientation tensor with lower order orientation tensors and from the unit tensor. In the context of this review the closure approximation is vital in establishing an equation of change for the average orientation state of the system and in calculating the extra stress contribution as a result of the hydrodynamic drag discussed later. In addition the higher order orientation tensors (tensors greater than second-order) arise in any continuum model that describes the mechanical or rheological properties of a two-phase system containing particles whose orientation can be anisotropic. Many closure approximations have been suggested; all of which follow basic normalization ( $A_{ii} = 1$ ) and symmetry ( $A_{ij} = A_{ji}$ ) constraints. If the closure approximation satisfies these conditions, it is then judged based on its accuracy when compared to the solution without the use of the approximation. This can be accomplished by numerically solving the equation of change for the distribution function, Eq. (2.32); then  $\psi(\mathbf{u}, t)$  can be numerically integrated at each time step to solve for the  $\mathbf{A}$  components.<sup>74</sup> Recently, Jack and Smith<sup>126</sup> proposed a method for reconstructing the orientation distribution function from successively higher order orientation tensors in a Fourier series representation. This approach allows direct comparison of the orientation tensors of varying order. Subsequently, we review the most commonly encountered closure approximations but note there have been many derived for specific flow fields and rod orientation

distributions; for a more complete review of closure approximations the reader is referred to Hand<sup>127</sup>, Hinch and Leal<sup>128</sup>, Barthés-Biesel and Acrivos<sup>129</sup>, Advani and Tucker<sup>130</sup>, Chung and Kwon<sup>131</sup>, and Jack and Smith<sup>126</sup>.

The quadratic closure is the simplest closure approximation that gives realistic predictions in all types of flows and as a result is one of the most commonly used closure approximation. It simply decouples the fourth-order tensor into the dyadic product of two second order tensors,<sup>115</sup>

$$A_{ijkl}^{quadratic} = A_{ij}A_{kl} \quad (2.50)$$

Equation (2.50), is the simplest to implement and is an exact representation of the fourth-order tensor for perfectly aligned rods. The quadratic closure preserves the symmetry and the trace of the original fourth-order tensor but leads to non-linear differential equations in  $\mathbf{A}$  that can have multiple solutions.<sup>102, 132</sup> In addition, the quadratic closure is well known to over predict the rate of fiber reorientation. Hand<sup>127</sup> proposed a linear approximation that is an exact representation of the fourth-order tensor for an isotropic suspension, as follows:

$$A_{ijkl}^{linear} = -\frac{1}{35} \left( I_{ij}I_{kl} + I_{ik}I_{jl} + I_{il}I_{jk} \right) + \frac{1}{7} \left( A_{ij}I_{kl} + A_{ik}I_{jl} + A_{il}I_{jk} + A_{kl}I_{ij} + A_{jl}I_{ik} + A_{jk}I_{il} \right) \quad (2.51)$$

The disadvantage of the linear closure approximation is that it suffers from nonphysical oscillations in certain flow kinematics. To take advantage of the exact nature of the

quadratic closure for a perfectly aligned system and the linear being exact for completely random system a hybrid closure approximation has been proposed for a range of orientations as follows:

$$A_{ijkl} = (1 - f) A_{ijkl}^{linear} + f A_{ijkl}^{quadratic} \quad (2.52)$$

where  $f$  is a generalization of Herman's orientation factor and a scalar invariant of  $\mathbf{A}$ . Two forms of  $f$  have been proposed by Advani and Tucker defined below as Eq. (2.53)<sup>74</sup> and Eq.(2.54)<sup>130</sup>,

$$f = c_1 \mathbf{A} : \mathbf{A} - c_2 \quad (2.53)$$

For a planar orientation  $c_1=2$  and  $c_2=1$  and for three-dimensional orientation  $c_1=3/2$  and  $c_2=1/2$ . Advani and Tucker<sup>130</sup> found that Eq. (2.53) performed well in planar simulations but poorly in three-dimensional. As a result the following was suggested,

$$f = 1 - N \det(\mathbf{A}) \quad (2.54)$$

where  $N$  is equal to 4 or 27 for planar and three-dimensional respectively. The hybrid closure approximation has been widely used in numerical simulations of complex flows since it shows stable behavior with reasonable solutions and costs relatively little computational effort. However, the hybrid closure approximation is well known to over-predict the fiber orientation.<sup>130, 133</sup>

Hinch and Leal<sup>128</sup> developed a number of closure approximations for use in modeling molecular rods affected to various extents by Brownian motion. In their papers “weak flows” referred to the case where Brownian motion had a significant impact on the static and dynamic behavior of the rods and “strong flows” where Brownian motion had little impact under dynamic conditions but was still significant under static conditions. For concentrated glass fiber systems unaffected by Brownian motion fiber interaction can behave as a randomizing potential and weak flows can be considered synonymous to large values for  $C_1$  and strong flows small values of  $C_1$  when using the Folgar-Tucker interaction term. Advani and Tucker<sup>130</sup> reviewed these closure approximations in detail for various values of  $C_1$  and found that the Hinch and Leal composite closure for weak flows, H&L1, gave good predictions in simple shear flow but gives physically impossible values in biaxial elongational flows. The H&L1 is defined as,

$$A_{ijkl} = \frac{2}{5}(I_{ij}A_{kl} + A_{ij}I_{kl}) - \frac{1}{5}(A_{ij}A_{kl}) + \frac{3}{5}(A_{ik}A_{jl} + A_{il}A_{jk}) - \frac{2}{5}(I_{ij}A_{km}A_{ml} + A_{im}A_{mj}I_{kl}) \quad (2.55)$$

The Hinch and Leal composite closure for strong flows, H&L2, gave good predictions for high values of  $C_1$  ( $C_1 \geq 0.1$ ) but unrealistic predictions in the case of simple flows for low values of  $C_1$ . The H&L2 is defined as,

$$\begin{aligned}
A_{ijkl} = & \frac{26\tilde{\lambda}}{315}(I_{ij}I_{kl}) + \frac{26\tilde{\lambda}}{315}(I_{ik}I_{jl} + I_{il}I_{jk}) + \frac{16\tilde{\lambda}}{63}(I_{ij}A_{kl} + A_{ij}I_{kl}) - \\
& \frac{4\tilde{\lambda}}{21}(A_{ik}I_{jl} + A_{jl}I_{ik} + A_{il}I_{jk} + A_{jk}I_{il}) + (A_{ij}A_{kl}) + \\
& (A_{ik}A_{jl} + A_{il}A_{jk}) - \frac{2}{A_{op}A_{po}}(A_{im}A_{mj}A_{kn}A_{nl})
\end{aligned} \tag{2.56}$$

with,  $\tilde{\lambda} = \exp\left[\frac{2(1-3A_{ij}A_{ji})}{1-A_{ij}A_{ji}}\right]$

Dupret and Verleye<sup>134</sup> developed the natural closure approximation. The approximation starts with a general description of  $\mathbf{A}_4$  in terms of  $\mathbf{A}$  and  $\mathbf{I}$  with coefficients weighting the various terms. The coefficients are polynomial functions in terms of the principle invariants of  $\mathbf{A}$  that are fit to the analytical solution to the solution to the distribution function such as in the case of Eq. (2.42). The Natural closure approximation produces reasonably accurate predictions but has been reported to have singularities in the solution. The natural closure approximation can be written as,<sup>135</sup>

$$\begin{aligned}
\bar{A}_{mm} = & C_{m,1} + C_{m,2}\lambda_1 + C_{m,3}\lambda_2 + C_{m,4}\lambda_1\lambda_2 + C_{m,5}\lambda_1^2 + C_{m,6}\lambda_2^2 + \\
& C_{m,7}\lambda_1^2\lambda_2 + C_{m,8}\lambda_2^2\lambda_1 + C_{m,9}\lambda_1^3 + C_{m,10}\lambda_2^3 + C_{m,11}\lambda_1^2\lambda_2^2 + \\
& C_{m,12}\lambda_1^3\lambda_2 + C_{m,13}\lambda_1\lambda_2^3 + C_{m,14}\lambda_1^4 + C_{m,15}\lambda_2^4
\end{aligned} \tag{2.57}$$

$m = 1, 3$ ; no sum on  $m$

Recently, Chung and Kwon<sup>131</sup> proposed an invariant-based orthotropic fitted (IBOF) closure approximation. The IBOF begins with the most general form of the fourth-order tensor  $\mathbf{A}_4$  as follows,

$$\begin{aligned}
A_{ijkl} = & \beta_1 S(I_{ij} I_{kl}) + \beta_2 S(I_{ij} A_{kl}) + \beta_3 S(A_{ij} A_{kl}) + \beta_4 S(I_{ij} A_{km} A_{ml}) + \\
& \beta_5 S(A_{ij} A_{km} A_{ml}) + \beta_6 S(A_{im} A_{mj} A_{kn} A_{nl})
\end{aligned} \tag{2.58}$$

where the operator  $S$  indicates the symmetric part of its argument such as,

$$\begin{aligned}
S(T_{ijkl}) = & \frac{1}{24} (T_{ijkl} + T_{jikl} + T_{ijlk} + T_{jilk} + T_{klji} + T_{lkij} + T_{klji} + T_{lkji} + \\
& T_{ikjl} + T_{kijl} + T_{iklj} + T_{kilj} + T_{jlik} + T_{ljik} + T_{jlki} + T_{lyki} + \\
& T_{iljk} + T_{lijk} + T_{ilkj} + T_{likj} + T_{jkil} + T_{kjil} + T_{jkli} + T_{kjli})
\end{aligned} \tag{2.59}$$

The IBOF assumes that the coefficients  $\beta_1 - \beta_6$  are polynomial expansions of the second and third invariants of  $\mathbf{A}$ . The authors performed a thorough analysis of the IBOF and found that the fifth-order polynomial offered the best trade off between computational efficiency and accuracy, the polynomial coefficients can be found elsewhere.<sup>131</sup>

### 2.3.2 Stress

In a glass fiber suspension the contributions to the total stress,  $\boldsymbol{\sigma}$ , arises from the suspending medium, the fiber, and the interaction between the fiber and the suspending medium. The fiber contribution to the total stress is highly dependent on the fiber concentration. For dilute and semidilute suspensions the stress contribution is primarily a result of hydrodynamic drag of the suspending medium over the fiber. In concentrated suspensions the proximity between neighboring fibers is on the order of the fiber diameter and fiber contact must contribute. Currently there is no theory for concentrated

suspensions that accounts for fiber contact. However, researchers use semidilute theory to predict the rheological behavior of concentrated suspensions which is included in the following discussion. Subsequently, we review the theoretical literature and the application of theory to modeling fiber suspensions in both Newtonian and non-Newtonian suspending mediums.

### 2.3.2.1 Newtonian Suspending Medium

#### 2.3.2.1.1 Dilute

A general expression for the total stress in a dilute suspension of high aspect ratio non-Brownian particles can be derived from the theories of Hand<sup>23</sup> and Giesekus<sup>21</sup> and is commonly referred to as the Lipscomb model:<sup>117, 136</sup>

$$\boldsymbol{\sigma} = -P\mathbf{I} + 2\eta_s\mathbf{D} + 2c_1\varphi\eta_s\mathbf{D} + 2\varphi\eta_s N\mathbf{D} : \mathbf{A}_4 \quad (2.60)$$

where  $\boldsymbol{\sigma}$  is the total stress,  $\eta_s$  is the suspending medium viscosity,  $c_1$  is a constant, and  $N$  is a dimensionless parameter that represents the coupling between hydrodynamic stress contribution and the fiber orientation. The third term on the right side of the equation is the viscosity enhancement as a result of the fiber and is similar to the enhancement term for a dilute suspension of spheres proposed by Einstein.<sup>103</sup> Lipscomb et al.<sup>117</sup> gives  $c_1$  to be equal to 2. The fourth term on the right side of the equation is the contribution to stress from the hydrodynamic drag of the fluid over the fiber. As in the equation for

evolution of fiber orientation, a closure approximation is need in Eq. (2.60) to express  $\mathbf{A}_4$  in terms of  $\mathbf{A}$ . Using Eq. (2.60) it is straightforward to show that the shear stress growth coefficient,  $\eta^+$ , and the first normal stress growth function,  $N_1^+$ , are,

$$\eta^+ = \sigma_{12} / \dot{\gamma} = \eta_s \left[ 1 + \varphi(c_1 + 2NA_{1212}) \right] \quad (2.61)$$

$$N_1^+ = 2\varphi\eta_s\dot{\gamma}N(A_{1112} - A_{2212}) \quad (2.62)$$

where the fourth-order tensor components are a function of time and can be predicted with the above analysis pertaining to the evolution of fiber orientation.

For dilute suspensions Lipscomb et al.<sup>117</sup> gives  $N$  to be a function of fiber aspect ratio,

$$N = \frac{a_r^2}{2 \ln a_r} \quad (2.63)$$

In addition, other works for dilute suspensions such as Batchelor<sup>30</sup> give  $N$  to be a function of the number of fibers per unit volume,  $c$ , and/or fiber length,  $L$ , and aspect ratio.

$$N = \frac{a_r^2}{3 \ln(2a_r)} f(\varepsilon), \quad f(\varepsilon) = \frac{1+0.64\varepsilon}{1-1.5\varepsilon} + 1.659\varepsilon^2, \quad \varepsilon = [\ln(2a_r)]^{-1} \quad (2.64)$$

### 2.3.2.1.2 Semidilute

In the semidilute régime inter-particle hydrodynamic interaction is the predominant phenomenon which can affect the dynamic behavior of the fiber microstructure and contribute to the extra stress. Equation (2.60) can also be applied to semidilute suspensions by replacing  $N$  for the dilute case to one that accounts for inter-particle hydrodynamics. As a note, some semidilute theories give  $c_1$  in Eq. (2.60) equal to zero. Dinh and Armstrong<sup>75</sup> followed the slender body theory of Batchelor to estimate the hydrodynamic drag as a function of inter-particle spacing as,

$$N = \frac{a_r^2}{3 \ln(2h/D)} \quad h = \begin{cases} (nL^2)^{-1} & \text{random} \\ (nL)^{-\frac{1}{2}} & \text{aligned} \end{cases} \quad (2.65)$$

where  $h$  is the inter-particle spacing given for a completely random and aligned fiber orientation, and  $D$  is the fiber diameter.

Predictions for the Dinh and Armstrong model are well documented and will be reviewed here; first in the case of simple shear flow, then elongational flow. In start up of shear flow the viscosity of the suspension is greater than the solvent viscosity by a factor of  $nL^3$  and the normal stress difference coefficients are equal to zero. The transient shear viscosity and normal stress difference coefficients are a function of shear strain alone and not shear rate. At large strains the model predicts  $\eta^+$  to approach, and at steady state be equal to, the viscosity of the suspending medium,  $\eta^+ \rightarrow \eta_s$ . This is a direct result of the approximation of the hydrodynamic drag on the fiber by a line integral

along the backbone of the fiber. The thickness is neglected in the calculation resulting in no contribution to the extra stress which becomes apparent when the fibers fully align in the principle flow direction. The transient normal stress differences approach zero at large strains. The dimensionless elongational stress growth viscosity is a function of the Hencky strain alone and not the strain rate. The steady state elongational viscosity is larger than the initial value.<sup>75, 137, 138</sup>

Shaqfeh and Fredrickson<sup>139</sup> proposed a theory for dilute and semidilute suspensions that was based on a diagrammatic representation of the multi-scattering expansion for the averaged Green's function to obtain an expression for the hydrodynamic energy dissipation from viscous drag of the fluid on the particle, the term in front of the fourth-order tensor. For an isotropic fiber orientation distribution they give:

$$N = \frac{4a_r^2}{3} \left\{ \frac{1}{\ln(1/\phi) + \ln \ln(1/\phi) + C''} \right\} \quad (2.66)$$

where  $C''$  is a constant given as  $C'' = -0.66$ , and  $0.16$  for random and aligned, respectively. Phan-Thien and Graham<sup>140</sup> proposed the following phenomenological expression,

$$N = \frac{a_r^2 (2 - \phi / G_v)}{2 [\ln(2a_r) - 1.5] (1 - \phi / G_v)^2} \quad (2.67)$$

where  $G_v = 0.53 - 0.013a_r$ , for the range of  $5 < a_r < 30$ . The predictions of both the theories of Shaqfeh and Fredrickson<sup>139</sup> and Phan-Thien and Graham<sup>140</sup> are similar to that

of the Dinh and Armstrong<sup>75</sup> model with the exception of the magnitude of the transients which is linked to the value of  $N$ .

### **2.3.2.1.3 Concentrated**

As previously discussed, currently there is no theory for concentrated suspensions that accounts for fiber contact. However, researchers use semidilute theory to predict the rheological behavior of concentrated suspensions. Another approach is to fit  $N$  to the rheological material functions of a fluid instead of calculating  $N$  from theory. However, the structure of the stress equation does not change.

### **2.3.2.2 Non-Newtonian Suspending Medium**

Subsequently we review the literature pertaining to the use of fiber suspension theory to model the rheological behavior of glass fibers suspended in non-Newtonian fluids. The common approach to including non-Newtonian effects in the Newtonian suspension theory, reviewed above, is to replace the Newtonian suspending medium viscosity,  $\eta_s$ , with a generalized Newtonian fluid or viscoelastic constitutive equation.

#### **2.3.2.2.1 Generalized Newtonian Fluid**

Gibson and Toll<sup>141</sup> derived a non-local constitutive equation for fibers suspended in a power-law fluid. The constitutive equation arises from the hydrodynamic drag of a

power-law fluid over a fiber whose motion was governed by Jeffery's equation for an infinitely large aspect ratio particle, Eq. (2.45). The authors used this approach to model the pressure distribution in an axisymmetric squeeze flow field but little discussion is given to validate the model by comparing the predictions to experimental data. However, it is shown that the constitutive relation reduces to the Dinh and Armstrong<sup>75</sup> model a homogeneous shear field.

#### **2.3.2.2.2 Viscoelastic Matrices**

Kitano and Funabashi<sup>142</sup> modeled the steady and transient shear rheology of a short glass fiber-filled polyethylene using the finite strain constitutive equations of Bogue<sup>143</sup> and Meister<sup>144</sup> to try and capture the non-linear behavior. Both theories are related to the network theory of Lodge.<sup>145</sup> The authors found that both theories were able to predict the steady and the transient shear rheology at low shear rates (shear rates of roughly 6.0 and lower). However, in transient stress growth tests, at larger shear rates, the models predicted the overshoot to occur at a premature strain. The model was unable to predict the transient normal stress difference behavior; prematurely predicting the normal stress difference overshoot at all shear rates tested. Also, these models give no indication of the fiber microstructure or its evolution under dynamic conditions.

Gmela and co-workers have worked extensively on an approach to modeling non-Newtonian fiber suspensions in the dilute and semidilute concentration range.<sup>146-149</sup> The analysis begins with a general framework for the governing equations that guaranteed the model would not violate the laws of thermodynamics when external forces are ignored.<sup>136</sup>

The work is based on the idea that fiber suspensions can be regarded as two component fluids. One being the fibers, modeled as a rigid body fluid, the other component the polymeric matrix. The rigid body fluid is handled in the same manner as the dilute suspension theory. The equation of motion for the fibers is represented using the Folgar-Tucker model with the improved  $C_I$  by Ranganathan and Advani<sup>150</sup>. The stress from the rods is then calculated from the hydrodynamic energy dissipation term from the Dinh and Armstrong model, Eq. (60), using the hybrid closure approximation, Eq. (53). The polymeric matrix is modeled using a second order symmetric tensor (conformation tensor) developed in the generalized Poisson bracket framework introduced by Grmela<sup>151-153</sup> with different Helmholtz energy functions including a finitely extensible nonlinear elastic (FENE-P) and Hookean type. The conformation tensor contains a mobility tensor, of which Ramazani et. al.<sup>148</sup> has considered many forms, that contains a term to account for fiber-matrix interaction. There are many forms of this approach which include fiber-matrix, fiber-fiber interaction, the viscoelastic nature of the matrix coupled and decoupled with the equation of motion for the fibers and more recently the idea of incorporating the flexibility of fibers.<sup>154</sup> In most cases the model contains four fitting parameters. Predictions for steady state and transient material functions for specific cases can be found in papers by Ramazani et. al.<sup>85, 148</sup> and Rajabian et. al.<sup>154</sup> The authors have shown that the approach can successfully predict the steady shear viscosity and steady shear primary normal stress differences of fiber suspensions. However, it is difficult to conclude on the model's ability to predict the transient behavior of polymeric fiber suspensions. It is clear that the model can successfully predict qualitatively the transient behavior of fiber suspensions, i.e. shear stress and first normal stress difference growth

overshoot. Under some conditions the model predicts a pseudo-plateau preceding the first normal stress difference growth that is lower than the steady state value. This qualitatively correlates to the behavior of non-Newtonian fiber suspensions in flow reversal tests.

In a latter paper, Sepehr et. al.<sup>136</sup> compared two families of models to the experimental data of a short glass fiber-filled polybutene (Newtonian-like fluid). The first was the modified Folgar-Tucker-Lipscomb (FTL) model, as previously described. The second model was based on the unpublished work of Grmela on extending Jeffery's equation for the motion of ellipsoids in a Newtonian fluid to non-Newtonian fluids but is believed to be an extension of his earlier work published in Grmela<sup>155</sup>. The theory also includes an equation to calculate the extra stress contribution. A detailed outline of this model can be found in the paper by Sepehr et. al.<sup>136</sup> In steady state this approach did not predict a Newtonian plateau but predicted a yield-like behavior. Also, the model predicted that the normal stress differences were independent of shear rate. In an attempt to improve on the steady state predictions authors substituted the extra stress equation given by Grmela for the Lipscomb equation. This approach was termed the Extended Jeffery and Lipscomb model, EJM model. The authors stated that both models were only able to predict the steady shear and transient stress growth behavior of the fiber suspension after some modification. For the extended FTL model the authors had to use a  $\lambda$  value of greater than 1 to extend the width of the overshoot peak. This is physically impossible as  $\lambda$  is the geometric constant describing the particles ellipticity and whose values have to be between -1 and 1. In transient shear flow the predictions of both models were improved when the slip coefficient introduced in Eq. (2.49) was used.

However, it appeared that both models had difficulty predicting the magnitude of the stress overshoot. It was found that the extended Jeffery's model by Grmela had more potential to accurately describe the behavior of concentrated systems but the model also had a larger number of parameters which make finding model parameters difficult.

Azaiez<sup>156</sup>, following Fan<sup>157</sup> and Ramazani et. al.<sup>85, 148</sup> developed a constitutive equation for fiber suspensions in a viscoelastic suspending medium. He also treated the suspension as a two component fluid, in which the Folgar-Tucker model was used for the equation of motion for the rods. The extra stress was calculated from the sum of the contributions from the fiber and the suspending medium. The extra stress contribution from the fiber came from the Dinh and Armstrong approach, Eq. (60), with various closure approximations. The stress contribution from the non-Newtonian suspending medium was calculated from macroscopic elastic dumbbell theory of which three were tested; the FENE-P, FENE-CR, and Giesekus models with a modified friction factor that depends on the fiber orientation state. Model predictions based on the different closure approximations were discussed and it was found that the transient shear viscosity shows a strong dependence on the type of closure approximation used for the fibers. This correlates to the findings of Advani and Tucker<sup>130</sup>. The model predictions for steady shear and transient shear flow material functions were given for various material parameters in an attempt to qualitatively correlate the model predictions with reviewed experimental results. However, it was difficult to assess the capabilities of the model without a direct comparison to experimental results.

Guo et. al.<sup>65</sup>, investigated the effect of fiber-fiber and fiber-matrix interaction through a systematic parametric study using the approach developed by Azaiez<sup>156</sup> for the case of a

fluid represented by the FENE-P model. They found that an increase in fiber interaction increased the steady-state viscosity but had no effect on the start and slope of the shear thinning behavior. Their simulations also showed that increased fiber-fiber interaction leads to a greater degree of fiber orientation distribution randomization. There was no mention of primary normal stress or transient rheology predictions.

Beaulne and Mitsoulis<sup>158</sup> modeled the steady shear and dynamic oscillatory data by Greene and Wilkes<sup>69</sup> who studied the rheology of multiple short glass fiber-filled non-Newtonian fluids. The authors used a combination of the K-BKZ constitutive model with the Dinh and Armstrong model. In their approach the total extra stress was found as the sum of the contributions from the matrix and the fibers using the two constitutive models. It was found that the approach was in good agreement with steady state  $\eta$  and  $N_1$  experimental results. However no predictions were given with regards to the transient predictions of the model.

### **2.3.2.3 Closure Approximations**

Studies of the accuracy and computational efficiency of the closure approximations for  $\mathbf{A}_4$  have focused on the equations for fiber orientation such as Eqs. (2.44)-(2.49). There is little discussion with respect to accuracy and computational efficiency in decoupling  $\mathbf{A}_4$  in the term associated with the hydrodynamic contribution to the extra stress. In the literature reviewed the authors use the same closure to decouple  $\mathbf{A}_4$  in both the orientation and stress equations.<sup>45, 53, 85, 89, 102, 156</sup>

### 2.3.3 Flexible Fibers

The relatively limited published literature relating to flexible fibers is an indication of the difficulty associated with modeling flexible fiber systems. The primary reason for the increased difficulty is that you can no longer represent the fiber orientation using a unit vector. Instead, each fiber must be discretized into nodes that is described using a position vector  $\mathbf{x}(s, t)$  where  $s$  is the arc length. Hinch<sup>159</sup> pioneered the work on flexible fibers by describing the motion of an inextensible but perfectly flexible fiber, i.e. the bending moment is 0.

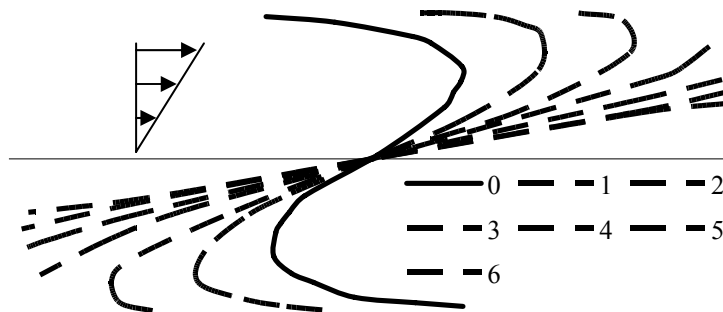


**Figure 2.26.** Motion of a flexible fiber from an initial distorted configuration as predicted by Eqs. (2.68) and (2.69). The fiber configuration is plotted for various  $\gamma$ . The numbers in the legend relate to the various strains with 0 representing the initial fiber orientation.<sup>159</sup>

To determine an equation of motion for a flexible fiber, Hinch performed a force balance on an infinitely thin thread where the tension forces,  $T$ , in the thread were set equal to the viscous forces. This resulted in two equations, one governing the tension within the thread, and the other governing the time rate of change of the position vector  $\mathbf{x}$ ,

Evolution equation 
$$\dot{\mathbf{x}} = \frac{\partial \mathbf{x}}{\partial t} = \nabla \mathbf{v} \cdot \mathbf{x} + \frac{\partial T}{\partial s} \frac{\partial \mathbf{x}}{\partial s} + \frac{1}{2} T \frac{\partial^2 \mathbf{x}}{\partial s^2} \quad (2.68)$$

Equation for tension 
$$\frac{\partial^2 T}{\partial s^2} - \frac{1}{2} \left( \frac{\partial^2 \mathbf{x}}{\partial s^2} \right)^2 T = - \frac{\partial \mathbf{x}}{\partial t} \cdot \mathbf{D} \cdot \frac{\partial \mathbf{x}}{\partial t} \quad (2.69)$$

Equations (2.68) and (2.69) can be solved given the initial fiber orientation and with boundary conditions that the tension is zero at the ends of the thread:  $T = 0$  at  $s = \pm L$ . The motion of a fiber as predicted by Eqs. (2.68) and (2.69) can be seen in Fig. 2.26. The theory predicts that the fiber straightens to align itself in the flow direction for simple shear or stretch direction for simple elongation.

Goddard and Huang<sup>160</sup> included the idea of mobility to Eqs. (2.68) and (2.69) as,

$$\dot{\mathbf{x}} = M_s \left( \frac{\partial T}{\partial s} \right) \frac{\partial \mathbf{x}}{\partial s} + T \mathbf{M}_v \cdot \frac{\partial^2 \mathbf{x}}{\partial s^2} + \nabla \mathbf{v} \cdot \mathbf{x} \quad (2.70)$$

$$M_s \frac{\partial^2 T}{\partial s^2} - \left| \frac{\partial^2 \mathbf{x}}{\partial s^2} \right|^2 M_n T = - \frac{\partial \mathbf{x}}{\partial s} \cdot \nabla \mathbf{v} \cdot \frac{\partial \mathbf{x}}{\partial s} \quad (2.71)$$

where  $M_s$  and  $M_n$  denote the longitudinal and normal components of the local filament mobility tensor  $\mathbf{M}$ ,

$$M_s = \frac{\partial \mathbf{x}}{\partial s} \cdot \mathbf{M} \cdot \frac{\partial \mathbf{x}}{\partial s} \text{ and, } M_n = \left( \frac{\partial^2 \mathbf{x}}{\partial s^2} \cdot \mathbf{M} \cdot \frac{\partial^2 \mathbf{x}}{\partial s^2} \right) \left| \frac{\partial^2 \mathbf{x}}{\partial s^2} \right|^{-2} \quad (2.72)$$

The mobility tensor represents the inverse of the hydrodynamic resistance per unit length, relating the velocity to force per unit length is given by,

$$\mathbf{M} = M_s \frac{\partial \mathbf{x}}{\partial s} \frac{\partial \mathbf{x}}{\partial s} + \mathbf{M}_v \quad (2.73)$$

where  $\mathbf{M}_v$  is the transverse mobility given by,

$$\mathbf{M}_v = \left(1 - \frac{\partial \mathbf{x}}{\partial s} \frac{\partial \mathbf{x}}{\partial s}\right) \cdot \mathbf{M} \cdot \left(1 - \frac{\partial \mathbf{x}}{\partial s} \frac{\partial \mathbf{x}}{\partial s}\right) \quad (2.74)$$

When  $\mathbf{M}$  is of the form,

$$\mathbf{M} = M_s \left(\frac{\partial \mathbf{x}}{\partial s} \frac{\partial \mathbf{x}}{\partial s}\right) + M_n \left(1 - \frac{\partial \mathbf{x}}{\partial s} \frac{\partial \mathbf{x}}{\partial s}\right) \quad (2.75)$$

the equations reduce to Hinch's analysis, Eqs. (2.68) and (2.69). For concentrated suspensions the lateral mobility  $\mathbf{M}_v$  is assumed to be small compared to the longitudinal mobility. Under these conditions the Goddard-Huang equations reduce to,<sup>161</sup>

$$\dot{\mathbf{x}} = M_s \left(\frac{\partial T}{\partial s}\right) \frac{\partial \mathbf{x}}{\partial s} + \nabla \mathbf{v} \cdot \mathbf{x} \quad (2.76)$$

$$M_s \frac{\partial^2 T}{\partial s^2} = - \frac{\partial \mathbf{x}}{\partial s} \cdot \nabla_{\mathbf{v}} \cdot \frac{\partial \mathbf{x}}{\partial s} \quad (2.77)$$

Currently there is no approach to extending the governing equations for an individual fiber to a large population of fibers. As a result, simulations of suspensions track individual fibers and the probability of their interaction. In addition, there is no theory to calculate the bulk stresses or associated rheological material functions of the fiber. However, dynamic simulations have been performed that treat each nodal point of the flexible fiber as a ball with a specific dimension. This allows one to compute the hydrodynamic stress contribution and contact forces in a dynamic simulation of a population of fibers but is not the focus of this review. A review of the dynamic simulations of flexible fibers can be found by Tang and Advani.<sup>162</sup>

### 2.3.4 Summary and Discussion

We have presented a review of literature pertaining to modeling the rheology and microstructure of rigid fibers suspended in non-Newtonian fluids. Because the majority of approaches to modeling non-Newtonian fluid suspensions begin with the theory for Newtonian suspensions, the review has also included the development of such theories. However, the review does not include a summary of model predictions for Newtonian suspension theory as this has been reviewed in detail elsewhere.<sup>60, 102</sup> We will summarize the review on modeling the rheology and microstructure of non-Newtonian fiber suspensions in two parts, the first with respect to the equation of motion for the rods and the second with respect to the contributions to the extra stress.

In almost every approach to modeling the rheology and microstructure of non-Newtonian fluid suspensions the dilute suspension theory for the equation of rod motion for an infinitely long fiber has been used regardless of the suspension fiber concentration. Dilute suspension theory for fiber motion predicts the rods to move affinely with the fluid flow and then fully align in the flow or stretch direction in simple flows. This can be a large source of error when modeling suspensions of fiber concentration higher than the dilute régime and non-Newtonian fluid suspensions because the model does not take into account fiber-fiber interactions and the fluid elastic effects that can hinder and/or affect fiber motion and orientation. One common step in trying to account for fiber-fiber interaction and predict a more realistic steady state fiber orientation distribution is to incorporate an isotropic diffusion term as in the Folgar-Tucker model. This allows for the control of the steady state fiber orientation but has little effect on the rate of fiber reorientation. Another, modification to dilute suspension theory is to incorporate the idea of slip or nonaffine motion of the fibers with the fluid. This increases the accuracy of the model predictions when compared to the stress growth behavior of fiber suspensions.

The exception to theoretical development regarding the equations of motion for nondilute fiber suspensions and non-Newtonian suspensions is Grmela's work on extending Jeffery's equation to viscoelastic fluids. Grmela's work on extending the Jeffery equation to viscoelastic fluids is unique and offers relatively good model predictions. However, model predictions are limited and the model has a large number of parameters which makes it difficult to obtain a unique set of parameters for a specific suspension. In addition, Sepehr et al.<sup>136</sup> had to use a  $\lambda$  value of greater than 1 to extend

the width of the overshoot peak. This is physically impossible as  $\lambda$  is the geometric constant describing the particles ellipticity and whose value has to be between 0 and 1.

In general there have been two approaches to calculating the extra stress contribution of a non-Newtonian suspension. The first calculates the extra stress contributions from Newtonian suspension theory which typically includes a Newtonian suspending medium term combined with a hydrodynamic energy dissipation contribution as with the Dinh and Armstrong model. In this method the rod contribution to the extra stress goes to zero at steady state. Other models like the Lipscomb and Shaqfeh and Fredrickson models include a third term which essentially accounts for the viscosity increase due to the presence of the fibers. The Newtonian suspension models predict the first normal stress difference to go to zero at steady state.

The second approach treats the suspension as a two component fluid, the rods and the suspending medium. The extra stress contribution from the rods is calculated from the Newtonian suspension theory and the extra stress contribution from the suspending medium is calculated using a non-Newtonian fluid constitutive equation. This approach seems to give better results when compared to the transient rheology of a suspension. However, there are issues with predicting the magnitude and width of the stress overshoot and the strain at which the overshoot occurs in transient tests. This becomes an even larger problem when modeling suspensions with a shear history as in flow reversal experiments. This is primarily a result of the equations of motion for the rods and relates back to the original issue of using dilute suspension Newtonian fluid theory to predict the motion of a concentrated system of rods in a non-Newtonian fluid.

The theory used to predict the time rate of change of fiber orientation in concentrated suspensions includes empirical modifications to account for behaviors that are believed to be a manifestation of direct fiber contact. However, the stress equations do not include fiber contact as a contribution. Though some researchers have shown the model predictions give qualitative agreement with rheological measurements there has been no experimental confirmation to whether the theory is predicting what is actually occurring within the suspension or what role fiber interaction plays. The barrier to expand the knowledge in model development rests on knowledge of the stress-microstructure relationship in concentrated suspensions.

The theory for flexible fiber suspensions is limited due to the difficulty in representing the fiber orientation. Hinch's theory allows one to track the evolution of fiber configuration but it is a slender body theory and does not take into account the fiber thickness. Also, the theory does not give an approach to calculating the stress associated with the fiber. Goddard and Huang included the idea of limited mobility in specific directions, i.e. longitudinal, latitudinal, and transverse, but no attempt was made to relate the fiber orientation to a stress contribution. In summary, currently there is no theory that can predict the bulk rheological properties as it relate to orientation of suspensions containing flexible fibers.

## 2.4 References

1. Macfarlane, A.; Martin, G., *Glass: A World History*. University of Chicago Press: 1992.
2. Advani, S. G.; Sozer, E. M., *Process Modeling in Composites Manufacturing*. Marcel Dekker Inc.: New York, 2003.
3. Spaude, R., Corrosion phenomena in glass fibers and glass fiber reinforced polymers. *Int. J. Mater. Prod. Technol.* **1987**, (2), 247-257.
4. Chu, W.; Karbhari, V. M., Effect of water sorption on performance of pultruded E-glass vinylester composites. *J. Mat. Civil Eng.* **2005**, 17, (1), 63-71.
5. He, X.; Yu, Z.; Jia, D.; Guo, Y., Effect of sintering additives on microstructures and mechanical properties of short-carbon-fiber-reinforced SiC composites prepared by precursor pyrolysis-hot pressing. *Ceramics Int.* **2006**, 32, 929-934.
6. Yue, C. Y.; Sui, G. X.; Looi, H. C., Effects of heat treatment on the mechanical properties of Kevlar-29 fibre. *Comp. Sci. Tech.* **2000**, 60, 421-427.
7. Darlington, M. W.; Smith, G. R., Voiding in glass fibre reinforced thermoplastic mouldings. *Polymer* **1975**, 16, 495-462.
8. Hine, P. J.; Duckett, R. A., Fiber orientation structures and mechanical properties of injection molded short glass fiber reinforced ribbed plates. *Poly. Comp.* **2004**, 25, (3), 237-254.
9. Folkes, M. J., *Short Fibre Reinforced Thermoplastics*. Research Studies Press: New York, 1982.
10. Greene, J. P., Numerical analysis of injection molding of glass fiber reinforced thermoplastics. Part 2: Fiber orientation. *Poly. Eng. Sci.* **1997**, 37, (6), 1019-1035.
11. Mobuchon, C.; Carreau, P. J.; Heuzey, M.-C.; Sepehr, M.; Ausias, G., Shear and extensional properties of short glass fiber reinforced polypropylene. *Poly. Comp.* **2005**, 26, (3), 247-264.
12. Bader, M. G.; Bowyer, W. H., An improved method of production for high strength fibre reinforced thermoplastics. *Composites* **1973**, 4, 150-156.
13. De, S. K.; White, J. R., *Short Fibre-Polymer Composites*. Woodhead Pub.: Cambridge, England, 1996.
14. Lefranche, E.; Drawczak, P.; Ciolczyk, J.-P.; Maugey, J., Injection moulding of long glass fiber reinforced polyamide 6,6: Processing conditions/microstructure/flexural properties relationship. *Adv. Poly. Technol.* **2005**, 24, (2), 114-131.
15. Darlington, M. W., Fiber orientation distribution in short fiber reinforced-plastics. *J. Mat. Sci.* **1975**, 10, (5), 906-909.
16. Lisy, F.; Hiltner, A.; Baer, E.; Katz, J. A.; Meunier, A., Application of scanning acoustic microscopy to polymeric materials. *J. Appl. Poly. Sci.* **1994**, 52, 329-352.
17. Thomas, K.; Meyer, D. E., Study of glass-fibre-reinforced thermoplastic mouldings. *Plastics and Rubber: Process* **1976**, 99-108.
18. Mavrich, A.; Fondeur, F.; Ishida, H.; Keonig, J. L.; Wagner, H. D., The study of fiber-matrix interactions via FT-IR microscopy and NMR imaging. *J. Adhesion* **1994**, 46, 91-102.

19. Kriete, A., Undesirable phenomena in 3D image cytometry. *Visualization Bio. Microscopies-3D Imaging Comp. Appl.* **1992**, 214-218.
20. Hine, P. J.; Davidson, N.; Duckett, R. A.; Ward, I. M., Measuring the fibre orientation and modeling the elastic properties of injection-moulded long-glass-fibre-reinforced nylon. *Comp. Sci. Tech.* **1993**, 53, 125-131.
21. Clarke, A. R.; Archenhold, G.; Davidson, N. C., A novel technique for determining the 3D spatial distribution of glass fibres in polymer composites. *Comp. Sci. Tech.* **1995**, 55, 75-91.
22. Clarke, A. R.; Davidson, N. C.; Archenhold, G., Measurements of fiber direction in reinforced polymer composites. *J. Microscopy- Oxford* **1993**, (171), 69-79.
23. Fischer, G.; Eyerer, P., Measuring spatial orientation of short fiber reinforced thermoplastics by image analysis. *Poly. Comp.* **1988**, 9, (4), 297-304.
24. Lee, Y.; Lee, S.; Youn, J.; Chung, K.; Kang, T., Characterization of fiber orientation in short fiber reinforced composites with an image processing technique. **2002**, 6, (2), 65.
25. Bay, R. S.; Tucker, C. L., Stereological measurement and error estimates for three dimensional fibre orientation. *Poly. Eng. Sci.* **1992**, 32, 240-253.
26. Moginger, B.; Eyerer, P., Determination of the weighting function  $g(B,r,v)$  for the fibre orientation analysis of the short fibre reinforced composites. *Composites* **1991**, 22, 394-398.
27. Doi, M.; Edwards, S. F., *The Theory of Polymer Dynamics*. Oxford University Press: New York, 1988.
28. Doi, M.; Kuzuu, N. Y., Non-linear elasticity of rodlike macromolecules in condensed state. *J. Poly. Sci. Part B - Poly Phys.* **1980**, 18, (3), 409-419.
29. Doi, M.; Edwards, S. F., Dynamics of rod-like macromolecules in concentrated solution. Part 1. *J. Chem. Soc. Faraday Trans.* **1977**, 74, (2), 560-570.
30. Batchelor, G. K., The stress generated in a non-dilute suspension of elongated particles by pure straining motion. *J. Fluid Mech.* **1971**, 46, 813-829.
31. Flory, P. J., Phase equilibria in solutions of rod-like particles. *Proc. R. Soc. London* **1956**, A234, 73-89.
32. Huq, A. M. A.; Azaiez, J., Effects of length distribution on the steady shear viscosity of semiconcentrated polymer-fiber suspensions. *Poly. Eng. Sci.* **2005**, 45, 1357-1368.
33. Kumar, K.; Bhatnagar, N.; Ghosh, A., Development of long glass fiber reinforced polypropylene composites: mechanical and morphological characteristics. *J. Reinf. Plastics Comp.* **2007**, 26, (3), 239-249.
34. Forgacs, O. L.; Mason, S. G., Particle motions in sheared suspensions IX. Spin and deformation of threadlike particles. *J. Colloid Sci.* **1958**, 14, 457-472.
35. Qi, D.; Cheng, G., Fatigue behavior of filament-wound glass fiber reinforced epoxy composite tubes under tension/torsion biaxial loading. *Poly. Comp.* **2007**, 28, (1), 116-123.
36. Ericsson, K. A.; Toll, S.; Manson, J.-A., Sliding plate rheometry of planar oriented concentrated fiber suspensions. *Rheol. Acta* **1997**, 36, 397-405.
37. Blankeney, W. R., Viscosity of suspensions of straight rigid rods. *J. Colloid Interface Sci.* **1966**, 22, (4), 324.

38. Milliken, W. J.; Mondy, L. A.; Gottlieb, M.; Graham, A. L.; Powell, R. L., The viscosity volume fraction relation for suspensions of randomly oriented rods by falling ball rheometry. *J. Non-Newt. Fluid Mech.* **1989**, 202, 217-232.
39. Nawab, M. A.; Mason, S. G., The viscosity of dilute suspensions of thread-like particles. *J. Physical Chem.* **1958**, 62, 1248-1253.
40. Powell, R. L., Rheology of suspensions of rodlike particles. *J. Stat. Phys.* **1990**, 62, 1073-1091.
41. Attanasio, A.; Bernini, U.; Galloppo, P.; Segre, G., Significance of viscosity measurements in macroscopic suspensions of elongated particles. *Trans. Soc. Rheol.* **1972**, 16, 147-154.
42. Mondy, L. A.; Geller, A. S.; Rader, D. J.; Ingber, M., Boundary element method calculations of the mobility of nonspherical particles. 2. Branched chains and flakes. *J. Aerosol Sci.* **1996**, 27, (4), 537-546.
43. Jeffery, G. B., The motion of ellipsoidal particles immersed in a viscous fluid. *Proc. R. Soc. Lond. A* **1922**, 102, 161-179.
44. Utracki, L. A., *Two-Phase Polymer Systems*. Oxford University Press: New York, 1991; p 277-331.
45. Sepehr, M.; Carreau, P. J.; Moan, M.; Ausias, G., Rheological properties of short fiber model suspensions. *J. Rheol.* **2004**, 48, (5), 1023-1048.
46. Owen, M. J., Flow, fiber orientation and mechanical property relationships in polyester DMC. *Proc. 33rd SPI Conf.* **1978**.
47. Laun, H. M., Orientation effects and rheology of short glass fiber-reinforced thermoplastics. *Colloid & Poly. Sci.* **1984**, 262, 257-269.
48. Segre, G.; Silberberg, A., Behaviour of macroscopic rigid spheres in Poiseuille flow. Part 1. Determination of local concentration by statistical analysis of particle passages through crossed light beams. *J. Fluid Mech.* **1962**, 14, 115-135.
49. Segre, G.; Silberberg, A., Behaviour of macroscopic rigid spheres in Poiseuille flow. Part 2. Experimental results and interpretation. *J. Fluid Mech.* **1962**, 14, 136-157.
50. Koh, C. J.; Hookham, P.; Leal, L. G., An experimental investigation of concentrated suspension flows in a rectangular channel. *J. Fluid Mech.* **1994**, 266, 1.
51. Wu, S., Order-disorder transitions in the extrusion of fiber-filled poly(ethylene terephthalate) and blends. *Poly. Eng. Sci.* **1979**, 19, 638-650.
52. Mondy, L. A.; Brenner, H.; Altobelli, S. A.; Abbott, J. R.; Graham, A. L., Shear-induced particle migration in suspensions of rods. *J. Rheol.* **1994**, 38, (2), 444-452.
53. Becraft, M. L.; Metzner, A. B., The rheology, fiber orientation, and processing behavior of fiber-filled fluids. *J. Rheol.* **1991**, 36, (1), 143-174.
54. Kalaprasad, G.; Mathew, G.; Pavithran, C.; Thomas, S., Melt rheological behavior of intimately mixed short sisal-glass hybrid fiber-reinforced low-density polyethylene composites. I. Untreated fibers. *J. Applied Poly. Sci.* **2003**, 89, 432-442.
55. Burgers, J. M., On the motion of small particles of elongated form suspended in a viscous liquid. Second report on viscosity and plasticity, chap. 3. *Kon. Ned. Akad. Wet. Verhand (Erste Sectie)* **1938**, 16, (4), 113-184.

56. Larson, R. G., *The Structure and Rheology of Complex Fluids*. Oxford University Press: New York, 1999.
57. Chaouche, M.; Koch, D. L., Rheology of non-Brownian rigid fiber suspensions with adhesive contacts. *J. Rheol.* **2001**, 45, (2), 369-382.
58. Dealy, J. M., Official nomenclature for material functions describing the response of a viscoelastic fluid to various shearing and extensional deformations. *J. Rheol.* **1995**, 39, (1), 253-265.
59. Ganani, E.; Powell, R. L., Rheological properties of rodlike particles in a Newtonian and a non-Newtonian fluid. *J. Rheol.* **1986**, 30, (5), 995-1013.
60. Zirnsak, M. A.; Hur, D. U.; Boger, D. V., Normal stresses in fibre suspensions. *J. Non-Newton. Fluid Mech.* **1994**, 54, 153-193.
61. Kalaprasad, G.; Thomas, S., Melt rheological behavior of intimately mixed short sisal-glass hybrid fiber-reinforced low-density polyethylene composites. II. Chemical Modification. *J. Applied Poly. Sci.* **2003**, 89, 443-450.
62. Han, C. D.; Lem, K. W., Rheology of unsaturated polyester resins. 1. Effects of filler and low-profile additive on the rheological behavior of unsaturated polyester resin. *J. Applied Poly. Sci.* **1983**, 28, (2), 743-762.
63. Iso, Y.; Koch, D. L.; Cohen, C., Orientation in simple shear flow of semi-dilute fiber suspensions. 1. Weakly elastic fluids. *J. Non-Newton. Fluid Mech.* **1996**, 62, (2-3), 115-134.
64. Iso, Y.; Koch, D. L.; Cohen, C., Orientation in simple shear flow of semi-dilute fiber suspensions. 2. Highly elastic fluids. *J. Non-Newton. Fluid Mech.* **1996**, 62, (2-3), 135-153.
65. Guo, R.; Azaiez, J.; Bellehumeur, C., Rheology of fiber filled polymer melts: Role of fiber-fiber interactions and polymer-fiber coupling. *Poly. Eng. Sci.* **2005**, 385-399.
66. Mutel, A. T. Rheological behavior and fiber orientation in simple flow of glass fiber filled polypropylene melts. Ph. D., McGill University, 1989.
67. Macosko, C. W., *Rheology Principles, Measurements, and Applications*. Wiley-VCH: New York, 1994.
68. Baird, D. G.; Collias, D. I., *Polymer Processing*. John Wiley & Sons, Inc.: New York, 1998.
69. Greene, J. P.; Wilkes, J. O., Steady-state and dynamic properties of concentrated fiber-filled thermoplastics. *Poly. Eng. Sci.* **1995**, 35, (21), 1670-1681.
70. Carter, L. F. A study of the rheology of suspensions of rod-shaped particles in a Navier-Stokes liquid. Ph. D., University of Michigan, Ann Arbor, MI, 1967.
71. Fایتel'son, L. A.; Kovtun, V. P., Experimental study of simple shear flow of monodisperse fibrous composites. *Polym. Mech.* **1975**, 11, 276-282.
72. Goto, S.; Nagazono, H.; Kato, H., The flow behavior of fiber suspensions in Newtonian fluids and polymer solutions. II: Capillary flow. *Rheol. Acta* **1986**, 25, 246-256.
73. Kitano, T.; Katoaka, T., The rheology of suspensions of vinylon fibers in polymer liquids. I. Suspensions in silicone oil. *Rheol. acta* **1981**, 20, 390-402.
74. Advani, S. G.; Tucker, C. L., The use of tensors to describe and predict fiber orientation in short fiber composites. *J. Rheol.* **1987**, 31, (8), 751-784.

75. Dinh, S. M.; Armstrong, R. C., A rheological equation of state for semiconcentrated fiber suspensions. *J. Rheol.* **1984**, 28, (3), 207-227.
76. Chan, Y.; White, J. L.; Oyanagi, Y., A fundamental study of the rheological properties of glass-fiber-reinforced polyethylene and polystyrene melts. *J. Rheol.* **1978**, 22, (5), 507-524.
77. Kim, J. K.; Song, J. H., Rheological properties and fiber orientation of short fiber-reinforced plastics. *J. Rheol.* **1997**, 41, (5), 1061-1085.
78. Thomasset, J.; Carreau, P. J., Rheological properties of long glass fiber filled polypropylene. *J. Non-Newt. Fluid Mech.* **2004**, 125, 25-34.
79. Mondy, L. A.; Morrison, T. G.; Graham, A. L.; Powell, R. L., Measurements of the viscosities of suspensions of oriented rods using falling ball rheometry. *Int. J. Multiphase Flow* **1990**, 16, (4), 651-662.
80. Cox, W. P.; Merz, E. H., Correlation of dynamic and steady flow viscosities. *J. Poly. Sci.* **1958**, 28, 619-622.
81. Mutel, A. T.; Kamal, M. R., The effect of glass fibers on the rheological behavior of polypropylene melts between rotating parallel plates. *Poly. Comp.* **1984**, 5, (1), 29-35.
82. Drozdov, A. D.; Al-Mulla, A.; Gupta, R. K., The viscoelastic behavior of melts of virgin and recycled polycarbonate reinforced with short glass fibers. *Mechanics Research Communications* **2003**, 30, 595-614.
83. Kitano, T.; Kataoka, T.; Nagatsuka, Y., Dynamic flow properties of vinylon fiber and glass-fiber reinforced polyethylene melts. *Rheol. Acta* **1984**, 23, (4), 408-416.
84. Sepehr, M.; Ausias, G.; Carreau, P. J., Rheological properties of short fiber filled polypropylene in transient shear flow. *J. Non-Newt. Fluid Mech.* **2004**, 123, 19-32.
85. Ramazani, A.; Ait-Kadi, A.; Grmela, M., Rheology of fiber suspensions in viscoelastic media: Experiments and model predictions. *J. Rheol.* **2001**, 45, (4), 945-962.
86. Ivanov, Y.; VanDeVen, T. G. M.; Mason, S. G., Damped oscillations in the viscosity of suspensions of rigid rods. I. Monomodal suspensions. *J. Rheol.* **1982**, 26, (2), 213-230.
87. Okagawa, A.; Cox, R. G.; Mason, S. G., The kinetics of flowing dispersions. VI. Transient orientation and rheological phenomena of rods and discs in shear flow. *J. Colloid Interface Sci.* **1973**, 45, 303.
88. Ganani, E.; Powell, R. L., Suspensions of rodlike particles: Literature review and data correlations. *J. Comp. Mat.* **1985**, 19, 194.
89. Ausias, G.; Agassant, J. F.; Vincent, M., Rheology of short glass fiber reinforced polypropylene. *J. Rheol.* **1992**, 36, (4), 525-542.
90. Meissner, J.; Stephenson, S. E.; Demarmels, A.; Portman, P., Multiaxial elongational flows of polymer melts-classification and experimental realization. *J. Non-Newt. Fluid Mech.* **1982**, 11, (3-4), 221-237.
91. Mewis, J.; Metzner, A. B., The rheological properties of suspensions of fibers in Newtonian fluids subjected to extensional deformations. *J. Fluid Mech.* **1974**, 62, 593-600.

92. Weinberger, G. B.; Goddard, J. D., Extensional flow behavior of polymer solutions and particle suspensions in spinning motion. *Int. J. Multiphase Flow* **1974**, 1, 465-486.
93. Kamal, M. R.; Mutel, A. T.; Utracki, L. A., Elongational behavior of short glass fiber reinforced polypropylene melts. *Poly. Comp.* **1984**, 5, 289-298.
94. Creasy, T. S.; Advani, S. G., Transient rheological behavior of a long discontinuous fiber-melt system. *J. Rheol.* **1996**, 40, (4), 497-519.
95. Binding, D. M., An approximate analysis for contraction and converging flows. *J. Non-Newt. Fluid Mech.* **1988**, 27, 173-189.
96. Cogswell, F. N., Converging flow of polymer melts in extrusion dies. *Poly. Eng. Sci.* **1972**, 12, 64-73.
97. Zhang, W.; Komoto, S.; Takahashi, M.; White, J., Biaxial extensional flow behavior and fiber dispersion and orientation in short glass fiber filled polypropylene melts. *J. Soc. Rheol., Japan* **2001**, 29, (3), 111-120.
98. Creasy, T. S.; Advani, S. G., A model long-discontinuous-fiber filled thermoplastic melt in extensional flow. *J. Non-Newt. Fluid Mech.* **1997**, 73, 261-278.
99. Crowson, R. J.; Folkes, M. J.; Bright, P. F., Rheology of short glass fiber reinforced thermoplastics and its application to injection molding I. Fiber motions and viscosity measurements. *Poly. Eng. Sci.* **1980**, 20, 925-933.
100. Knuttson, B. A.; White, J. L., Rheological and extrusion characteristics of glass fiber reinforced polycarbonate. *J. Applied Poly. Sci.* **1981**, 26, 2347-2362.
101. Leal, L. G.; Hinch, E. J., The effect of weak Brownian rotations on particles in shear flow. *J. Fluid Mech.* **1971**, 46, 685-703.
102. Petrie, C. J. S., The rheology of fibre suspensions. *J. Non-Newt. Fluid Mech.* **1999**, 87, (2-3), 369-402.
103. Einstein, A., A new determination of molecular dimensions. *Ann Phys* **1906**, 19, 289-306.
104. Barbosa, S. E.; Bibbo, M. A., Fiber motion and the rheology of suspensions with uniform fiber orientation. *J. Poly. Sci., Part: B, Polym. Phys.* **2000**, 38, 1788-1799.
105. Bretherton, F. P., The motion of rigid particles in a shear flow at low Reynolds number. *J. Fluid Mech.* **1962**, 14, 284-304.
106. Cox, R. G., The motion of long slender bodies in a viscous fluid. Part 2: Shear flow. *J. Fluid Mech.* **1971**, 45, 625-657.
107. Brenner, H., Rheology of a dilute suspension of axisymmetric Brownian particles. *Int. J. Multiphase Flow* **1974**, 1, 195-341.
108. Trevelyan, B. J.; Mason, S. G., Particle motions in sheared suspensions. I. Rotations. *J. Colloid Sci.* **1951**, 6, 354-367.
109. Anczurowski, E.; Cox, R. G.; Mason, S. G., The kinetics of flowing dispersions IV. Transient orientations of cylinders. *J. Colloid Int. Sci.* **1967**, 23, 547-562.
110. Frattini, P. L.; Fuller, G. G., Rheo-optical studies of the effect of weak Brownian rotations in sheared suspensions. *J. Fluid Mech.* **1986**, 168, 119-150.
111. Moses, K. B.; Advani, S. G.; Reinhardt, A., Investigation of fiber motion near solid boundaries in simple shear flow. *Rheol. Acta* **2001**, 40, 296-306.

112. Giesekus, H., Stromungen mit konstantem Geschwindigkeitsgradienten und die Bewegung von darin suspendierten Teilchen. Teil I: Raumliche Stromungen. *Rheol. Acta* **1962**, 2, 101-112.
113. Giesekus, H., Stromungen mit konstantem Geschwindigkeitsgradienten und die Bewegung von darin suspendierten Teilchen. Teil II: Ebene Stromungen undeine experimentelle Anordnung zu ihrer Realisierung. *Rheol. Acta* **1962**, 2, 112-122.
114. Hand, G. L., A theory of dilute suspensions. *Arch. Rational Mech. Anal.* **1961**, 7, 81-86.
115. Doi, M.; Edwards, S. F., *The Theory of Polymer Dynamics*. Clarendon Press: Oxford, 1987.
116. Hinch, E. J.; Leal, L. G., The effect of Brownian motion on the rheological properties of a suspension of non-spherical particles. *J. Fluid Mech.* **1972**, 52, 683-712.
117. Lipscomb, G. G.; Denn, M. M.; Hur, D. U.; Boger, D. V., The flow of fiber suspensions in complex geometries. *J. Non-Newt. Fluid Mech.* **1988**, 26, (3), 297-325.
118. Lipscomb, G. G., Analysis of suspension rheology in complex flows. *Ph. D. Dissertation, Univ. Cal. Berkeley* **1987**.
119. Evans, J. G. The flow of a suspension of force-free rigid rods in a Newtonian fluid. Ph. D., Cambridge University, 1975.
120. Altan, M. C., A review of fiber-reinforced injection molding: Flow kinematics and particle orientation. *J. Thermoplastic Comp. Mat.* **1990**, 3, (4), 275-313.
121. Folgar, F. P.; Tucker, C. L., Orientation behavior of fibers in concentrated suspensions. *J. Rein. Plast. Comp.* **1984**, 3, 98-119.
122. Bay, R. S. Fiber orientation in injection molded composites: A comparison of theory and experiment. Ph. D., University of Illinois Urbana-Champaign, 1991.
123. Bay, R. S.; III, C. L. T., Fiber orientation in simple injection moldings. Part II. Experimental results. *Polym. Compos.* **1992**, 13, 332-341.
124. Phan-Thien, N.; Fan, X.-J.; Tanner, R. I.; Zheng, R., Folgar-Tucker constant for fiber suspension in a Newtonian fluid. *J. Non-Newt. Fluid Mech.* **2002**, 103, 251-260.
125. Huynh, H. M. Improved Fiber Orientation Predictions for Injection-Molded Composites. University of Illinois at Urbana-Champaign, 2001.
126. Jack, D. A.; Smith, D. E., Assessing the use of tensor closure methods with orientation distribution reconstruction functions. *J. Comp. Mat.* **2004**, 38, (21), 1851-1871.
127. Hand, G. L., A theory of anisotropic fluids. *J. Fluid Mech.* **1962**, 13, 33-62.
128. Hinch, E. J.; Leal, L. G., Constitutive equations in suspension mechanics. 2. Approximate forms for a suspension of rigid particles affected by Brownian rotations. *J. Fluid Mech.* **1976**, 76, 187-208.
129. Barthes-Biesel, D.; Acrivos, A., The rheology of suspensions and its relation to phenomenological theories for non-Newtonian fluids. *Int. J. Multiphase Flow* **1973**, 1, 1-24.
130. Advani, S. G.; Tucker, C. L., Closure approximations for three-dimensional structure tensors. *J. Rheol.* **1990**, 34, (3), 367.

131. Chung, D. H.; Kwon, T. H., Improved model of orthotropic closure approximation for flow induced fiber orientation. *Polym. Compos.* **1999**, 22, (5), 636-649.
132. Petrie, C. J. S., Some asymptotic results for planar extension. *J. Non-Newt. Fluid Mech.* **1990**, 34, 37-62.
133. Chung, D. H.; Kwon, T. H., Fiber orientation in the processing of polymer composites. *Korean-Australian Rheol. J.* **2002**, 14, (4), 175-188.
134. Verleye, V.; Dupret, F., Numerical prediction of fiber orientation in complex injection molded parts. *Proc. ASME Winter Annual Mtg. MD-Vol49 HTD-Vol283* **1994**, 264-279.
135. Cintra, J. S.; III, C. L. T., Closure approximations for flow-induced fiber orientation. *J. Rheol.* **1995**, 39, (1095-1122).
136. Sepehr, M.; Carreau, P. J.; Grmela, M.; Ausias, G.; Lafleur, P. G., Comparison of rheological properties of fiber suspensions with model predictions. *J. Poly. Eng.* **2004**, 24, (6), 579-610.
137. Malamataris, N.; Papanastasiou, T. C., Closed-form material functions for semidilute fiber suspensions. *J. Rheol.* **1991**, 35, (3), 449-464.
138. Bibbo, M. A.; Dinh, S. M.; Armstrong, R. C., Shear flow properties of semiconcentrated fiber suspensions. *J. Rheol.* **1985**, 29, (6), 905-929.
139. Shaqfeh, E. S. G.; Fredrickson, G. H., The hydrodynamic stress in a suspension of rods. *Phys. Fluids A* **1990**, 2, 7-25.
140. Phan-Thien, N.; Graham, A. L., A new constitutive model for fiber suspensions. *Rheol. Acta* **1991**, 30, 44-57.
141. Gibson, A. G.; Toll, S., Mechanics of the squeeze flow of planar fiber suspensions. *J. Non-Newt. Fluid Mech.* **1999**, 82, 1-24.
142. Kitano, T.; Funabashi, M., Transient shear flow properties of fiber-filled polyethylene melts. *Rheol. Acta* **1986**, 25, 606-617.
143. Bogue, D. C., Explicit constitutive equation based on integrated strain history. *Ind. Eng. Chem. Fund.* **1966**, 5, (2), 253.
144. Meister, B. J., An integral constitutive equation based on molecular network theory. *J. Rheol.* **1971**, 15, 63-89.
145. Lodge, A. S., *Elastic Liquids*. Academic Press: New York, 1964.
146. Ghosh, T.; Grmela, M.; Carreau, P. J., Rheology of short fiber filled thermoplastics. *Poly. Comp.* **1995**, 16, (2), 144-153.
147. Ghosh, T.; Grmela, M.; Carreau, P. J., A family of rheological models at the conformation tensor level. *Preprint, Ecole Polytechnique de Montreal* **1993**.
148. Ramazani, A.; Ait-Kadi, A.; Grmela, M., Rheological modelling of short fiber thermoplastic composites. *J. Non-Newt. Fluid Mech.* **1997**, 73, 241-260.
149. Ait-Kadi, A.; Grmela, M., Modeling the rheological behavior of fiber suspensions in viscoelastic media. *J. Non-Newt. Fluid Mech.* **1994**, 53, 65-81.
150. Ranganathan, S.; Advani, S. G., Characterization of orientation clustering in short fibers. *J. Poly. Sci., Part: B, Polym. Phys.* **1991**, 28, 2651-2672.
151. Grmela, M., Bracket formulation of dissipative fluid-mechanics equations. *Phys. Let.* **1984**, 102A, 355-358.
152. Grmela, M., Bracket formulation of dissipative time evolution-equations. *Phys. Let.* **1985**, 111A, (1-2), 36-40.

153. Grmela, M., Hamiltonian-dynamics of incompressible elastic fluids. *Phys. Let.* **1988**, 130A, (2), 81-86.
154. Rajabian, M.; Dubois, C.; Grmela, M., Suspensions of semiflexible fibers in polymeric fluids: Rheology and thermodynamics. *Rheol. Acta* **2005**, 44, 521-535.
155. Grmela, M.; Ait-Kadi, A.; Lafleur, P. G., Suspensions of fibers in viscoelastic fluids: Rheology. *J. Chem. Phys.* **1998**, 109, (16), 6973-6981.
156. Azaiez, J., Constitutive equations for fiber suspensions in viscoelastic media. *J. Non-Newt. Fluid Mech.* **1996**, 66, 35-54.
157. Fan, X. J.; Moldenaers, P.; Keunings(Eds), R., *Theoretical and Applied Rheology, Proc. XI Int. Cong. Rheo. Brussles* **1992**, 850-852.
158. Beaulne, M.; Mitsoulis, E., Rheological characterization of fiber-filled polymer composites via constitutive modeling. *J. Rein. Plast. Comp.* **2003**, 22, (17), 1625-1640.
159. Hinch, E. J., The distortion of a flexible inextensible thread in a shearing flow. *J. Fluid Mech.* **1976**, 74, 317-333.
160. Goddard, J. D.; Huang, Y.-H., On the motion of flexible threads in a Stokes shear field. *J. Non-Newt. Fluid Mech.* **1983**, 13, 47-62.
161. Balasubramanyam, R., Numerical prediction of the shape of a fiber in flowing concentrated suspensions. *Composites* **1989**, 20, (1), 14-20.
162. Tang, W.; Advani, S. G., Dynamic simulation of long flexible fibers in shear flow. *CMES* **2005**, 8, (2), 165-176.

### **3.0 Obtaining Reliable Transient Rheological Data on Concentrated Short Fiber Suspensions using a Rotational Rheometer**

#### Preface

This chapter discusses the issues associated with the use of parallel disk geometry to characterize the transient shear rheological behavior of short glass fiber-filled polymeric melts. In addition, this chapter discusses a novel approach in which a “donut” shaped sample is used in combination with cone-and-plate geometry. This chapter is organized as a manuscript for publication.

### **3.0 Obtaining Reliable Transient Rheological Data on Concentrated Short Fiber Suspensions using a Rotational Rheometer**

Aaron P. R. Eberle <sup>a</sup>, Donald G. Baird <sup>a\*</sup>, Peter Wapperom <sup>b</sup>, Gregorio M. Vélez-García <sup>c</sup>

<sup>a</sup> Department of Chemical Engineering, <sup>b</sup> Department of Mathematics, <sup>c</sup> Department of Macromolecular Science and Engineering, Virginia Tech, Blacksburg, VA, 24061

\* Author to whom correspondence should be addressed; email: dbaird@vt.edu

#### **3.1 Abstract**

The conventional method for obtaining transient rheological data on fiber suspensions is to use parallel disk (PP) geometry set at a gap where the measurements are independent of disk spacing. Large transient stress overshoot behaviors were observed during startup of flow measurements on a 30 wt% short glass fiber-filled polybutylene terephthalate using the PP geometry. A contributing factor to this behavior is believed to be induced fiber collisions caused by the inhomogeneous velocity gradient. A novel approach is taken in which a “donut” shaped sample is used in a cone-and-plate device (CP-D) to maintain a sufficient gap to fiber length ratio. The magnitude of the first normal stress difference is reduced by 70% and the time to reach steady state is reduced by 100 strain units. The Lipscomb model coupled with the Folgar-Tucker model for evolution of fiber orientation is fit to the stress growth behavior measured using both the PP geometry and

CP-D. Fit model parameters were found to be dependent on the initial condition for fiber orientation and the stress growth measurement. It is believed that the CP-D allows for a quantitative measure of the stress growth behavior and eventually will lead to obtaining unambiguous model parameters.

Key words: short glass fiber, glass fiber suspension, rheology, rotational rheometer

### 3.2 Introduction

The physical properties of parts manufactured by means of injection or compression molding of short glass fiber composites significantly depend on the orientation of the fibers generated during mold filling. As a result it is desired to accurately predict fiber orientation as a function of mold design and composite rheological properties. Hence, the rheological behavior of these materials and its connection to fiber orientation as determined in simple shear flow is of significant relevance to the development of constitutive relations that can accurately predict fiber orientation in complex flow situations.

The rheological behavior of suspensions containing short glass fibers is complex because it not only depends on the suspending medium but the fiber and its orientation. The dynamic behavior of the fiber is dependent on the degree interaction, i.e. hydrodynamic and/or direct contact. As a result it is common to classify fiber suspensions into three concentration régimes based on excluded volume defined through the fiber volume fraction,  $\phi$ , and aspect ratio,  $a_r$ , of the fiber: dilute ( $\phi \ll a_r^{-2}$ ),

semidilute ( $a_r^{-2} \ll \phi \ll a_r^{-1}$ ) and concentrated ( $\phi > a_r^{-1}$ ).<sup>1</sup> Typically, the aspect ratio of short glass fibers lie in the range  $15 < a_r < 100$  and composites of industrial interest typically have fiber concentrations  $\phi > 0.1$  which places the materials of interest in the concentrated régime.<sup>2</sup>

Characterizing the rheological behavior of composite melts containing glass fibers has proven to be a formidable task. To prevent wall effects on the dynamic behavior of the fiber, Blankeney<sup>3</sup> suggested that the rheometer gap be greater than three times the fiber length,  $L$ . In rotational rheometers cone-and-plate (CP) fixtures impose a homogeneous velocity gradient but the gap height varies linearly from the center ( $\sim 50 \mu\text{m}$ ) to the plate rim. At the center of the plates where the rheometer gap is small compared to the fiber length, excessive fiber boundary interaction can cause a suppression of the transient behavior.<sup>4</sup> As a result, it is common practice for researchers to use the parallel disk (PP) geometry in rotational rheometers to perform the rheological measurements as it allows for a certain amount of gap control. However, in the PP fixtures the tangential velocity at any point on the moving plate is a function of the radial position.<sup>5</sup> This results in an inhomogeneous velocity gradient. Both experimental<sup>6,7</sup> and theoretical<sup>8</sup> results have shown that for dilute and semidilute suspensions of fibers where external forces, inter-particle contact and hydrodynamic forces are neglected, the rate of change of the particle orientation is a function of the velocity gradient.<sup>6</sup> For concentrated suspensions where the inter-particle spacing can be on the order of the fiber diameter, we believe that the inhomogeneous velocity gradient may induce excessive fiber contact resulting in a misleading measurement of the suspensions stress response to deformation.

Many researchers have studied the experimental stress growth behavior of non-dilute suspensions of short glass fibers. A good summary of some of these works can be found in Laun<sup>9</sup>, Ganani and Powell,<sup>10</sup> Powell,<sup>11</sup> Zirnsak et al.,<sup>12</sup> Sepehr et al.,<sup>13</sup> and Eberle et al.<sup>14</sup> From these works it can be shown that in general, as the concentration and/or aspect ratio of the fiber increases, the overshoot behavior of the shear stress growth coefficient,  $\eta^+$ , and first normal stress difference growth function,  $N_1^+$ , increases. The overshoot is attributed to a reorientation of the fibers as they try to establish an orientation along the fluid streamlines which is the orientation of least resistance to flow.

Current fiber-suspension theories used to predict the stress growth behavior depend on the ability to account for the relationship between the dynamic behavior of the fiber microstructure (average orientation) and the macroscopic rheological properties.<sup>15-17</sup> The result is a stress tensor describing the contribution from the presence of the fiber as a result of the hydrodynamic drag that is coupled to an equation describing the temporal evolution of the fiber orientation. Currently there is no theory for concentrated suspensions, but it is common practice in the literature to use the dilute or semidilute suspension theories of Lipscomb et al.,<sup>16</sup> Dinh and Armstrong,<sup>9</sup> Shaqfeh and Fredrickson<sup>10</sup> or Phan-Thien and Graham<sup>11</sup> to simulate the concentrated suspensions. These theories give a fundamental approach to calculating the model parameter associated with magnitude of the hydrodynamic stress as a function of the fiber concentration and aspect ratio. However, Sepehr et al.<sup>17, 18</sup> were only able to accurately predict the rheological behavior of a concentrated short glass fiber-filled polymer melt when model parameters were fit to stress growth measurements. This suggests that the model parameters may be determined for a specific composite fluid with knowledge of

the stress growth behavior. To obtain accurate parameters by fitting what truly represents the stress response to deformation of a fluid, one must first have an accurate measure of the transient stresses.

The purpose of this paper is to establish a method to obtain reliable transient rheological data for suspensions containing short glass fibers using a rotational rheometer that could be used to fit unambiguous model parameters. First, we present experimental results of the stress growth behavior as a function of gap height for a 30 wt % short glass fiber-filled polybutylene terephthalate (PBT-30), a matrix that behavior similar to a Newtonian fluid, using the PP geometry which is the conventional approach. Measurements performed using PP geometry are then compared to measurements performed using a novel technique in which a “donut” shape sample is used in a cone-and-plate (CP-D) geometry to maintain a sufficient gap to fiber length ratio. Second, the Lipscomb model coupled with the Folgar-Tucker model for orientation is fit to the transient stress growth behavior. The effect of the model parameters determined from fitting stress growth data measured using the PP geometry and the CP-D and using both random and experimentally determined initial conditions for fiber orientation is discussed.

### 3.3 Theory

**Orientation tensors:** The orientation of a single fiber can be described with a unit vector  $\mathbf{u}$  along the fiber axis as shown in Fig. 3.1. The average orientation of a large number of fibers of similar length can be described using a distribution function,  $\psi(\mathbf{u}, t)$ .

A widely used and compact way to represent the average orientation state is with the second- and fourth-order orientation tensors which are defined as the second- and fourth-moments of the orientation distribution function<sup>19</sup>

$$\mathbf{A}(t) = \int \mathbf{u}\mathbf{u}\psi(\mathbf{u}, t) d\mathbf{u} \quad (3.1)$$

$$\mathbf{A}_4(t) = \int \mathbf{u}\mathbf{u}\mathbf{u}\mathbf{u}\psi(\mathbf{u}, t) d\mathbf{u} \quad (3.2)$$

The trace of  $\mathbf{A}$  is always equal to 1 and for a completely random orientation state  $\mathbf{A} = 1/3 \mathbf{I}$ , where  $\mathbf{I}$  is the unity tensor. In the limit that all the fibers are perfectly aligned in the  $x_1$  direction the only non-zero component is  $A_{11} = 1$ .

**Evolution of fiber orientation:** The first theoretical work describing the evolution of high aspect ratio particle orientation that is easily extendable to rigid rods is that of Jeffery<sup>20</sup>. Jeffery extended Einstein's<sup>21</sup> approach to solving the equations of motion for the flow of a Newtonian fluid around a spherical particle to that of a neutrally buoyant ellipsoidal particle in the absence of Brownian motion. The generalized Jeffery equation for the evolution of the vector  $\mathbf{u}$  can be written as,<sup>22-24</sup>

$$\dot{\mathbf{u}} = \frac{D\mathbf{u}}{Dt} = \mathbf{W} \cdot \mathbf{u} + \lambda [\mathbf{D} \cdot \mathbf{u} - \mathbf{u}(\mathbf{u} \cdot \mathbf{D} \cdot \mathbf{u})] \quad (3.3)$$

where  $D/Dt$  is the material derivative,  $\lambda$  is a constant describing the ellipticity of the particle,  $\mathbf{W} = [(\nabla \mathbf{v})' - \nabla \mathbf{v}]/2$  is the vorticity,  $\mathbf{D} = [\nabla \mathbf{v} + (\nabla \mathbf{v})']/2$  is the rate of strain

tensor and  $\nabla \mathbf{v} = \partial v_j / \partial x_i$ . For fibers it is common to assume  $\lambda \rightarrow 1$  which corresponds to a fiber with an infinitely large  $a_r$ . Using this approximation, Eq. (3.3) can be solved analytically for two equations describing the motion of the fiber in terms of the spherical angles  $\varphi$  and  $\theta$ , defined in Fig. 3.1, as,<sup>8</sup>

$$\tan \theta(t) = \tan \theta_o \left[ (\dot{\gamma}t)^2 \sin^2 \varphi_o + 2\dot{\gamma}t \sin \varphi_o \cos \varphi_o + 1 \right]^{1/2} \quad (3.4)$$

$$\tan \varphi(t) = \frac{1}{\cot(\varphi_o) + \dot{\gamma}t} \quad (3.5)$$

where  $\varphi_o$  and  $\theta_o$  are initial conditions. Both  $\theta(t)$  and  $\varphi(t)$  are functions of time and shear rate,  $\dot{\gamma}$  (the scalar magnitude of  $\mathbf{D}$ ) or strain,  $\gamma = \dot{\gamma}t$ . For non-dilute suspensions Folgar and Tucker<sup>25</sup> modified Eq. (3.3) to include a phenomenological term to account for fiber interaction. The Folgar-Tucker (F-T) model can be written in terms of  $\mathbf{A}$  for  $\lambda = 1$  as follows:<sup>19</sup>

$$\frac{D\mathbf{A}}{Dt} = (\mathbf{W} \cdot \mathbf{A} - \mathbf{A} \cdot \mathbf{W}) + (\mathbf{D} \cdot \mathbf{A} + \mathbf{A} \cdot \mathbf{D} - 2\mathbf{D} : \mathbf{A}_4) + 2C_1 \dot{\gamma} (\mathbf{I} - 3\mathbf{A}) \quad (3.6)$$

where  $C_1$  is a phenomenological parameter.

**Extra Stress:** Lipscomb et al.<sup>16</sup> proposed a stress equation for a suspension of high aspect ratio particles following the work of Hand<sup>23</sup> and Giesekus<sup>21</sup> as,

$$\boldsymbol{\sigma} = -P\mathbf{I} + 2\eta_s\mathbf{D} + 2c_1\phi\eta_s\mathbf{D} + 2\phi\eta_s N\mathbf{D} : \mathbf{A}_4 \quad (3.7)$$

where  $\boldsymbol{\sigma}$  is the total stress,  $\eta_s$ ,  $c_1$  is a constant, is the suspending medium viscosity and  $N$  is a dimensionless parameter that represents the coupling between hydrodynamic stress contribution and the fiber orientation. Lipscomb et al. give  $c_1 = 2$  and  $N$  to be a function of the particle aspect ratio. Other theories of a similar form such as Dinh and Armstrong,<sup>15</sup> Shaqfeh and Fredrickson,<sup>26</sup> or Phan-Thien and Graham<sup>27</sup> give  $N$  to be a function of the fiber length, fiber diameter, number of fibers and the average spacing between the fibers. However,  $N$  is frequently used as a fit parameter which is the approach we use in this work.

For the predicted material functions,  $\eta^+$  and  $N_1^+$ , in which the velocity gradient is homogeneous we use the superscript notation CP to refer to the homogeneous velocity gradient found in the CP geometry.  $\eta^{\text{CP}}$ , and  $N_1^{\text{CP}}$  for simple shear flow kinematics ( $v_1 = \dot{\gamma}y$  and  $v_2 = v_3 = 0$ ) can be written as,

$$\eta^{\text{CP}} = \sigma_{12} / \dot{\gamma} = \eta_s + c_1\eta_s\phi + 2\eta_s\phi N A_{1212} \quad (3.8)$$

$$N_1^{\text{CP}} = 2\phi\eta_s\dot{\gamma}N(A_{1211} - A_{1222}) \quad (3.9)$$

This is in contrast to the equations used to predict the material functions in which the velocity gradient is inhomogeneous. In the case of an inhomogeneous velocity gradient, as in PP rheometers, the shear strain, and hence, average fiber orientation varies with

radial position. The material functions  $\eta^+$  and  $N_1^+ - N_2^+$  in this case are denoted by the superscript PP and have the form,

$$\eta^{\text{PP}} = \sigma_{12} / \dot{\gamma}_R = \eta_s + c_1 \varphi \eta_s + \frac{8\varphi \eta_s N}{\dot{\gamma}_R^4} \int_0^{\dot{\gamma}_R} A_{1212} \gamma^3 d\gamma \quad (3.10)$$

$$N_1^{\text{PP}} - N_2^{\text{PP}} = \frac{6\eta_s \varphi N \dot{\gamma}_R}{\dot{\gamma}_R^3} \int_0^{\dot{\gamma}_R} (A_{1211} - 2A_{1222} + A_{1233}) \gamma^2 d\gamma \quad (3.11)$$

## 3.4 Experimental

### 3.4.1 Materials

For this work a commercially available 30wt% (volume fraction  $\phi = 0.1766$ ) short glass fiber filled polybutylene terephthalate (PBT-30) by GE Plastics under the trade name Valox 420 was used. Linear viscoelastic measurements confirmed that the matrix exhibits little complex viscosity dependence on frequency and a small storage modulus.<sup>28</sup> To examine the effect of fiber concentration on the rheological behavior, PBT-30 was diluted to concentrations of 4.07, 8.42, 15, 20 and 25 wt%. The concentrations of 4.07 and 8.42 wt% relate to roughly 40% below and 25% above the semidilute upper boundary respectively. Compounding was accomplished by passing dry blended amounts of PBT-30 and the neat matrix through the extruder section of an Arburg Alrounder 221-55-250 injection molder at an rpm of 200. The extrudate was collected before entering the runner of the mold and pelletized. The pellets were then compression

molded for rheological testing to a fixture appropriate disk at 260 °C. Precautions were taken to minimize the degree of thermo-oxidative degradation of the PBT matrix by drying the materials at 120 °C for a minimum of 12 hours in a vacuum oven at a pressure smaller than 0.4 in.Hg before sample extrusion, molding or testing.<sup>29</sup>

To characterize the glass fiber within the suspension, pyrolysis was performed on the PBT-30 pellets after extrusion at 500 °C to separate the fibers from the matrix. The fiber length was determined by randomly measuring the length of 1,000 fibers. The number average and weight average fiber length of PBT-30 was found to be  $L_n = 0.3640$  and  $L_w = 0.4388$  mm, respectively. The same fiber length measurement was performed on all the diluted concentrations and was found to be within  $0.3640 \leq L_n \leq 0.3740$  and  $0.4388 \leq L_w \leq 0.4578$  mm. The fiber diameter,  $D$ , was determined directly from images taken of fiber cross sections using a confocal laser microscope, discussed later, and the average diameter of 1,000 fibers was found to be  $D = 12.9$   $\mu\text{m}$ . This relates to a number average aspect ratio for PBT-30 of  $a_r \cong 28.2$ . The glass fibers within the suspension can be considered non-Brownian as the Peclet number,  $Pe$ , was approximately  $10^{13}$ .<sup>30</sup>

### **3.4.2 Rheological Measurements**

All rheological measurements were performed on a Rheometrics Mechanical Spectrometer (RMS-800) at 260 °C in a nitrogen environment with a freshly loaded pre-formed sample. Rheological measurements on the PBT matrix were performed with 25 mm fixture with 0.1 radian cone angle. For measurements performed on the PBT-30 two

sets of rheometer fixtures were used: a 25 mm diameter parallel plate, PP, a 50 mm diameter cone and plate, CP, with a 0.1 radian cone angle.

In this work we are primarily interested in the transient rheological behavior at the startup of shear flow. For measurements performed using the PP fixtures,  $\eta^+$  and  $N_1^+ - N_2^+$  were calculated as functions of torque,  $M(t)$ , and normal force,  $F(t)$ , as follows,<sup>31</sup>

$$\eta^+(t) = \frac{M(t)}{2\pi R^3 \dot{\gamma}_R} \left( 3 + \frac{d \ln M}{d \ln \dot{\gamma}_R} \right) \quad (3.12)$$

and,

$$N_1^+(t) - N_2^+(t) = \frac{F_z(t)}{\pi R^2 \dot{\gamma}_R} \left( 2 + \frac{d \ln F_z}{d \ln \dot{\gamma}_R} \right) \quad (3.13)$$

where  $R$  is the radius of the plate and  $\dot{\gamma}_R$  is the shear rate at  $R$ . Because the neat PBT exhibits little shear rate dependence the quantity  $(d \ln M / d \ln \dot{\gamma}_R) = 1$ . In addition the suspending medium exhibited little elasticity and the normal stresses that arise as a result of the fibers have been shown to be proportional to  $\dot{\gamma}_R$ ,<sup>13</sup> so the quantity  $(d \ln F_z / d \ln \dot{\gamma}_R) = 1$ .

Measurements with the CP fixture were performed with two different samples: preformed CP sample disks and modified CP sample disks which we refer to as “donut” samples. The donut samples were produced by taking preformed disks and boring a hole through the center. A schematic drawing of the donut sample can be found in Fig. 3.2

and is discussed later. Using the CP fixtures, the measured material functions  $\eta^+$  and  $N_1^+$  were calculated from the following equations,<sup>31</sup>

$$\eta^+(t) = \frac{3M(t)}{2\pi\dot{\gamma}}(R_o^3 - R_i^3)^{-1} \quad (3.14)$$

$$N_1^+(t) = \frac{2F_z(t)}{\pi}(R_o^2 - R_i^2)^{-1} \quad (3.15)$$

where  $R_o$ ,  $R_i$  are the integration limits of the outer and inner diameter, respectively. The radius of the void space in the donut sample was measured after each rheological test to account for the effect of sample loading on  $R_i$ . The experimental reproducibility of measurements performed using the CP geometry was found to be  $\eta^+ \pm 5\%$  and  $N_1 \pm 7\%$ .

### 3.4.3 Measurement of Fiber Orientation

The initial fiber orientation of the PBT-30 parallel plate and donut samples were experimentally determined to aid in the discussion of the stress growth behavior and for the initial conditions of the model predictions. The initial orientation of the unmodified CP sample was assumed to be the same as the donut sample. Samples were loaded into their respective rheometer fixture at 260°C to give the same shear history as the samples used for measurements. Each sample was imaged perpendicular to the flow direction ( $x_2$  -  $x_3$  plane). We define  $x_1$  as the flow direction,  $x_2$  as the direction of velocity gradient and  $x_3$  as the neutral direction. The samples were prepared by embedding quartered sections

in epoxy, sanding to a specific plane depth, and then polishing to a final abrasive particle size of  $0.3 \mu\text{m}$   $\text{Al}_2\text{O}_3$  following standardized techniques.<sup>32</sup> Extreme precaution was taken to ensure all sanding and polishing was performed parallel to the plane of interest. A schematic drawing of the polished planes and locations where the images were taken can be found in Fig. 3.3. To establish the average orientation through the sample, images were taken at three locations, at distances of 4.0, 6.25, and 8.5 mm from the outer edge denoted by PD-1, PD-2, and PD-3 respectively for the donut sample and 4.0, 7.0, and 10.0 mm from the outer edge denoted by PP-1, PP-2, and PP-3 respectively for the parallel plate sample.

Images were taken using a Zeiss LSM510 confocal laser scanning microscope fitted with a 40x water immersion objective lens and a laser excitation wavelength of 543 nm. The final image was  $230 \times 230 \mu\text{m}$  with a resolution of  $1024 \times 1024$  pixels. For each sample, sequential images were taken from the bottom to the top in the direction of the velocity gradient and at two planes of depth. The confocal laser is able to penetrate the sample surface and focus at various depths. This allowed for a full 3D description of the fiber orientation and removed the ambiguity associated with reflection microscopy techniques such as the Leeds method.<sup>33</sup> For the PBT-30 the maximum penetration was found to be  $8 \mu\text{m}$ . In an image the cross section of each fiber appears as circles or ellipse-like shapes. To process the image, the circumference of each fiber intersection was traced by hand to improve the contrast between the fibers and the matrix and converted to a binary image. A computer program was written combined with image analysis software in Matlab that measured the position of center of mass, the major and minor axis and local angle between the image axis and the major axis of the ellipse. The

components of  $\mathbf{u}$  for each fiber were determined from the elliptical “footprint” at two cross sectional planes. A full description of this technique can be found elsewhere.<sup>28, 34, 35</sup>

With knowledge of the components of the vector  $\mathbf{u}$  for each fiber the tensor  $\mathbf{A}$  is determined as a weighted sum of all fibers.<sup>36</sup>

$$A_{ij} = \frac{\sum (u_i u_j)_n F_n}{\sum F_n}, \quad F_n = \frac{M_n}{m_n} \quad (3.16)$$

where  $F_n$  is a weighting function for the  $n$ th fiber. The weighting function is based on the probability of a 2D plane intersecting a fiber. Meaning, a fiber aligned perpendicular to the plane is more likely to be severed than one aligned parallel. Using the weighting function, the larger the aspect ratio of the ellipse, the more that fiber is weighted. The reproducibility of the  $A_{ij}$  components between different samples was found to be  $\pm 8\%$ .

### 3.5 Results and Discussion

#### 3.5.1 Experimental

**Donut sample design:** Gap effects on the transient rheological behavior of suspensions containing short glass fibers have been reported by other researchers. In semidilute<sup>4</sup> and concentrated<sup>37</sup> suspensions insufficient gap heights have been shown to suppress the overshoot behavior. For our work it was crucial to determine the dependence on rheometer gap height for two reasons. One was to perform measurements using the PP geometry that were independent of gap height and reproducible. The other

reason was to determine the minimum gap height at which the measurements were independent of gap height to aid in the design of the donut sample. This was accomplished by performing startup of flow experiments on PBT-30 using various gaps in the PP geometry. The results can be seen in Figs. 3.4 (a) and (b) for  $\eta^+$  and  $N_1^+ - N_2^+$ , respectively vs.  $\dot{\gamma}$  at  $\dot{\gamma}_R = 1 \text{ s}^{-1}$ . For gaps  $\leq 2L_n$  (gaps: 0.2, 0.4, 0.6, and 0.8 mm) the rheological properties were highly dependent on the gap height. At the smallest gaps (gaps: 0.2 and 0.4)  $\eta^+$  was enhanced and took a much longer time for the overshoot to approach a steady state,  $N_1^+ - N_2^+$  was very “noisy” and suppressed compared to measurements at the other gaps. As a note, the measurements performed using gaps  $\leq 0.6$  mm were not reproducible and the plots in Figs. 3.4 (a) and (b) are a representation only. As the gap was increased to 0.8 mm, the measurements of  $\eta^+$  and  $N_1^+ - N_2^+$  became reproducible and developed an overshoot. However, the overshoot was gap dependent until 1.0 mm which is  $> 2L_n$ . For gaps 1.0 and 1.2 mm  $\eta^+$  exhibited an overshoot that was reproducible within relative error of the experiment,  $\pm 5\%$ . As a result, all further experiments using the PP were performed at a gap of 1.0 mm.

In designing the donut sample, the purpose of the hole was to remove any excessive fiber-boundary interaction at the center that could potentially affect the transient rheological behavior. The experiments discussed above, using the PP geometry with various gap heights, showed that for PBT-30 there was a negligible effect on the stress growth behavior when the gap was greater than twice the number average fiber length. The gap within the 50 mm cone and plate fixture varies linearly from 2.51 mm at the outer edge to 0.05 mm at the center. As a result, a 25.4 mm diameter hole was removed from the center of the molded CP samples which ensured the gap was always greater than

2L<sub>n</sub>. Figure 3.5 shows the stress growth behavior of the neat PBT with the 50 mm CP geometry with an unmodified sample and with the donut sample. Measurements performed using donut samples were found to be within experimental error when compared to measurements performed with unmodified samples.

**Stress growth behavior:** The rheological behavior of a suspension containing high aspect ratio particles is highly dependent on the orientation distribution of those particles.<sup>14</sup> As a result the transient response at the startup of shear flow of a suspension is dependent on the initial orientation of the fiber which is a function of the systems deformation history. In literature it is commonly assumed that the fiber orientation is initially random.<sup>17, 38</sup> However, we find that the initial orientation is closer to a planar orientation with the majority of the fibers aligned in the  $x_1$  and  $x_3$  directions. The fiber orientation data for the donut and the PP sample is reported in Table 1 for the three positions imaged on each sample and the average of the three positions. For both the donut and PP samples the majority of the fibers were aligned in the  $x_1$  and  $x_3$  directions with little orientation in the  $x_2$  direction. The  $A_{22}$  component for the PP sample was higher on average than for the donut sample. The large  $A_{11}$ ,  $A_{33}$  and small  $A_{22}$  component is believed to be a result of the sample shear history as when the samples were compression molded. All samples were molded in the same fashion so it is assumed that all the donut and PP samples had a similar initial fiber orientation.

We now consider the effect of fiber concentration on the stress growth behavior measured using the CP-D and PP geometry. The shear stress growth coefficient,  $\eta^+$ , vs.  $\gamma$  as a function of fiber concentration measured using the PP geometry and using the CP-D can be seen in Figs. 3.6 (a) and (b), respectively. Up to 15 wt%, the maximum value of

$\eta^+$  measured using both techniques is relatively similar, within experimental error. However, for higher concentrations, the magnitude of  $\eta^+$  measured using the PP geometry is always much larger, with the greatest difference being at the largest concentration of fiber, 30 wt%. A similar trend can be seen in the normal stress differences measured using the PP and CP geometries.

The normal stress difference growth,  $N_1^+ - N_2^+$  (for the PP fixture),  $N_1^+$  (for the CP geometry) vs. strain as a function of concentration can be seen in Figs. 3.7 (a) and (b) respectively. For up to 8.42 wt%, the maximum value of  $N_1^+ - N_2^+$  and  $N_1^+$  are within experimental error of each other. However, the difference drastically increases with concentration from 56% for 15 wt% to 214% for 30 wt% fiber when compared to the CP-D measurements.

In this work we compare directly  $N_1^+ - N_2^+$  measured using the PP geometry with  $N_1^+$  measured using the CP. For viscoelastic fluids it is typically found that  $-N_2 < 10\% N_1$ , where  $N_1$  and  $N_2$  relate the steady state first and second normal stress differences.<sup>5</sup> The published data relating to the magnitude of  $N_2$  in glass fiber suspensions is limited but what is available suggests the same trend applies,  $-N_2 < 10\% N_1$ .<sup>12, 39</sup> There is no published experimental data relating to the magnitude of  $N_2^+$ , at least to our knowledge, but simulations show the magnitude of  $N_2^+$  is small compared to  $N_1^+$ . In addition, at low concentrations ( $\leq 8.42$  wt%),  $N_1^+ - N_2^+$  and  $N_1^+$  are of similar magnitude. As a result we assume that  $N_2^+$  is a negligible quantity compared to  $N_1^+$ .

As discussed above, the greatest difference between the measured material functions is found to be at the highest concentration. In addition, the highest concentration is the one of greatest practical interest and as a result the rest of the paper focuses on the stress

growth behavior of PBT-30. The stress growth behavior of PBT-30 in startup of flow measured using the PP geometry at  $\dot{\gamma}_R = 1 \text{ s}^{-1}$  and CP geometry at  $\dot{\gamma} = 1 \text{ s}^{-1}$  can be seen in Figs. 3.8 (a) and (b). In Fig. 3.8 (a)  $\eta^+$  vs. strain is shown for measurements performed with the PP fixture, the CP fixture with unmodified sample and the CP fixture combined with the donut sample, CP-D. First we compare the differences between  $\eta^+$  measured with the CP fixtures using the unmodified sample and the donut sample. The value of the peak of the  $\eta^+$  overshoot is within experimental error between the two measurements. However,  $\eta^+$  decays toward a lower steady state value in the case of the donut sample. This behavior is attributed to the small gaps at the center of the plate inducing excessive fiber-boundary interaction and interfering with the evolution of the fiber microstructure in the unmodified sample.

We now compare the stress growth behavior measured using the CP-D with that measured using the PP geometry.  $\eta^+$  measured using the CP-D and the PP fixture can be seen in Fig. 3.8 (a). The overshoot for  $\eta^+$  is much greater in the measurement using the PP geometry. In addition, the onset of steady state occurs at roughly 150 strain units which is in contrast to the roughly 50 strain units at which the CP-D measurement approaches a steady state. In Fig. 3.8 (b)  $N_1^+$  is shown measured using the CP fixture for both the modified sample and the donut sample and  $N_1^+ - N_2^+$  measured using the PP fixture. First we compare  $N_1^+$  measured using the CP fixture for both the unmodified sample and the CP-D. Similar to the behavior seen for  $\eta^+$ , the overshoot of  $N_1^+$  measured with the donut sample decays at a faster rate than that measured using the unmodified sample. Again, we attribute this behavior to the small gaps at the center of the plate inducing excessive fiber-boundary interaction, interfering with the evolution of the fiber

microstructure in the unmodified sample. The differences between the measurements performed using the PP fixture and the CP-D are much greater. The peak value of the overshoot measured using the PP geometry is more than 3x that measured using the CP-D. In addition, the onset of steady state occurs at roughly 150 strain units for  $N_1^+ - N_2^+$  in contrast to the roughly 50 strain units for  $N_1^+$ .

The same differences in the stress growth behavior measured using the PP geometry and the CP-D also occur at different shear rates. Figures 3.9 (a) and (b) shows the stress growth behavior in startup of flow measurements for PBT-30 at  $\dot{\gamma} = 4 \text{ s}^{-1}$  for  $\eta^+$  and  $N_1^+ - N_2^+$ ,  $N_1^+$  vs. strain, respectively. In both Figs. 3.9 (a) and (b), the stresses measured using the CP-D are smaller in magnitude and approach a steady state at a smaller strain than that measured using the PP geometry.

As a result of the inhomogeneous velocity gradient, one would expect the width of the overshoot to be greater for the measurement performed using the PP fixture. However, the difference in magnitude is not as intuitive. One plausible hypothesis of why the transient stresses measured using the PP geometry are greater than those measured using the CP-D can be found by looking at suspension theory. In dilute suspension theory the motion of a fiber, in terms of spherical angles  $\theta$  and  $\varphi$ , is governed by Eqs. (3.4) and (3.5) respectively. Both  $\theta$  and  $\varphi$  are functions of time and shear rate. In Fig. 3.10,  $\theta$  and  $\varphi$  vs. time is depicted using initial conditions  $\theta_o = 60^\circ$  and  $\varphi_o = 175^\circ$  for various shear rates,  $\dot{\gamma} = 1, 0.2, \text{ and } 0.1 \text{ s}^{-1}$ . Fibers subject to higher shear rates rotate faster than those at lower shear rates. Moses et al.<sup>6</sup> confirmed Jeffery's analysis for a dilute suspension of Nylon fibers in a Newtonian suspending medium. In concentrated suspensions where the proximity of a neighboring fiber is on the order of the fiber

diameter the inhomogeneous velocity gradient imposed by the PP fixture could induce a high degree of direct fiber contact. As a result, the stresses measured using the PP geometry could be an inaccurate representation of the stress growth behavior that manifests from direct particle-particle contact induced by the inhomogeneous velocity gradient. If this is true then fitting theory to measurements performed using the PP geometry would also lead to inaccurate model parameters.

### 3.5.2 Model Predictions

**Numerical method and fitting:** For Eqs. (3.6), and (3.8)-(3.11) the fourth-order orientation tensor  $\mathbf{A}_4$  was decoupled using the quadratic closure approximation,  $\mathbf{A}_4 = \mathbf{A}\mathbf{A}$ .<sup>1</sup> Equation (3.6) governing the time rate of change of the fiber orientation was solved numerically using Gears implicit predictor-corrector method at a time step of 0.01 s; the results were confirmed to be independent of time step by comparing the predictions at 0.001 s. Initial conditions are discussed later. To solve for the material functions  $\eta^{\text{PP}}$  and  $N_1^{\text{PP}}-N_2^{\text{PP}}$  Eqs. (3.10) and (3.11) were integrated using the trapezoid rule at each strain. The model parameter  $N$  was obtained by fitting the predictions of  $\eta^{\text{CP}}$  and  $\eta^{\text{PP}}$  to  $\eta^+$  measured using the CP and PP geometry, respectively.  $C_1$  was determined by fitting the predictions of  $N_1^{\text{CP}}$  and  $N_1^{\text{PP}}-N_2^{\text{PP}}$  to the onset of steady state plateau of  $N_1^+$  or  $N_1^+-N_2^+$ . The suspending medium viscosity was measured to be  $\eta_s = 372$  Pa.s.

**Model predictions:** It has been shown that model parameters for a given fluid may possibly be obtained by fitting suspension theory predictions to stress growth measurements.<sup>18</sup> In the previous section we showed that there is a large difference

between the stress growth measurements performed using the CP-D and the PP geometries. The objective of the following section is to show that different material parameters can be obtained depending on the initial conditions used in the model predictions and which measurement the model is fit to, i.e. measurements performed using the CP-D and the PP geometries.

The effect of Initial conditions on the predictions of Eqs. (3.6), (3.8) and (3.9) fit to the stress growth data for PBT-30 measured using the CP-D at  $\dot{\gamma} = 1 \text{ s}^{-1}$  can be seen in Fig. 3.11. The fit model parameters using the experimentally determined initial conditions were found to be  $N = 104$  and  $C_1 = 0.00001$ , and for the random initial conditions  $N = 14$ ,  $C_1 = 0.0004$ . First, there is almost an order of magnitude difference in the value of  $N$  and  $C_1$  fit using the different Initial conditions. Secondly, there are a number of differences between the predictions. With the experimentally determined initial conditions, the prediction of  $N_1^{\text{CP}}$  is relatively good. The predicted peak value of  $N_1^{\text{CP}}$  is within 7% of the measured peak value of  $N_1^+$ . Also the width of the overshoot is of similar magnitude. However, the peak value of the  $\eta^+$  and  $N_1^+$  overshoot occur at a larger strain than the predicted  $\eta^{\text{CP}}$  and  $N_1^{\text{CP}}$ . This is in sharp contrast to the predictions using the random initial conditions. Using the random initial conditions there is roughly a 71% difference between the predictions of the peak values of  $N_1^{\text{CP}}$  and the measured  $N_1^+$ . Also, the predictions of the width of the overshoot of  $\eta^{\text{CP}}$  and  $N_1^{\text{CP}}$  are much smaller than  $\eta^+$  and  $N_1^+$ .

We now consider the effect of fitting the model parameters to the stress growth data measured using the CP-D and the PP geometry. In Figs. 3.12 (a) and (b) the experimental data and model predictions of the stress growth functions for a

homogeneous (CP geometry) and inhomogeneous (PP geometry) velocity gradient denoted by superscript CP and PP, respectively, at similar shear rates of  $\dot{\gamma} = \dot{\gamma}_R = 1 \text{ s}^{-1}$  is shown. The initial conditions were taken to be those found experimentally. For  $\eta^+$  measured using the CP-D,  $N = 104$  and for the PP sample  $N = 136.6$ . The difference in the  $N$  fit to the  $\eta^+$  overshoot peak value is roughly 30%. The model predictions of both  $\eta^{\text{CP}}$  and  $\eta^{\text{PP}}$  are unable to predict the width of the overshoot but the predictions are better for the case of  $\eta^{\text{CP}}$ . In Fig. 3.12 (b) the experimental  $N_1^+$ ,  $N_1^+ - N_2^+$  and predicted  $N_1^{\text{CP}}$ ,  $N_1^{\text{PP}} - N_2^{\text{PP}}$  vs. strain are shown. The predictions for  $N_1^{\text{CP}}$  were very close to the measured values when the magnitude of the overshoot peak value is compared. This is in sharp contrast to the predictions of  $N_1^{\text{PP}} - N_2^{\text{PP}}$  compared to the measured values. The magnitude of the overshoot peak value for  $N_1^{\text{PP}} - N_2^{\text{PP}}$  is over 50% less than the measured value. For both  $N_1^{\text{CP}}$  and  $N_1^{\text{PP}} - N_2^{\text{PP}}$  the models are unable to predict the width of the overshoot but the predictions are better for the case of  $N_1^{\text{CP}}$ .

### 3.6 Conclusions

We propose that the inhomogeneous velocity gradient imposed by a PP geometry leads to radially dependent periods of rotation for the fiber inducing excessive fiber-fiber interaction when the orientation is evolving with time. This exaggerates the magnitude of the stress growth functions and possibly the width of the overshoot. If this hypothesis is correct, PP fixtures should not be used to quantitatively characterize the stress growth functions of concentrated suspensions containing glass fibers. This work also suggests that PP fixtures should not be used to quantitatively characterize the stress growth

functions of any suspension containing high aspect ratio particles where the inter-particle distance is less than the length of the largest dimension of the particle. In addition, fitting model parameters to stress growth functions of concentrated suspensions containing high aspect ratio particles measured with a PP geometry would give inaccurate values.

We suggest an approach to characterizing the rheological behavior of suspensions containing short glass fibers that uses a donut shaped sample in a cone-and-plate geometry. We believe that measurements performed using this approach give an accurate representation of the stress response to deformation in simple shear flow. However, these results are given in light of the effect that the curvilinear stream lines might have on the rheological behavior. Future experiments using a sliding plate rheometer, which imposes rectilinear streamlines within a homogeneous velocity gradient, will be used to confirm our findings.

### **3.7 Acknowledgments**

The financial support for this work from the National Science Foundation and Department of Energy through Grant No. DMI-0521918 is gratefully acknowledged. We thank GE Plastics for supplying the materials used in this work.

### 3.8 References

1. Doi, M.; Edwards, S. F., *The Theory of Polymer Dynamics*. Oxford University Press: New York, 1988.
2. Advani, S. G.; Sozer, E. M., *Process Modeling in Composites Manufacturing*. Marcel Dekker Inc.: New York, 2003.
3. Blankeney, W. R., Viscosity of suspensions of straight rigid rods. *J. Colloid Interface Sci.* **1966**, 22, (4), 324.
4. Utracki, L. A., *Two-Phase Polymer Systems*. Oxford University Press: New York, 1991; p 277-331.
5. Bird, R. B.; Armstrong, R. C.; Hassager, O., *Dynamics of Polymeric Liquids*. John Wiley & Sons, Inc.: New York, 1987; Vol. 1.
6. Moses, K. B.; Advani, S. G.; Reinhardt, A., Investigation of fiber motion near solid boundaries in simple shear flow. *Rheol. Acta* **2001**, 40, 296-306.
7. Iso, Y.; Koch, D. L.; Cohen, C., Orientation in simple shear flow of semi-dilute fiber suspensions. 1. Weakly elastic fluids. *J. Non-Newt. Fluid Mech.* **1996**, 62, (2-3), 115-134.
8. Barbosa, S. E.; Bibbo, M. A., Fiber motion and the rheology of suspensions with uniform fiber orientation. *J. Poly. Sci., Part: B, Polym. Phys.* **2000**, 38, 1788-1799.
9. Laun, H. M., Orientation effects and rheology of short glass fiber-reinforced thermoplastics. *Colloid & Poly. Sci.* **1984**, 262, 257-269.
10. Ganani, E.; Powell, R. L., Suspensions of rodlike particles: Literature review and data correlations. *J. Comp. Mat.* **1985**, 19, 194.
11. Powell, R. L., Rheology of suspensions of rodlike particles. *J. Stat. Phys.* **1990**, 62, 1073-1091.
12. Zirnsak, M. A.; Hur, D. U.; Boger, D. V., Normal stresses in fibre suspensions. *J. Non-Newt. Fluid Mech.* **1994**, 54, 153-193.
13. Sepehr, M.; Carreau, P. J.; Moan, M.; Ausias, G., Rheological properties of short fiber model suspensions. *J. Rheol.* **2004**, 48, (5), 1023-1048.
14. Eberle, A. P. R.; Baird, D.; Wapperom, P., Rheology of non-Newtonian fluids containing glass fibers: A review of experimental literature. *Ind. Eng. Chem. Res.* **2008**, 47, (10), 3470-3488.
15. Dinh, S. M.; Armstrong, R. C., A rheological equation of state for semiconcentrated fiber suspensions. *J. Rheol.* **1984**, 28, (3), 207-227.
16. Lipscomb, G. G.; Denn, M. M.; Hur, D. U.; Boger, D. V., The flow of fiber suspensions in complex geometries. *J. Non-Newt. Fluid Mech.* **1988**, 26, (3), 297-325.
17. Sepehr, M.; Carreau, P. J.; Grmela, M.; Ausias, G.; Lafleur, P. G., Comparison of rheological properties of fiber suspensions with model predictions. *J. Poly. Eng.* **2004**, 24, (6), 579-610.
18. Sepehr, M.; Ausias, G.; Carreau, P. J., Rheological properties of short fiber filled polypropylene in transient shear flow. *J. Non-Newt. Fluid Mech.* **2004**, 123, 19-32.
19. Advani, S. G.; Tucker, C. L., The use of tensors to describe and predict fiber orientation in short fiber composites. *J. Rheol.* **1987**, 31, (8), 751-784.

20. Jeffery, G. B., The motion of ellipsoidal particles immersed in a viscous fluid. *Proc. R. Soc. Lond. A* **1922**, 102, 161-179.
21. Einstein, A., A new determination of molecular dimensions. *Ann Phys* **1906**, 19, 289-306.
22. Giesekus, H., Stromungen mit konstantem Geschwindigkeitsgradienten und die Bewegung von darin suspendierten Teilchen. Teil I: Raumliche Stromungen. *Rheol. Acta* **1962**, 2, 101-112.
23. Giesekus, H., Stromungen mit konstantem Geschwindigkeitsgradienten und die Bewegung von darin suspendierten Teilchen. Teil II: Ebene Stromungen undeine experimentelle Anordnung zu ihrer Realisierung. *Rheol. Acta* **1962**, 2, 112-122.
24. Hand, G. L., A theory of dilute suspensions. *Arch. Rational Mech. Anal.* **1961**, 7, 81-86.
25. Folgar, F. P.; Tucker, C. L., Orientation behavior of fibers in concentrated suspensions. *J. Rein. Plast. Comp.* **1984**, 3, 98-119.
26. Shaqfeh, E. S. G.; Fredrickson, G. H., The hydrodynamic stress in a suspension of rods. *Phys. Fluids A* **1990**, 2, 7-25.
27. Phan-Thien, N.; Graham, A. L., A new constitutive model for fiber suspensions. *Rheol. Acta* **1991**, 30, 44-57.
28. Eberle, A. P. R. The Dynamic Behavior of a Concentrated Composite Fluid Containing Non-Brownian Glass Fibers in Rheometrical Flows. Virginia Tech, Blacksburg, 2008.
29. Botelho, G.; Queiros, A.; Liberal, S.; Gijsman, P., Studies on thermal and thermo-oxidative degradation of poly(ethylene terephthalate) and poly(butylene terephthalate). *Polym Degrad Stab* **2001**, 74, (10), 39-48.
30. Larson, R. G., *The Structure and Rheology of Complex Fluids*. Oxford University Press: New York, 1999.
31. Macosko, C. W., *Rheology Principles, Measurements, and Applications*. Wiley-VCH: New York, 1994.
32. Sawyer, L. C.; Grubb, D., *Polymer Microscopy*. 2nd ed.; Springer: 1995.
33. Hine, P. J.; Davidson, N.; Duckett, R. A.; Ward, I. M., Measuring the fibre orientation and modeling the elastic properties of injection-moulded long-glass-fibre-reinforced nylon. *Comp. Sci. Tech.* **1993**, 53, 125-131.
34. Lee, Y.; Lee, S.; Youn, J.; Chung, K.; Kang, T., Characterization of fiber orientation in short fiber reinforced composites with an image processing technique. **2002**, 6, (2), 65.
35. Eberle, A. P. R.; Baird, D. G.; Wapperom, P.; Velez-Garcia, G. M., Fiber Orientation Kinetics of a Concentrated Short Glass Fiber Suspension in Startup of Simple Shear Flow. **2008**.
36. Bay, R. S.; Tucker, C. L., Stereological measurement and error estimates for three dimensional fibre orientation. *Poly. Eng. Sci.* **1992**, 32, 240-253.
37. Djalili-Moghaddam, M.; Ebrahimzadeh, R.; Toll, S., Study of geometry effects in torsional rheometry of fiber suspensions. *Rheol. Acta* **2004**, 44, 29-37.
38. Ramazani, A.; Ait-Kadi, A.; Grmela, M., Rheology of fiber suspensions in viscoelastic media: Experiments and model predictions. *J. Rheol.* **2001**, 45, (4), 945-962.

39. Chan, Y.; White, J. L.; Oyanagi, Y., A fundamental study of the rheological properties of glass-fiber-reinforced polyethylene and polystyrene melts. *J. Rheol.* **1978**, 22, (5), 507-524.

**Table 3.1.** The initial fiber orientation represented through the components of the orientation order parameter tensor,  $\mathbf{A}$ . The components of  $\mathbf{A}$  were found to be reproducible to  $A_{ij} \pm 8\%$ .

<b>Location</b>	<b><math>A_{11}</math></b>	<b><math>A_{22}</math></b>	<b><math>A_{33}</math></b>	<b><math>A_{12}</math></b>	<b><math>A_{13}</math></b>	<b><math>A_{23}</math></b>
PD-1	0.5140	0.0441	0.4419	0.1106	0.0130	0.0113
PD-2	0.4044	0.0415	0.5541	0.0581	0.1170	0.0545
PD-3	0.3808	0.0261	0.5931	0.0596	0.0562	0.0306
<b>PD-average</b>	<b>0.4371</b>	<b>0.0377</b>	<b>0.5252</b>	<b>0.0777</b>	<b>0.0604</b>	<b>0.0314</b>
PP-1	0.4408	0.0472	0.5121	0.0895	-0.0172	-0.0215
PP-2	0.5416	0.0494	0.4089	0.089	-0.0549	-0.0221
PP-3	0.4579	0.0911	0.451	0.1075	0.0023	-0.0415
<b>PP-average</b>	<b>0.4811</b>	<b>0.0618</b>	<b>0.4570</b>	<b>0.0950</b>	<b>-0.0241</b>	<b>-0.0280</b>

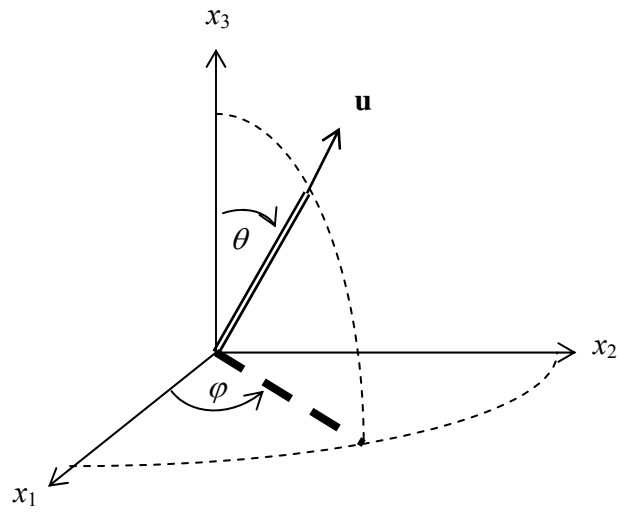


**Figure 3.1.** Unit vector  $\mathbf{u}$  describing the orientation state of a rigid fiber in spherical coordinates.

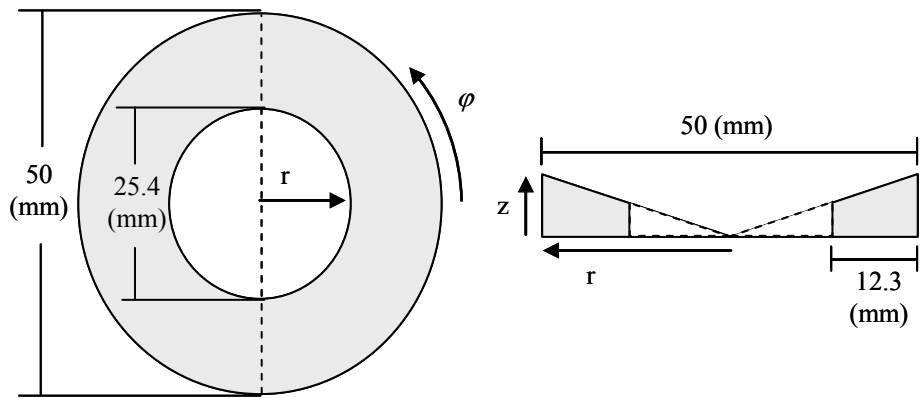


**Figure 3.2.** Schematic drawing and cross-sectional profile of the donut sample.

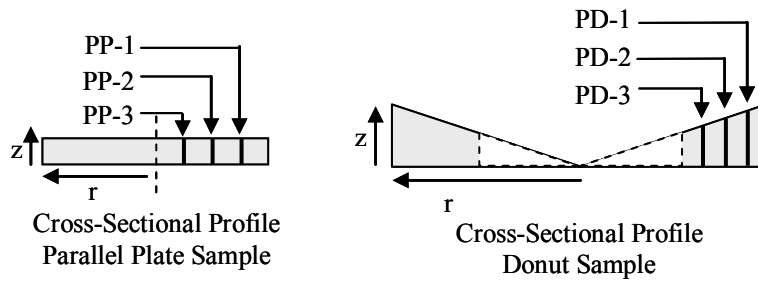
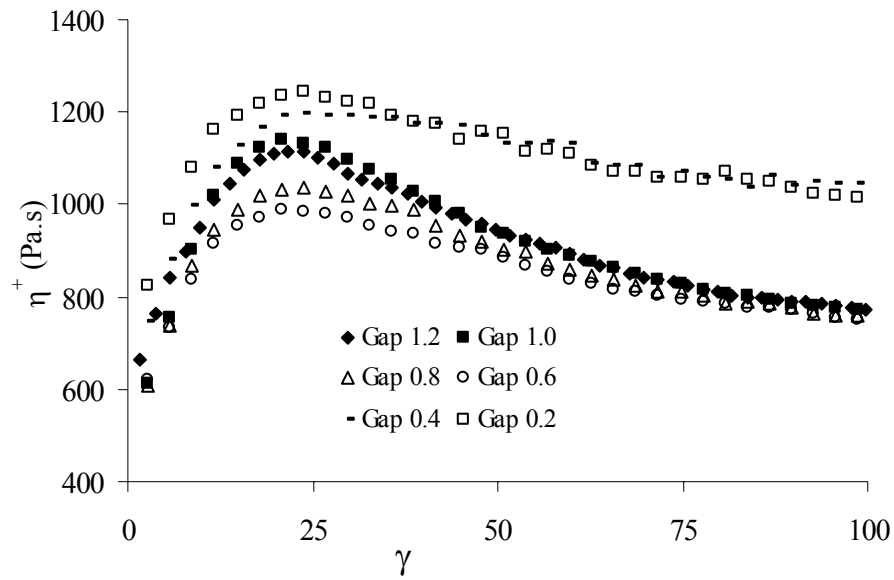
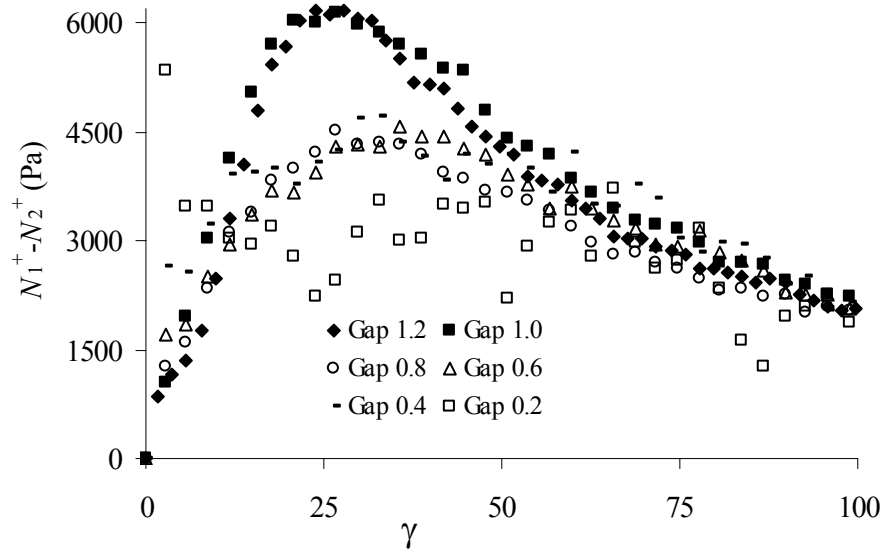


**Figure 3.3.** Representative drawing of the cross-sectional profile of a parallel plate and donut sample. The confocal laser microscopy images were taken for the parallel plate sample at a distance of 4.0, 7.0, and 10.0 mm from the outer edge denoted by PP-1, PP-2, PP-3 respectively. Similarly, the images were taken for the donut sample at a distance of 4.0, 6.25, and 8.5 mm from the outer edge denoted by PD-1, PD-2, PD-3.



(a)



(b)

**Figure 3.4.** The effect of the PP geometry gap height on the stress growth behavior of PBT-30 in startup of flow experiments at  $\dot{\gamma} = 1 \text{ s}^{-1}$ . (a)  $\eta^+$  vs. strain and (b)  $N_1^+ - N_2^+$  vs. strain. The various data points relate to measurements performed at different gap heights in millimeters.

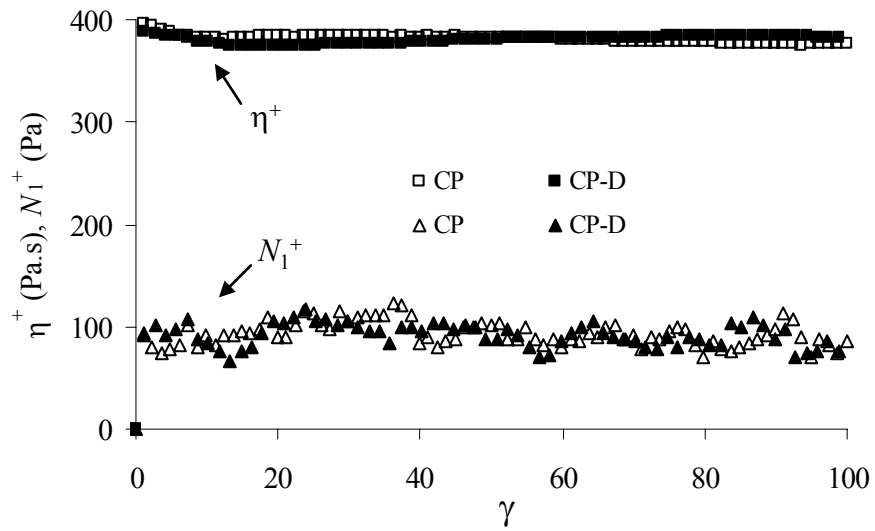
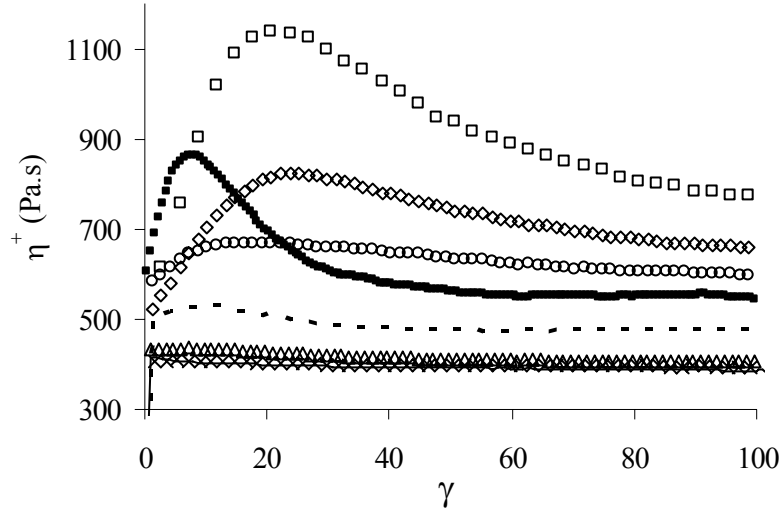
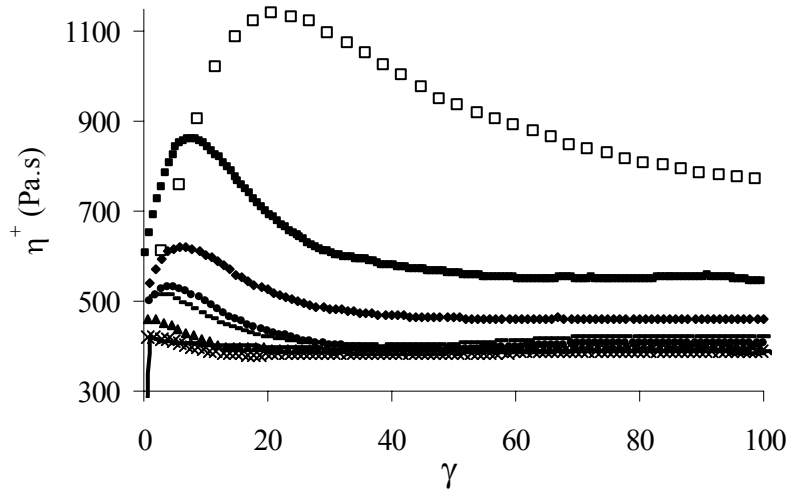


**Figure 3.5.** The stress growth behavior of the neat PBT measured using the 50 mm CP geometry with an unmodified sample and with the donut sample, CP and CP-D, respectively. Measurements were performed at  $\dot{\gamma} = 1 \text{ s}^{-1}$ .

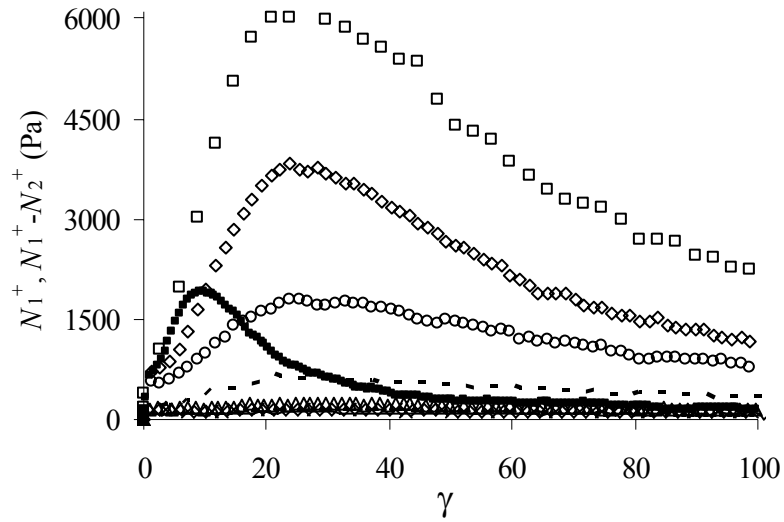


(a)

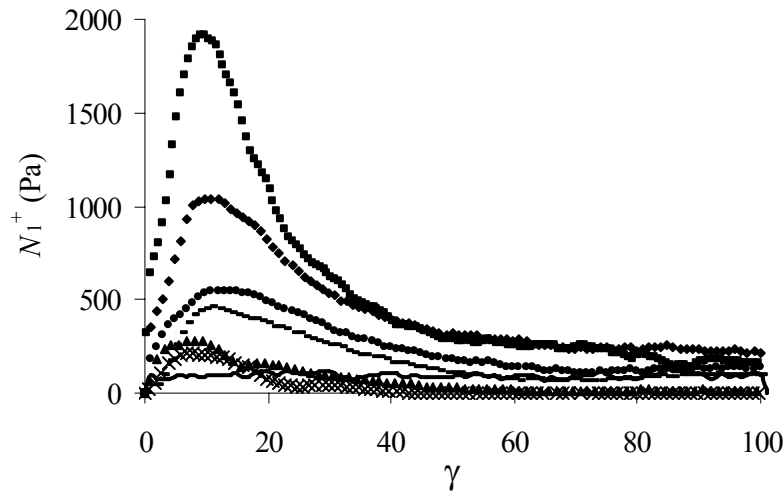


(b)

**Figure 3.6.**  $\eta^+$  vs. strain as a function of concentration at  $\dot{\gamma} = \dot{\gamma}_R = 1 \text{ s}^{-1}$ . (a) Measurements performed using the PP geometry. The symbols (x), ( $\Delta$ ), (-), (o), ( $\diamond$ ) and ( $\square$ ) represent fiber wt% 4.07, 8.42, 15, 20, 25 and 30. The symbol ( $\blacksquare$ ) represents  $\eta^+$  of PBT-30 measured using the CP-D for comparison. (b) Measurements performed using the CP-D. The symbols (x), ( $\blacktriangle$ ), (-), ( $\bullet$ ), ( $\blacklozenge$ ) and ( $\blacksquare$ ) represent fiber wt% 4.07, 8.42, 15, 20, 25 and 30. The symbol ( $\square$ ) represents the stress growth of PBT-30 measured using the PP geometry for comparison. The line shows the neat PBT for comparison in both graphs.

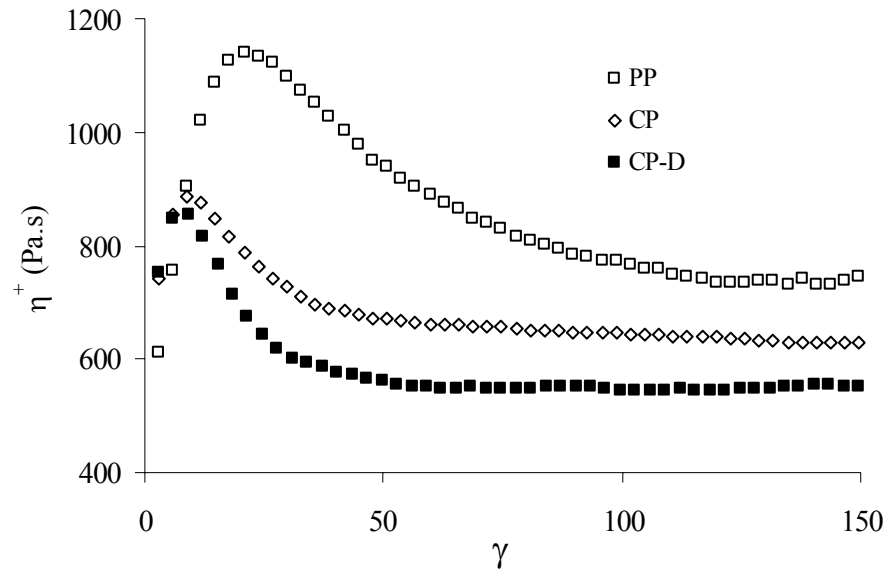


(a)

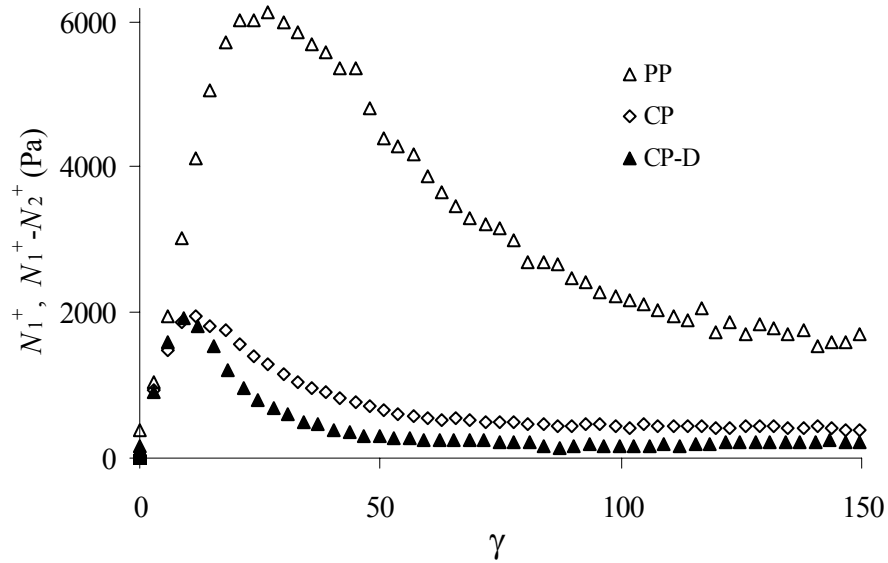


(b)

**Figure 3.7.**  $N_1^+$  and  $N_1^+ - N_2^+$  vs. strain at  $\dot{\gamma} = \dot{\gamma}_R = 1 \text{ s}^{-1}$ . (a) Measurements performed using the PP geometry. The symbols (x), ( $\Delta$ ), (-), (o), ( $\diamond$ ) and ( $\square$ ) represent fiber wt% 4.07, 8.42, 15, 20, 25 and 30. The symbol ( $\blacksquare$ ) represents the  $N_1^+$  of PBT-30 measured using the CP-D for comparison. (b) Measurements performed using the CP-D. The symbols (x), ( $\blacktriangle$ ), (-), ( $\bullet$ ), ( $\blacklozenge$ ) and ( $\blacksquare$ ) represent fiber wt% 4.07, 8.42, 15, 20, 25 and 30. The line shows the neat PBT for comparison in both graphs.

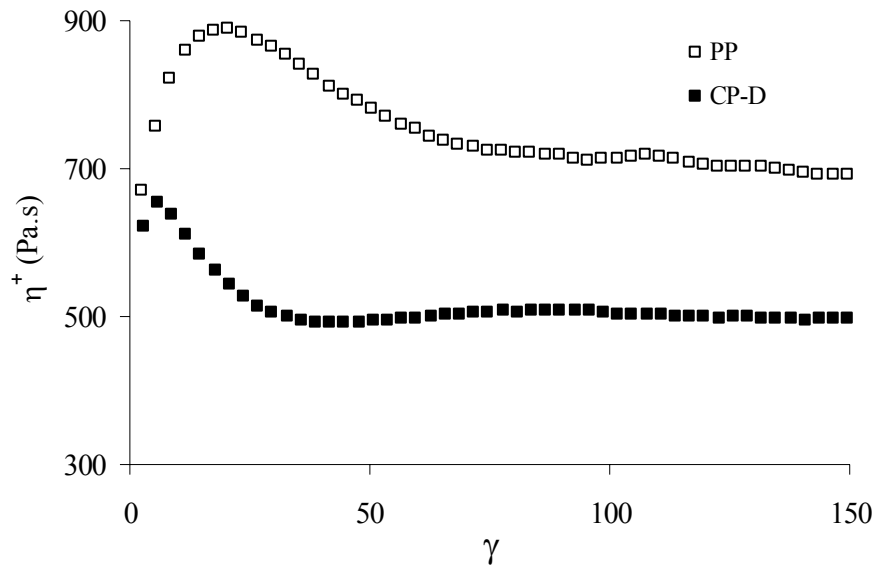


(a)

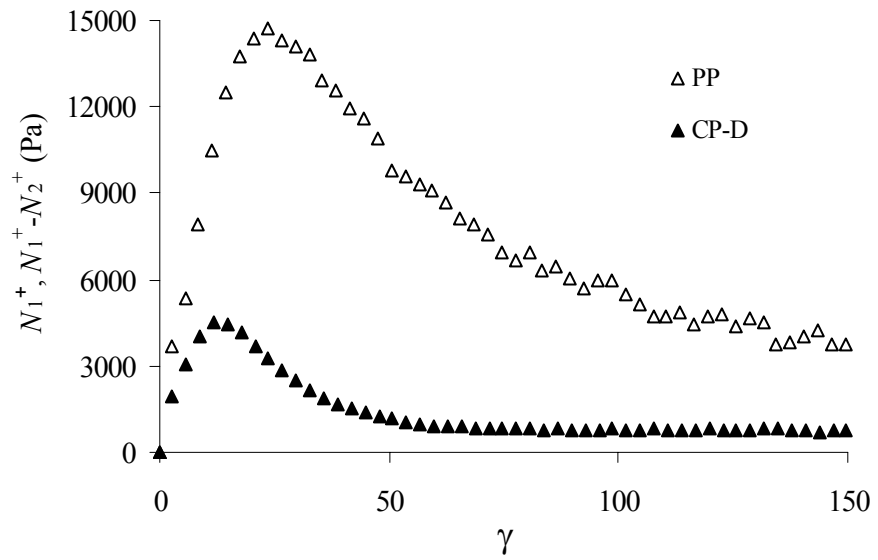


(b)

**Figure 3.8.** Stress growth in startup of flow measurements for PBT-30 at  $\dot{\gamma} = \dot{\gamma}_R = 1 \text{ s}^{-1}$ . (a)  $\eta^+$  and (b)  $N_1^+ - N_2^+$ ,  $N_1^+$  vs. strain. For both graphs PP, CP and CP-D refers to measurements performed using PP geometry, CP geometry with the unmodified sample and the CP geometry with the donut sample, respectively.



(a)



(b)

**Figure 3.9.** Stress growth in startup of flow measurements for PBT-30 at  $\dot{\gamma} = \dot{\gamma}_R = 4 \text{ s}^{-1}$ . (a)  $\eta^+$  and (b)  $N_1^+ - N_2^+$ ,  $N_1^+$  vs. strain. For both graphs PP and CP-D refers to measurements performed using PP geometry and the CP geometry with the donut sample respectively.

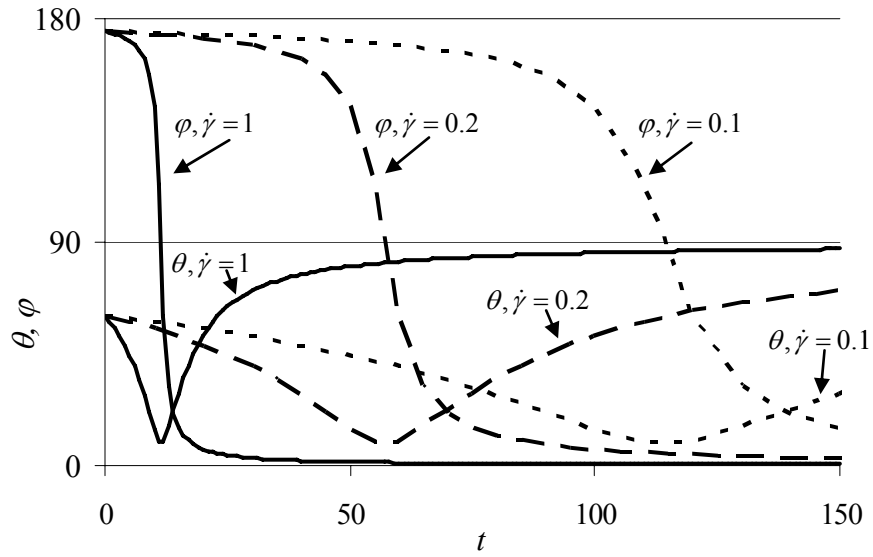


**Figure 3.10.** Spherical angles  $\theta$  and  $\varphi$  representing the reorientation of a fiber subject to simple shear flow vs. time as predicted by Eqs. (3.4) and (3.5) for various shear rates,  $\dot{\gamma} = 1, 0.2, 0.1 \text{ s}^{-1}$ . The initial conditions were  $\varphi_o = 175^\circ$ ,  $\theta_o = 60^\circ$ .

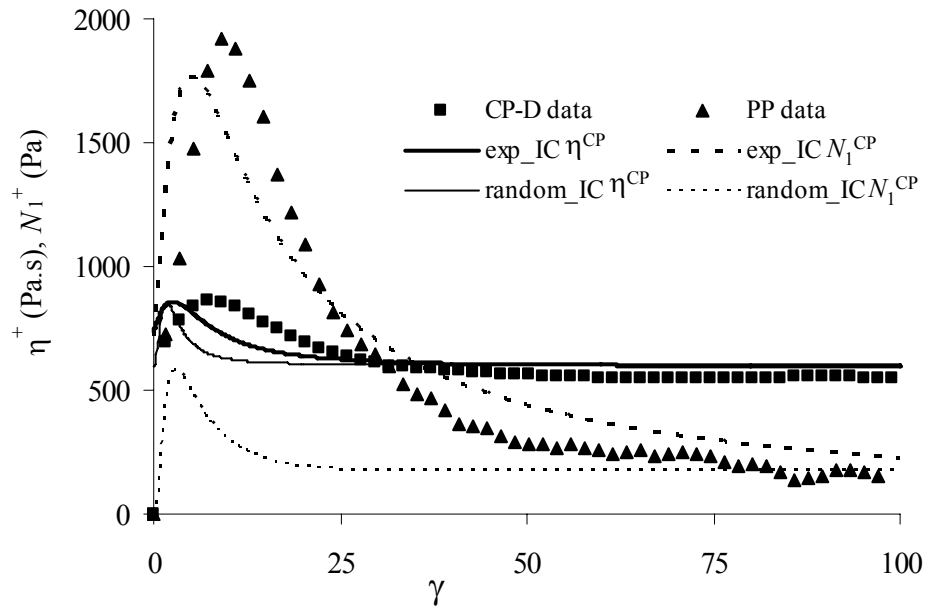
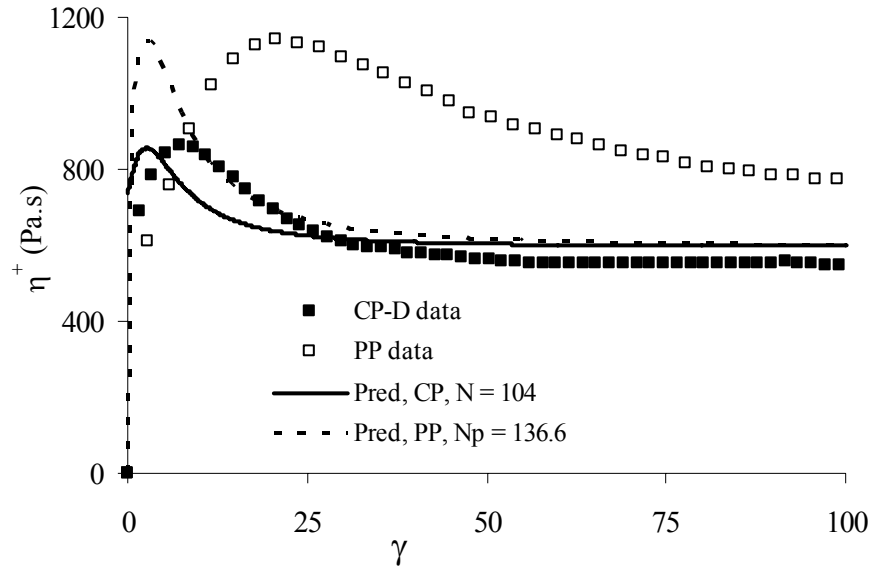
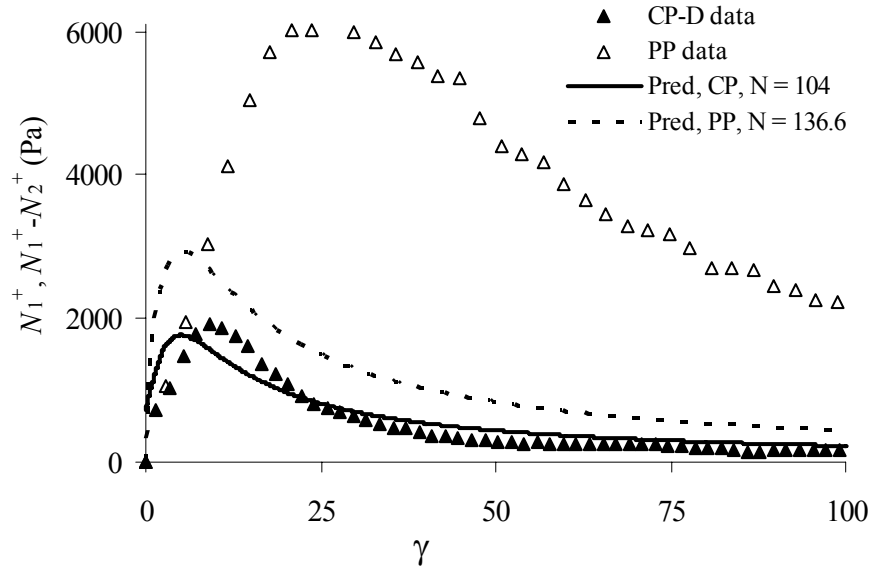


**Figure 3.11.** Effect of initial conditions on model fit to stress growth data for PBT-30 measured using the CP-D at  $\dot{\gamma} = 1 \text{ s}^{-1}$ . Predictions were made using Eqs. (3.6), (3.8) and (3.9). Model parameters, fit to  $\eta^+$ , using the experimentally determined initial conditions were  $N = 104$  and  $C_1 = 0.00001$ , and for the random  $N = 14$ ,  $C_1 = 0.0004$ .



(a)



(b)

**Figure 3.12.** Experimental data for PBT-30 and model predictions of the stress growth functions for a homogeneous and inhomogeneous velocity gradient denoted by CP and PP, respectively, at  $\dot{\gamma} = \dot{\gamma}_R = 1 \text{ s}^{-1}$ . (a) Experimental and predicted  $\eta^+$  vs. strain.  $\eta^+$  is calculated for CP and PP using Eqs. (3.8) and (3.10) respectively. (b) Experimental and predicted  $N_1^+$ ,  $N_1^+ - N_2^+$  and vs. strain.  $N_1^+$ ,  $N_1^+ - N_2^+$  were calculated for CP and PP using Eqs. (3.9) and (3.11) respectively. For all predictions  $\eta_s = 372 \text{ Pa.s}$ ,  $C_1 = 0.00001$  and  $N$  is shown in the legend.

## **4.0 Fiber Orientation Kinetics of a Concentrated Short Glass Fiber Suspension in Startup of Simple Shear Flow**

### **Preface**

The emphasis of this chapter is to assess the performance of fiber orientation theory by comparing model predictions to that determined experimentally in startup of simple shear flow. The orientation models that are discussed include Jeffery's equation, the Folgar-Tucker model, and the addition of a strain reduction factor or slip coefficient to both models. This chapter is organized as a manuscript for publication.

## **4.0 Fiber Orientation Kinetics of a Concentrated Short Glass Fiber Suspension in Startup of Simple Shear Flow**

Aaron P. R. Eberle <sup>a</sup>, Gregorio M. Vélez-García <sup>b</sup>, Donald G. Baird <sup>a\*</sup>, Peter Wapperom <sup>c</sup>

<sup>a</sup> Department of Chemical Engineering, <sup>b</sup> Department of Macromolecular Science and Engineering, <sup>c</sup> Department of Mathematics, Virginia Tech, Blacksburg, VA, 24061

\* Author to whom correspondence should be addressed; email: dbaird@vt.edu

### **4.1 Abstract**

The common approach for simulating the evolution of fiber orientation during flow in concentrated suspensions is to use Jeffery's equation or an empirically modified form of Jeffery's equation referred to as the Folgar-Tucker model. Direct measurements of fiber orientation were performed in startup of shear flow for a 30 wt % short glass fiber-filled polybutylene terephthalate (PBT-30); a matrix that behaves similar to a Newtonian fluid. The experimental results show that the fiber orientation evolves much slower than the models predict. Rheological measurements of the stress growth functions show that the stress overshoot phenomenon approaches a steady state at a similar strain as the fiber microstructure, at roughly 50 units. However, fiber orientation measurements suggest that a steady state is not reached as the fiber orientation continues to slowly evolve, even up to 200 strain units. Model predictions with the addition of a "slip" term show better

agreement compared to experimental results of the fiber orientation and rheological stress growth functions.

Key words: short glass fiber, fiber orientation, concentrated suspension, transient rheology

## 4.2 Introduction

Parts made from short glass fiber composite materials are typically produced in the melt state using injection or compression molding. During mold filling the macroscopic flow field generates a preferred orientation in the fiber microstructure which dramatically impacts the local mechanical, thermal and insulative properties of the part.<sup>1</sup> To optimize the mold design in relation to the desired part properties it is desirable to be able to simulate fiber orientation as a function of flow field and composite fluid rheological properties.

The first theoretical frame work describing evolution of orientation of axisymmetric particles that is easily extendable to fibers is the work of Jeffery.<sup>2</sup> Jeffery showed that the motion of a single ellipsoidal particle suspended in a Newtonian fluid in a Stokes flow field will rotate around the vorticity axis. Blunt ended particles such as rigid rods or fibers follow similar orbits that one can predict using Jeffery's equation by defining an equivalent aspect ratio. This theory can be applied to dilute suspensions ( $\phi \ll a_r^{-2}$ , where  $\phi$  is the volume fraction) where forces other than the macroscopic flow field do not effect the particle dynamics.<sup>3</sup>

In the semidilute régime ( $a_r^{-2} \ll \phi \ll a_r^{-1}$ ), inter-particle hydrodynamic interaction is the predominant phenomenon that can significantly affect or prevent periodic particle rotation.<sup>4</sup> Petrich et al.<sup>5</sup> studied the microstructure-stress relationship for various semidilute fiber suspensions in a Newtonian suspending medium using a concentric cylinder flow visualization apparatus and digital recorder. Their results showed the period of rotation to be in good agreement with theory for concentrations near the semidilute régime lower boundary. At concentrations in the semidilute régime near the upper boundary the period of rotation was hindered due to hydrodynamic interaction. In transient shear rheological measurements, shear stress oscillations have been observed and linked directly to the oscillating fiber orientation. However, the measured shear stress oscillations can dampen over time and is attributed to several interactions including boundary, particle-particle, hydrodynamic, or slight aspect ratio variations.<sup>6</sup> As the shear stress approaches a steady state, a pseudo-equilibrium fiber orientation state is reached, which, after a short period of time, may slowly change with time.<sup>7</sup>

In concentrated suspensions ( $\phi > a_r^{-1}$ ) the distance between fibers is on the order of the fiber diameter or less, and multi-particle simulations show that under dynamic conditions fiber-fiber contact can severely affect the fiber motion.<sup>8,9</sup> To our knowledge the dynamic behavior of fibers in a concentrated suspension has not been studied. Rheological measurements in startup of flow suggest that fibers reorient themselves from their initial orientation state to align themselves parallel to the fluid streamlines and do not rotate toward the vorticity axis.<sup>10</sup>

In the first attempts of simulating fiber orientation in injection molding, Jeffery's equation for infinitely long fibers was used.<sup>11</sup> Comparison between fiber orientation

measurements of injection molded parts and simulation results suggested Jeffery's equation over predicted the degree of alignment and the shear strain needed to align the fibers. As a result Folgar and Tucker<sup>12</sup> modified Jeffery's theory to include a phenomenological term that prevented full alignment of fiber orientation, termed the Folgar-Tucker model (F-T). The F-T model improved the predictions of the steady state fiber orientation but had little effect on the strain at which the steady state orientation occurred.<sup>13</sup> As a result, Huynh<sup>13</sup> introduced the strain reduction factor using the argument that the fibers move in clusters and experience less strain than the bulk.

Model predictions of the rheological stress growth functions using the F-T model compared to experimental results suggest that the rate of fiber reorientation is much slower than theory predicts.<sup>14, 15</sup> This was attributed to fiber-fiber contact reducing the rate of fiber orientation. As a result Sepehr et al.<sup>14</sup> introduced a "slip" parameter to the F-T model, effectively reducing the rate of fiber reorientation. In simple shear flow this is exactly the same as the strain reduction factor of Huynh.<sup>13</sup> With the addition of slip the model predictions of the transient rheological behavior were much closer to experimental results. We do note, however, that the stress growth experiments used in the comparison were performed in a rotational rheometer with parallel disk geometry in which there is a varying shear rate from the center of the plates to the rim. Recent results have suggested that the inhomogeneous shear field in the parallel disk geometry induces excessive fiber-fiber interaction in concentrated fiber suspensions. This can have a severe effect on the magnitude of the stress growth overshoot peak and width of the overshoot.<sup>16, 17</sup> As a note, the addition of the slip or strain reduction factor to the equations governing fiber motion results in a loss of objectivity of the equation.

The objective of this paper is to establish whether current theory for fiber orientation can predict the evolution of fiber orientation of a concentrated short glass fiber suspension of industrial significance in a well defined flow field. Donut shaped samples of a 30 wt% short glass fiber filled polybutylene terephthalate (PBT-30) were subject to simple shear flow in a cone-and-plate device in which the sample geometry was designed to eliminate the interaction of the fiber with the plate walls. At specific strains of interest in a shear stress growth verse strain plot, the fiber orientation was characterized using confocal laser microscopy. The experimental results were then compared to the Jeffery's equation, the F-T model and the models with the addition of the slip term.

### 4.3 Theory

**Orientation tensors:** The orientation of a single fiber can be described with a unit vector  $\mathbf{u}$  along the fiber axis as shown in Fig. 4.1. The average orientation of a large number of fibers of similar length can be described using a distribution function,  $\psi(\mathbf{u},t)$ . A widely used and compact way to represent the average orientation state is with the second- and fourth-order orientation tensors which are defined as the second- and fourth-moments of the orientation distribution function,<sup>18</sup>

$$\mathbf{A}(t) = \int \mathbf{u}\mathbf{u} \psi(\mathbf{u},t) d\mathbf{u} \quad (4.1)$$

$$\mathbf{A}_4(t) = \int \mathbf{u}\mathbf{u}\mathbf{u}\mathbf{u} \psi(\mathbf{u},t) d\mathbf{u} \quad (4.2)$$

The trace of  $\mathbf{A}$  is always equal to 1 and for a completely random orientation state  $\mathbf{A} = 1/3 \mathbf{I}$ , where  $\mathbf{I}$  is the unit tensor. In the limit that all the fibers are perfectly aligned in the  $x_1$  direction the only non-zero component of  $\mathbf{A}$  is  $A_{11} = 1$ .

**Evolution of fiber orientation:** The first theoretical work describing the evolution of high aspect ratio particle orientation that is easily extendable to rigid rods or fibers is that of Jeffery<sup>2</sup>. Jeffery extended Einstein's<sup>19</sup> approach to solving the equations of motion for the flow of a Newtonian fluid around a spherical particle to that of a neutrally buoyant ellipsoidal particle in the absence of Brownian motion. The time rate of change of an ideal suspension consisting of a large number of rods that are identical in size and shape and whose concentration is spatially uniform can be derived from Jeffery's analysis and written in terms of the second- and fourth-order orientation tensors as follows,<sup>18</sup>

$$\frac{D\mathbf{A}}{Dt} = (\mathbf{W} \cdot \mathbf{A} - \mathbf{A} \cdot \mathbf{W}) + \lambda (\mathbf{D} \cdot \mathbf{A} + \mathbf{A} \cdot \mathbf{D} - 2\mathbf{D} : \mathbf{A}_4) \quad (4.3)$$

where  $D/Dt$  is the material derivative,  $\lambda$  is a shape function  $\lambda = (a_r^2 - 1)/(a_r^2 + 1)$ ,  $\mathbf{W} = [(\nabla \mathbf{v})^t - \nabla \mathbf{v}]/2$  is the vorticity tensor,  $\mathbf{D} = [\nabla \mathbf{v} + (\nabla \mathbf{v})^t]/2$  is the rate of strain tensor and  $\nabla \mathbf{v} = \partial v_j / \partial x_i$ . For fibers it is common to assume the particle's aspect ratio approaches infinity, in which case  $\lambda \rightarrow 1$ . Eq. (4.3) contains the fourth-order orientation tensor in which a closure approximation is needed. However, for an initially random fiber orientation Lipscomb et al.,<sup>20</sup> following Dinh and Armstrong,<sup>21</sup> showed a solution exists that does not contain  $\mathbf{A}_4$ ,

$$\mathbf{A} = \int_{\mathbf{u}} \frac{\mathbf{u}\mathbf{u}}{\left\{4\pi \left[ (\mathbf{E}^{-1})^t \cdot \mathbf{E}^{-1} : \mathbf{u}\mathbf{u} \right]^{1.5} \right\}} d\mathbf{u} \quad (4.4)$$

where  $\mathbf{E}$  is the Cauchy strain tensor.<sup>22</sup>

For non-dilute suspensions Folgar and Tucker<sup>12</sup> modified Eq. (4.3) to include a phenomenological term to account for fiber interaction preventing complete fiber alignment termed the Folgar-Tucker (F-T) model:<sup>18</sup>

$$\frac{D\mathbf{A}}{Dt} = (\mathbf{W} \cdot \mathbf{A} - \mathbf{A} \cdot \mathbf{W}) + (\mathbf{D} \cdot \mathbf{A} + \mathbf{A} \cdot \mathbf{D} - 2\mathbf{D} : \mathbf{A}_4) + 2C_1 \dot{\gamma} (\mathbf{I} - 3\mathbf{A}) \quad (4.5)$$

where  $C_1$  is a phenomenological parameter and  $\dot{\gamma}$  is the scalar magnitude of  $\mathbf{D}$ . The last term on the right hand side of the equation is very similar to the isotropic diffusivity term in theories for Brownian rods.<sup>23</sup> The strain reduction factor introduced by Huynh<sup>13</sup> which is similar to the slip coefficient introduced by Sepehr et al.<sup>14</sup> can be incorporated into the F-T model as follows,

$$\frac{D\mathbf{A}}{Dt} = \alpha \left[ (\mathbf{W} \cdot \mathbf{A} - \mathbf{A} \cdot \mathbf{W}) + (\mathbf{D} \cdot \mathbf{A} + \mathbf{A} \cdot \mathbf{D} - 2\mathbf{D} : \mathbf{A}_4) + 2C_1 \dot{\gamma} (\mathbf{I} - 3\mathbf{A}) \right] \quad (4.6)$$

where the slip coefficient,  $\alpha$ , is some value between 0-1.

To solve equations Eqs. (4.3), (4.5) or (4.6) a closure approximation is needed to express the fourth-order tensor  $\mathbf{A}_4$  in terms of  $\mathbf{A}$ . Many closure approximations have been proposed including the quadratic,<sup>23</sup> hybrid,<sup>18</sup> eigenvalue-<sup>24</sup> and invariant-based

optimal fitted<sup>25</sup> to name a few. A good review of their accuracy can be found in.<sup>26, 27</sup> For this work we use the invariant-based orthotropic fitted (IBOF) closure approximation.<sup>25</sup> The IBOF begins with the most general form of the fourth-order tensor  $\mathbf{A}_4$  as follows,

$$A_{ijkl} = \beta_1 S(I_{ij} I_{kl}) + \beta_2 S(I_{ij} A_{kl}) + \beta_3 S(A_{ij} A_{kl}) + \beta_4 S(I_{ij} A_{km} A_{ml}) + \beta_5 S(A_{ij} A_{km} A_{ml}) + \beta_6 S(A_{im} A_{mj} A_{kn} A_{nl}) \quad (4.7)$$

where the operator  $S$  indicates the symmetric part of its argument such as,

$$S(T_{ijkl}) = \frac{1}{24} (T_{ijkl} + T_{jikl} + T_{ijlk} + T_{jilk} + T_{klij} + T_{lkij} + T_{klji} + T_{lkji} + T_{ikjl} + T_{kijl} + T_{iklj} + T_{kijl} + T_{jlik} + T_{ljik} + T_{jlki} + T_{ljki} + T_{iljk} + T_{lijk} + T_{ilkj} + T_{likj} + T_{jkil} + T_{kjil} + T_{jkli} + T_{kjli}) \quad (4.8)$$

The IBOF assumes that the coefficients  $\beta_1 - \beta_6$  are polynomial expansions of the second and third invariants of  $\mathbf{A}$ . We use the fifth-order polynomial for which the polynomial coefficients can be found elsewhere.<sup>25</sup>

**Stress:** Lipscomb et al.<sup>20</sup> proposed a stress equation for a dilute suspension of high aspect ratio particles following the work of Hand<sup>23</sup> and Giesekus<sup>21</sup> as,

$$\boldsymbol{\sigma} = -p\mathbf{I} + 2\eta_s \mathbf{D} + 2c_1 \varphi \eta_s \mathbf{D} + 2\varphi \eta_s N \mathbf{D} : \mathbf{A}_4 \quad (4.9)$$

where  $\boldsymbol{\sigma}$  is the total stress,  $p$  is pressure,  $\eta_s$  the suspending medium viscosity,  $c_1$  a constant, and  $N$  a dimensionless parameter that represents the coupling between

hydrodynamic stress contribution and the fiber orientation. Lipscomb et al. give  $c_I$  to be equal to 2 for dilute suspensions, but we choose to use it as a fit parameter. Also, Lipscomb et al. give  $N$  to be a function of the particle aspect ratio. Semidilute suspension theories such as the Dinh and Armstrong,<sup>21</sup> Shaqfeh and Fredrickson,<sup>28</sup> or Phan-Thien and Graham<sup>29</sup> can also be written in the form of Eq. (4.9) noting that some assume the third term is negligible or  $c_I = 0$ . These theories focus on an expression for  $N$  considering inter-particle hydrodynamics. For predicting the rheological behavior of concentrated suspensions  $N$  is frequently is frequently determined by fitting predictions to experimental results and is the approach we use in this work. Equation (4.9) simplifies to the shear stress growth coefficient,  $\eta^+$ , and first normal stress difference growth function,  $N_1^+$ , in simple shear flow kinematics ( $v_1 = \dot{\gamma}y$  and  $v_2 = v_3 = 0$ ),

$$\eta^+ = \sigma_{12} / \dot{\gamma} = \eta_s + c_1 \eta_s \phi + 2\eta_s \phi N A_{1212} \quad (4.10)$$

and,

$$N_1^+ = 2\phi \eta_s \dot{\gamma} N (A_{1211} - A_{1222}) \quad (4.11)$$

## 4.4 Experimental

### 4.4.1 Materials

For this work a commercially available 30wt% (volume fraction,  $\phi = 0.1766$ ) short glass fiber filled polybutylene terephthalate (PBT-30) provided by GE Plastics under the

trade name Valox 420 was used. Linear viscoelastic measurements confirmed that the matrix was Newtonian-like, i.e. exhibits little complex viscosity dependence on frequency and a small storage modulus.<sup>16</sup> To examine the effect of fiber concentration on the rheological behavior, PBT-30 was diluted to concentrations of 4.07, 8.42, 15, 20 and 25 wt%. The concentrations of 4.07 and 8.42 wt% relate to roughly 40% below and 25% above the semidilute upper boundary respectively. Compounding was accomplished by passing dry blended amounts of PBT-30 and the neat matrix through the extruder section of an Arburg Alrounder 221-55-250 injection molder at an rpm of 200. The extrudate was collected before entering the runner of the mold and pelletized. The pellets were then compression molded for rheological testing to a cone-and-plate disk at 260 °C. Precautions were taken to minimize the degree of thermo-oxidative degradation of the PBT matrix by drying the materials at 120 °C for a minimum of 12 hours in a vacuum oven at a pressure smaller than 0.4 in.Hg before sample extrusion, molding or testing.<sup>30</sup>

To characterize the glass fiber within the suspension, pyrolysis was performed on the PBT-30 pellets at 500 °C after extrusion to separate the fibers from the matrix. The fiber length was determined by randomly measuring the length of 1,000 fibers. The number average and weight average fiber length of PBT-30 was found to be  $L_n = 0.3640$  and  $L_w = 0.4388$  mm, respectively. The same fiber length measurement was performed on all the diluted concentrations and was found to be within  $0.3640 \leq L_n \leq 0.3740$  and  $0.4388 \leq L_w \leq 0.4578$  mm. The fiber diameter,  $D$ , was determined directly from images taken of fiber cross sections using a confocal laser microscope, discussed later, and the average diameter of 1,000 fibers was found to be  $D = 12.9$   $\mu\text{m}$ . This relates to a number average aspect ratio for PBT-30 of  $a_r \cong 28.2$ .

#### 4.4.2 Rheological Measurements

All rheological measurements were performed on a Rheometrics Mechanical Spectrometer (RMS-800) at 260 °C. To minimize the degree of thermo-oxidative degradation, all experiments were performed in a nitrogen environment with a freshly loaded pre-formed sample. Rheological measurements on the PBT matrix were performed with a 25 mm cone-and-plate fixture with 0.1 radian cone angle.

The common approach to characterizing the rheological behavior of short glass fiber filled polymer melts is to use a rotational rheometer with parallel disk geometry set to a gap where measurements are independent of gap height. However, recent results suggest that the inhomogeneous velocity gradient imposed by the parallel disk geometry can lead to exaggerated measurements of the rheological material functions. As a result, it was of primary importance to perform the experiments on the glass fiber-filled suspensions in a rheometer that imposes a homogeneous shear field such as the cone-and-plate geometry.<sup>22</sup> For our measurements a 50 mm diameter cone-and-plate fixture was fabricated and used. The cone had a 0.1 radian cone angle and was truncated to allow for a gap of 50  $\mu\text{m}$  at the center. To minimize the degree of fiber-boundary interaction Blankeney<sup>31</sup> and Attanasio<sup>32</sup> suggested that the rheometer gap be at least three times the length of the longest dimension of the suspension particle. Experimental results using parallel plate geometry with various rheometer gaps confirmed that for the PBT-30 there is a negligible effect on the stress growth and steady state rheological behavior when the gap is roughly three times the number average fiber length.<sup>16</sup> The gap within the 50 mm

cone and plate fixture varies linearly from 2.51 mm at the outer edge to 0.05 mm at the center. To remove the excessive fiber-boundary interaction near the center, a 25.4 mm diameter hole was drilled through the center of the pre-formed disks creating a donut shaped sample which we refer to as “donut” samples. A schematic drawing of the donut sample can be seen in Fig. 4.2. After each experiment the void space at the center was measured to account for sample loading as the gap is squeezed to proper dimensions. The hole diameter varied slightly,  $23.8 \pm 0.5\text{mm}$  and was accounted for in calculating the stresses for each run. A complete analysis of the effect of rheometer geometry and description of the donut sample can be found elsewhere.<sup>16</sup>

For measurements performed using the cone and plate fixtures,  $\eta^+$  and  $N_1^+$  were calculated as functions of torque,  $M(t)$ , and normal force,  $F(t)$ , from the following equations,<sup>33</sup>

$$\eta^+(t) = \sigma^+ / \dot{\gamma} = \frac{3M(t)}{2\pi\dot{\gamma}} (R_o^3 - R_i^3)^{-1} \quad (4.12)$$

and,

$$N_1^+(t) = \frac{2F_z(t)}{\pi} (R_o^2 - R_i^2)^{-1} \quad (4.13)$$

where  $R_o$ ,  $R_i$  are the outer and inner radius, respectively. The experimental reproducibility was found to be  $\eta^+ \pm 5\%$  and  $N_1 \pm 7\%$ .

#### 4.4.3 Measurement of Fiber Orientation

The fiber microstructure was characterized using confocal laser microscopy in a similar approach to that proposed by Lee et al.<sup>34</sup> Donut samples composed of PBT-30 were deformed using the RMS-800 at  $\dot{\gamma} = 1 \text{ s}^{-1}$  for a specified amount time relating to strain,  $\gamma = \dot{\gamma}t$ . Immediately after deformation, and taking precaution not to disturb the sample melt, the temperature was lowered below the melt temperature “locking-in” the flow generated fiber microstructure.

Each sample was imaged at two planes, perpendicular to the neutral direction ( $x_1 - x_2$  plane) and perpendicular to the flow direction ( $x_2 - x_3$  plane). We define  $x_1$  as the flow direction,  $x_2$  as the direction of velocity gradient and  $x_3$  as the neutral direction. The samples were prepared by sanding embedded sections of the donut sample in epoxy to a specific plane depth, and then polishing the surface to a final abrasive particle size of  $0.3 \mu\text{m}$  aluminum oxide ( $\text{Al}_2\text{O}_3$ ) following standardized techniques.<sup>35</sup> A schematic drawing of the polished planes and locations where the images were taken can be found in Fig. 4.3. A series of images were taken at three locations in the  $x_2 - x_3$  plane, at distance of 4.0, 6.25, and 8.5 mm from the outer edge denoted by PD-1, PD-2 and PD-3 respectively and depicted in Fig. 4.3. For the  $x_1 - x_2$  plane images were only taken at one location denoted by PD-4 at a depth of 4.0 mm from the outer edge. PD-1 and PD-4 can be considered mutually perpendicular planes of different sections of the donut sample.

The images were taken using a Zeiss LSM510 confocal laser scanning microscope fitted with a 40x water immersion objective lens and a laser excitation wavelength of 543 nm. The final image was  $230 \times 230 \mu\text{m}$  with a resolution of  $1024 \times 1024$  pixels. For

each sample, sequential images were taken from the bottom to the top in the direction of the velocity gradient and at two planes of depth. In the image the cross section of each fiber appeared as circles or ellipse-like shapes. To process the image, the circumference of each fiber intersection was traced by hand in power point to improve the contrast between the fibers and the matrix and converted to a binary image. A computer program was written in combination with image analysis software in Matlab that measured the position of center of mass, the major and minor axis and local angle between a fixed coordinate frame and the major axis of the ellipse. The components of  $\mathbf{u}$  for each fiber were determined from the elliptical “footprint” at two cross sectional planes.

With knowledge of  $\mathbf{u}$  for each fiber the tensor  $\mathbf{A}$  can be constructed as follows:

$$A_{ij} = \frac{\sum (u_i u_j)_n F_n}{\sum F_n}, \quad F_n = \frac{M_n}{m_n} \quad (4.14)$$

where  $F_n$  is a weighting factor for the  $n$ th fiber.<sup>36</sup> The weighting function is based on the probability of a 2D plane intersecting the  $n^{\text{th}}$  fiber. Meaning, a fiber aligned perpendicular to the plane is more likely to be severed than one aligned parallel. Using the weighting function, the larger the aspect ratio of the ellipse, the more that fiber is weighted. In the results and discussion section the orientation tensor  $\mathbf{A}$  will be used to describe the average orientation state of the system. The experimental reproducibility of the  $A_{ij}$  components between similar samples was found to be  $\pm 8\%$ .

## 4.5.0 Results and Discussion

### 4.5.1 Experimental

**Transient rheology:** The stress growth behavior as a function of concentration (wt %) can be seen in Figs. 4.4 (a) and (b) for the shear stress growth coefficient,  $\eta^+$ , and the first normal stress difference growth function,  $N_1^+$ , respectively. In Fig. 4.4 (a)  $\eta^+$  for the 30 wt% exhibits a typical transient stress growth behavior of a concentrated short glass fiber-filled fluid of an un-deformed sample. Initially there is a large transient overshoot that reaches a maximum in approximately 7 strain units which decays towards a steady state value. It is difficult to say exactly when a steady state is reached but the majority of the overshoot occurs between 25 and 30 strain units, after which, the stresses approach a steady state in roughly 50. The magnitude of the overshoot decreases with decreasing fiber concentration. For the 4.07 and 8.42 wt% no maximum occurs and the  $\eta^+$  decays from the beginning of flow to a steady state value. The development of the large overshoot behavior with a maximum appears to occur around 15 to 20 wt%.

$N_1^+$  is plotted vs. strain in Fig. 4.4 (b) for the various concentrations. Similar to  $\eta^+$ ,  $N_1^+$  for the 30 wt% exhibits a large initial overshoot that is commonly reported for concentrated suspensions that reaches a steady state around 50 strain units. The overshoot peak is more than 8 times the steady state value. All the concentrations tested exhibited an overshoot which increased with fiber concentration. However, there seemed to be a broadening of the overshoot and a significant increase in the magnitude that occurred at the 15 wt%. The dramatic increase in the magnitude and broadening of the

overshoot is believed to be a result of significant fiber contact at the higher concentrations. For this work we were interested in the dynamic behavior of a concentrated suspension of industrial significance. All but the lowest concentration is in the concentrated régime, but stress growth behavior of the 30 wt% exhibited the most dramatic behavior and so was chosen for the fiber orientation experiments.

During sample preparation for the fiber orientation measurements it was assumed that the fibers maintained their orientation during stress relaxation. To reinforce this assumption, interrupted stress growth experiments were performed after the overshoot region and at the peak of the  $N_1^+$  overshoot depicted in Figs. 4.5 (a) and (b), respectively. The results of two interrupted tests on two different samples can be seen in Fig. 4.5 (a). Initially they were both deformed for 100 s at a  $\dot{\gamma} = 1 \text{ s}^{-1}$ , after which the flow was stopped. For the first sample, the flow was turned back on after 50 s, and for the second the flow was turned back on after 200 seconds. In both cases the stress immediately grew to their previous value independent of the time between flows. This test was performed up to a maximum wait time of 1,000 s and shows the overshoot region is not recoverable. A similar test was performed except the flow was removed at the peak of the  $N_1^+$  overshoot and can be seen in Fig. 4.5 (b). When the flow is reapplied the stresses immediately rise to their previous value. The behavior exhibited by PBT-30 in both Figs. 4.5 (a) and (b) suggest that the fibers do maintain their orientation during stress relaxation. If this assumption is correct, then even at very long times the fiber orientation should remain constant under static conditions if unaffected by external forces such as Brownian motion or gravity.

The relative effect of Brownian motion on the orientation of the fibers within the suspension can be determined by comparing the experimental shear rate,  $\dot{\gamma}$ , to the rotational diffusion constant,  $D_r$ , also known as the Péclet number,  $Pé = \dot{\gamma} / D_r$ . For a fiber  $D_r = 3k_bT[\ln(a_r)-0.8]/\pi\eta_sL^3$ , where  $k_b$  is Boltzmann's constant,  $T$  is the temperature in Kelvin,  $\eta_s$  is the viscosity of the suspending medium and  $L$  is the fiber length.<sup>23</sup> This relates to,  $Pé \approx 10^{13}$  and therefore, can be considered non-Brownian.<sup>37</sup> To estimate the relative effect of gravity on fiber orientation Chaouche and Koch<sup>38</sup> proposed an expression to estimate the relative time scale for sedimentation,  $t_s$ , the time required for a fiber parallel to the vertical direction to sediment over its length, as  $t_s = 8\eta_sL/\Delta g\rho d^2[\ln(2a_r)-0.72]$ . For an average fiber in PBT-30  $t_s \approx 45$  hrs and represents the minimum estimated time for a fiber to settle as fiber contact would act to increase  $t_s$ .

**Fiber orientation measurements:** In total the fiber orientation was measured for 11 samples which correspond to various points of interest on an interrupted stress growth vs. strain plot: strains 0, 4, 7, 9, 12, 25, 50, 100 and 200. Strains 4, 25, 100 and 200 were imaged at locations PD-1 and PD-4, all other strains were imaged at locations PD-1 thru PD-4 as depicted in Fig. 4.3. Strain 0 relates to the initial fiber orientation. Strains 7 and 9 relate to the peaks of the  $\eta^+$  and  $N_1^+$  overshoot, respectively. Strains 25 and 50 relate to the onset of steady state for  $\eta^+$  and  $N_1^+$ , respectively. Strains 4 and 12 represent intermediate overshoot growth and relaxation points respectively; strains 100 and 200 represent the plateau region in which stresses do not exhibit large changes.

The orientation of each fiber is described in spherical coordinates using a unit vector,  $\mathbf{u}$ , along the backbone a fiber depicted in Fig. 4.1. The zenith and azimuthal angles  $\theta$ ,  $\varphi$  defining the components of  $\mathbf{u}$  for a each fiber are calculated based on the ratio of the

minor and major axis using Eq. (4.15), and is dependant on which plane is being processed; the other angle was measured directly from the image.<sup>34</sup> In Eq. (4.15) the subscript 1-2 refers to the  $x_1 - x_2$  plane.

$$\cos\theta|_{1-2} = \frac{m}{M} \quad (4.15)$$

Figure 4.6 (a) depicts the elliptical foot print in the  $x_1 - x_2$  plane and the angle  $\varphi$  measured directly from the image. The limitation of calculating the angle based on Eq. (4.15) is that the calculated angle is always between 0 and  $\pi$  causing an inherent ambiguity. For example, in the  $x_1 - x_2$  plane it is impossible to distinguish between a fiber that is oriented  $(\theta_1, \varphi_1)$  and  $(\pi - \theta_1, \varphi_1)$  because their cross sections are identical. Figure 4.6 (b) depicts two possible unit vectors  $\mathbf{u}$  for the same elliptical footprint. As a note, for these geometric equations to be valid it is assumed that the fibers are perfectly rigid circular cylinders. Forgacs and Mason<sup>39</sup> developed an equation to estimate the critical shear stress at which the shear-induced axial compression can cause a rotating fiber to buckle,  $\tau_{\text{critical}} = E_f[\ln(2a_r) - 1.75]/2a_r^4$ , where  $E_f$  is the flexural modulus. Assuming for the glass fibers within the PBT-30 suspension  $E_f \approx 73 \text{ GPa}$ ,<sup>40</sup> then  $\tau_{\text{critical}} \approx 1.3 \times 10^5 \text{ Pa}$  and can be considered rigid at  $\dot{\gamma} = 1 \text{ s}^{-1}$ .

To increase the accuracy of the 3D description of fiber orientation and reduce the inherent ambiguity in the method previously described, imaging was performed using a confocal laser microscope. This allowed for images to be taken at multiple depths parallel to the plane of interest and fully describe the 3D fiber orientation without ambiguity. Figure 4.6 (b) illustrates a fiber cross section with two possible unit vectors

whose orientation is the mirror image of each other. When only one plane is analyzed it is impossible to determine the correct vector  $\mathbf{u}$ . However, when images from two depths are compared, the center of mass displacement confirms the appropriate  $\mathbf{u}$  vector. This is slightly different from the work of Lee et al.<sup>34</sup> who calculated the angle based on the measured displacement.

After processing the images relating to the experimental data, it was found that change in center of mass of the two elliptical footprints was only detectable when the aspect ratio of the ellipse was roughly greater than three or at an angle of greater than roughly  $50^\circ$  due to the limited depth of penetration of the laser. For the PBT-30 the maximum penetration was found to be  $8 \mu\text{m}$ . For this reason we term our analysis “pseudo-3D” in that there is still a certain amount of ambiguity with the calculated angle for fibers which were mostly aligned in the direction perpendicular to the plane of interest.

#### 4.5.2 Simulations

**Numerical method:** Equation (4.4) was solved using the Gaussian quadrature numerical integration scheme. In all models that contained  $\mathbf{A}_4$ , the IBOF closure approximation was used to express  $\mathbf{A}_4$  in terms of  $\mathbf{A}$ . Equations (4.3), (4.5) and (4.6) were solved numerically using Gear’s implicit predictor-corrector method at a time step of 0.01 s. Numerical simulations at a refined time step of 0.001 s confirmed the results to be within  $A_{ij} \pm 10^{-4}$ . The initial conditions and model parameters are discussed later.

**IBOF closure:** A major objective of this work is to compare the ability of current theory for predicting the time rate of change of fiber orientation to that experimentally determined for a highly concentrated fiber suspension. Jeffery's equation, Eq. (4.3), contains the fourth-order orientation tensor,  $\mathbf{A}_4$ , in which a closure approximation is needed to generate a solution. The IBOF closure approximation was used in this work for its high degree of accuracy and computational efficiency in predicting the F-T model, Eq. (4.5), for a range of values of  $C_I$  of 0.01 to 0.0001.<sup>25</sup> However, no predictions were found in literature that compare the predictions of Jeffery's equation without the Folgar-Tucker modification using the IBOF closure to a solution in which no closure is used. As a result, Jeffery's equation with the IBOF closure is compared to the numerical solution to Eq. (4.4) which does not contain a closure and can be seen in Figs. 4.7 (a) and (b). Here the predictions of the  $A_{ii}$  and  $A_{12}$  components vs. strain, respectively, are compared for an initially random fiber orientation at a  $\dot{\gamma} = 1 \text{ s}^{-1}$ . From Fig. 4.7 (a) it is clear that the use of the IBOF results in highly accurate predictions of the  $A_{ii}$  components when the predictions begin from an initial random state. However, in Fig. 4.7 (b) it is shown that the prediction for  $A_{12}$  using the IBOF exhibits a slight enhancement, on the order of  $A_{12} + 10^{-2}$ , at large strains that does not appear to approach zero asymptotically as does Jeffery's with no closure. This is an unfortunate deficiency in the closure but because the closure has a high degree of accuracy in predicting the  $A_{ii}$  components we chose to use the IBOF closure for all predictions of Eq. (4.3).

**Effect of  $C_I$  and  $\alpha$ :** The effect of the model parameters,  $C_I$  and  $\alpha$ , on the predictions of the  $A_{11}$  component vs. strain by means of Eqs. (4.5) and (4.6) can be seen in Figs. 4.8 (a) and (b) compared to the predictions of Jeffery's equation by means of Eq. (4.3) for

random initial conditions. In Fig. 4.8 (a) the effect of increasing  $C_1$  and decreasing  $\alpha$  on the predictions of the F-T model and Jeffery's + slip is shown. For increasing values of  $C_1$  the steady state value of  $A_{11}$  decreases, but predictions have a negligible effect on the initial growth rate of  $A_{11}$ . In contrast decreasing values of  $\alpha$  decrease the growth rate of the  $A_{11}$  component but have no effect on the steady state asymptote. In Fig. 4.8 (b) the effect of increasing  $C_1$  and decreasing  $\alpha$  on the predictions of F-T + slip is shown. The parameters do not seem to have an effect on each other. Meaning the predictions for F-T + slip with a given  $C_1$  reaches the same steady state value as the F-T model with that same  $C_1$ . Similarly, the value of  $C_1$  seems to have little effect on the change in growth rate determined by  $\alpha$ .

**Model predictions:** The stress growth behavior of a suspension containing high aspect ratio particles is highly dependent on the orientation distribution of those particles.<sup>4</sup> The fiber orientation within a rheometer sample is generated by the sample deformation history. The experimentally measured average initial orientation of the PBT-30 donut sample is shown in Eq. (4.16), represented using the orientation tensor  $\mathbf{A}$ ,

$$\mathbf{A}|_{\gamma=0} = \begin{pmatrix} .5167 & - & - \\ .0753 & .0349 & - \\ .0584 & .0347 & .4484 \end{pmatrix} \quad (4.16)$$

The experimental data represented in Eq. (4.16) shows that the majority of the fibers are initially oriented in the  $x_1$  and  $x_3$  directions with very few aligned in the  $x_2$  direction. This is attributed to the deformation history given to the sample during compression molding of the sample disk and while it is loaded into the rheometer.

Predictions using Eq. (4.3) with the experimentally determined initial conditions exhibited nonphysical oscillations in the components of  $\mathbf{A}$ . We believe this is a direct result of the IBOF closure approximation. To stabilize the model predictions the F-T model was used with a small  $C_1 = 0.00015$ . The nonphysical oscillations as predicted by Eq. (4.3) and the stabilized predictions of Eq. (4.5) can be seen in Fig. 4.9 for the  $A_{11}$  and  $A_{33}$  components. The small  $C_1$  value had a significant effect on stabilizing the predictions, preventing the nonphysical behavior but otherwise had a negligible effect on the steady state asymptote. As a result the stabilized form of the Jeffery's model predictions will be referred to as Jeff-S and is essentially the F-T model with a small  $C_1$  value.

In Figs. 4.10 (a) and (b) the experimentally determined  $A_{ii}$  components vs. strain are compared to the Jeff-S and the F-T model. For the F-T model  $C_1 = 0.006$  was determined by fitting the F-T model to the  $A_{ii}$  components at a strain of 200, and is used for all subsequent predictions of the F-T model. The experimentally determined  $A_{11}$  component, shown in Fig. 4.10 (a), increases with increasing strain. This relates to the fibers orienting themselves in the flow direction during the startup of shear flow. The rate of fiber reorientation is fastest between strains 0 and 50; after a strain of 50 the rate dramatically decreases. Interestingly this relates to the onset of steady state exhibited by the  $N_1^+$  overshoot. The predictions of Jeff-S drastically over predict the  $A_{11}$  component growth rate. The F-T model also over predicts the  $A_{11}$  component growth rate and predicts that a steady state is reached in  $\sim 40$  strain units. However, the fiber orientation appears to be continually evolving, even up to the largest strain measured, 200.

In Fig. 4.10 (b) the experimentally determined  $A_{22}$  and  $A_{33}$  components vs. strain are shown. The experimental values of the  $A_{33}$  component decays with increasing strain at a similar rate to the  $A_{11}$  component growth. This shows that the fibers, whose initial orientation is mostly in the  $x_1 - x_3$  plane, reorient out of the  $x_3$  direction toward the  $x_1$  direction. The  $A_{22}$  component shows an initial increase that decays slightly to what appears to be a statistical steady state at 25 strain units. Interestingly this coincides with the onset of steady state in  $\eta^+$ . Similar to the  $A_{11}$  component, the predictions of Jeff-S over predicts the  $A_{33}$  component rate of decay. The F-T model also over predicts the  $A_{33}$  component rate decay and predicts that a steady state is reached in  $\sim 50$  strain units. However, the experimentally determined  $A_{33}$  component appears to be continuously evolving. The predictions of the  $A_{ii}$  components using the F-T model shown in Figs. 4.10 (a) and (b) are relatively accurate at the largest strain which is expected as the  $C_1$  was parameter was adjust to fit the F-T model at that strain. However, the continuously evolving fiber orientation in the  $A_{22}$  and  $A_{33}$  components suggests that a correct value would be smaller than  $C_1 = 0.006$ .

To look at the rate of growth and decay of the  $A_{11}$  and  $A_{33}$  components a line (of the form  $A_{ii} = m\gamma + b$  where  $m$  is the slope of the line and  $b$  is the  $A_{ii}$ -intercept) was fit to the last three data points relating to strains 50, 100 and 200. The best fit line and coefficient of determination,  $R^2$ , was found to be  $A_{11} = 0.0004\gamma + 0.73$  and  $A_{33} = -0.0004\gamma + 0.2173$  with  $R^2 = 0.999$  for both fits. The line fit to the experimental data can be seen in Fig. 4.11. The absolute value of the slopes were equal and if the  $A_{11}$  component continued to grow at the same rate it would lead to full alignment ( $A_{11} = 1$ ) at a strain of 1825.

The predictions of Jeff-S + slip and F-T + slip vs. strain compared to the experimentally determined  $A_{ii}$  components are shown in Figs. 4.12 (a) and (b). The slip parameter  $\alpha$  was determined by fitting the Jeff-S + slip predictions to the experimental  $A_{11}$  and  $A_{33}$  components over the strain range of 0-25 and found to be  $\alpha = 0.3$ . The Jeff-S + slip model shows good agreement for the  $A_{11}$  and  $A_{33}$  components at small strains but appears to over predict the degree of orientation at large strains. The F-T + slip shows good agreement with the fiber orientation for all strains tested. However, by strain 200 the F-T + slip predicts that a steady state has been reached in the fiber orientation. This is a direct result of the  $C_1$  fit to the largest strain and suggests a smaller  $C_1$  value.

The  $A_{12}$  component is indirectly related to the stresses. Predictions of Jeff-S + slip and F-T + slip vs. strain of the  $A_{12}$  compared to the experimental values can be seen in Fig. 4.13. For the experimental data there is a rise in the values of  $A_{12}$  from  $\gamma = 0$ , passing through a maximum at  $\gamma = 7$  and then decaying slowly with increasing strain. On the other hand the Jeff-S + slip and F-T + slip models decay from the initial value and predict no maximum. We hypothesize that direct fiber contact causes this increase in the  $A_{12}$  component as the fiber orientation is evolving from the  $x_1 - x_3$  plane to the  $x_1$  direction. The models do not account for direct particle contact and as a result do not predict the increase in the  $A_{12}$  component. As a result we also show model predictions beginning from the experimentally determined fiber orientation at  $\gamma = 7$ , which are given in Eq. (4.17). Both the Jeff-S + slip and F-T + slip show good agreement with the rate of decay from the peak value. However, the  $A_{12}$  component appears to reach a statistical steady state of greater magnitude than predicted by both models.

$$\mathbf{A}|_{\gamma=7} = \begin{pmatrix} .5457 & - & - \\ .1378 & .0789 & - \\ -.0400 & -.0049 & .3754 \end{pmatrix} \quad (4.17)$$

We now compare the predictions of the stress growth functions  $\eta^+$  and  $N_1^+$  vs. strain by way of Eqs. (4.10) and (4.11), in combination with the Jeff-S + slip and F-T + slip models for fiber orientation to the experimental results. Predictions begin at a strain of 7 as previously discussed. For the Jeff-S + slip and F-T + slip models the same parameter values of  $C_I$  and  $\alpha$  that were determined by fitting the evolving fiber orientation were used,  $C_I = 0.006$  and  $\alpha = 0.3$ . The model parameters  $c_I$  and  $N$  were determined through a visual best fit of the predicted  $\eta^+$  and  $N_1^+$  to the measured  $\eta^+$  and  $N_1^+$ . The best fit parameter values using the Jeff-S + slip model and F-T + slip model was found to be  $c_I = 1.5$ ,  $N = 35$ , and  $c_I = 0$ ,  $N = 35$ , respectively. The comparison of the experimental and predicted values of  $\eta^+$  can be seen in Fig. 4.14 (a). The Jeff-S + slip model produces the best fit; model shows good agreement with the experimental results over the entire range of  $\gamma$  shown. In contrast, when the F-T + slip model was used for the fiber orientation with the  $C_I = 0.006$  we were unable to fit the overshoot maximum and the steady state values simultaneously. The experimental and predicted  $N_1^+$  vs. strain can be seen in Fig. 4.14 (b). With both the Jeff-S + slip and F-T + slip models we were unable to fit the magnitude of the overshoot region. This is attributed to direct fiber contact that is not accounted for in the Lipscomb stress equation. However the predictions using the Jeff-S + slip show better agreement with the experimental results as  $N_1^+$  approaches a steady state.

## 4.6 Conclusions

The common approach to predicting the fiber orientation is to use Jeffery's equation or the F-T model. Direct measurement of fiber orientation in startup of flow of a concentrated composite fluid shows that the fiber orientation evolves much slower than the theories predict. In addition, a linear fit to the  $A_{11}$  and  $A_{33}$  components of  $\mathbf{A}$  at the last three strains of 50, 100, and 200 suggest that the fiber is still evolving even after 200 strain units. Model predictions using the F-T + slip model with the  $C_I = 0.006$  fit to the experimental data at the strain of 200 compared to the experimental stress growth behavior over predict the magnitude of the stress as they approach a steady state. This also suggests that the fiber orientation is continuously evolving. It is unclear at what strain the fibers would reach a steady state, but we believe the fiber orientation does continue to evolve to very large strains where some maximum alignment is reached. As a result, the F-T model + slip would give the best predictions of the evolving fiber orientation as the isotropic diffusivity term allows one to control the steady state alignment and the rate of fiber reorientation. If the fibers do fully align then the Jeff + slip would be the most accurate model.

In startup of flow the  $A_{12}$  component initially increases. Theory was unable to predict this phenomenon and we attribute it to fiber contact as the fiber reorients from a mostly planar orientation to align itself in the flow direction. Model predictions of the stress growth functions showed good agreement with  $\eta^+$  but we were unable to predict the magnitude of the  $N_1^+$  overshoot. This difference was also attributed to direct fiber contact.

We show that the IBOF closure approximation combined with Jeffery's equation gives excellent agreement to  $A_{ii}$  components with values calculated using no closure approximation is used. However, Jeffery's equation with the IBOF closure can exhibit non-physical oscillations depending on the initial conditions. This is a result of the IBOF closure and not Jeffery's model. The addition of an isotropic diffusivity term, essentially the F-T model, with a small  $C_I$  value stabilizes the non-physical oscillations.

#### **4.7 Acknowledgments**

The financial support for this work from the National Science Foundation and Department of Energy through Grant No. DMI-0521918 is gratefully acknowledged. We thank Kevin Ortman for his persistent help with the CLM images and GE Plastics for supplying the materials used in this work.

## 4.8 References

1. Advani, S. G.; Sozer, E. M., *Process Modeling in Composites Manufacturing*. Marcel Dekker Inc.: New York, 2003.
2. Jeffery, G. B., The motion of ellipsoidal particles immersed in a viscous fluid. *Proc. R. Soc. Lond. A* **1922**, 102, 161-179.
3. Moses, K. B.; Advani, S. G.; Reinhardt, A., Investigation of fiber motion near solid boundaries in simple shear flow. *Rheol. Acta* **2001**, 40, 296-306.
4. Eberle, A. P. R.; Baird, D.; Wapperom, P., Rheology of non-Newtonian fluids containing glass fibers: A review of experimental literature. *Ind. Eng. Chem. Res.* **2008**, 47, (10), 3470-3488.
5. Petrich, M. P.; Koch, D. L.; Cohen, C., An experimental determination of the stress-microstructure relationship in semi-concentrated fiber suspensions. *J. Non-Newt. Fluid Mech.* **2000**, 95, 101-133.
6. Ivanov, Y.; VanDeVen, T. G. M.; Mason, S. G., Damped oscillations in the viscosity of suspensions of rigid rods. I. Monomodal suspensions. *J. Rheol.* **1982**, 26, (2), 213-230.
7. Iso, Y.; Koch, D. L.; Cohen, C., Orientation in simple shear flow of semi-dilute fiber suspensions. 1. Weakly elastic fluids. *J. Non-Newt. Fluid Mech.* **1996**, 62, (2-3), 115-134.
8. Petrich, M. P.; Koch, D. L., Interactions between contacting fibers. *Phys. Fluids* **1998**, 10, 2111-2113.
9. Sundararajakumar, R. R.; Koch, D. L., Structure and properties of sheared fiber suspensions with mechanical contacts. *J. Non-Newt. Fluid Mech.* **1997**, 73, (3), 205-239.
10. Sepehr, M.; Carreau, P. J.; Moan, M.; Ausias, G., Rheological properties of short fiber model suspensions. *J. Rheol.* **2004**, 48, (5), 1023-1048.
11. Altan, M. C., A review of fiber-reinforced injection molding: Flow kinematics and particle orientation. *J. Thermoplastic Comp. Mat.* **1990**, 3, (4), 275-313.
12. Folgar, F. P.; Tucker, C. L., Orientation behavior of fibers in concentrated suspensions. *J. Rein. Plast. Comp.* **1984**, 3, 98-119.
13. Huynh, H. M. Improved Fiber Orientation Predictions for Injection-Molded Composites. University of Illinois at Urbana-Champaign, 2001.
14. Sepehr, M.; Ausias, G.; Carreau, P. J., Rheological properties of short fiber filled polypropylene in transient shear flow. *J. Non-Newt. Fluid Mech.* **2004**, 123, 19-32.
15. Sepehr, M.; Carreau, P. J.; Grmela, M.; Ausias, G.; Lafleur, P. G., Comparison of rheological properties of fiber suspensions with model predictions. *J. Poly. Eng.* **2004**, 24, (6), 579-610.
16. Eberle, A. P. R. The Dynamic Behavior of a Concentrated Composite Fluid Containing Non-Brownian Glass Fibers in Rheometrical Flows. Virginia Tech, Blacksburg, 2008.
17. Eberle, A. P. R.; Baird, D. G.; Wapperom, P.; Velez-Garcia, G., Obtaining Reliable Transient Rheological Data on Concentrated Short Fiber Suspensions using a Rotational Rheometer. *Submitted to J. Rheol.* **2008**.

18. Advani, S. G.; Tucker, C. L., The use of tensors to describe and predict fiber orientation in short fiber composites. *J. Rheol.* **1987**, 31, (8), 751-784.
19. Einstein, A., A new determination of molecular dimensions. *Ann Phys* **1906**, 19, 289-306.
20. Lipscomb, G. G.; Denn, M. M.; Hur, D. U.; Boger, D. V., The flow of fiber suspensions in complex geometries. *J. Non-Newt. Fluid Mech.* **1988**, 26, (3), 297-325.
21. Dinh, S. M.; Armstrong, R. C., A rheological equation of state for semiconcentrated fiber suspensions. *J. Rheol.* **1984**, 28, (3), 207-227.
22. Bird, R. B.; Armstrong, R. C.; Hassager, O., *Dynamics of Polymeric Liquids*. John Wiley & Sons, Inc.: New York, 1987; Vol. 1.
23. Doi, M.; Edwards, S. F., *The Theory of Polymer Dynamics*. Oxford University Press: New York, 1988.
24. Cintra, J. S.; III, C. L. T., Closure approximations for flow-induced fiber orientation. *J. Rheol.* **1995**, 39, (1095-1122).
25. Chung, D. H.; Kwon, T. H., Improved model of orthotropic closure approximation for flow induced fiber orientation. *Polym. Compos.* **1999**, 22, (5), 636-649.
26. Advani, S. G.; Tucker, C. L., Closure approximations for three-dimensional structure tensors. *J. Rheol.* **1990**, 34, (3), 367.
27. Chung, D. H.; Kwon, T. H., Fiber orientation in the processing of polymer composites. *Korean-Australian Rheol. J.* **2002**, 14, (4), 175-188.
28. Shaqfeh, E. S. G.; Fredrickson, G. H., The hydrodynamic stress in a suspension of rods. *Phys. Fluids A* **1990**, 2, 7-25.
29. Phan-Thien, N.; Graham, A. L., A new constitutive model for fiber suspensions. *Rheol. Acta* **1991**, 30, 44-57.
30. Botelho, G.; Queiros, A.; Liberal, S.; Gijsman, P., Studies on thermal and thermo-oxidative degradation of poly(ethylene terephthalate) and poly(butylene terephthalate). *Polym Degrad Stab* **2001**, 74, (10), 39-48.
31. Blankeney, W. R., Viscosity of suspensions of straight rigid rods. *J. Colloid Interface Sci.* **1966**, 22, (4), 324.
32. Attanasio, A.; Bernini, U.; Galloppo, P.; Segre, G., Significance of viscosity measurements in macroscopic suspensions of elongated particles. *Trans. Soc. Rheol.* **1972**, 16, 147-154.
33. Macosko, C. W., *Rheology Principles, Measurements, and Applications*. Wiley-VCH: New York, 1994.
34. Lee, Y.; Lee, S.; Youn, J.; Chung, K.; Kang, T., Characterization of fiber orientation in short fiber reinforced composites with an image processing technique. **2002**, 6, (2), 65.
35. Sawyer, L. C.; Grubb, D., *Polymer Microscopy*. 2nd ed.; Springer: 1995.
36. Bay, R. S.; Tucker, C. L., Stereological measurement and error estimates for three dimensional fibre orientation. *Poly. Eng. Sci.* **1992**, 32, 240-253.
37. Larson, R. G., *The Structure and Rheology of Complex Fluids*. Oxford University Press: New York, 1999.
38. Chaouche, M.; Koch, D. L., Rheology of non-Brownian rigid fiber suspensions with adhesive contacts. *J. Rheol.* **2001**, 45, (2), 369-382.

39. Forgacs, O. L.; Mason, S. G., Particle motions in sheared suspensions IX. Spin and deformation of threadlike particles. *J. Colloid Sci.* **1959**, 14, 457-472.
40. Qi, D.; Cheng, G., Fatigue behavior of filament-wound glass fiber reinforced epoxy composite tubes under tension/torsion biaxial loading. *Polym. Compos.* **2007**, 28, (1), 116-123.

**Figures**

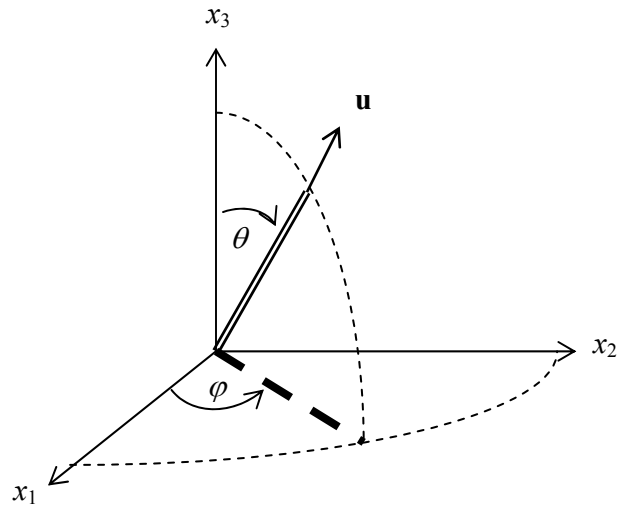


**Figure 4.1.** Unit vector  $\mathbf{u}$  describing the orientation state of a rod in spherical coordinates.

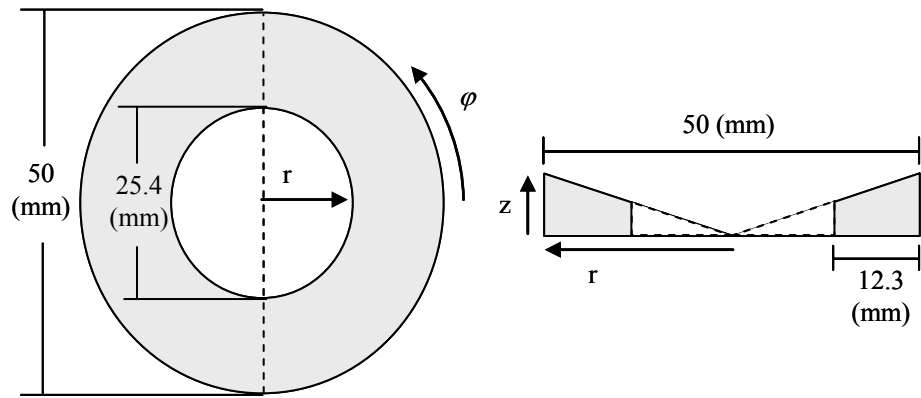


**Figure 4.2.** Schematic drawing and cross-sectional profile of the donut sample.

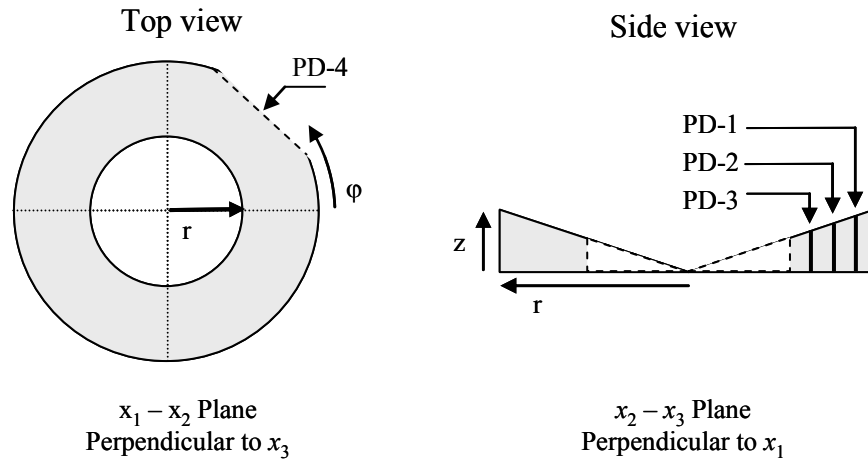
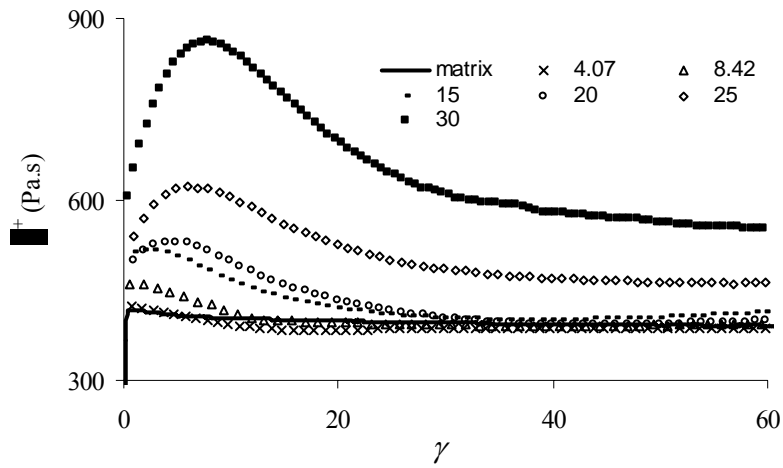
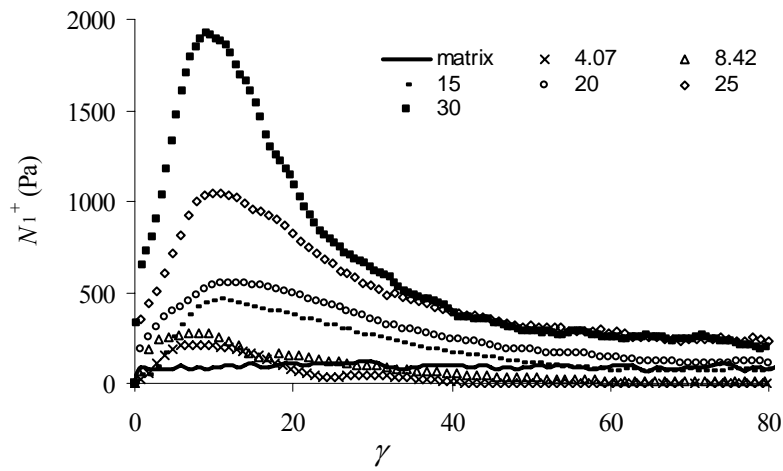


**Figure 4.3.** Schematic drawing of the polished and imaged planes perpendicular to the neutral,  $x_3$ , and flow,  $x_1$ , directions. The  $x_2 - x_3$  plane images were taken of the sample at a distance of 4.0, 6.25, and 8.5 mm from the outer edge denoted by PD-1, PD-2, PD-3. For the  $x_1 - x_2$  plane, images were taken in one location denoted by PD-4. In all locations images were taken through the entire height of the sample.

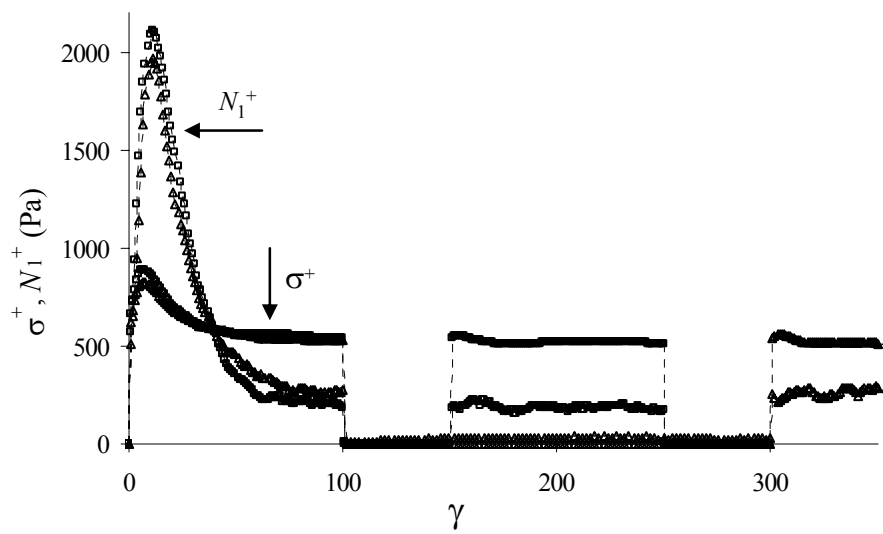


(a)

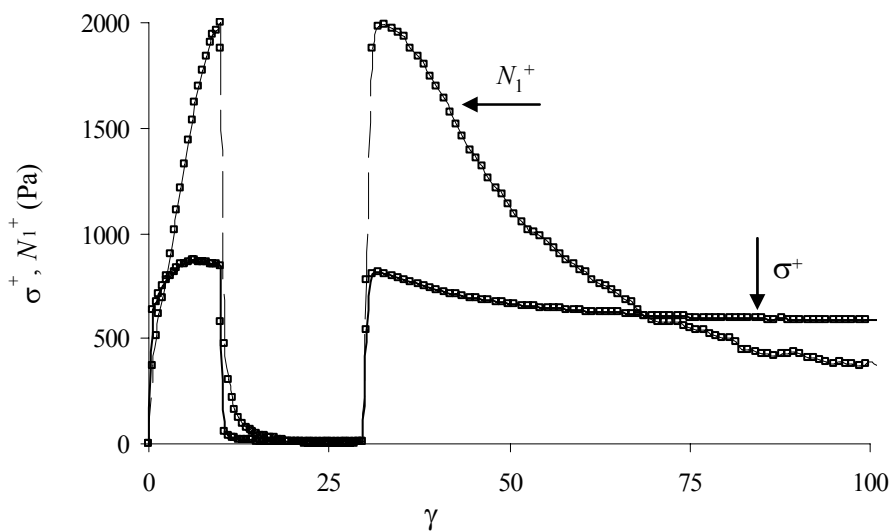


(b)

**Figure 4.4.** Stress growth behavior of PBT and PBT containing various concentrations of short glass fiber at  $\dot{\gamma} = 1 \text{ s}^{-1}$ . (a) Shear stress growth coefficient,  $\eta^+$ , (b) first normal stress growth,  $N_1^+$ , vs. strain. The numbers in the legend relate to the wt% of glass fiber.



(a)



(b)

**Figure 4.5.**  $\sigma^+$  and  $N_1^+$  vs. strain,  $\gamma$ , for PBT-30 in interrupted flow experiments at  $\dot{\gamma} = 1 \text{ s}^{-1}$ . (a) Two interrupted experiments were performed on two different samples. In one experiment the flow was removed for 50 s and in the other experiment flow was removed for 200 s. (b) An interrupted flow experiment where a fresh sample was subject to flow at  $\dot{\gamma} = 1 \text{ s}^{-1}$  for 10 s, the flow was removed for 20 s, then the flow was applied.

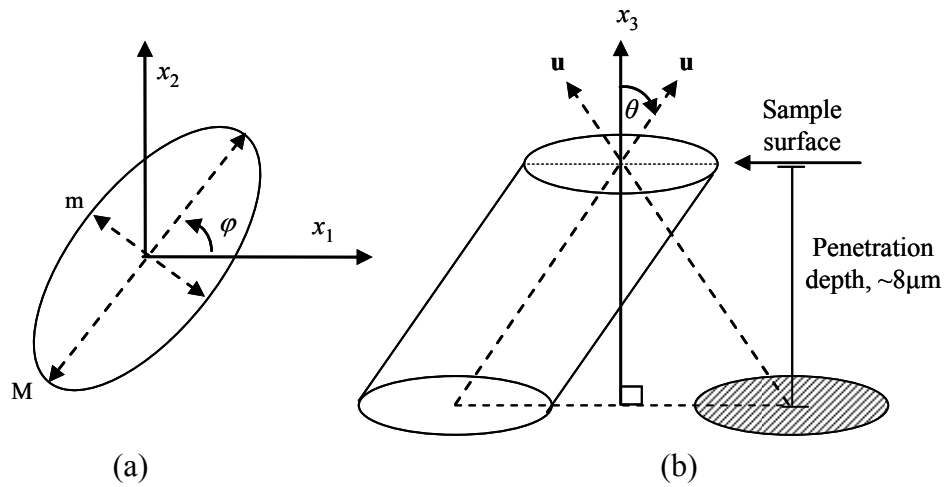
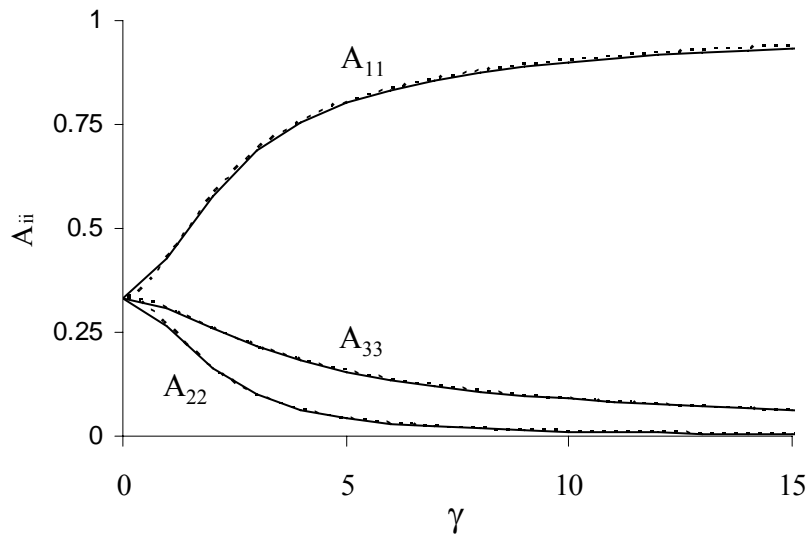
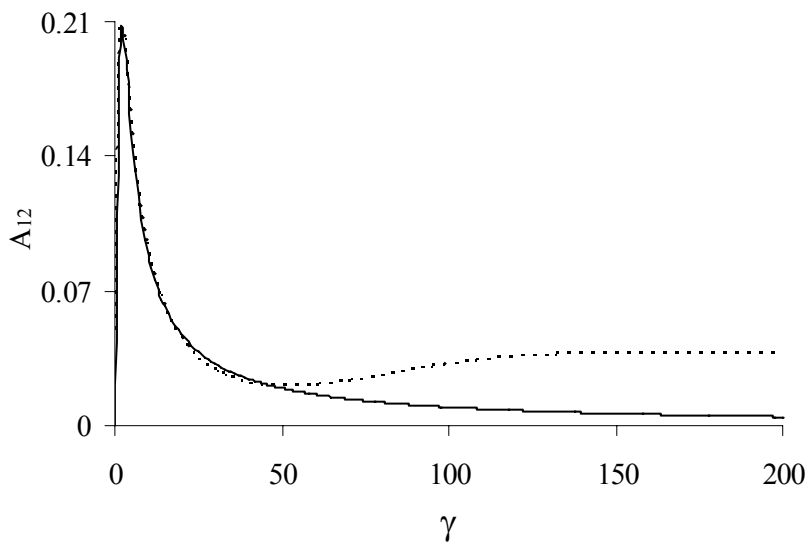


**Figure 4.6.** (a) Elliptical “footprint” of fiber cross section where  $M$  is the major axis and  $m$  is the minor axis. (b) Two possible unit vectors,  $\mathbf{u}$ , along the backbone of the fiber and depiction of the positive angle  $\theta$ .

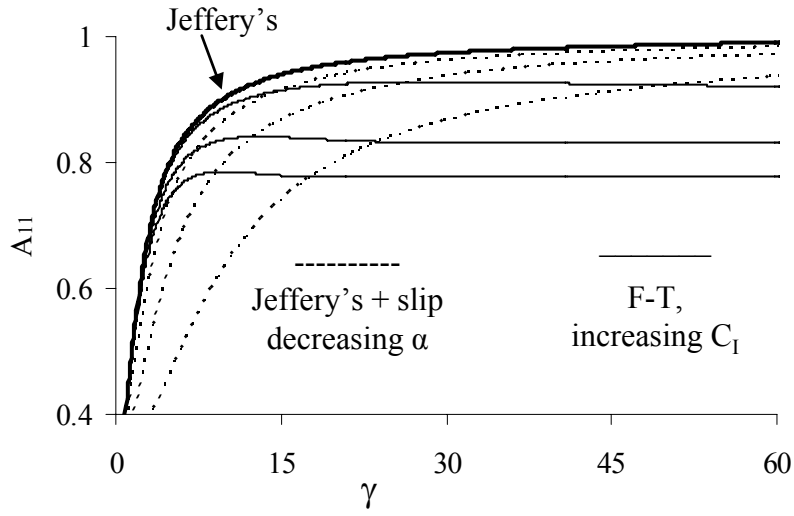


(a)

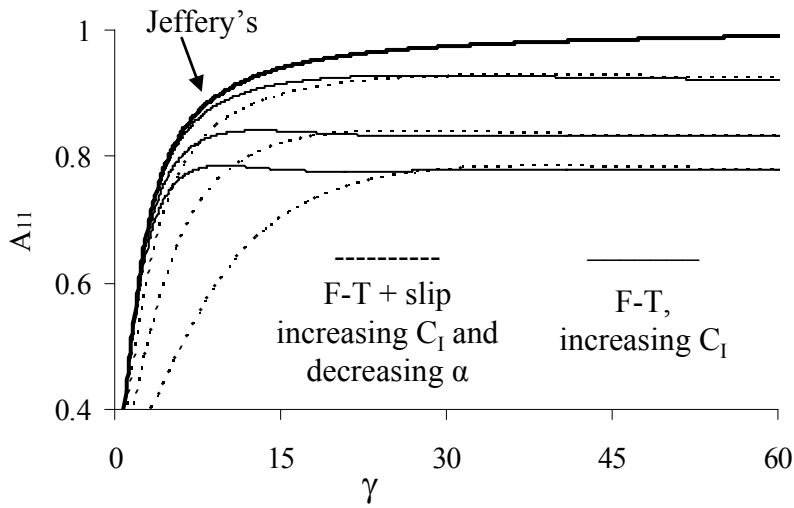


(b)

**Figure 4.7.** Comparison of predictions of Jeffery's equation with and without the IBOF closure approximation. The dashed line represents Jeffery's with the use of the IBOF closure, Eq. (4.3), and the solid line represents the predictions without the use of a closure approximation using Eq. (4.4). For the predictions random initial conditions were used at a  $\dot{\gamma} = 1 \text{ s}^{-1}$ .



(a)



(b)

**Figure 4.8.** Effect of the slip constant,  $\alpha$ , and the Folgar-Tucker constant,  $C_I$ , on the predictions of the  $A_{11}$  component at  $\dot{\gamma} = 1 \text{ s}^{-1}$ . In the figures Jeffery's represents Eq. (4.3). F-T represents Eqs. (4.5), Jeffery's + slip represents Eq. (4.6) with  $C_I = 0$ , and F-T + slip represents Eq. (4.6). Decreasing  $\alpha$  refers to values  $\alpha = 0.75, 0.5$  and  $0.25$ , and increasing  $C_I$  refers to values of  $C_I = 0.001, 0.005$  and  $0.01$ .

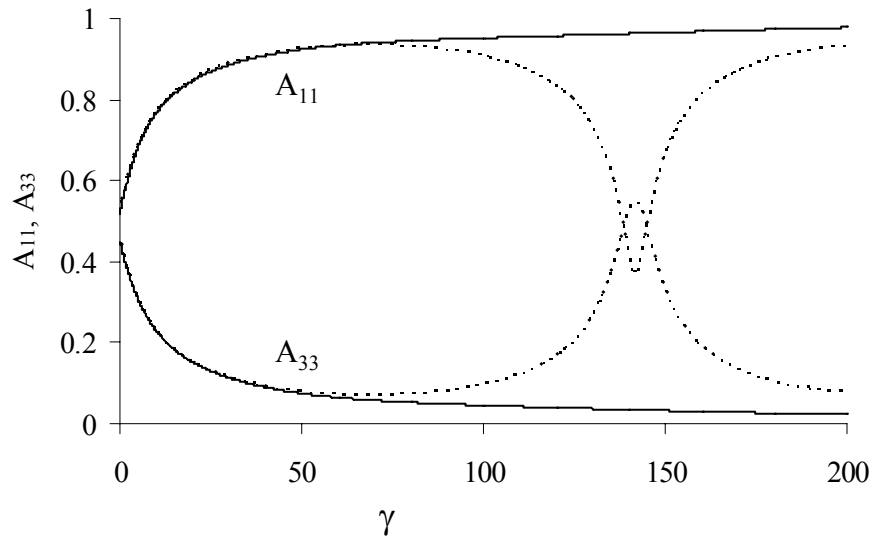
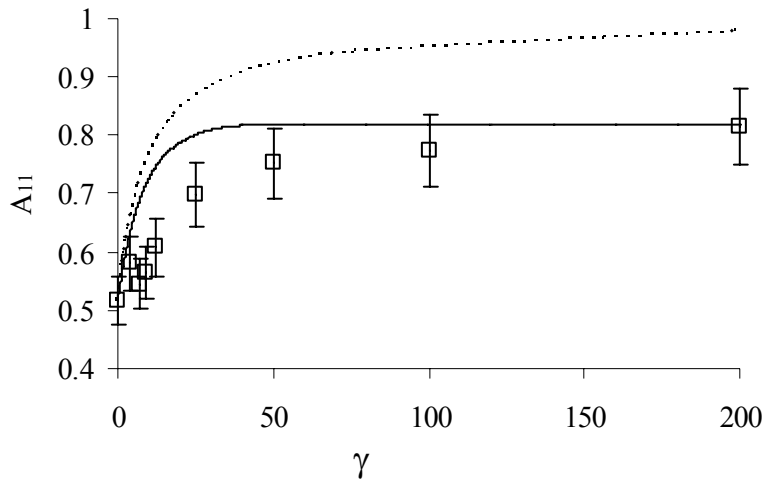
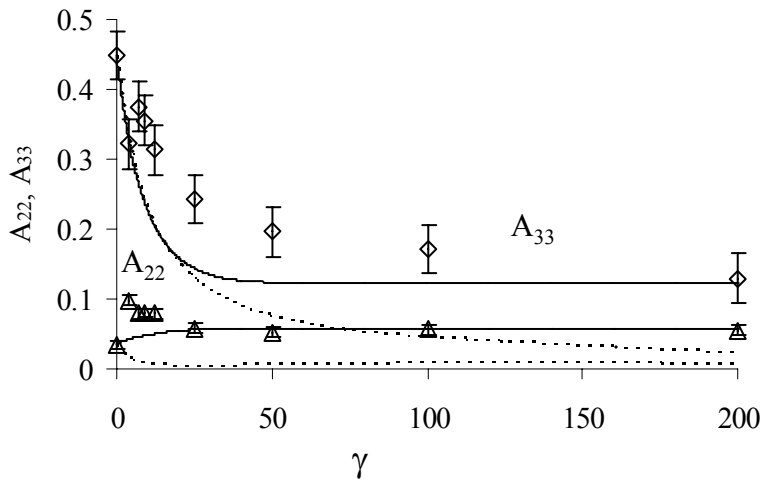


**Figure 4.9.** Non-physical oscillations in  $A_{11}$  and  $A_{33}$  as predicted by Jeffery's Eq. (4.3) using the IBOF closure approximation with experimentally determined initial conditions at  $\dot{\gamma} = 1 \text{ s}^{-1}$ . The dashed line represents Jeffery's and the solid line represent the stabilized Jeffery's, Jeff-S, with the Folgar-Tucker constant with small  $C_1 = 0.00015$ .



(a)



(b)

**Figure 4.10.** Experimental and predicted fiber orientation represented through the  $A_{ii}$  components in startup of simple shear flow at  $\dot{\gamma} = 1 \text{ s}^{-1}$ . The dashed line represents the Jeff-S model and the solid the F-T model with a  $C_1 = 0.006$ . (a) the  $A_{11}$  component, (b) the  $A_{22}$  and  $A_{33}$  components vs. strain.

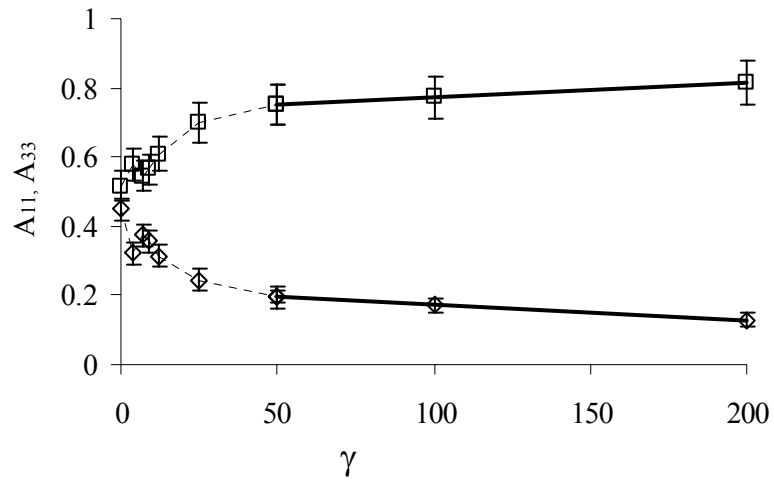
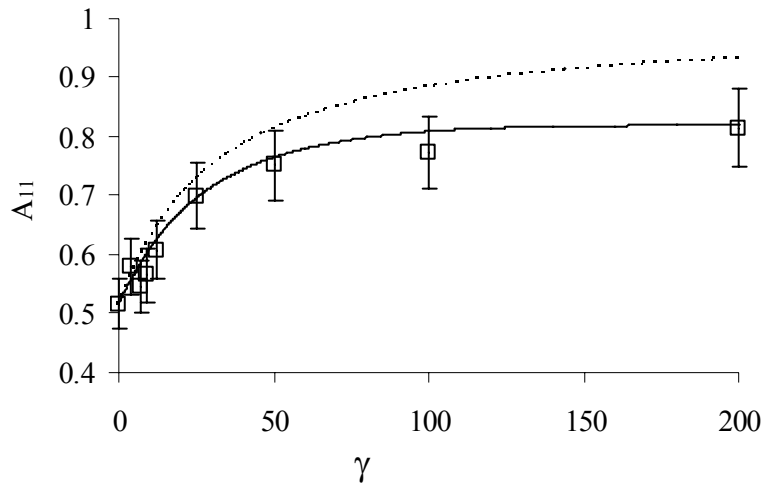
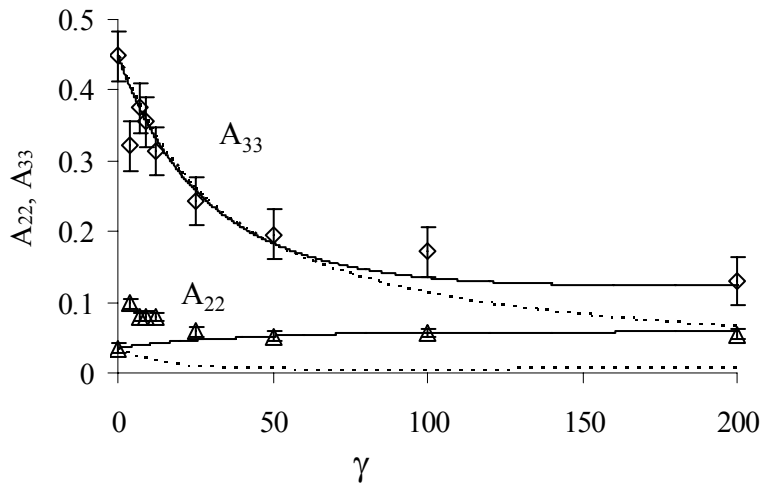


**Figure 4.11.** Linear fit of the last three data points (strains 50, 100, 200) of the  $A_{11}$  and  $A_{33}$  components.



(a)



(b)

**Figure 4.12.** Experimental and predicted fiber orientation represented through the  $A_{ii}$  components in startup of simple shear flow at  $\dot{\gamma} = 1 \text{ s}^{-1}$ . The dashed line represents the Jeff-S + slip model and the solid line the F-T + slip model with a  $C_1 = 0.006$ . (a) the  $A_{11}$  component, (b) the  $A_{22}$  and  $A_{33}$  components vs. strain.

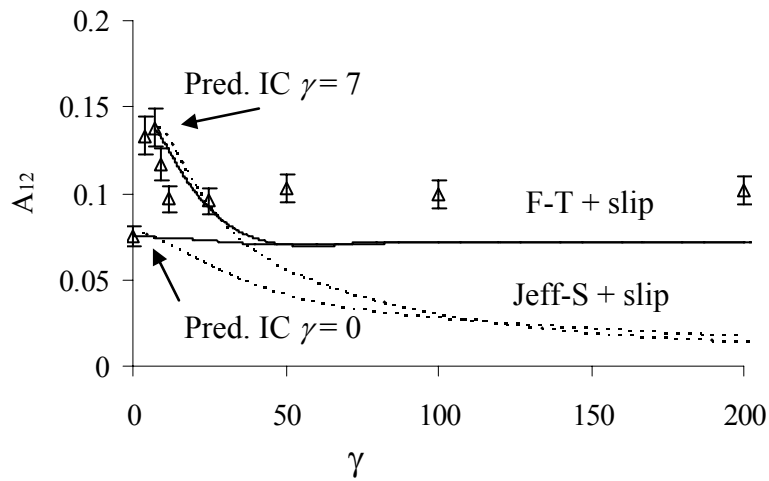
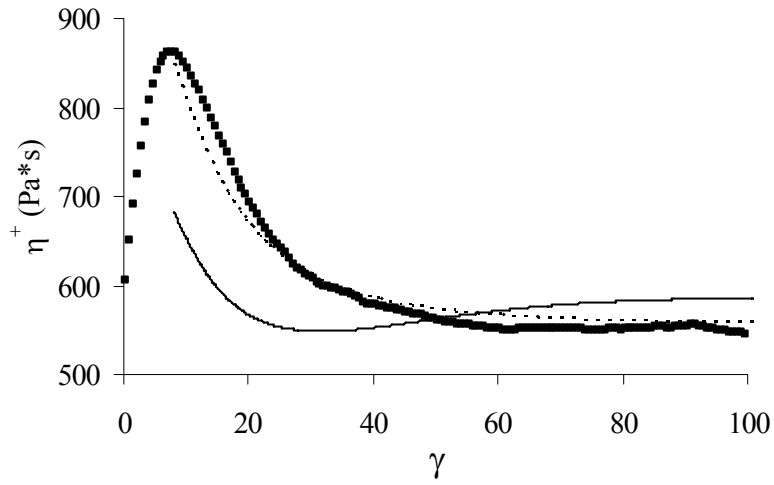
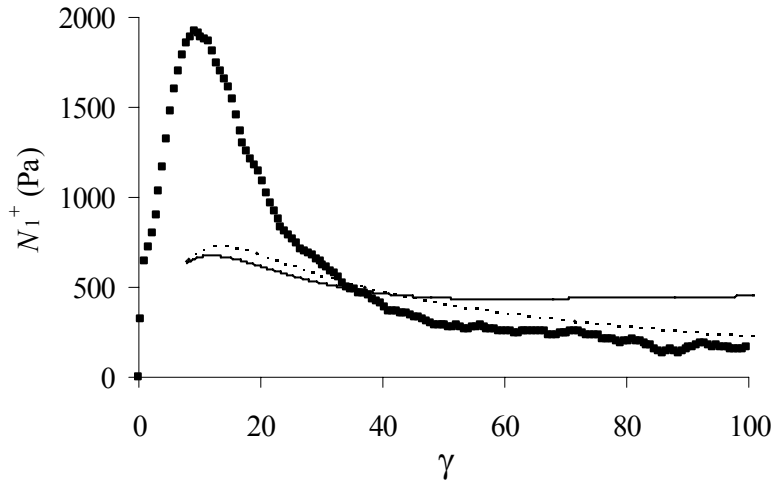


**Figure 4.13.** Experimental and predicted fiber orientation represented through the  $A_{12}$  component in startup of simple shear flow at  $\dot{\gamma} = 1 \text{ s}^{-1}$ . The dashed line represents the Jeff-S + slip model and the solid the F-T + slip model with a  $C_1 = 0.006$ . Predictions were performed starting at a strain of 0 and 7 shown as Pred. IC  $\gamma = 0$  and Pred. IC  $\gamma = 7$ , respectively, in the figure.



(a)



(b)

**Figure 4.14.** Experimental and predicted stress growth functions in startup of simple shear flow at  $\dot{\gamma} = 1 \text{ s}^{-1}$ . The dashed line represents the Jeff-S + slip model and the solid the F-T + slip model with a  $C_1 = 0.006$  for fiber orientation.  $\eta^+$  and  $N_1^+$  were produced by means of Eqs. (4.10) and (4.11), respectively. (a)  $\eta^+$ , (b)  $N_1^+$  vs. strain.

## **5.0 Using Transient Rheology to Determine Material Parameters in Fiber Suspension Theory**

### Preface

In this chapter we explore an approach to determining fiber suspension theory material parameters by fitting model predictions to experimental data in rheometrical flows. Parameters determined at one shear rate are then used to predict the transient rheological behavior at other shear rates. This chapter is organized as a manuscript for publication.

## 5.0 Using Transient Rheology to Determine Material Parameters in Fiber Suspension Theory

Aaron P. R. Eberle <sup>a</sup>, Donald G. Baird <sup>a\*</sup>, Peter Wapperom <sup>b</sup>, Gregorio M. Vélez-García <sup>c</sup>

<sup>a</sup> Department of Chemical Engineering, <sup>b</sup> Department of Mathematics, <sup>c</sup> Department of Macromolecular Science and Engineering, Virginia Tech, Blacksburg, VA, 24061

\* Author to whom correspondence should be addressed; email: dbaird@vt.edu

### 5.1 Abstract

Fiber suspension theory model parameters for use in the simulation of fiber orientation in complex flows are either calculated from theory or fit to experimentally determined fiber orientation generated in processing flows. The feasibility of determining unambiguous model parameters for a composite fluid in simple flows was investigated by fitting model predictions to measured shear rheological material functions. For this work the transient shear rheology of a commercially available short glass fiber-filled polybutylene terephthalate was studied. Stress growth measurements in startup of flow and flow reversal in the shear rate range,  $\dot{\gamma} = 1-10 \text{ s}^{-1}$ , were performed. Predictions using the Lipscomb model coupled with the Folgar-Tucker model (with a strain reduction factor) for fiber orientation were fit to the transient stresses. Model parameters determined by fitting at  $\dot{\gamma} = 6 \text{ s}^{-1}$  allowed for reasonable predictions of the transient stresses in flow

reversal experiments at all the shear rates tested. In addition, we were able to predict the time rate of change of the measured fiber orientation using the fit parameters. The results suggest that fitting model predictions to the stress response in well defined flows could lead to unambiguous model parameters provided the initial fiber orientation is known.

Key words: short glass fiber, model fitting, fiber suspension, transient stresses

## 5.2 Introduction

Parts made from short glass fiber composites are typically manufactured using injection or compression molding where the composite melt is forced into a mold cavity which results in the formation of a layered fiber microstructure.<sup>1</sup> Depending on the complexity of the part and the mold filling process, local variations can arise in the fiber orientation distribution which can severely affect the mechanical, thermal and insulative properties. As a result it is highly desirable to be able to predict the flow behavior of the composite fluid in relation to the associated fiber microstructure to optimize mold design and processing conditions to maximize the part performance.

The simulation of fiber suspensions has been the subject of many publications over the past three decades. Most, if not all of the theoretical framework describing the evolution of fiber orientation begins with the pioneering work of Jeffery.<sup>2</sup> Jeffery derived the motion of a single ellipsoidal particle suspended in a Newtonian fluid subjected to a Stokes flow field. Jeffery's equation is easily extended to blunt-ended particles, such as fibers, by defining an equivalent aspect ratio.<sup>3,4</sup> For non-dilute fiber suspensions Folgar

and Tucker<sup>5</sup> added an isotropic diffusivity term that is proportional to the velocity gradient to Jeffery's equation for fiber motion to account for fiber interaction influencing the degree of fiber alignment, which is referred to as the Folgar-Tucker model (F-T). Currently there is no theoretical approach to calculate the interaction coefficient,  $C_1$ , in the F-T model. For complex flow simulations  $C_1$  is typically determined by fitting simulation results of fiber orientation to experimentally determined fiber orientation which can be very time intensive to produce.<sup>6</sup> Empirical relations have been proposed by Bay<sup>7</sup> and Phan-Thien<sup>8</sup> which indicate that  $C_1$  is a function of fiber volume fraction and aspect ratio. However, these relations have not been confirmed.

The theoretical work of Jeffery was extended to fibers and to include stress contributions from the fiber to the bulk extra stress by a number of researchers such as Hand,<sup>9</sup> Giesekus,<sup>10</sup> Batchelor<sup>11</sup> and Cox<sup>12</sup> and is now referred to as dilute fiber suspension theory. In non-dilute suspensions inter-particle hydrodynamic and contact forces significantly influence the dynamic behavior of the fiber and stress contribution. In the theories of Batchelor,<sup>13</sup> Evans,<sup>14</sup> Dinh and Armstrong,<sup>15</sup> Shaqfeh and Fredrickson,<sup>16</sup> and Phan-Thien and Graham,<sup>17</sup> expressions for the extra stress are derived as a result of inter-particle hydrodynamic interaction.

Sepehr et al.<sup>18, 19</sup> found they were only able to predict the stress growth behavior of a non-dilute short glass fiber suspension when the material parameters were fit to the rheological measurements and a slip parameter was added to the F-T model, F-T-S. This suggests that the theoretically determined material parameters are highly inaccurate and could be a large source of error in the complex flow simulations. We do note, however, that the stress growth experiments used in the comparison were performed in a rotational

rheometer with parallel disk geometry in which there is a varying shear rate from the center of the plates to the rim. Recent results have shown that the inhomogeneous shear field in the parallel disk geometry induces excessive fiber-fiber interaction in concentrated fiber suspensions.<sup>20</sup> This can have a severe effect on the magnitude of the stress growth overshoot peak and width of the overshoot. Also, in the predictions of Sepehr et al.<sup>18, 19</sup> the initial fiber orientation was assumed random. However, recent results clearly show that the initial fiber orientation in rheometer samples is closer to a planar orientation which can have a large impact on the transient predictions.<sup>20</sup>

In a previous work we showed that the F-T-S is currently the most accurate fiber orientation model.<sup>20, 21</sup> In this work an approach for determining unambiguous model parameters for the F-T-S model combined with the Lipscomb stress equation by fitting model predictions to transient shear rheological experiments performed using a donut sample in a CP rheometer is shown. Stress growth measurements in startup of simple shear flow and flow reversal were performed on a 30 wt% short glass fiber filled polybutylene terephthalate (PBT-30) at various shear rates. The Lipscomb model combined with the SRF model for fiber orientation was fit to the stress growth behavior at a shear rate of  $6 \text{ s}^{-1}$ . The same model parameters were then used to predict the stress growth behavior at other shear rates.

## 5.3 Theory

### 5.3.1 Orientation Tensors

The conventional method for describing the average orientation state of a distribution of fibers is with the use of orientation tensors. The second- and fourth-order orientation tensors,  $\mathbf{A}$  and  $\mathbf{A}_4$  respectively, have been defined as the second- and fourth-moments of the orientation distribution function,  $\psi(\mathbf{u}, t)$ :<sup>22</sup>

$$\mathbf{A}(t) = \int \mathbf{u}\mathbf{u} \psi(\mathbf{u}, t) d\mathbf{u} \quad (5.1)$$

$$\mathbf{A}_4(t) = \int \mathbf{u}\mathbf{u}\mathbf{u}\mathbf{u} \psi(\mathbf{u}, t) d\mathbf{u} \quad (5.2)$$

where  $\mathbf{u}$  is a unit vector parallel to the backbone of each fiber.  $\mathbf{A}$  is symmetric and has a trace equal to 1. For a completely random orientation state  $\mathbf{A} = 1/3 \mathbf{I}$ , where  $\mathbf{I}$  is the unity tensor and in the limit that all the fibers are perfectly aligned in the  $x_1$  direction the only non-zero component of  $\mathbf{A}$  is  $A_{11} = 1$ .

### 5.3.2 Orientation Evolution Equation

The common approach to predicting the motion of a single fiber begins from Jeffery's equation derived for non-Brownian axisymmetric particles.<sup>2</sup> For a large population of similar, non-interacting particles whose orientation is represented with the orientation

tensors the material derivative ( $D/Dt$ ) of  $\mathbf{A}$  can be derived from Jeffery's analysis and written as,<sup>22</sup>

$$\frac{D\mathbf{A}}{Dt} = (\mathbf{W} \cdot \mathbf{A} - \mathbf{A} \cdot \mathbf{W}) + \lambda (\mathbf{D} \cdot \mathbf{A} + \mathbf{A} \cdot \mathbf{D} - 2\mathbf{D} : \mathbf{A}_4) \quad (5.3)$$

where  $\lambda$  is a constant that depends on the aspect ratio,  $a_r$ , of the particle  $\lambda = (a_r^2 - 1) / (a_r^2 + 1)$ ,  $\mathbf{W} = [(\nabla \mathbf{v})^t - \nabla \mathbf{v}] / 2$  is the vorticity,  $\mathbf{D} = [\nabla \mathbf{v} + (\nabla \mathbf{v})^t] / 2$  is the rate of strain tensor and  $\nabla \mathbf{v} = \partial v_j / \partial x_i$ . For fibers it is common to assume the particle's aspect ratio approaches infinity, in which case  $\lambda \rightarrow 1$ . The time rate of change of  $\mathbf{A}$  in Eq. (5.3) is governed purely by the macroscopic flow field and does not account for Brownian effects, gravity, or particle interactions i.e. hydrodynamic or direct contact. For non-dilute suspensions Folgar and Tucker<sup>5</sup> hypothesized that fiber interaction acted similarly to isotropic diffusion and as a result added a diffusion term to Jeffery's equation,

$$\frac{D\mathbf{A}}{Dt} = (\mathbf{W} \cdot \mathbf{A} - \mathbf{A} \cdot \mathbf{W}) + (\mathbf{D} \cdot \mathbf{A} + \mathbf{A} \cdot \mathbf{D} - 2\mathbf{D} : \mathbf{A}_4) + 2C_1 \dot{\gamma} (\mathbf{I} - 3\mathbf{A}) \quad (5.4)$$

where  $C_1$  is the interaction coefficient and  $\dot{\gamma}$  is the scalar magnitude of  $\mathbf{D}$ . The F-T model allows for the control of the steady state fiber orientation through the magnitude of  $C_1$  but the rate of fiber reorientation is still dominated by the flow field for typical values of  $C_1$  in the range of 0.016 - 0.0001.<sup>7</sup> Bay<sup>7</sup> developed an empirical expression for concentrated suspensions ( $\phi > a_r^{-1}$ , where  $\phi$  is the volume fraction),

$$C_1 = 0.0184 \exp(-0.7148 \phi a_r) \quad (5.5)$$

Eq. (5.5) predicts that  $C_1$  decreases for increasing  $\phi a_r$ , an effect known as screening.

Phan-Thien et al.<sup>8</sup> proposed a model in which  $C_1$  increases with increasing  $\phi a_r$  as,

$$C_1 = M [1.0 - \exp(-N \phi a_r)] \quad (5.6)$$

where  $M$  and  $N$  are fit parameters which they found to be,  $M = 0.03$ ,  $N = 0.224$ .

The slip parameter proposed by Sepehr et al.<sup>18</sup> can be incorporated into the F-T model, as follows,

$$\frac{D\mathbf{A}}{Dt} = \alpha [(\mathbf{W} \cdot \mathbf{A} - \mathbf{A} \cdot \mathbf{W}) + (\mathbf{D} \cdot \mathbf{A} + \mathbf{A} \cdot \mathbf{D} - 2\mathbf{D} : \mathbf{A}_4) + 2C_1 \dot{\gamma} (\mathbf{I} - 3\mathbf{A})] \quad (5.7)$$

where the slip coefficient,  $\alpha$ , is some value between 0 and 1. This modification renders Eq. (5.7) non-objective, see for example Tanner.<sup>23</sup> As a note, the slip parameter proposed by Sepehr et al.<sup>18</sup> is essentially equivalent to the strain reduction factor proposed by Huynh<sup>24</sup> used in complex flow simulations.

To solve Eq. (5.4) or (5.7) a closure approximation is needed to decouple the fourth-order tensor  $\mathbf{A}_4$  into a system of second-order tensors. Many closure approximations have been proposed including the quadratic,<sup>25</sup> hybrid,<sup>22</sup> eigenvalue-<sup>26</sup> and invariant-based optimal fitted.<sup>27</sup> A good review of their accuracy can be found elsewhere.<sup>28, 29</sup> For this work we use the invariant-based orthotropic fitted (IBOF) closure approximation with the

fifth order polynomial coefficients for its high degree of accuracy compared to the quadratic and hybrid closures, and computational efficiency compared to the eigenvalue-based closures. A complete description of the IBOF, its accuracy and polynomial coefficients can be found elsewhere.<sup>27</sup>

### 5.3.3 Stress Equation

A general expression for high aspect ratio non-Brownian particles can be derived from the theories of Hand<sup>23</sup> and Giesekus<sup>21</sup> and is commonly referred to as the Lipscomb model.<sup>19, 30</sup>

$$\boldsymbol{\sigma} = -p\mathbf{I} + 2\eta_s\mathbf{D} + 2c_l\varphi\eta_s\mathbf{D} + 2\varphi\eta_s N\mathbf{D} : \mathbf{A}_4 \quad (5.8)$$

where  $\boldsymbol{\sigma}$  is the total stress,  $p$  is pressure,  $\eta_s$  is the suspending medium viscosity,  $c_l$  is a material constant, and  $N$  is a dimensionless parameter that represents the coupling between hydrodynamic stress and fiber orientation. The third term on the right hand side of Eq. (5.8) is the viscosity enhancement as a result of the fiber and is similar to the enhancement term for a dilute suspension of spheres proposed by Einstein.<sup>31</sup> Lipscomb et al.<sup>30</sup> give  $c_l$  to be equal to 2 for the limiting case  $a_r \rightarrow \infty$ , but we choose to use it as a fit parameter. The fourth term on the right hand side of Eq. (5.8) is the contribution to stress from the hydrodynamic drag of the fluid as it flows past a particle. Using Eq. (5.8) it is straightforward to show that the shear stress growth coefficient,  $\eta^+$ , and the first normal stress growth function,  $N_1^+$ , are,

$$\eta^+ = \sigma_{12} / \dot{\gamma} = \eta_s + c_1 \eta_s \phi + 2\eta_s \phi N A_{1212} \quad (5.9)$$

and,

$$N_1^+ = 2\phi \eta_s \dot{\gamma} N (A_{1211} - A_{1222}) \quad (5.10)$$

where the fourth-order tensor components are a function of time.

Subsequently we define various theories for calculating the material  $N$  for comparison to that determined by fitting. For dilute suspensions ( $\phi \ll a_r^{-2}$ ) Lipscomb et al.<sup>30</sup> and Batchelor<sup>13</sup> give  $N$  to be a function of  $a_r$ ,

$$N = \frac{a_r^2}{2 \ln a_r} \quad (5.11)$$

and,

$$N = \frac{a_r^2}{3 \ln(2a_r)} f(\varepsilon), \quad f(\varepsilon) = \frac{1+0.64\varepsilon}{1-1.5\varepsilon} + 1.659\varepsilon^2, \quad \varepsilon = [\ln(2a_r)]^{-1} \quad (5.12)$$

respectively. Equation (5.8) can also be applied to semidilute theories ( $a_r^{-2} \ll \phi \ll a_r^{-1}$ ) by replacing  $N$  for the dilute case to one that accounts for inter-particle hydrodynamics such as the Dinh and Armstrong<sup>15</sup> model,

$$N = \frac{a_r^2}{3 \ln(2h/D)} \quad (5.13)$$

$$h = \begin{cases} (nL^2)^{-1} & \text{random} \\ (nL)^{-\frac{1}{2}} & \text{aligned} \end{cases}$$

where  $h$  is the inter-particle spacing given for a completely random and aligned fiber orientation,  $D$  is the fiber diameter and  $n$  is the number of fibers per unit volume. Shaqfeh and Fredrickson<sup>16</sup> derived an expression for dilute and semidilute suspensions,

$$N = \frac{4a_r^2}{3} \left\{ \frac{1}{\ln(1/\phi) + \ln \ln(1/\phi) + C''} \right\} \quad (5.14)$$

where  $C''$  is a constant which for random  $C'' = -0.66$  and for aligned  $C'' = 0.16$ . Phan-Thien and Graham<sup>32</sup> proposed the following phenomenological expression,

$$N = \frac{a_r^2 (2 - \phi/G_v)}{2 [\ln(2a_r) - 1.5] (1 - \phi/G_v)^2} \quad (5.15)$$

where  $G_v = 0.53 - 0.013a_r$ , for the range of  $5 < a_r < 30$ . As a note, semi-dilute suspension theories typically neglect the third term on the right side of the equals in Eq. (5.8). As a result, when the fibers completely align themselves in the flow direction, as predicted by

Jeffery's equation with  $\lambda = 1$ ,  $N_1^+$  approaches zero and  $\eta^+$  approaches the suspending medium viscosity,  $\eta$ .

## 5.4 Experimental

### 5.4.1 Materials

For this work a commercially available 30wt% (volume fraction,  $\phi = 0.1766$ ) short glass fiber filled polybutylene terephthalate, (PBT-30), provided by GE Plastics under the trade name Valox 420 was used. To examine the effect of fiber concentration on the rheological behavior, PBT-30 was diluted to increasing concentrations of 4.07, 8.42, 15, 20 and 25 wt%. The concentration of 4.07 wt% relates to roughly 40% below the semidilute régime upper boundary  $\phi \ll a_r^{-1}$ . All other concentrations can be considered concentrated. Compounding was accomplished by passing dry blended amounts of PBT-30 and the neat matrix through the extruder section of an Arburg Alrounder 221-55-250 injection molder at an rpm of 200. The extrudate was collected before entering the runner of the mold and pelletized. The pellets were then compression molded for rheological testing to a cone-and-plate geometry sample at 260 °C. Precautions were taken to minimize the degree of thermo-oxidative degradation of the PBT matrix by drying the materials at 120 °C for a minimum of 12 hours in a vacuum oven at a pressure smaller than 0.4 in.Hg before sample extrusion, molding or testing.<sup>33</sup>

To characterize the glass fiber within the suspension, pyrolysis was performed on the PBT-30 pellets at 500 °C after extrusion to separate the fibers from the matrix. The fiber

length was determined by randomly measuring the length of 1,000 fibers. The number average and weight average fiber length of PBT-30 was found to be  $L_n = 0.3640$  and  $L_w = 0.4388$  mm, respectively. The same fiber length measurement was performed on all the diluted concentrations and was found to be slightly higher for all other concentrations, and within  $0.3640 \leq L_n \leq 0.3740$  and  $0.4388 \leq L_w \leq 0.4578$  mm. The fiber diameter was determined directly from images taken of fiber cross sections using a confocal laser microscope, discussed later, and the average diameter of 1,000 fibers was found to be  $D = 12.9$   $\mu\text{m}$ . This relates to a number average aspect ratio for PBT-30 of  $a_r \cong 28.2$ .

#### **5.4.2 Rheological Measurements**

All rheological measurements were performed on a Rheometrics Mechanical Spectrometer (RMS-800) at 260 °C. To minimize the degree of thermo-oxidative degradation, all experiments were performed in a nitrogen environment with a freshly loaded pre-formed sample. Rheological measurements on the PBT matrix and the glass fiber-filled PBT were performed with 25 mm and 50 mm cone-and-plate fixtures respectively, both of which had a 0.1 radian cone angle. For the fiber-filled PBT, donut shaped samples were used to eliminate the interaction of the fibers with the plate walls near the center of the plates where the rheometer gap is small compared to the fiber length. The dimensions of the donut sample can be seen in Fig. 5.1 before sample loading. A detailed discussion of the donut sample design and testing can be found elsewhere.<sup>20</sup> After each experiment the void space at the center was measured to account for sample loading as the gap was adjusted to proper dimensions. The hole diameter

varied slightly,  $23.8 \pm 0.5\text{mm}$  and was accounted for when calculating the stresses for each run.

In this work we are primarily interested in the transient rheological behavior at the startup of shear flow and flow reversal following startup of flow. In the flow reversal experiments a sample was subject to startup of flow in the clockwise (CW) direction. When the stresses reached a steady state the flow was removed and reapplied in the counter clockwise direction (CCW) at the same shear rate. The quiescent period between flows in the CW and CCW directions was roughly 10 s. The experiments were limited to a maximum shear rate of  $\dot{\gamma} = 10 \text{ s}^{-1}$  due to transducer overload. For the measurements,  $\eta^+$  and  $N_1^+$  were calculated as functions of torque,  $M(t)$ , and normal force,  $F(t)$ , from the following equations,<sup>34</sup>

$$\eta^+(t) = \sigma_{12}^+ / \dot{\gamma} = \frac{3M(t)}{2\pi\dot{\gamma}} (R_o^3 - R_i^3)^{-1} \quad (5.16)$$

and,

$$N_1^+(t) = \frac{2F_z(t)}{\pi} (R_o^2 - R_i^2)^{-1} \quad (5.17)$$

where  $R_o$ ,  $R_i$  are the outer and inner radius of the sample, respectively. The experimental reproducibility was found to be  $\eta^+ \pm 5\%$  and  $N_1^+ \pm 7\%$ .

### 5.4.3 Measurement of Fiber Orientation

Donut samples composed of PBT-30 were deformed using the RMS-800 at  $\dot{\gamma} = 1 \text{ s}^{-1}$  for a specified amount of time. The flow induced fiber microstructure within the rheological samples was characterized using confocal laser microscopy in a similar approach to that proposed by Lee et al.<sup>35</sup> In total, the fiber orientation was measured for 11 samples which corresponded to the following strains,  $\gamma = 0, 4, 7, 9, 12, 25, 50, 100$  and  $200$ . Strains  $4, 25, 100$  and  $200$  were imaged at locations PD-1 and PD-4, all other strains were imaged at locations PD-1 thru PD-4 as depicted in Fig. 5.2. Strain  $0$  relates to the initial fiber orientation. In addition,  $\gamma = 9$  was repeated to determine the experimental reproducibility of the analysis and the components of  $\mathbf{A}$  were found to be  $A_{ij} \pm 8\%$ .

Each sample was imaged at two planes, perpendicular to the neutral direction,  $x_3$ , and perpendicular to the flow direction,  $x_1$ . The samples were prepared by embedding quartered sections of the donut sample in epoxy, sanding to a specific plane depth, and then polishing to a final abrasive particle size of  $0.3 \mu\text{m}$  aluminum oxide ( $\text{Al}_2\text{O}_3$ ) following standardized techniques.<sup>36</sup> A schematic drawing of the polished planes and locations where the images were taken can be found in Fig. 5.2. A series of images were taken at three locations at distance of  $4.0, 6.25,$  and  $8.5 \text{ mm}$  from the outer edge denoted by PD-1, PD-2 and PD-3 respectively. Images in the neutral direction were only taken at one location denoted by PD-4 at a depth of  $4.0 \text{ mm}$  from the outer edge. PD-1 and PD-4 can be considered mutually perpendicular planes of different sections of the donut sample.

Images were taken using a Zeiss LSM510 confocal laser scanning microscope fitted with a 40x water immersion objective lens and a laser excitation wavelength of 543 nm. The final image was 230 x 230  $\mu\text{m}$  with a resolution of 1024 x 1024 pixels. For each sample, sequential images were taken from the bottom to the top in the direction of the velocity gradient and at two planes of depth. For PBT-30 the maximum penetration was found to be 8  $\mu\text{m}$ . This allowed for a full 3D description of the fiber orientation and removed the ambiguity associated with reflection microscopy techniques such as the Leeds method.<sup>37</sup> In the image the cross section of each fiber appeared as circles or ellipse-like shapes. To process the image, the circumference of each fiber intersection was traced by hand in power point to improve the contrast between the fibers and the matrix and converted to a binary image. A computer program was written combined with image analysis software in Matlab that measured the position of center of mass, the major and minor axis and local angle between the image axis and the major axis of the ellipse. The components of  $\mathbf{u}$  for each fiber were determined from the elliptical “footprint” at two cross sectional planes. A full description of this technique can be found elsewhere.<sup>20</sup>

With knowledge of the components of the vector  $\mathbf{u}$  for each fiber the tensors  $\mathbf{A}$  and  $\mathbf{A}_4$  were determined as follows:

$$A_{ij} = \frac{\sum (u_i u_j)_n F_n}{\sum F_n}, \quad F_n = \frac{M_n}{m_n} \quad (5.18)$$

$$A_{ijkl} = \frac{\sum (u_i u_j u_k u_l)_n F_n}{\sum F_n} \quad (5.19)$$

where  $F_n$  is a weighting factor for the  $n$ th fiber.<sup>38</sup> The weighting function is based on the probability of a 2D plane intersecting a fiber. Meaning, a fiber aligned perpendicular to the plane is more likely to be severed than one aligned parallel. Using the weighting function, the larger the aspect ratio of the ellipse, the more that fiber is weighted.

## 5.5 Results and Discussion

### 5.5.1 Rheology

**Linear viscoelastic behavior of neat PBT:** The linear viscoelastic behavior of the neat suspending medium including the magnitude of the complex viscosity,  $|\eta^*|$ , the storage modulus,  $G'$ , and loss modulus  $G''$  vs. frequency,  $\omega$ , can be seen in Fig. 5.3. This measurement was performed at 3% strain; a strain sweep at a frequency,  $\omega = 100$  rad/s confirmed that 3% was in the linear viscoelastic régime. The suspending medium does exhibit a storage modulus but its magnitude is small relative to the loss modulus and  $|\eta^*|$  shows little dependence on frequency over the range tested (0.1-100 rad/s). Hence the suspending medium behaves similar to a Newtonian fluid.

**First normal stress difference,  $N_1$ :** Many researchers have reported nonzero steady state first normal stress difference,  $N_1$ , values in Newtonian fluids that arise due to the presence of the fiber; not an enhancement to the elastic behavior of the suspending medium.<sup>39</sup> Literature also shows that the presence of glass fiber actually acts to impede the elastic behavior of the suspending medium.<sup>40</sup> To aid in the discussion of the contributing factors to the first normal stress growth function ( $N_1^+$ ),  $N_1$  is plotted as a

function of concentration in Fig. 5.4. The neat PBT exhibits a small  $N_1 \sim 100$  Pa at  $\dot{\gamma} = 1$   $s^{-1}$ . Interestingly, the addition of 4.07 wt% fiber causes a dramatic reduction in  $N_1$  to  $\sim 2.18$  Pa. This behavior coincides with literature in that the addition of fiber seems to dramatically impede the elastic component of the suspending medium.<sup>40</sup> From 4.07 to 30 wt%  $N_1$  appears to have a linear dependence on fiber volume fraction which is attributed to the fiber and not an enhancement to the elastic component of the suspending medium.

**Stress growth in startup flow:** The stress growth behavior of a suspension containing high aspect ratio particles is highly dependent on the orientation distribution of those particles.<sup>40</sup> In addition, the fiber orientation at any point subject to deformation is highly dependent on the initial orientation of the fiber which is a function of the systems deformation history. The average initial orientation of the PBT-30 donut samples is shown in Eq. (5.20),

$$\mathbf{A}|_{\gamma=0} = \begin{pmatrix} .5167 & - & - \\ .0753 & .0349 & - \\ .0584 & .0347 & .4484 \end{pmatrix} \quad (5.20)$$

The experimental data represented in Eq. (5.20) shows that the majority of the fibers are initially oriented in the flow,  $x_1$ , and neutral,  $x_3$ , directions with very few in the shear,  $x_2$ , direction. This is attributed to the deformation history given to the sample during compression molding of the sample disk and while it is loaded into the rheometer. Since all samples were prepared in the same way, it is assumed that they had a similar initial fiber orientation.

The experimental  $\eta^+$  measured during startup of flow as a function of shear rate in the range of  $\dot{\gamma} = 1-10 \text{ s}^{-1}$  for PBT-30 can be seen in Fig. 5.5 (a). The magnitude of  $\eta^+$  vs. strain in Fig. 5.5 (a) decreases by more than 20 % over the shear rate range tested but the neat suspending medium only exhibits a 3 % reduction in viscosity. It is not exactly clear why the shear thinning behavior of PBT-30 is larger than the matrix. When  $\eta^+$  is normalized by the steady state viscosity, depicted in Fig. 5.5 (b), the overshoot region of  $\eta^+/\eta$  scales in magnitude and strain for  $\dot{\gamma} > 1 \text{ s}^{-1}$  but for  $\dot{\gamma} = 1 \text{ s}^{-1}$ ,  $\eta^+/\eta$  exhibits a slightly enhanced behavior compared to higher shear rates. It is also not directly intuitive as to why  $\eta^+/\eta$  at  $\dot{\gamma} = 1 \text{ s}^{-1}$  does not scale in strain and magnitude with measurements at other shear rates.

$N_1^+/\dot{\gamma}$  vs. strain is depicted in Fig. 5.6 for PBT-30 as a function of shear rate in the range  $\dot{\gamma} = 1-10 \text{ s}^{-1}$  in startup of flow.  $N_1^+/\dot{\gamma}$  scales in magnitude and strain for  $\dot{\gamma} > 2 \text{ s}^{-1}$  but for  $\dot{\gamma} \leq 2 \text{ s}^{-1}$   $N_1^+/\dot{\gamma}$  exhibits an enhanced behavior compared to higher shear rates. Similar to  $\eta^+/\eta$  it is unclear why at low shear rates,  $\dot{\gamma} \leq 2 \text{ s}^{-1}$ ,  $N_1^+/\dot{\gamma}$  exhibits an enhanced value compared to higher shear rates.

**Flow reversal:**  $\eta^+$  vs. strain as a function of shear rate,  $\dot{\gamma} = 1-10 \text{ s}^{-1}$ , in flow reversal following startup of flow for PBT-30, can be seen in Fig. 5.7 (a). In addition, the shear stress growth behavior of PBT-30 at  $\dot{\gamma} = 6 \text{ s}^{-1}$  was added for direct comparison. Similar to the shear stress growth behavior in start up of flow,  $\eta^+$  exhibits a transient overshoot that decays toward a steady state. However, the overshoot grows at a slower rate, resulting in an overshoot peak that occurs at a strain of  $\sim 14.7$  more than twice the strain at which the peak occurs in  $\eta^+$  during start up of flow. In addition the magnitude of the

$\eta^+$  overshoot is smaller for the flow reversal experiment. For example, at  $\dot{\gamma} = 6 \text{ s}^{-1}$  the reverse overshoot maximum is roughly 6 % less than the initial overshoot peak. In addition,  $\eta^+$  decreases by more than 20 % over the  $\dot{\gamma}$  range tested. Figure 5.7 (b) depicts  $\eta^+$  normalized by the suspending medium viscosity,  $\eta$ , vs. strain. Interestingly,  $\eta^+/\eta$  scales in relatively well in magnitude and strain for all shear rates tested. In addition, the magnitude of  $\eta^+/\eta$  in flow reversal is very similar to the magnitude of  $\eta^+/\eta$  measured in startup of flow for  $\dot{\gamma} > 1 \text{ s}^{-1}$ .

The overshoot in  $\eta^+$  measured in flow reversal experiments for suspensions containing short glass fibers has been previously reported in literature.<sup>41</sup> It is attributed to “some” of the fibers which were not completely aligned in the flow direction, rotating in the opposite direction. It is proposed that only a fraction of the fibers change their steady state orientation because the magnitude of the overshoot is typically less than the initial overshoot. However, we find the magnitude of  $\eta^+/\eta$  in startup of flow and flow reversal to be of similar magnitude.

The first normal stress difference growth function normalized by the shear rate,  $N_1^+/\dot{\gamma}$ , as a function of  $\dot{\gamma}$  in flow reversal for PBT-30 can be seen in Fig. 5.8. In addition, the first normal stress difference growth behavior of PBT-30 at  $\dot{\gamma} = 6 \text{ s}^{-1}$  is added for direct comparison.  $N_1^+/\dot{\gamma}$  in flow reversal behaves very differently than in startup of flow.  $N_1^+$  initially exhibits a negative value that decreases to a minimum before increasing to a positive value where it then goes through a maximum that decays to steady state. Similarly to  $\eta^+$ , the difference between  $N_1^+/\dot{\gamma}$  measured at  $\dot{\gamma} = 1$  and  $10 \text{ s}^{-1}$  is more than 20 %.

### 5.5.2 Model Predictions

**Carreau-Yasuda model fit:** As previously discussed, the neat PBT behaved similarly to a Newtonian fluid. However it did exhibit a slight dependence on frequency over the range tested. To predict this change in viscosity the Carreau-Yasuda model was used, defined as,

$$\frac{\eta_0 - \eta_\infty}{\eta_0 - \eta_\infty} = \left[ 1 + (\lambda \dot{\gamma})^a \right]^{(n-1)/a} \quad (5.21)$$

where  $\eta_0$  is the zero-shear-rate viscosity,  $\eta_\infty$  is the infinite-shear-rate viscosity,  $\lambda$  is a time constant,  $n$  is the power-law exponent,  $a$  is a dimensionless parameter and  $\dot{\gamma}$  is taken equal to  $\omega$ . Using the Cox-Merz rule, Eq. (5.21) was fit to the magnitude of the complex viscosity over the frequency range of  $\omega = .1 - 100$  rad/s using a least squares approach, which can be seen in Fig. 5.3. The fit model parameters can be found in Table 1. For the subsequent model predictions the suspending medium viscosity,  $\eta_s$ , was predicted using Eq. (5.21).

**Numerical method and model fitting:** For the evolution of fiber orientation Eq. (5.7) was solved numerically using Gears implicit predictor-corrector method at a time step of 0.01 s. The model predictions were repeated at a time step of 0.001 s for the highest  $\dot{\gamma} = 10 \text{ s}^{-1}$  and the values were found to be within  $10^{-4}$ . Also, for Eqs. (5.9) and (5.10) the IBOF closure approximation was used to decouple the fourth-order tensor components. Subsequent model predictions use Eq. (5.7) for the fiber orientation

combined with Eqs. (5.9) and (5.10) to calculate the  $\eta^+$  and  $N_1^+$  respectively. Model predictions, including the rate of fiber reorientation and magnitude of the transient stresses, were found to be highly dependent on the initial conditions used in the model. As a result we were only able to determine unambiguous parameters with knowledge of the fiber orientation at some point in the simulation.<sup>42</sup>

Simulations of  $\eta^+$  using the experimentally determined initial conditions given in Eq. (5.20) predicts  $\eta^+$  to decrease from  $t = 0$ . We believe that this is a deficiency in the model, specifically Eq. (5.7). As a result the model predictions for startup of flow begin from  $\gamma = 7$ , the peak of the  $\eta^+$  which coincides with the experimentally determined maximum in the  $A_{12}$  component. The average orientation at  $\gamma = 7$  for PBT-30 was found to be,

$$\mathbf{A}|_{\gamma=7} = \begin{pmatrix} .5457 & - & - \\ .1378 & .0789 & - \\ -.0400 & -.0049 & .3754 \end{pmatrix} \quad (5.22)$$

Predictions of the stress growth functions in flow reversal begin from the steady state orientation of the startup of flow predictions.

In the model there are two fit parameters  $\alpha$  and  $C_1$  for the fiber orientation Eq. (5.7).  $\alpha$  determines the rate of fiber reorientation and  $C_1$  controls the steady state fiber orientation. For the stress growth functions there are two parameters  $c_1$  and  $N$ .  $c_1$  affects the magnitude of  $\eta^+$  only and  $N$  controls the magnitude of  $\eta^+$  and  $N_1^+$  as a result of the hydrodynamic drag of the fluid over the fiber. Since  $C_1$  controls the steady state fiber orientation the combination of  $C_1$ ,  $N$  and  $c_1$  is simultaneously fit to the peak of the  $\eta^+$

overshoot in addition to the steady state values of  $\eta^+$  and  $N_1^+$ .  $\alpha$  can then be fit to the transient stress growth behavior in the flow reversal the experiments i.e. the width of the  $\eta^+$  overshoot and the  $N_1^+$  undershoot.

The model fit to the stress growth behavior in startup of flow and flow reversal at  $\dot{\gamma} = 6 \text{ s}^{-1}$  can be seen in Figs. 5.9 (a) and (b) respectively; the fit parameters can be found in Table 2. In Fig. 5.9 (a) the model predictions show good agreement with the experimental results for  $\eta^+$  over the complete range of strain. In contrast the model severely under predicts the magnitude of  $N_1^+$  in the overshoot region. The model fits of  $\eta^+$  and  $N_1^+$  in flow reversal give good agreement with the experimental results over the complete range of strain which can be seen in Fig. 5.9 (b). By comparing the model fits of startup of flow and flow reversal following startup of flow the inability to fit the large  $N_1^+$  in startup of flow suggest that there is a high degree of direct fiber contact as the fibers rotate from mostly a planar orientation state to align themselves toward the flow direction that is not accounted for in the stress equation.

**Predictions:** We now discuss the model predictions of the flow reversal experiments at  $\dot{\gamma} = 1$  and  $10 \text{ s}^{-1}$  using the parameters fit at  $\dot{\gamma} = 6 \text{ s}^{-1}$ . In Fig. 5.10 (a), depicting  $\eta^+$  vs.  $\gamma$ , the model predictions show close agreement with the experimental results. At  $\dot{\gamma} = 1 \text{ s}^{-1}$   $\eta^+$  does predict the width of the experimental overshoot and the onset of steady state but deviates slightly at the overshoot maximum. At  $\dot{\gamma} = 10 \text{ s}^{-1}$  the predicted  $\eta^+$  shows good agreement to the overshoot maximum but the onset of steady state is enhanced compared to the experimental values. The difference in the model predictions at  $\dot{\gamma} = 1 \text{ s}^{-1}$  and  $\dot{\gamma} = 10 \text{ s}^{-1}$  is a result of the suspending medium viscosity determined by the Carreau-Yasuda model fit to the neat suspending medium. The discrepancy between the

model predictions and the experimental results for the onset of steady state of  $\eta^+$  at  $\dot{\gamma} = 10 \text{ s}^{-1}$  suggests the suspending medium viscosity is lower than the predicted value. This is a direct result of the enhanced shear thinning exhibited by the fiber suspension and not the suspending medium. The model predictions and experimental results for  $N_1^+$  at  $\dot{\gamma} = 1$  and  $10 \text{ s}^{-1}$  can be seen in Fig. 5.10 (b). Predictions at both  $\dot{\gamma} = 1$  and  $10 \text{ s}^{-1}$  show good agreement with the experimental results. However, in a similar fashion to  $\eta^+$  the model predictions of the onset of steady state for  $N_1^+$  at  $\dot{\gamma} = 10 \text{ s}^{-1}$  are slightly enhanced compared to the experimental results.

We have shown that model parameters can be determined by fitting to the transient stresses in startup of flow and flow reversal. To discuss the accuracy of the fit parameters Fig. 5.11 depicts the predictions of Eq. (5.7) compared to the experimentally determined fiber orientation in start up of flow at  $\dot{\gamma} = 1 \text{ s}^{-1}$ . The predictions show reasonable agreement with the experimentally determined fiber orientation. Especially at long strains which suggest that the  $C_1$  parameter is accurate. However, the model does over predict the rate of fiber reorientation suggesting the fit  $\alpha$  parameter is slightly too large.

To determine the accuracy of the parameters  $c_1$  and  $N$ , associated with the magnitude of the stresses, the fourth order tensor components in Eqs. (5.9) and (5.10) were calculated from the experimental fiber orientation. The peak value of  $\eta^+$  determined using the experimentally determined  $A_{1212}$  with the fit model parameters was found to be  $\eta^+ = 876 \text{ Pa.s}$  and the experimental  $\eta^+ = 854 \text{ Pa.s}$ . Interestingly, they are within experimental error. In contrast  $N_1^+$  determined using the experimentally determined  $A_{1112} - A_{2212}$  with the fit parameters was found to be  $N_1^+ = 386 \text{ Pa}$  and the experimental  $N_1^+ =$

1909 Pa. The discrepancy between the calculated  $N_1^+$  using the fit parameters and the measured  $N_1^+$  is attributed to fiber contact which the model does not account for. It also suggests that  $\eta^+$  can be described using simple hydrodynamic theory and that fiber contact contributes mostly to  $N_1^+$  while the fibers are reorienting.

The fit model parameters are listed in Table 1 along with the calculated values from theory or empirical expressions. Both the empirical expressions of Bay<sup>7</sup> and Phan-Thien et al.<sup>8</sup> give  $C_1$  values which differ by roughly an order of magnitude from the  $C_1$  we determined by fitting. The constant  $N$  calculated from the various theories defined in Eqs. (5.11) - (5.15) over predicted the magnitude  $N$  compared to the fit value. Lipscomb's theory predicted the closest  $N$  compared to the experimental and that of Phan-Thien and Graham<sup>32</sup> deviated the most.

## 5.6 Conclusions

In this work we show how model parameters may be determined by fitting predictions to the stress response to deformation of a short glass fiber composite fluid in a well defined flow field. The model used in this work does include the affects of direction fiber contact in the equation governing fiber motion, Eq. (5.7), through the Folgar-Tucker isotropic diffusion term and the strain reduction factor  $\alpha$  but does not include the contribution of fiber contact in the calculation of the stresses. As such the model was unable to represent the large overshoot exhibited by  $N_1^+$  during startup of flow where there is an inevitable high degree of direct fiber contact as the fibers rotate from a mostly planar orientation state to align themselves in the flow direction. However, we show that

$\eta^+$  in start up of flow and  $\eta^+$  and  $N_1^+$  in flow reversal following startup of flow can be explained using simple hydrodynamic theory. As a result we believe this approach can lead to obtaining unambiguous and accurate model parameters. In addition we believe that fitting can lead to more accurate parameters than those determined using the available theory or empirical relations. Also, fitting allows one to determine parameters in which no mathematical expression currently exists such as  $\alpha$ .

## **5.7 Acknowledgments**

The financial support for this work from the National Science Foundation and Department of Energy through Grant No. DMI-0521918 is gratefully acknowledged. We thank GE Plastics for supplying the materials used in this work.

## 5.8 References

1. Advani, S. G.; Sozer, E. M., *Process Modeling in Composites Manufacturing*. Marcel Dekker Inc.: New York, 2003.
2. Jeffery, G. B., The motion of ellipsoidal particles immersed in a viscous fluid. *Proc. R. Soc. Lond. A* **1922**, 102, 161-179.
3. Bretherton, F. P., The motion of rigid particles in a shear flow at low Reynolds number. *J. Fluid Mech.* **1962**, 14, 284-304.
4. Cox, R. G., The motion of long slender bodies in a viscous fluid. Part 2: Shear flow. *J. Fluid Mech.* **1971**, 45, 625-657.
5. Folgar, F. P.; Tucker, C. L., Orientation behavior of fibers in concentrated suspensions. *J. Rein. Plast. Comp.* **1984**, 3, 98-119.
6. Bay, R. S.; III, C. L. T., Fiber orientation in simple injection moldings. Part II. Experimental results. *Polym. Compos.* **1992**, 13, 332-341.
7. Bay, R. S. Fiber orientation in injection molded composites: A comparison of theory and experiment. Ph. D., University of Illinois Urbana-Champaign, 1991.
8. Phan-Thien, N.; Fan, X.-J.; Tanner, R. I.; Zheng, R., Folgar-Tucker constant for fiber suspension in a Newtonian fluid. *J. Non-Newt. Fluid Mech.* **2002**, 103, 251-260.
9. Hand, G. L., A theory of dilute suspensions. *Arch. Rational Mech. Anal.* **1961**, 7, 81-86.
10. Giesekus, H., Stromungen mit konstantem Geschwindigkeitsgradienten und die Bewegung von darin suspendierten Teilchen. Teil I: Raumliche Stromungen. *Rheol. Acta* **1962**, 2, 101-112.
11. Batchelor, G. K., The stress system in a suspension of force-free particles. *J. Fluid Mech.* **1970**, 41, (3), 545-570.
12. Cox, R. G.; Brenner, H., The rheology of a suspension of particles in a Newtonian fluid. *Chem. Eng. Sci.* **1971**, 26, 63-95.
13. Batchelor, G. K., The stress generated in a non-dilute suspension of elongated particles by pure straining motion. *J. Fluid Mech.* **1971**, 46, 813-829.
14. Evans, J. G. The flow of a suspension of force-free rigid rods in a Newtonian fluid. Ph. D., Cambridge University, 1975.
15. Dinh, S. M.; Armstrong, R. C., A rheological equation of state for semiconcentrated fiber suspensions. *J. Rheol.* **1984**, 28, (3), 207-227.
16. Shaqfeh, E. S. G.; Fredrickson, G. H., The hydrodynamic stress in a suspension of rods. *Phys. Fluids A* **1990**, 2, 7-25.
17. Zheng, R.; Kennedy, P.; Phan-Thien, N.; Fan, X.-J., Thermoviscoelastic simulation of thermally and pressure-induced stresses in injection moulding for the prediction of shrinkage and warpage for fiber-reinforced thermoplastics. *J. Non-Newt. Fluid Mech.* **1999**, 84, 159-190.
18. Sepehr, M.; Ausias, G.; Carreau, P. J., Rheological properties of short fiber filled polypropylene in transient shear flow. *J. Non-Newt. Fluid Mech.* **2004**, 123, 19-32.
19. Sepehr, M.; Carreau, P. J.; Grmela, M.; Ausias, G.; Lafleur, P. G., Comparison of rheological properties of fiber suspensions with model predictions. *J. Poly. Eng.* **2004**, 24, (6), 579-610.

20. Eberle, A. P. R. The Dynamic Behavior of a Concentrated Composite Fluid Containing Non-Brownian Glass Fibers in Rheometrical Flows. Virginia Tech, Blacksburg, 2008.
21. Eberle, A. P. R.; Baird, D. G.; Wapperom, P.; Velez-Garcia, G. M., Fiber Orientation Kinetics of a Concentrated Short Glass Fiber Suspension in Startup of Simple Shear Flow. **2008**.
22. Advani, S. G.; Tucker, C. L., The use of tensors to describe and predict fiber orientation in short fiber composites. *J. Rheol.* **1987**, 31, (8), 751-784.
23. Bird, R. B.; Armstrong, R. C.; Hassager, O., *Dynamics of Polymeric Liquids*. John Wiley & Sons, Inc.: New York, 1987; Vol. 1.
24. Huynh, H. M. Improved Fiber Orientation Predictions for Injection-Molded Composites. University of Illinois at Urbana-Champaign, 2001.
25. Doi, M.; Edwards, S. F., *The Theory of Polymer Dynamics*. Oxford University Press: New York, 1988.
26. Cintra, J. S.; III, C. L. T., Closure approximations for flow-induced fiber orientation. *J. Rheol.* **1995**, 39, (1095-1122).
27. Chung, D. H.; Kwon, T. H., Improved model of orthotropic closure approximation for flow induced fiber orientation. *Polym. Compos.* **1999**, 22, (5), 636-649.
28. Advani, S. G.; Tucker, C. L., Closure approximations for three-dimensional structure tensors. *J. Rheol.* **1990**, 34, (3), 367.
29. Chung, D. H.; Kwon, T. H., Fiber orientation in the processing of polymer composites. *Korean-Australian Rheol. J.* **2002**, 14, (4), 175-188.
30. Lipscomb, G. G.; Denn, M. M.; Hur, D. U.; Boger, D. V., The flow of fiber suspensions in complex geometries. *J. Non-Newt. Fluid Mech.* **1988**, 26, (3), 297-325.
31. Einstein, A., A new determination of molecular dimensions. *Ann Phys* **1906**, 19, 289-306.
32. Phan-Thien, N.; Graham, A. L., A new constitutive model for fiber suspensions. *Rheol. Acta* **1991**, 30, 44-57.
33. Botelho, G.; Queiros, A.; Liberal, S.; Gijsman, P., Studies on thermal and thermo-oxidative degradation of poly(ethylene terephthalate) and poly(butylene terephthalate). *Polym Degrad Stab* **2001**, 74, (10), 39-48.
34. Macosko, C. W., *Rheology Principles, Measurements, and Applications*. Wiley-VCH: New York, 1994.
35. Lee, Y.; Lee, S.; Youn, J.; Chung, K.; Kang, T., Characterization of fiber orientation in short fiber reinforced composites with an image processing technique. **2002**, 6, (2), 65.
36. Sawyer, L. C.; Grubb, D., *Polymer Microscopy*. 2nd ed.; Springer: 1995.
37. Hine, P. J.; Davidson, N.; Duckett, R. A.; Ward, I. M., Measuring the fibre orientation and modeling the elastic properties of injection-moulded long-glass-fibre-reinforced nylon. *Comp. Sci. Tech.* **1993**, 53, 125-131.
38. Bay, R. S.; Tucker, C. L., Stereological measurement and error estimates for three dimensional fibre orientation. *Poly. Eng. Sci.* **1992**, 32, 240-253.
39. Zirnsak, M. A.; Hur, D. U.; Boger, D. V., Normal stresses in fibre suspensions. *J. Non-Newt. Fluid Mech.* **1994**, 54, 153-193.

40. Eberle, A. P. R.; Baird, D.; Wapperom, P., Rheology of non-Newtonian fluids containing glass fibers: A review of experimental literature. *Ind. Eng. Chem. Res.* **2008**, 47, (10), 3470-3488.
41. Sepehr, M.; Carreau, P. J.; Moan, M.; Ausias, G., Rheological properties of short fiber model suspensions. *J. Rheol.* **2004**, 48, (5), 1023-1048.
42. Eberle, A. P. R.; Baird, D. G.; Wapperom, P.; Velez-Garcia, G., Obtaining Reliable Transient Rheological Data on Concentrated Short Fiber Suspensions using a Rotational Rheometer. *Submitted to J. Rheol.* **2008**.

**Table 5.1.** Carreau-Yasuda model parameters for neat PBT.

$\eta_0$ (Pa.s)	$\eta_\infty$ (Pa.s)	$\lambda$ (s)	$n$	$a$
428.2	0	96.7	0.973	5

**Table 5.2.** Suspension theory fit and calculated model parameters.

	$\alpha$	$C_1$	$N$	$c_1$
Fit to startup flow at $\dot{\gamma} = 6 \text{ s}^{-1}$	0.4	0.002	27	0.4
Bay <sup>7</sup>				
Eq. (5.5)		.00052		
Phan-Thien et al. <sup>8</sup>				
Eq. (5.6)		0.0202		
Lipscomb et al. <sup>30</sup>				
Eq. (5.11)			119.2	
Batchelor <sup>13</sup>				
Eq. (5.12)			128.1	2
Dinh and Armstrong <sup>15</sup>				
Eq. (5.13)			184.4 (aligned)	
Shaqfeh and Fredrickson <sup>16</sup>			653.7 (random)	
Eq. (5.14)			434.4 (aligned)	
Phan-Thien and Graham <sup>32</sup>				
Eq. (5.15)			21, 251.7	

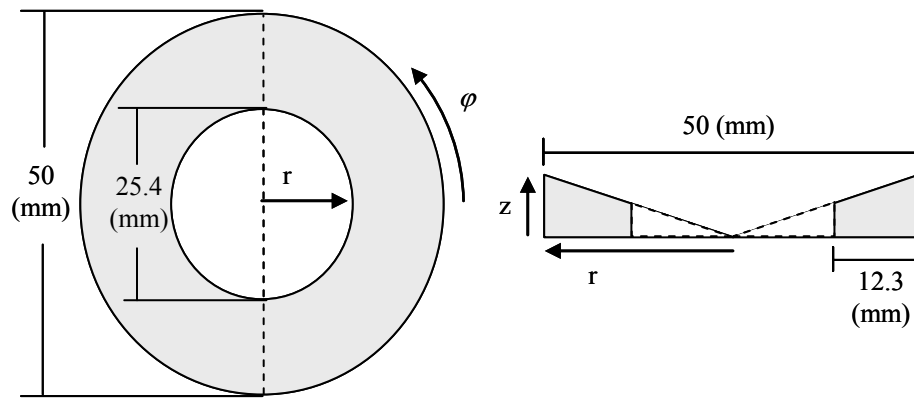


**Figure 5.1.** Schematic drawing and cross-sectional profile of the donut sample.

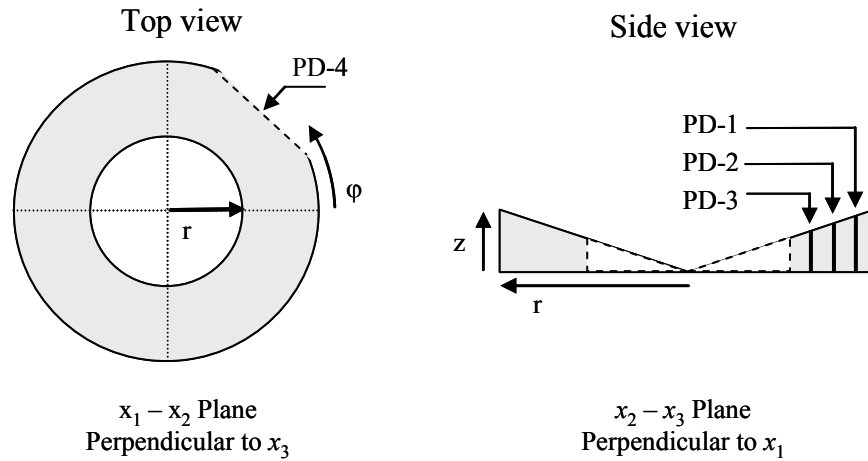


**Figure 5.2.** Schematic drawing of the polished and imaged planes perpendicular to the neutral,  $x_3$ , and flow,  $x_1$ , directions. The  $x_2 - x_3$  plane images were taken of the sample at a distance of 4.0, 6.25, and 8.5 mm from the outer edge denoted by PD-1, PD-2, PD-3. For the  $x_1 - x_2$  plane, images were taken in one location denoted by PD-4. In all locations images were taken through the entire height of the sample cross-sections.

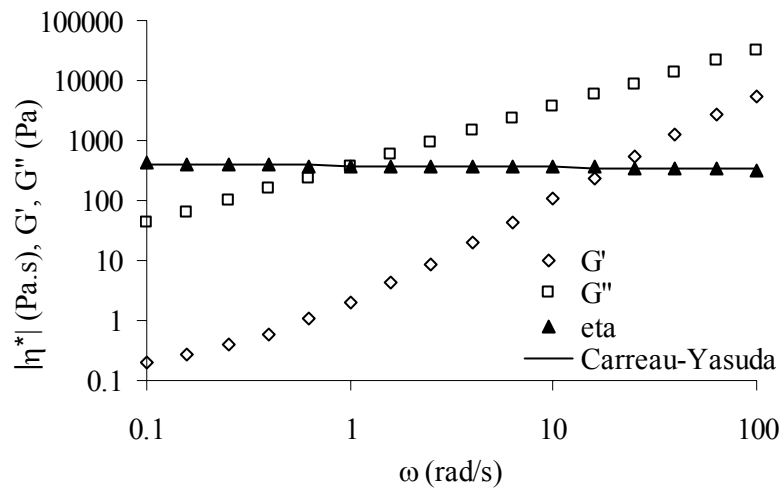


**Figure 5.3.** The linear viscoelastic behavior of the neat PBT, and the Carreau-Yasuda model fit to the magnitude of the complex viscosity. Carreau-Yasuda parameters can be found in Table 5.1.

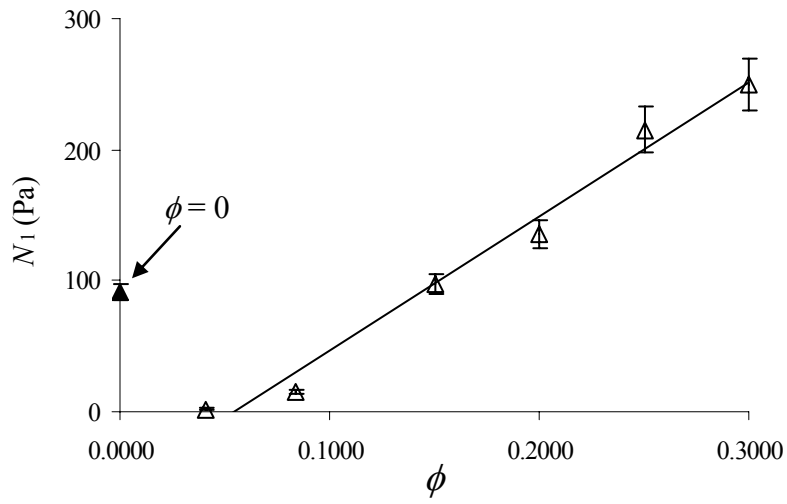
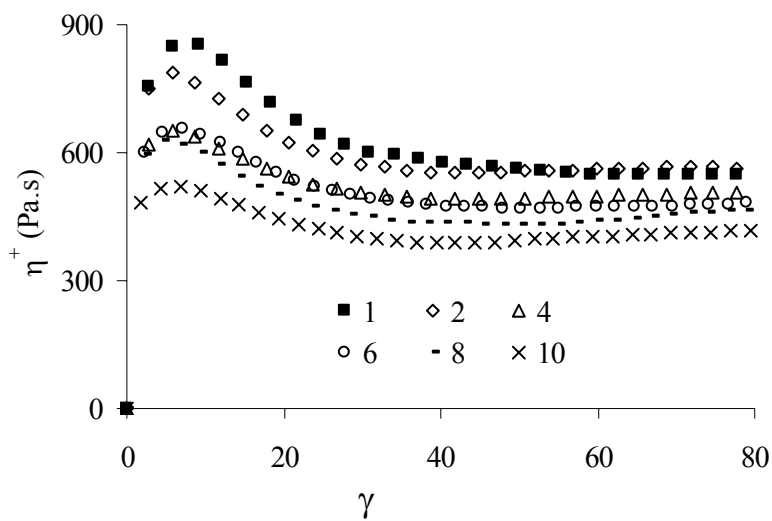
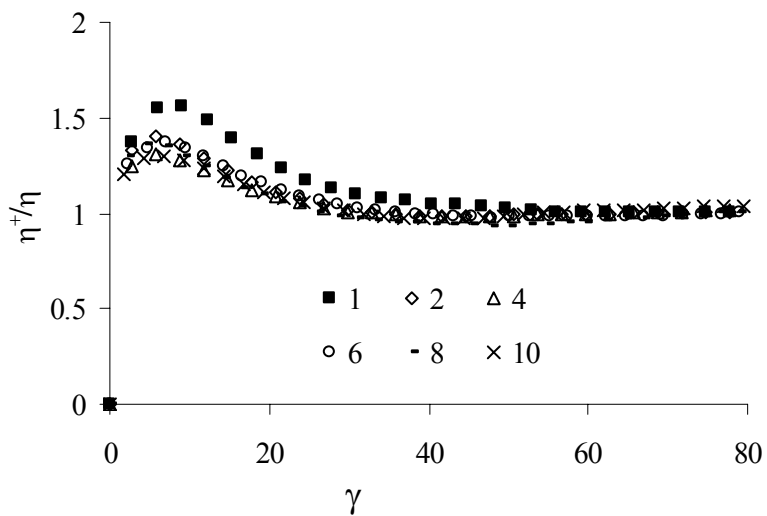


**Figure 5.4.**  $N_1$  as a function of fiber volume fraction at  $\dot{\gamma} = 1 \text{ s}^{-1}$ .



(a)



(b)

**Figure 5.5.** Shear stress growth coefficient,  $\eta^+$ , as a function of shear rate  $\dot{\gamma} = 1-10 \text{ s}^{-1}$ . (a)  $\eta^+$  (b)  $\eta^+/\eta$  where  $\eta$  is the quasi-steady state viscosity taken at 200 strain units. The numbers in the legend relate to the different shear rates.

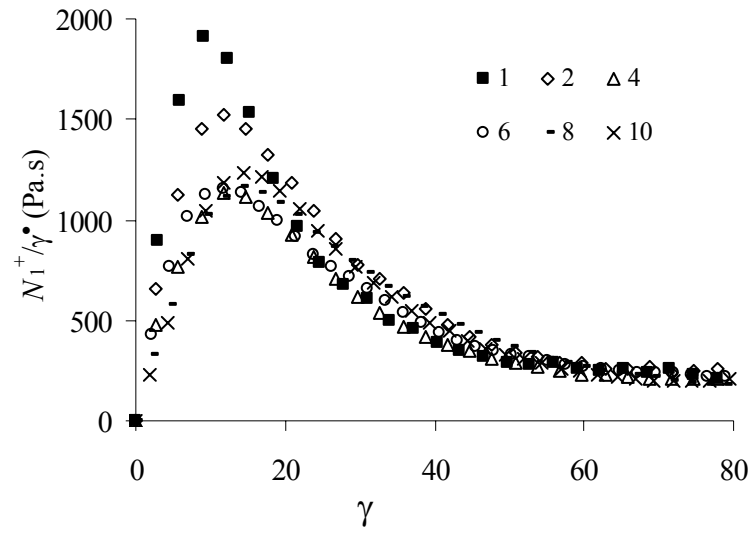
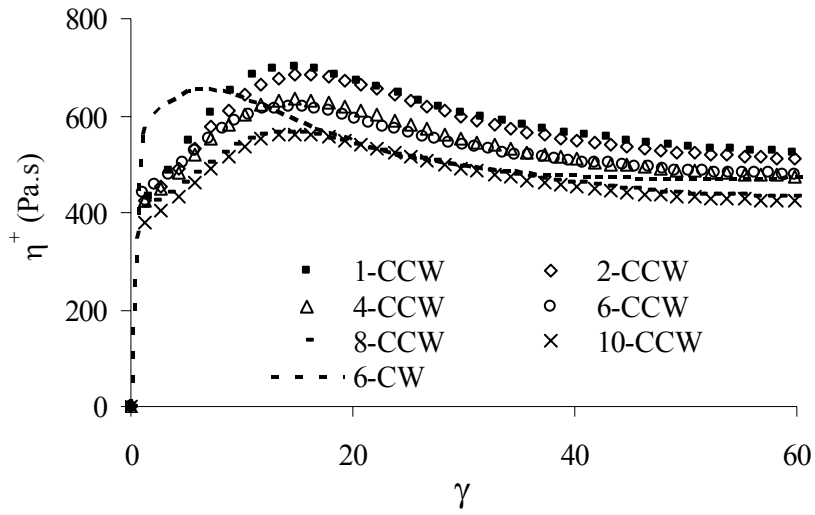
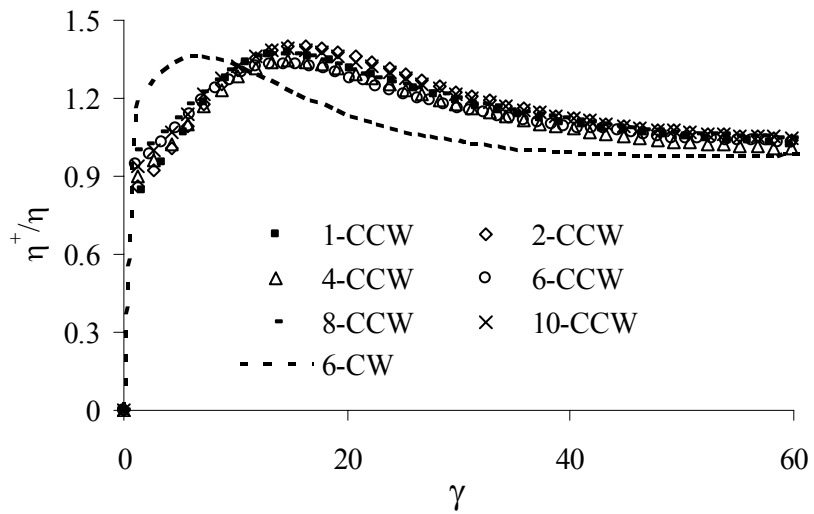


**Figure 5.6.** First normal stress difference growth function,  $N_1^+$ , normalized by the shear rate,  $\dot{\gamma}$ , as a function of shear rate  $\dot{\gamma} = 1-10 \text{ s}^{-1}$ . The numbers in the legend relate to the different shear rates.



(a)



(b)

**Figure 5.7.** Shear stress growth coefficient,  $\eta^+$ , in flow reversal following startup of flow as a function of shear rate  $\dot{\gamma} = 1-10 \text{ s}^{-1}$ . (a)  $\eta^+$  (b)  $\eta^+/\eta$  where  $\eta$  is the quasi-steady state viscosity taken at 200 strain units. The numbers in the legend relate to the different shear rates. 6-CW relates to the stress growth behavior in the clockwise direction (CW) previous to the flow reversal in the counter clockwise direction (CCW).

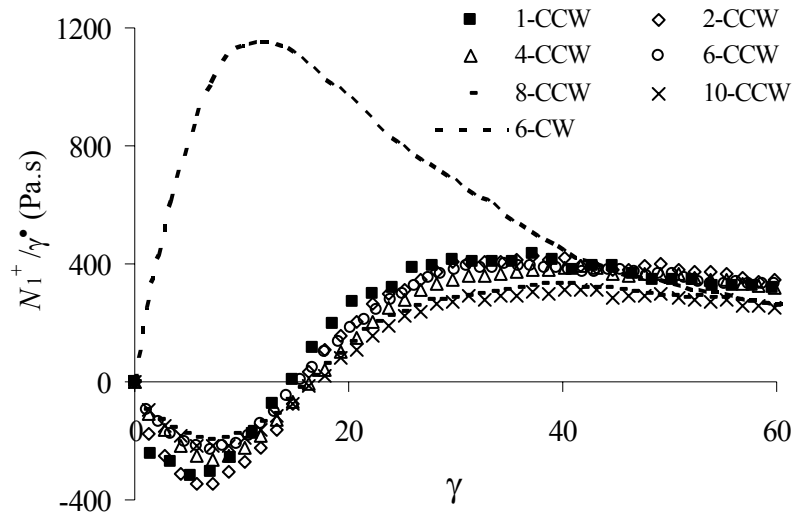
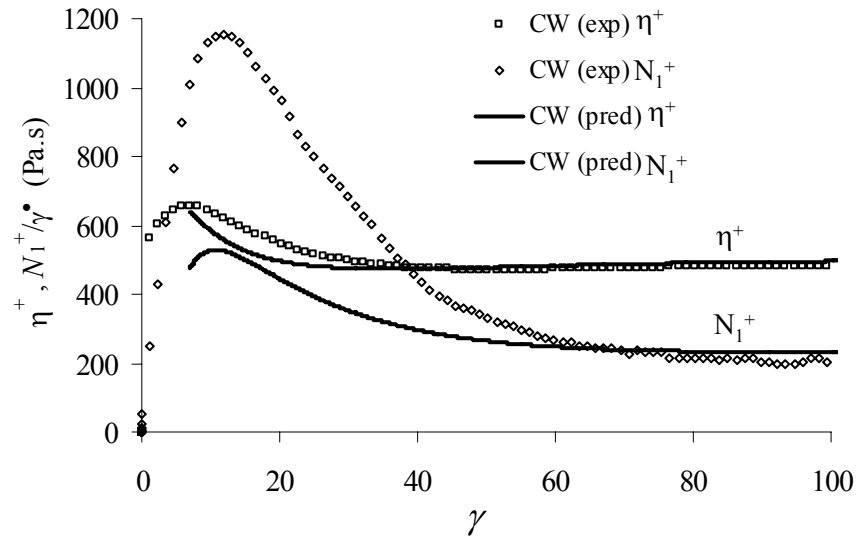
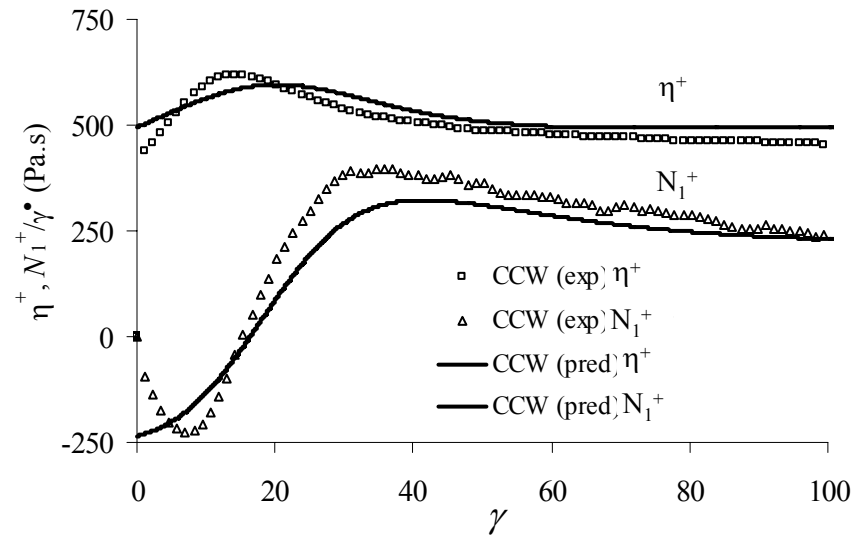


**Figure 5.8.** First normal stress difference growth function,  $N_1^+$ , normalized by the shear rate,  $\dot{\gamma}$ , in flow reversal following startup of flow as a function of shear rate  $\dot{\gamma} = 1-10 \text{ s}^{-1}$ . The numbers in the legend relate to the different shear rates. 6-CW relates to the stress growth behavior in the clockwise direction (CW) previous to the flow reversal in the counter clockwise direction (CCW).

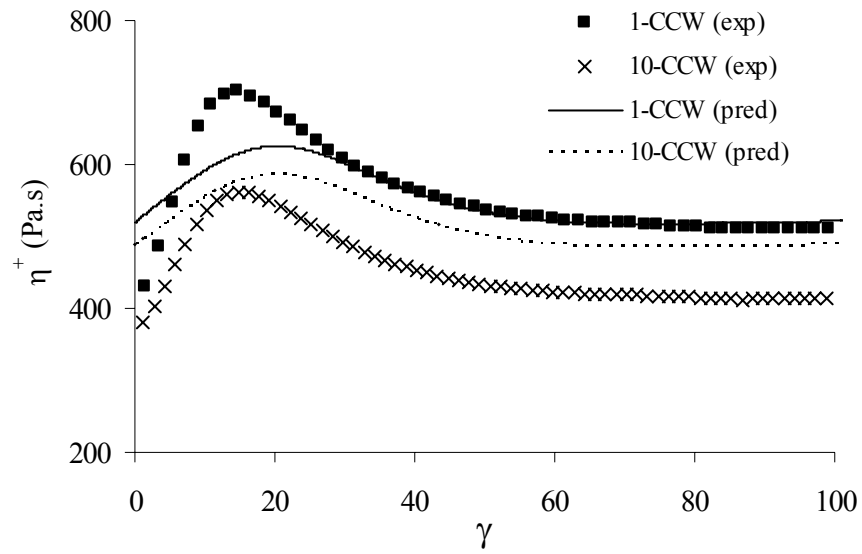


(a)

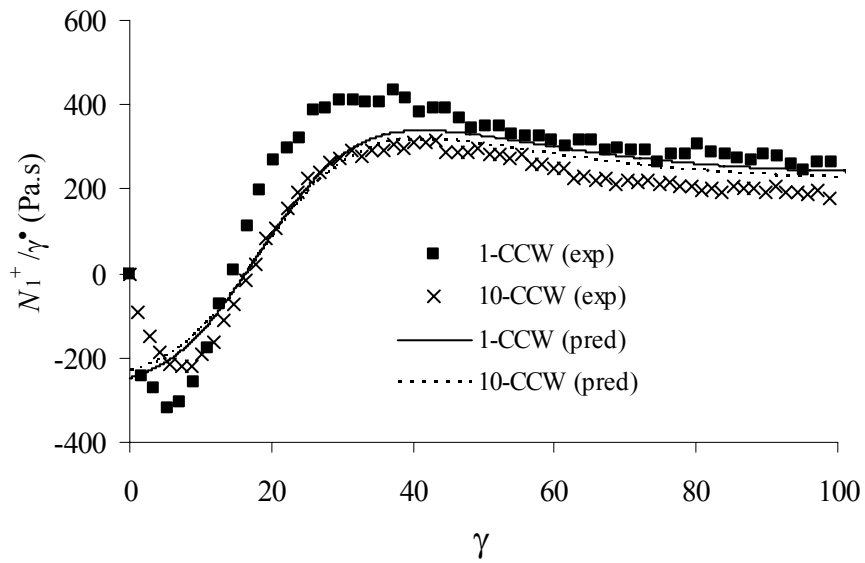


(b)

**Figure 5.9.** Experimental results and model predictions of the stress growth functions in (a) startup of flow, (b) flow reversal following startup of flow at  $\dot{\gamma} = 6 \text{ s}^{-1}$ . Model parameters can be found in Tables 5.1 and 5.2.



(a)



(b)

**Figure 5.10.** Experimental results and model predictions of the stress growth functions in flow reversal following startup of flow. (a) The shear stress growth coefficient,  $\eta^+$ , and (b) the first normal stress growth function,  $N_1^+$ . Model parameters can be found in Tables 5.1 and 5.2.

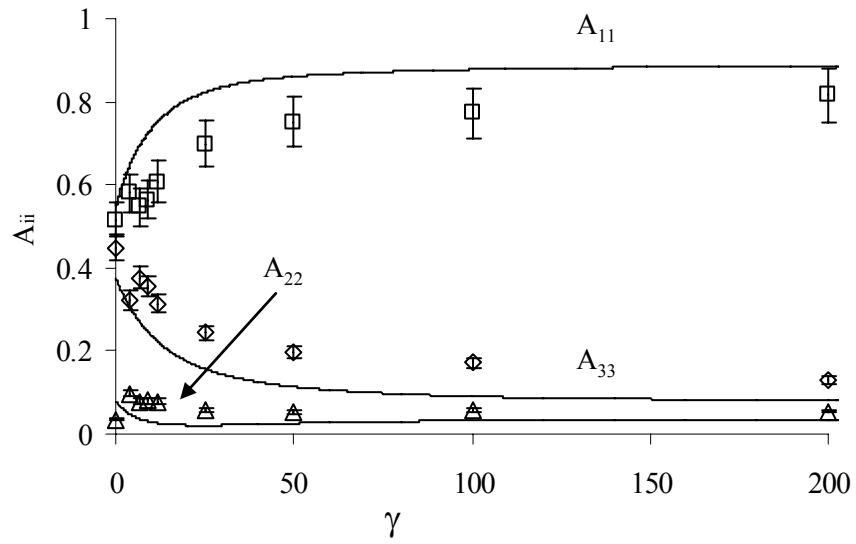


**Figure 5.11.** Experimental and predicted fiber orientation represented through the  $A_{ii}$  components in startup of simple shear flow at  $\dot{\gamma} = 1 \text{ s}^{-1}$ . The lines represent the model predictions of Eq. (5.7). Model parameters can be found in Table 5.2.

## **6.0 Recommendations**

## 6.0 Recommendations

### 6.1 Material Considerations

**Extensional Rheology:** The literature pertaining to the extensional rheology or the stress response to deformation in shear-free flows of short glass fiber-filled fluids is extremely limited. This is an indication of the complexity relating to measuring this property. We were unable to measure the shear-free flow material functions for the PBT class of glass fiber suspensions. In addition, we attempted to measure the shear-free flow material functions of a polypropylene class of short glass fiber composite fluids with no success. This was a direct result of a phenomenon termed “necking” where the sample, deformed in a Meisner-type extensional rheometer, would not uniformly elongate leading to premature rupture. The recommendation is to begin with a polymer known to have excellent shear-free flow deformation characteristics. This is common in polymers who exhibit strain hardening behavior. An example would be a highly branched polyethylene (PE). One could then compound PE and glass fiber to form various concentrations beginning with very low concentrations, in the dilute regime and incrementally increase the concentration.

**Fiber orientation analysis:** The advantage to using confocal laser microscopy to analyze fiber orientation is it allows one to focus into the depth of the sample. The disadvantage is the sample has to auto fluoresce. Polybutylene terephthalate does auto fluoresce, but unfortunately has a high degree of crystallinity limiting the depth of penetration. The recommendation is to use a matrix that auto fluoresces but either does

not crystallize or has a slow rate of crystallization allowing the sample to be cooled below the matrix melt temperature before significant crystallization occurs. This would increase the depth of penetration and allow for a better characterization of the fiber orientation.

In this research we only studied the dynamic behavior of a composite melt subject to shear deformation at a shear rate of  $1 \text{ s}^{-1}$ . Since the transient behavior has been shown to strain scale this is sufficient to base conclusions on the stress growth relationship to fiber microstructure. However, steady state rheological measurements at different shear rates suggest that the steady state fiber orientation is a function of shear rate. It is believed that higher shear rates impart a higher degree of fiber orientation in the flow direction. This has not been experimentally confirmed. The recommendation is to characterize the steady state fiber orientation as a function of shear rate.

## **6.2 Rheological Characterization**

**Shear Rheology:** A significant contribution of this research is the description of an approach to accurately characterizing the transient rheological behavior of short glass fiber-filled polymeric fluids using a cone-and-plate rheometer combined with a donut shaped sample (CP-D). This approach is believed to result in an accurate measure of the “true” stress response to deformation. A complete discussion of this can be found in chapter 3.0. However, the analysis does not include the affect that curvilinear stream lines in the rotational rheometer might have on the measurements. The recommendation is to compare the measured material functions using the CP-D to that measured using a

sliding plate rheometer. The sliding plate rheometer imposes rectilinear streamlines with a homogeneous velocity gradient.

A conclusion of this research is that fiber contact acts to reduce the rate of fiber reorientation compared to theory. However, little is known about the reduced rate of fiber reorientation. For example, how does it depend on fiber concentration, aspect ratio, and orientation distribution? The dependence on fiber concentration and aspect ratio could be studied with a well defined set of materials. However, the dependence of orientation distribution could be accomplished with a well defined set of rheological tests using different initial fiber orientations. The recommendation is to make a series of samples of different initial fiber orientations including: aligned in the direction of velocity gradient, aligned in the neutral direction, random in the plane, and completely random. Stress growth measurements during startup of simple shear flow would allow for conclusions relating to the rate of fiber reorientation as a function of fiber orientation and possibly lead to an empirical strain reduction equation that is a function of fiber orientation distribution.

Using the conventional rotational rheometers, transient measurements are limited to low shear rates, roughly less than  $10 \text{ s}^{-1}$ . However processing applications can reach shear rates on the order of  $10^4$  or higher. The steady state behavior can be studied using a capillary rheometer, but this type of device is incapable of measuring the transient rheology. It is of practical interest to understand the transient rheological behavior of short glass fiber-filled suspensions at high shear rates. The recommendation is to use a sliding plate rheometer to study the rheological behavior of short glass fiber-filled polymeric fluids at high shear rates.

**Elongational Rheology:** During the course of this work we only attempted to measure the extensional rheology using a Meissner-type extensional rheometer with cylindrical samples. McGrady and Baird proposed a novel approach in where a polymer which undergoes necking is encapsulated in another polymer that exhibits excellent elongational characteristics. The recommendation is to try the encapsulation approach with short glass fiber-filled suspension in which the shell could be the neat matrix. There are two other recommendations for measuring the elongational behavior of short glass fiber filled polymers that could lead to promising results. One would be to try the SER. The other would be to try lubricated squeezing flow.

### **6.3 Modeling**

A major deficiency in current fiber suspension theory is the inability to account for fiber contact in the stress equations. This is very evident in the model predictions of the transient first normal stress difference in startup of flow. The recommendation is to explore the possibility of incorporating fiber contact into the bulk stress equations.

## **Appendix A. Rheological Data**

## Appendix A. Rheological Data

### A.1 Neat PBT

A.1.1 Frequency sweep data at 3 strain %.

Rheometer fixture: 25mm cone-and-plate  
Temperature: 260 °C

$\omega$ (rad/s)	$G'$ (Pa)	$G''$ (Pa)	$ \eta^* $ (Pa.s)
1.000E-01	2.045E-01	4.204E+01	4.204E+02
1.585E-01	2.794E-01	6.320E+01	3.988E+02
2.512E-01	4.000E-01	9.818E+01	3.909E+02
3.981E-01	6.000E-01	1.532E+02	3.847E+02
6.310E-01	1.100E+00	2.389E+02	3.786E+02
1.000E+00	2.047E+00	3.729E+02	3.729E+02
1.585E+00	4.200E+00	5.866E+02	3.701E+02
2.512E+00	8.257E+00	9.271E+02	3.691E+02
3.981E+00	2.000E+01	1.456E+03	3.659E+02
6.310E+00	4.183E+01	2.292E+03	3.633E+02
1.000E+01	1.078E+02	3.603E+03	3.605E+02
1.585E+01	2.384E+02	5.649E+03	3.567E+02
2.512E+01	5.476E+02	8.831E+03	3.522E+02
3.981E+01	1.221E+03	1.374E+04	3.465E+02
6.310E+01	2.620E+03	2.116E+04	3.379E+02
1.000E+02	5.427E+03	3.202E+04	3.248E+02

A.1.2 Stress growth, startup of flow at  $\dot{\gamma} = 1 \text{ s}^{-1}$

Rheometer fixture: 50 mm cone-and-plate

Temperature: 260 °C

Time (s)	$\eta^+$ (Pa.s)	$N_1^+$ (Pa)	Time (s)	$\eta^+$ (Pa.s)	$N_1^+$ (Pa)
0.00	0.00	0.00	54.88	381.92	99.22
1.13	395.57	93.19	56.13	381.61	86.91
2.38	393.47	79.58	57.38	382.01	81.41
3.63	391.07	73.28	58.63	381.88	87.37
4.88	387.64	78.39	59.88	381.42	80.69
6.13	385.04	82.01	61.13	381.06	88.54
7.38	384.42	100.81	62.38	380.46	85.11
8.63	382.92	80.80	63.63	380.15	94.07
9.88	382.17	91.89	64.88	380.38	89.98
11.13	381.96	81.74	66.13	379.77	99.16
12.38	381.21	90.87	67.38	379.48	102.30
13.63	382.16	91.65	68.63	379.24	87.50
14.88	382.87	94.73	69.88	378.49	91.17
16.13	382.95	93.27	71.13	378.58	77.16
17.38	383.55	98.26	72.38	378.65	88.84
18.63	383.50	109.85	73.63	378.37	88.40
19.88	383.78	89.19	74.88	378.35	95.19
21.13	383.94	90.24	76.13	377.79	100.48
22.38	382.32	101.99	77.38	377.98	98.24
23.63	384.18	115.03	78.63	377.91	81.97
24.88	383.86	113.02	79.88	377.64	69.34
26.13	383.54	102.21	81.13	377.94	86.53
27.38	383.97	97.71	82.38	377.51	77.25
28.63	385.08	114.31	83.63	377.07	75.14
29.88	385.32	105.19	84.88	376.84	79.28
31.13	385.08	109.43	86.13	376.33	83.94
32.38	384.38	110.92	87.38	376.01	87.84
33.63	384.01	110.84	88.63	376.25	91.45
34.88	383.82	111.21	89.88	375.75	97.87
36.13	383.26	122.94	91.13	375.70	112.63
37.38	383.71	121.71	92.38	375.89	106.57
38.63	383.35	111.20	93.63	375.46	90.62
39.88	382.92	83.74	94.88	375.94	69.94
41.13	383.66	89.17	96.13	375.98	87.17
42.38	383.07	79.05	97.38	376.10	82.62
43.63	383.16	86.36	98.63	376.72	73.74
44.88	383.46	88.51	99.88	376.57	86.66
46.13	383.15	98.92	100.56	376.90	103.46
47.38	383.35	99.27			
48.63	383.19	103.02			
49.88	382.65	101.96			
51.13	382.75	103.91			
52.38	382.40	88.69			
53.63	382.60	88.39			

A.1.3 Stress growth, startup of flow at  $\dot{\gamma} = 1 \text{ s}^{-1}$

Rheometer fixture: 50 mm cone-and-plate with donut sample

Temperature: 260 °C

Time (s)	$\eta^+$ (Pa.s)	$N_1^+$ (Pa)	Time (s)	$\eta^+$ (Pa.s)	$N_1^+$ (Pa)
0.00	0.00	0.00	65.75	382.84	382.84
1.25	387.47	387.47	67.25	382.76	382.76
2.75	386.71	386.71	68.75	382.63	382.63
4.25	385.29	385.29	70.25	383.32	383.32
5.75	383.47	383.47	71.75	383.20	383.20
7.25	381.59	381.59	73.25	383.00	383.00
8.75	379.35	379.35	74.75	383.58	383.58
10.25	377.61	377.61	76.25	383.95	383.95
11.75	376.48	376.48	77.75	383.56	383.56
13.25	375.32	375.32	79.25	383.85	383.85
14.75	374.27	374.27	80.75	384.13	384.13
16.25	374.12	374.12	82.25	384.37	384.37
17.75	374.28	374.28	83.75	384.58	384.58
19.25	374.35	374.35	85.25	384.71	384.71
20.75	374.67	374.67	86.75	384.87	384.87
22.25	375.47	375.47	88.25	384.90	384.90
23.75	375.50	375.50	89.75	384.69	384.69
25.25	375.36	375.36	91.25	384.15	384.15
26.75	376.06	376.06	92.75	384.21	384.21
28.25	375.99	375.99	94.25	384.31	384.31
29.75	376.46	376.46	95.75	383.21	383.21
31.25	376.41	376.41	97.25	383.24	383.24
32.75	376.40	376.40	98.75	383.40	383.40
34.25	376.88	376.88	100.25	383.00	383.00
35.75	377.19	377.19			
37.25	377.51	377.51			
38.75	378.19	378.19			
40.25	378.85	378.85			
41.75	379.06	379.06			
43.25	379.33	379.33			
44.75	380.09	380.09			
46.25	380.19	380.19			
47.75	381.00	381.00			
49.25	381.26	381.26			
50.75	381.27	381.27			
52.25	381.61	381.61			
53.75	381.98	381.98			
55.25	381.58	381.58			
56.75	381.69	381.69			
58.25	381.98	381.98			
59.75	381.87	381.87			
61.25	381.98	381.98			
62.75	382.40	382.40			
64.25	382.77	382.77			

## A.2 Short glass fiber-filled PBT, 4.07 wt%

### A.2.1 Stress growth, startup of flow at $\dot{\gamma} = 1 \text{ s}^{-1}$

Rheometer fixture: 25 mm parallel plate, Gap = 1.0 mm

Temperature: 260 °C

Time (s)	$\eta^+$ (Pa.s)	$N_1^+ - N_2^+$ (Pa)	Time (s)	$\eta^+$ (Pa.s)	$N_1^+ - N_2^+$ (Pa)
0.00	0.00	0.00	70.94	395.69	121.63
1.56	408.01	135.36	72.81	395.58	126.05
3.44	408.49	140.95	74.69	395.39	124.01
5.31	408.95	137.43	76.56	395.42	114.02
7.19	408.55	128.99	78.44	395.38	122.66
9.06	408.30	129.78	80.31	395.53	117.65
10.94	406.86	125.21	82.19	395.45	126.30
12.81	405.96	130.65	84.06	395.34	128.18
14.69	405.33	137.18	85.94	395.27	125.53
16.56	404.54	140.45	87.81	395.18	122.19
18.44	403.56	148.27	89.69	395.55	117.13
20.31	403.02	137.29	91.56	395.50	119.75
22.19	402.24	145.75	93.44	395.32	121.68
24.06	401.41	144.68	95.31	394.86	126.70
25.94	401.02	150.90	97.19	394.87	120.45
27.81	400.41	145.92	99.06	394.84	119.05
29.69	399.71	144.81	100.94	394.74	115.59
31.56	399.23	142.33			
33.44	398.81	139.12			
35.31	398.63	136.90			
37.19	398.05	141.70			
39.06	398.02	135.11			
40.94	397.60	138.73			
42.81	397.21	134.27			
44.69	396.89	147.61			
46.56	396.57	138.39			
48.44	396.71	135.55			
50.31	396.42	126.95			
52.19	396.08	128.65			
54.06	395.79	131.77			
55.94	395.58	125.53			
57.81	396.05	121.43			
59.69	395.94	120.00			
61.56	395.76	120.25			
63.44	395.47	123.50			
65.31	395.69	127.81			
67.19	395.79	122.74			
69.06	395.95	120.04			

A.2.2 Stress growth, startup of flow at  $\dot{\gamma} = 1 \text{ s}^{-1}$

Rheometer fixture: 50 mm cone-and-plate with donut sample

Temperature: 260 °C

Time (s)	$\eta^+$ (Pa.s)	$N_1^+$ (Pa)	Time (s)	$\eta^+$ (Pa.s)	$N_1^+$ (Pa)	Time (s)	$\eta^+$ (Pa.s)	$N_1^+$ (Pa)
0.00	0.00	0.00	37.75	385.83	21.24	75.75	388.19	5.89
0.75	421.32	26.64	38.75	385.89	15.08	76.75	388.00	5.40
1.75	420.36	52.55	39.75	386.06	8.92	77.75	388.05	0.95
2.75	417.67	110.58	40.75	386.05	6.71	78.75	387.78	2.84
3.75	414.14	155.64	41.75	386.23	5.36	79.75	387.93	5.12
4.75	410.57	186.18	42.75	386.53	4.90	80.75	387.89	4.81
5.75	406.14	207.29	43.75	386.18	1.80	81.75	387.94	1.39
6.75	402.56	212.09	44.75	386.37	2.95	82.75	387.69	0.32
7.75	399.29	209.88	45.75	386.31	2.59	83.75	387.80	5.55
8.75	396.47	206.61	46.75	386.64	2.31	84.75	387.78	4.82
9.75	393.75	204.11	47.75	386.54	2.74	85.75	387.74	6.74
10.75	390.84	200.65	48.75	386.62	0.83	86.75	387.60	4.71
11.75	388.55	195.33	49.75	386.42	2.45	87.75	387.44	4.22
12.75	386.56	189.54	50.75	386.53	6.46	88.75	387.64	0.74
13.75	385.14	177.39	51.75	386.62	3.58	89.75	387.55	1.95
14.75	383.37	164.14	52.75	386.67	3.65	90.75	387.49	3.81
15.75	382.63	152.96	53.75	386.59	2.39	91.75	387.38	1.75
16.75	382.02	136.82	54.75	386.51	4.29	92.75	387.47	2.22
17.75	381.84	115.28	55.75	386.64	3.06	93.75	387.38	0.91
18.75	382.25	94.43	56.75	386.65	5.13	94.75	387.41	4.30
19.75	382.92	75.85	57.75	386.93	4.67	95.75	387.43	4.29
20.75	383.42	62.94	58.75	386.71	3.51	96.75	387.58	2.55
21.75	383.84	49.96	59.75	387.27	2.12	97.75	387.46	-0.90
22.75	384.21	42.85	60.75	386.90	0.58	98.75	387.41	2.57
23.75	384.54	38.02	61.75	387.10	0.85	99.75	387.68	4.38
24.75	384.94	37.42	62.75	387.21	1.32	100.75	387.60	5.41
25.75	385.30	36.92	63.75	387.38	3.90			
26.75	385.53	42.96	64.75	387.55	1.44			
27.75	385.46	43.99	65.75	387.41	-0.99			
28.75	385.61	44.44	66.75	387.58	-0.16			
29.75	385.58	44.76	67.75	387.58	1.16			
30.75	385.98	44.94	68.75	387.86	0.88			
31.75	385.89	40.13	69.75	387.57	-0.79			
32.75	385.52	34.50	70.75	387.83	0.05			
33.75	385.77	29.76	71.75	387.69	-1.00			
34.75	385.75	28.13	72.75	387.88	1.32			
35.75	385.97	22.77	73.75	387.89	2.69			
36.75	385.70	23.63	74.75	388.17	2.61			

### A.3 Short glass fiber-filled PBT, 8.42 wt%

#### A.3.1 Stress growth, startup of flow at $\dot{\gamma} = 1 \text{ s}^{-1}$

Rheometer fixture: 25 mm parallel plate, Gap = 1.0 mm

Temperature: 260 °C

Time (s)	$\eta^+$ (Pa.s)	$N_1^+ - N_2^+$ (Pa)	Time (s)	$\eta^+$ (Pa.s)	$N_1^+ - N_2^+$ (Pa)	Time (s)	$\eta^+$ (Pa.s)	$N_1^+ - N_2^+$ (Pa)
0.00	0.00	0.00	47.19	412.38	206.67	94.69	406.70	156.45
0.94	431.78	153.87	48.44	412.31	212.76	95.94	407.26	143.89
2.19	433.09	170.79	49.69	411.67	218.99	97.19	406.44	141.42
3.44	432.80	164.51	50.94	411.33	203.66	98.44	406.78	146.54
4.69	433.69	163.25	52.19	410.46	199.91	99.69	406.51	143.03
5.94	434.70	165.51	53.44	410.38	192.32	100.94	406.75	140.42
7.19	435.91	166.43	54.69	409.91	185.42			
8.44	434.01	165.70	55.94	409.49	195.01			
9.69	434.27	154.69	57.19	409.44	200.65			
10.94	433.56	164.49	58.44	409.20	207.02			
12.19	433.21	184.25	59.69	408.89	203.84			
13.44	431.81	185.91	60.94	408.43	192.18			
14.69	430.99	194.35	62.19	408.88	184.19			
15.94	430.41	210.65	63.44	408.78	188.64			
17.19	428.97	224.42	64.69	408.86	194.78			
18.44	428.07	217.97	65.94	408.31	185.09			
19.69	426.67	222.40	67.19	408.20	178.77			
20.94	425.80	222.28	68.44	408.41	181.75			
22.19	424.29	227.36	69.69	408.09	173.95			
23.44	423.63	224.08	70.94	408.56	180.87			
24.69	422.45	228.49	72.19	407.83	177.38			
25.94	422.93	249.78	73.44	408.09	172.01			
27.19	420.68	242.79	74.69	407.71	161.55			
28.44	419.90	233.70	75.94	407.86	163.25			
29.69	419.35	240.82	77.19	407.68	165.64			
30.94	418.50	237.06	78.44	407.97	169.24			
32.19	417.93	226.11	79.69	407.60	167.07			
33.44	416.98	230.41	80.94	407.41	160.13			
34.69	417.03	228.85	82.19	407.83	152.23			
35.94	416.80	214.03	83.44	407.18	162.03			
37.19	417.08	227.69	84.69	407.63	165.06			
38.44	415.88	235.09	85.94	407.23	152.22			
39.69	415.80	217.46	87.19	407.18	156.47			
40.94	416.06	232.24	88.44	407.25	161.78			
42.19	413.67	228.16	89.69	406.97	157.29			
43.44	413.91	227.23	90.94	406.78	149.64			
44.69	412.83	218.22	92.19	407.14	149.72			
45.94	412.71	210.12	93.44	407.02	155.13			

### A.3.2 Stress growth, startup of flow at $\dot{\gamma} = 1 \text{ s}^{-1}$

Rheometer fixture: 50 mm cone-and-plate with donut sample

Temperature: 260 °C

Time (s)	$\eta^+$ (Pa.s)	$N_1^+$ (Pa)	Time (s)	$\eta^+$ (Pa.s)	$N_1^+$ (Pa)	Time (s)	$\eta^+$ (Pa.s)	$N_1^+$ (Pa)
0.00	0.00	0.00	46.88	390.97	31.25	94.38	400.99	9.48
0.63	460.59	68.35	48.13	390.15	29.31	95.63	400.12	11.05
1.88	458.93	184.20	49.38	391.53	28.85	96.88	400.00	15.40
3.13	452.29	236.68	50.63	391.11	30.55	98.13	401.10	15.99
4.38	446.76	256.07	51.88	391.31	25.99	99.38	399.55	12.98
5.63	438.42	260.21	53.13	392.35	20.10	100.63	399.89	12.47
6.88	430.40	279.18	54.38	391.67	16.98			
8.13	424.34	278.28	55.63	392.37	16.74			
9.38	415.93	276.86	56.88	393.28	17.97			
10.63	409.24	254.02	58.13	392.13	18.37			
11.88	403.94	234.33	59.38	393.95	16.15			
13.13	399.75	205.50	60.63	393.56	12.96			
14.38	398.82	170.20	61.88	393.25	11.83			
15.63	398.74	142.19	63.13	395.16	10.67			
16.88	396.97	145.50	64.38	394.63	9.80			
18.13	397.25	161.21	65.63	395.00	11.77			
19.38	396.37	156.77	66.88	396.68	12.18			
20.63	395.51	152.74	68.13	395.33	7.96			
21.88	395.64	145.69	69.38	396.21	6.66			
23.13	394.37	135.49	70.63	397.27	8.75			
24.38	393.99	123.36	71.88	396.25	10.04			
25.63	394.00	117.75	73.13	397.56	8.67			
26.88	392.66	108.81	74.38	398.10	13.32			
28.13	392.74	96.97	75.63	397.45	15.08			
29.38	392.60	98.31	76.88	398.48	14.33			
30.63	391.17	94.79	78.13	398.48	13.10			
31.88	391.56	85.00	79.38	398.28	15.01			
33.13	391.14	80.85	80.63	399.21	18.38			
34.38	389.96	76.19	81.88	398.90	17.23			
35.63	390.89	71.36	83.13	399.42	15.07			
36.88	389.74	68.15	84.38	399.95	13.54			
38.13	389.08	61.09	85.63	399.24	9.84			
39.38	390.60	55.97	86.88	400.20	8.44			
40.63	389.50	55.58	88.13	400.37	14.31			
41.88	389.90	49.18	89.38	399.58	15.41			
43.13	390.71	48.67	90.63	400.66	17.47			
44.38	389.64	43.42	91.88	399.89	14.99			
45.63	390.66	33.26	93.13	399.36	14.71			

## A.4 Short glass fiber-filled PBT, 15 wt%

### A.4.1 Stress growth, startup of flow at $\dot{\gamma} = 1 \text{ s}^{-1}$

Rheometer fixture: 25 mm parallel plate, Gap = 1.0 mm

Temperature: 260 °C

Time (s)	$\eta^+$ (Pa.s)	$N_1^+ - N_2^+$ (Pa)	Time (s)	$\eta^+$ (Pa.s)	$N_1^+ - N_2^+$ (Pa)
0.00	0.00	0.00	56.75	475.78	513.59
1.25	504.28	222.11	58.25	474.58	497.01
2.75	510.74	219.92	59.75	474.56	506.38
4.25	516.26	226.93	61.25	473.88	478.11
5.75	519.73	206.30	62.75	475.36	464.34
7.25	524.61	310.17	64.25	473.52	464.18
8.75	526.98	339.59	65.75	474.15	477.66
10.25	527.51	363.15	67.25	475.19	442.28
11.75	528.88	477.01	68.75	475.62	458.00
13.25	523.98	480.33	70.25	475.48	447.22
14.75	518.95	474.63	71.75	476.46	431.56
16.25	516.73	494.02	73.25	476.72	434.77
17.75	513.53	542.93	74.75	476.21	398.05
19.25	509.10	580.38	76.25	475.99	383.06
20.75	514.36	698.79	77.75	475.78	394.49
22.25	503.16	660.35	79.25	475.72	401.12
23.75	500.89	648.73	80.75	476.94	429.11
25.25	496.65	641.85	82.25	476.20	399.16
26.75	493.60	618.24	83.75	475.31	404.32
28.25	491.40	627.82	85.25	475.89	409.45
29.75	489.50	635.29	86.75	475.41	398.13
31.25	487.19	628.81	88.25	475.63	390.56
32.75	485.45	602.59	89.75	475.68	377.53
34.25	483.93	610.60	91.25	475.62	385.92
35.75	481.67	600.45	92.75	475.68	331.63
37.25	480.87	587.11	94.25	476.04	357.09
38.75	481.04	568.51	95.75	475.58	344.79
40.25	479.73	563.38	97.25	476.93	367.57
41.75	477.99	563.66	98.75	476.52	369.58
43.25	477.20	560.92	100.25	474.05	353.92
44.75	477.89	566.28			
46.25	476.57	564.40			
47.75	476.26	533.79			
49.25	475.68	526.63			
50.75	475.31	524.25			
52.25	475.84	494.05			
53.75	476.09	480.94			
55.25	475.00	487.98			

A.4.2 Stress growth, startup of flow at  $\dot{\gamma} = 1 \text{ s}^{-1}$

Rheometer fixture: 50 mm cone-and-plate with donut sample

Temperature: 260 °C

Time (s)	$\eta^+$ (Pa.s)	$N_1^+$ (Pa)	Time (s)	$\eta^+$ (Pa.s)	$N_1^+$ (Pa)	Time (s)	$\eta^+$ (Pa.s)	$N_1^+$ (Pa)
0.00	0.00	0.00	37.88	400.08	187.35	75.88	421.28	73.86
0.88	510.97	46.13	38.88	400.17	180.25	76.88	421.73	75.44
1.88	515.00	42.98	39.88	400.33	165.54	77.88	421.99	70.21
2.88	515.22	91.96	40.88	400.65	160.35	78.88	422.12	69.92
3.88	511.97	166.36	41.88	400.54	156.63	79.88	421.88	78.65
4.88	505.18	257.74	42.88	401.07	154.01	80.88	421.90	84.30
5.88	497.60	318.44	43.88	401.20	143.13	81.88	421.60	84.82
6.88	489.62	372.31	44.88	402.00	137.76	82.88	422.21	80.45
7.88	480.95	417.99	45.88	401.99	132.87	83.88	421.79	92.56
8.88	472.60	436.71	46.88	402.86	125.85	84.88	421.70	84.76
9.88	465.00	445.64	47.88	403.98	116.24	85.88	422.04	90.83
10.88	458.71	456.87	48.88	403.99	108.97	86.88	422.06	91.46
11.88	452.34	447.65	49.88	404.32	104.72	87.88	421.67	95.90
12.88	446.35	434.39	50.88	404.71	105.11	88.88	421.59	92.55
13.88	441.47	425.35	51.88	405.37	101.11	89.88	421.28	95.82
14.88	436.73	414.42	52.88	405.98	99.11	90.88	421.53	94.04
15.88	432.29	406.28	53.88	406.90	93.32	91.88	421.05	99.78
16.88	428.34	400.69	54.88	407.86	87.65	92.88	421.09	102.63
17.88	424.85	393.41	55.88	408.60	89.20	93.88	421.25	100.59
18.88	422.26	385.43	56.88	409.65	84.71	94.88	421.11	100.08
19.88	419.32	369.42	57.88	410.56	79.44	95.88	420.86	97.65
20.88	416.56	356.81	58.88	411.43	79.18	96.88	420.74	97.20
21.88	414.63	351.69	59.88	411.90	71.06	97.88	420.92	100.36
22.88	412.32	337.48	60.88	412.40	67.87	98.88	420.44	100.04
23.88	410.22	321.06	61.88	413.42	73.51	99.88	420.16	97.73
24.88	408.43	315.82	62.88	414.24	73.78	100.44	40.88	47.14
25.88	407.30	301.66	63.88	414.56	71.37			
26.88	405.92	292.60	64.88	415.53	68.13			
27.88	405.11	277.70	65.88	416.71	68.08			
28.88	403.90	267.03	66.88	416.76	63.36			
29.88	403.39	260.26	67.88	417.49	63.73			
30.88	402.22	253.03	68.88	418.22	70.16			
31.88	401.79	242.95	69.88	418.81	71.95			
32.88	401.34	228.62	70.88	418.56	66.28			
33.88	400.92	218.31	71.88	419.35	66.36			
34.88	400.50	207.82	72.88	419.94	65.08			
35.88	400.59	198.80	73.88	420.29	65.97			
36.88	400.73	190.33	74.88	420.86	73.34			

## A.5 Short glass fiber-filled PBT, 20 wt%

### A.5.1 Stress growth, startup of flow at $\dot{\gamma} = 1 \text{ s}^{-1}$

Rheometer fixture: 25 mm parallel plate, Gap = 1.0 mm

Temperature: 260 °C

Time (s)	$\eta^+$ (Pa.s)	$N_1^+ - N_2^+$ (Pa)	Time (s)	$\eta^+$ (Pa.s)	$N_1^+ - N_2^+$ (Pa)
0.00	0.00	0.00	56.75	628.41	1315.58
1.25	581.68	575.62	58.25	625.82	1333.11
2.75	595.17	545.77	59.75	622.82	1302.28
4.25	614.26	611.98	61.25	621.19	1208.54
5.75	630.98	680.31	62.75	622.20	1222.78
7.25	643.80	782.16	64.25	619.51	1175.43
8.75	651.80	886.40	65.75	618.10	1199.71
10.25	659.09	978.44	67.25	615.25	1144.61
11.75	664.73	1121.69	68.75	613.17	1153.14
13.25	667.04	1218.70	70.25	612.47	1133.61
14.75	667.47	1405.84	71.75	612.90	1094.95
16.25	667.52	1460.28	73.25	611.05	1077.10
17.75	668.52	1528.94	74.75	610.16	1096.13
19.25	668.81	1610.25	76.25	610.74	1011.13
20.75	667.26	1646.80	77.75	607.37	1025.63
22.25	668.72	1742.81	79.25	606.64	942.70
23.75	666.99	1788.07	80.75	607.27	905.67
25.25	664.73	1804.28	82.25	606.73	909.77
26.75	662.62	1768.37	83.75	605.53	932.13
28.25	661.21	1719.05	85.25	605.59	921.15
29.75	658.00	1696.96	86.75	606.68	930.34
31.25	658.58	1731.83	88.25	606.95	886.34
32.75	659.16	1753.96	89.75	602.85	887.96
34.25	656.10	1742.17	91.25	602.91	890.28
35.75	655.27	1739.54	92.75	602.06	872.90
37.25	652.68	1674.64	94.25	600.85	897.39
38.75	650.42	1665.45	95.75	600.38	838.05
40.25	647.96	1641.73	97.25	598.91	844.29
41.75	646.12	1618.24	98.75	598.60	791.21
43.25	645.07	1551.58	100.25	598.08	750.63
44.75	643.71	1499.78			
46.25	641.24	1455.37			
47.75	637.65	1449.29			
49.25	635.92	1492.07			
50.75	634.67	1459.80			
52.25	632.19	1433.36			
53.75	632.39	1390.46			
55.25	630.40	1371.13			

A.5.2 Stress growth, startup of flow at  $\dot{\gamma} = 1 \text{ s}^{-1}$

Rheometer fixture: 50 mm cone-and-plate with donut sample

Temperature: 260 °C

Time (s)	$\eta^+$ (Pa.s)	$N_1^+$ (Pa)	Time (s)	$\eta^+$ (Pa.s)	$N_1^+$ (Pa)	Time (s)	$\eta^+$ (Pa.s)	$N_1^+$ (Pa)
0.00	0.00	0.00	37.88	393.18	264.76	75.88	407.24	122.40
0.88	499.61	186.81	38.88	392.74	250.44	76.88	406.72	122.11
1.88	514.98	249.12	39.88	391.88	242.88	77.88	407.13	120.10
2.88	525.02	307.49	40.88	392.18	236.81	78.88	407.55	123.54
3.88	529.34	358.59	41.88	392.05	232.36	79.88	407.12	114.51
4.88	529.63	398.09	42.88	391.64	227.75	80.88	408.12	108.32
5.88	527.71	418.60	43.88	392.15	220.80	81.88	407.67	113.43
6.88	522.40	451.05	44.88	392.66	210.56	82.88	406.77	125.29
7.88	515.19	479.59	45.88	393.47	200.02	83.88	406.82	132.51
8.88	507.17	515.13	46.88	393.28	191.75	84.88	406.35	130.55
9.88	498.83	535.28	47.88	393.65	189.51	85.88	406.07	131.64
10.88	489.98	548.26	48.88	393.40	185.00	86.88	406.00	132.28
11.88	482.02	549.43	49.88	394.14	184.04	87.88	406.67	128.98
12.88	473.17	549.42	50.88	394.09	174.12	88.88	406.00	125.61
13.88	466.58	544.42	51.88	394.24	168.59	89.88	406.33	136.70
14.88	459.91	543.93	52.88	394.75	164.84	90.88	406.47	128.10
15.88	453.91	538.95	53.88	395.44	168.19	91.88	407.04	129.24
16.88	448.25	532.58	54.88	395.86	164.37	92.88	405.93	134.58
17.88	442.42	518.79	55.88	396.57	168.41	93.88	405.54	127.94
18.88	438.05	510.76	56.88	396.96	161.53	94.88	405.68	136.30
19.88	434.21	495.91	57.88	397.24	152.25	95.88	405.98	134.14
20.88	429.64	479.46	58.88	397.79	143.99	96.88	405.93	139.42
21.88	425.46	464.47	59.88	398.52	138.75	97.88	405.32	133.68
22.88	422.39	451.24	60.88	399.30	141.81	98.88	405.02	133.35
23.88	419.79	435.99	61.88	400.97	135.53	99.88	405.07	142.62
24.88	416.64	426.31	62.88	401.34	137.20	100.44	41.70	55.48
25.88	413.39	414.86	63.88	402.25	124.67			
26.88	410.40	395.20	64.88	402.57	117.94			
27.88	408.19	380.53	65.88	402.88	121.33			
28.88	406.10	370.49	66.88	404.28	125.71			
29.88	403.86	354.57	67.88	404.48	117.30			
30.88	402.18	336.65	68.88	405.24	114.87			
31.88	400.60	319.83	69.88	405.75	110.70			
32.88	399.21	316.50	70.88	406.92	106.79			
33.88	397.66	301.16	71.88	406.89	110.26			
34.88	396.82	294.01	72.88	407.28	108.12			
35.88	395.63	285.63	73.88	407.11	112.78			
36.88	394.38	276.23	74.88	407.23	109.94			

## A.6 Short glass fiber-filled PBT, 25 wt%

### A.6.1 Stress growth, startup of flow at $\dot{\gamma} = 1 \text{ s}^{-1}$

Rheometer fixture: 25 mm parallel plate, Gap = 1.0 mm

Temperature: 260 °C

Time (s)	$\eta^+$ (Pa.s)	$N_1^+ - N_2^+$ (Pa)	Time (s)	$\eta^+$ (Pa.s)	$N_1^+ - N_2^+$ (Pa)
0.00	0.00	0.00	56.75	726.53	2332.66
1.25	523.46	711.38	58.25	721.94	2312.41
2.75	551.83	781.83	59.75	718.21	2161.04
4.25	580.80	856.84	61.25	714.60	2099.05
5.75	614.56	1044.48	62.75	708.29	2002.80
7.25	645.30	1315.47	64.25	707.92	1893.96
8.75	675.22	1636.55	65.75	707.06	1883.22
10.25	704.28	1952.03	67.25	701.92	1895.80
11.75	731.61	2302.58	68.75	698.92	1876.31
13.25	750.87	2558.92	70.25	695.50	1787.48
14.75	769.32	2830.03	71.75	693.03	1696.82
16.25	783.63	3087.24	73.25	689.36	1664.38
17.75	797.32	3302.12	74.75	685.68	1678.36
19.25	809.16	3484.57	76.25	683.16	1591.97
20.75	814.89	3637.54	77.75	681.42	1562.94
22.25	821.51	3748.41	79.25	679.95	1565.41
23.75	824.66	3816.15	80.75	677.79	1477.71
25.25	821.15	3749.45	82.25	675.70	1469.68
26.75	818.92	3721.65	83.75	673.85	1530.35
28.25	816.99	3765.42	85.25	669.54	1416.44
29.75	812.01	3686.58	86.75	668.97	1376.94
31.25	811.68	3611.41	88.25	666.81	1358.76
32.75	807.27	3528.02	89.75	665.91	1355.61
34.25	802.70	3523.47	91.25	664.92	1350.38
35.75	793.70	3439.43	92.75	663.93	1268.58
37.25	787.24	3370.10	94.25	661.70	1240.24
38.75	780.56	3249.80	95.75	661.39	1204.36
40.25	776.68	3179.18	97.25	659.98	1239.58
41.75	773.25	3113.12	98.75	657.67	1163.20
43.25	766.89	3041.87	100.25	656.97	1115.03
44.75	761.88	2923.81			
46.25	755.22	2875.48			
47.75	750.58	2771.80			
49.25	746.64	2648.54			
50.75	740.18	2611.24			
52.25	737.52	2571.66			
53.75	734.82	2467.34			
55.25	732.73	2384.34			

A.6.2 Stress growth, startup of flow at  $\dot{\gamma} = 1 \text{ s}^{-1}$

Rheometer fixture: 50 mm cone-and-plate with donut sample

Temperature: 260 °C

Time (s)	$\eta^+$ (Pa.s)	$N_1^+$ (Pa)	Time (s)	$\eta^+$ (Pa.s)	$N_1^+$ (Pa)	Time (s)	$\eta^+$ (Pa.s)	$N_1^+$ (Pa)
0.00	0.00	0.00	37.88	470.73	420.65	75.88	461.53	233.11
0.88	539.50	357.08	38.88	469.94	409.90	76.88	461.22	234.90
1.88	569.27	439.68	39.88	469.55	400.86	77.88	461.49	247.44
2.88	591.94	504.01	40.88	468.54	385.51	78.88	461.81	241.97
3.88	609.30	602.92	41.88	467.53	378.18	79.88	461.45	226.80
4.88	617.38	715.51	42.88	466.75	369.52	80.88	461.47	232.70
5.88	620.79	814.50	43.88	465.49	363.81	81.88	461.08	248.37
6.88	619.85	928.52	44.88	464.73	347.25	82.88	460.82	243.70
7.88	616.71	1002.13	45.88	464.96	342.44	83.88	460.88	250.97
8.88	610.81	1030.74	46.88	464.30	329.70	84.88	460.68	253.62
9.88	603.91	1040.53	47.88	463.60	319.23	85.88	460.51	244.62
10.88	596.55	1041.84	48.88	463.20	310.89	86.88	459.76	232.46
11.88	588.29	1036.46	49.88	463.67	323.32	87.88	459.93	234.22
12.88	578.75	1019.35	50.88	462.67	312.91	88.88	459.78	231.27
13.88	569.31	989.26	51.88	461.64	306.18	89.88	459.22	233.71
14.88	559.65	957.43	52.88	461.48	305.88	90.88	458.77	225.70
15.88	551.69	942.19	53.88	461.73	307.01	91.88	459.22	229.45
16.88	544.78	918.65	54.88	461.00	290.72	92.88	459.12	223.64
17.88	537.59	899.27	55.88	460.82	287.79	93.88	458.80	220.30
18.88	530.40	867.05	56.88	460.66	283.89	94.88	458.52	222.86
19.88	524.96	824.13	57.88	461.36	289.25	95.88	460.01	232.94
20.88	519.62	779.90	58.88	461.33	291.79	96.88	459.92	223.88
21.88	514.52	747.97	59.88	461.64	279.04	97.88	459.96	218.75
22.88	509.00	710.12	60.88	461.84	285.69	98.88	459.62	223.84
23.88	504.35	680.58	61.88	461.50	273.61	99.88	459.22	217.80
24.88	500.36	654.36	62.88	461.66	257.84	100.44	459.18	221.81
25.88	496.60	620.70	63.88	461.89	257.31			
26.88	493.13	601.74	64.88	462.20	256.19			
27.88	488.87	581.47	65.88	461.95	252.16			
28.88	486.23	551.97	66.88	462.48	243.81			
29.88	484.09	537.24	67.88	461.58	243.31			
30.88	482.50	519.10	68.88	461.84	234.78			
31.88	480.75	487.43	69.88	461.72	236.81			
32.88	478.88	490.62	70.88	461.67	245.16			
33.88	476.71	474.63	71.88	461.64	239.17			
34.88	474.55	461.68	72.88	461.04	240.03			
35.88	472.84	453.71	73.88	461.53	250.28			
36.88	471.82	442.59	74.88	461.33	243.12			

## A.7 Short glass fiber-filled PBT, 30 wt%

### A.7.1 Stress growth, startup of flow

#### A.7.1.1 Parallel Plate (PP): 25 mm diameter

Temperature: 260 °C, Gap: 0.2 mm

Shear rate:  $\dot{\gamma} = 1 \text{ s}^{-1}$

Time (s)	$\eta^+$ (Pa.s)	$N_1^+ - N_2^+$ (Pa)
0.00	0.00	0.00
2.75	822.98	5332.40
5.75	967.01	3476.92
8.75	1078.07	3482.94
11.75	1161.03	3036.21
14.75	1193.58	2959.44
17.75	1217.20	3203.95
20.75	1237.17	2795.33
23.75	1243.42	2236.48
26.75	1231.30	2462.48
29.75	1222.31	3123.97
32.75	1219.77	3551.50
35.75	1193.21	3012.11
38.75	1178.12	3024.30
41.75	1174.42	3512.32
44.75	1138.65	3443.47
47.75	1155.52	3527.21
50.75	1151.37	2192.87
53.75	1113.84	2922.71
56.75	1117.23	3251.74
59.75	1111.58	3418.24
62.75	1085.14	2777.92
65.75	1072.90	3720.48
68.75	1072.68	2986.62
71.75	1059.54	2617.78
74.75	1055.95	2734.80
77.75	1054.71	3173.48
80.75	1069.80	2351.49
83.75	1053.41	1612.74
86.75	1050.30	1258.97
89.75	1037.05	1950.17
92.75	1024.82	2102.47
95.75	1018.23	2255.86
98.75	1013.29	1865.04
101.75	1025.07	1311.97

Temperature: 260 °C, Gap: 0.4 mm  
Shear rate:  $\dot{\gamma} = 1 \text{ s}^{-1}$

Time (s)	$\eta^+$ (Pa.s)	$N_1^+ - N_2^+$ (Pa)
0.00	0.00	0.00
2.75	747.92	2649.99
5.75	881.55	2568.82
8.75	997.79	3228.68
11.75	1079.33	3905.85
14.75	1129.20	3948.13
17.75	1165.76	3994.33
20.75	1190.57	3780.36
23.75	1194.81	4085.93
26.75	1191.95	4250.82
29.75	1192.63	4692.44
32.75	1187.32	4715.37
35.75	1187.23	4353.93
38.75	1176.13	4159.86
41.75	1174.63	3823.52
44.75	1172.71	4188.64
47.75	1150.53	4056.19
50.75	1133.35	4199.99
53.75	1133.55	3997.92
56.75	1134.71	3676.93
59.75	1129.65	4203.02
62.75	1087.44	3504.28
65.75	1085.46	3470.47
68.75	1084.64	3783.23
71.75	1057.89	3570.62
74.75	1068.85	3032.05
77.75	1056.95	2845.98
80.75	1053.51	2971.31
83.75	1037.83	2935.98
86.75	1061.56	2746.14
89.75	1039.35	2388.30
92.75	1049.95	2500.80
95.75	1046.25	2052.03
98.75	1046.73	2145.67
101.75	1030.34	2154.46

Temperature: 260 °C, Gap: 0.6 mm  
 Shear rate:  $\dot{\gamma} = 1 \text{ s}^{-1}$

Time (s)	$\eta^+$ (Pa.s)	$N_1^+ - N_2^+$ (Pa)
0.00	0.00	0.00
2.75	618.72	1272.08
5.75	734.22	1585.31
8.75	838.82	2349.28
11.75	913.50	3111.29
14.75	952.29	3402.07
17.75	971.24	3830.34
20.75	987.60	4003.78
23.75	985.52	4228.15
26.75	981.03	4509.42
29.75	971.99	4327.58
32.75	953.13	4355.47
35.75	939.91	4317.43
38.75	934.87	4191.22
41.75	917.15	3949.11
44.75	906.15	3854.23
47.75	902.58	3703.73
50.75	883.27	3667.76
53.75	867.55	3567.29
56.75	854.96	3413.50
59.75	838.04	3198.65
62.75	828.70	2980.04
65.75	814.83	2810.91
68.75	811.67	2833.13
71.75	802.76	2708.20
74.75	794.63	2617.88
77.75	788.86	2477.48
80.75	784.26	2324.70
83.75	776.96	2343.76
86.75	776.46	2222.63
89.75	773.22	2260.63
92.75	762.70	2014.65
95.75	756.66	2082.35
98.75	752.14	2039.43
101.75	745.09	1818.38

Temperature: 260 °C, Gap: 0.8 mm  
Shear rate:  $\dot{\gamma} = 1 \text{ s}^{-1}$

Time (s)	$\eta^+$ (Pa.s)	$N_1^+ - N_2^+$ (Pa)
0.00	0.00	0.00
2.75	609.83	1711.31
5.75	738.59	1856.66
8.75	866.97	2520.60
11.75	946.67	2943.26
14.75	988.41	3369.29
17.75	1019.88	3696.20
20.75	1031.72	3669.27
23.75	1036.96	3941.43
26.75	1029.40	4310.94
29.75	1020.15	4316.70
32.75	999.91	4294.48
35.75	996.30	4580.39
38.75	987.77	4444.98
41.75	954.36	4433.79
44.75	933.17	4278.09
47.75	918.17	4177.38
50.75	901.19	3912.41
53.75	895.72	3775.89
56.75	871.50	3441.87
59.75	857.65	3735.69
62.75	845.61	3433.79
65.75	836.66	3275.05
68.75	822.85	3170.02
71.75	810.91	2958.05
74.75	810.70	2932.23
77.75	802.39	3149.80
80.75	785.89	2846.47
83.75	789.46	2728.73
86.75	787.13	2588.62
89.75	776.05	2288.64
92.75	763.71	2266.70
95.75	760.49	2254.63
98.75	757.81	2060.48
101.75	756.39	2221.30

Temperature: 260 °C, Gap: 1.0 mm  
 Shear rate:  $\dot{\gamma} = 1 \text{ s}^{-1}$

Time (s)	$\eta^+$ (Pa.s)	$N_1^+ - N_2^+$ (Pa)	Time (s)	$\eta^+$ (Pa.s)	$N_1^+ - N_2^+$ (Pa)
0.00	0.00	0.00	116.75	740.99	2056.16
2.75	613.09	1053.64	119.75	734.43	1732.44
5.75	757.03	1961.88	122.75	736.47	1871.36
8.75	903.62	3024.63	125.75	735.84	1700.79
11.75	1018.87	4132.77	128.75	737.16	1843.90
14.75	1087.86	5049.81	131.75	738.31	1773.25
17.75	1124.44	5702.20	134.75	733.00	1715.86
20.75	1139.57	6023.99	137.75	740.32	1766.53
23.75	1133.71	6020.80	140.75	732.48	1544.01
26.75	1122.79	6132.22	143.75	731.01	1597.28
29.75	1096.24	5981.63	146.75	738.14	1601.72
32.75	1073.61	5862.53	149.75	747.08	1702.55
35.75	1052.21	5694.36	152.75	736.47	1550.92
38.75	1027.24	5569.35			
41.75	1004.20	5368.41			
44.75	978.57	5351.46			
47.75	948.49	4794.67			
50.75	937.70	4395.50			
53.75	917.77	4298.07			
56.75	904.24	4175.06			
59.75	890.60	3867.09			
62.75	877.50	3658.07			
65.75	863.76	3447.38			
68.75	848.65	3291.67			
71.75	839.07	3226.13			
74.75	829.88	3167.30			
77.75	815.97	2985.38			
80.75	807.56	2689.64			
83.75	801.71	2700.11			
86.75	795.00	2663.18			
89.75	784.26	2460.32			
92.75	782.10	2407.93			
95.75	774.86	2268.25			
98.75	772.75	2235.52			
101.75	768.17	2158.71			
104.75	760.54	2120.06			
107.75	759.34	2032.70			
110.75	750.20	1954.93			
113.75	745.41	1886.87			

Temperature: 260 °C, Gap: 1.2 mm  
 Shear rate:  $\dot{\gamma} = 1 \text{ s}^{-1}$

Time (s)	$\eta^+$ (Pa.s)	$N_1^+ - N_2^+$ (Pa)	Time (s)	$\eta^+$ (Pa.s)	$N_1^+ - N_2^+$ (Pa)
0.00	0.00	0.00	77.75	816.59	2607.87
1.75	665.64	846.21	79.75	810.28	2612.28
3.75	761.96	1149.53	81.75	802.79	2569.89
5.75	839.72	1363.53	83.75	800.20	2515.49
7.75	898.70	1763.61	85.75	797.74	2424.31
9.75	949.25	2471.59	87.75	792.49	2481.62
11.75	1008.87	3304.78	89.75	791.07	2414.91
13.75	1046.52	4053.39	91.75	790.39	2257.33
15.75	1075.31	4789.48	93.75	785.54	2175.50
17.75	1098.98	5435.59	95.75	782.78	2088.27
19.75	1110.98	5667.41	97.75	778.77	2039.07
21.75	1116.36	6040.75	99.75	773.52	2055.02
23.75	1115.03	6178.74	101.75	768.11	1963.37
25.75	1102.86	6113.17			
27.75	1089.86	6162.53			
29.75	1068.80	6075.77			
31.75	1052.88	6035.76			
33.75	1045.32	5750.12			
35.75	1035.23	5500.22			
37.75	1023.59	5172.80			
39.75	1005.39	5143.91			
41.75	993.35	5103.08			
43.75	979.13	4812.13			
45.75	968.79	4579.90			
47.75	957.60	4444.30			
49.75	947.46	4307.76			
51.75	934.47	4176.73			
53.75	925.70	3875.19			
55.75	916.31	3820.22			
57.75	906.17	3786.76			
59.75	893.08	3566.79			
61.75	879.17	3443.55			
63.75	868.39	3306.08			
65.75	861.31	3051.30			
67.75	848.46	3038.52			
69.75	840.71	3035.55			
71.75	837.05	2914.81			
73.75	833.24	2871.79			
75.75	824.95	2806.85			

Temperature: 260 °C, Gap: 1.0 mm  
 Shear rate:  $\dot{\gamma} = 4 \text{ s}^{-1}$

Time (s)	$\eta^+$ (Pa.s)	$N_1^+ - N_2^+$ (Pa)	Time (s)	$\eta^+$ (Pa.s)	$N_1^+ - N_2^+$ (Pa)
0	0	0	131.5	703.0956	4490.871
2.5	669.8489	3669.068	134.5	698.9699	3727.46
5.5	756.7945	5314.032	137.5	697.6054	3812.612
8.5	820.7997	7939.521	140.5	695.1492	4033.399
11.5	859.296	10507.02	143.5	692.7251	4228.545
14.5	878.6243	12532.13	146.5	692.2114	3777.784
17.5	887.0203	13723.94	149.5	692.6609	3769.876
20.5	888.722	14367.13	152.5	690.1566	3934.348
23.5	884.2752	14703.26			
26.5	874.1454	14299.07			
29.5	865.3963	14110.55			
32.5	854.3676	13787.84			
35.5	840.385	12907.56			
38.5	827.2854	12562.48			
41.5	811.264	11971.05			
44.5	799.9623	11570.7			
47.5	790.9724	10911.85			
50.5	780.056	9789.696			
53.5	771.1303	9550.217			
56.5	759.4112	9283.898			
59.5	753.1023	9102.251			
62.5	744.2567	8681.764			
65.5	739.0554	8128.516			
68.5	733.4046	7916.675			
71.5	728.6688	7561.69			
74.5	724.7357	6924.089			
77.5	723.2107	6670.87			
80.5	722.6328	6947.733			
83.5	722.4401	6349.114			
86.5	719.0688	6439.538			
89.5	717.7525	6072.57			
92.5	713.6107	5728.768			
95.5	710.994	5988.377			
98.5	714.5578	5941.248			
101.5	713.6107	5456.697			
104.5	716.5806	5161.142			
107.5	717.9612	4749.202			
110.5	717.303	4734.025			
113.5	712.7117	4886.515			
116.5	707.8957	4448.934			
119.5	706.4027	4733.386			
122.5	703.9786	4763.581			
125.5	702.8548	4392.699			
128.5	703.6415	4649.752			

A.7.1.2 Cone-and-plate: 50 mm diameter

Temperature: 260 °C, Sample: Un-modified

Shear rate:  $\dot{\gamma} = 1 \text{ s}^{-1}$

Time (s)	$\eta^+$ (Pa.s)	$N_1^+$ (Pa)	Time (s)	$\eta^+$ (Pa.s)	$N_1^+$ (Pa)
0.00	0.00	0.00	119.75	638.44	407.45
2.75	742.46	931.28	122.75	636.48	409.79
5.75	854.66	1485.68	125.75	634.90	437.69
8.75	886.98	1877.81	128.75	632.29	425.79
11.75	875.19	1962.31	131.75	631.60	432.42
14.75	847.20	1811.87	134.75	629.18	418.92
17.75	815.14	1746.89	137.75	628.25	401.89
20.75	789.39	1568.98	140.75	629.92	448.66
23.75	762.95	1395.47	143.75	627.72	400.74
26.75	742.71	1302.86	146.75	628.63	397.38
29.75	726.36	1141.42	149.75	627.42	382.17
32.75	709.95	1050.03	152.75	626.27	401.72
35.75	696.12	952.23			
38.75	690.10	895.25			
41.75	683.81	818.41			
44.75	677.16	774.07			
47.75	672.38	701.47			
50.75	670.05	662.98			
53.75	666.65	616.35			
56.75	664.29	577.80			
59.75	661.29	543.43			
62.75	660.17	532.79			
65.75	661.79	561.93			
68.75	657.29	528.73			
71.75	658.43	498.41			
74.75	656.92	483.90			
77.75	654.80	492.81			
80.75	651.79	457.99			
83.75	650.06	465.77			
86.75	649.82	439.95			
89.75	648.17	438.06			
92.75	646.61	473.38			
95.75	646.81	466.74			
98.75	645.34	437.19			
101.75	644.21	423.86			
104.75	644.07	456.80			
107.75	642.24	443.29			
110.75	641.19	434.99			
113.75	638.98	446.70			
116.75	639.23	437.29			

Temperature: 260 °C, Sample: Donut sample  
 Shear rate:  $\dot{\gamma} = 1 \text{ s}^{-1}$

Time (s)	$\eta^+$ (Pa.s)	$N_1^+$ (Pa)	Time (s)	$\eta^+$ (Pa.s)	$N_1^+$ (Pa)
0.00	0.00	0.00	134.06	550.25	229.56
2.81	753.39	899.17	137.19	552.59	224.19
5.94	847.59	1591.17	140.31	554.37	232.84
9.06	854.71	1909.84	143.44	553.92	239.28
12.19	816.11	1802.51	146.56	552.48	226.61
15.31	765.20	1532.66	149.69	551.26	209.94
18.44	715.23	1208.18	152.81	548.08	237.20
21.56	676.55	966.58			
24.69	644.28	790.00			
27.81	617.75	680.74			
30.94	600.48	606.60			
34.06	593.60	501.85			
37.19	585.65	461.63			
40.31	576.46	385.65			
43.44	571.62	352.06			
46.56	566.06	315.68			
49.69	560.50	288.80			
52.81	555.82	273.93			
55.94	552.82	284.48			
59.06	550.47	256.74			
62.19	548.25	244.34			
65.31	548.92	256.15			
68.44	550.70	236.32			
71.56	549.48	258.73			
74.69	548.47	231.12			
77.81	549.03	206.63			
80.94	549.31	213.34			
84.06	550.47	171.85			
87.19	550.54	149.84			
90.31	552.98	166.61			
93.44	550.99	178.86			
96.56	546.92	166.48			
99.69	543.86	163.22			
102.81	543.81	170.04			
105.94	543.14	163.88			
109.06	545.09	179.39			
112.19	546.80	166.96			
115.31	544.42	189.92			
118.44	544.92	185.60			
121.56	545.86	220.27			
124.69	547.14	209.24			
127.81	548.04	215.36			
130.94	548.99	228.95			

Temperature: 260 °C, Sample: Donut sample  
Shear rate:  $\dot{\gamma} = 2 \text{ s}^{-1}$

Time (s)	$\eta^+$ (Pa.s)	$N_1^+$ (Pa)
0.00	0.00	0.00
2.75	747.83	1317.05
5.75	787.60	2242.43
8.75	763.69	2906.16
11.75	724.34	3052.42
14.75	688.22	2909.20
17.75	653.55	2640.09
20.75	625.72	2364.64
23.75	603.27	2086.36
26.75	586.48	1814.21
29.75	573.46	1543.16
32.75	565.76	1419.96
35.75	559.59	1266.88
38.75	555.38	1117.80
41.75	553.07	963.17
44.75	553.80	836.48
47.75	553.52	754.42
50.75	556.95	672.76
53.75	558.80	635.37
56.75	559.48	572.78
59.75	560.89	569.08
62.75	561.84	516.10
65.75	563.63	513.32
68.75	565.76	535.79
71.75	566.27	479.86
74.75	566.32	491.38
77.75	564.70	513.09
80.75	563.68	525.31
83.75	562.74	515.61
86.75	563.01	494.37
89.75	562.52	503.21
92.75	562.28	541.84
95.75	561.44	516.20
98.75	562.01	502.61
101.75	562.23	534.60

Temperature: 260 °C, Sample: Donut sample  
 Shear rate:  $\dot{\gamma} = 4 \text{ s}^{-1}$

Time (s)	$\eta^+$ (Pa.s)	$N_1^+$ (Pa)	Time (s)	$\eta^+$ (Pa.s)	$N_1^+$ (Pa)
0.00	0.00	0.00	128.75	498.70	736.84
2.75	621.00	1927.74	131.75	498.47	809.61
5.75	653.40	3064.85	134.75	497.48	841.58
8.75	638.36	4047.12	137.75	496.50	767.50
11.75	611.07	4520.82	140.75	494.60	780.03
14.75	584.80	4454.70	143.75	496.11	711.46
17.75	561.50	4138.08	146.75	496.94	764.54
20.75	542.87	3703.63	149.75	496.94	779.82
23.75	526.98	3261.66	152.75	496.66	775.25
26.75	514.24	2830.40			
29.75	504.82	2465.96			
32.75	500.43	2147.31			
35.75	494.89	1883.16			
38.75	492.80	1677.83			
41.75	491.34	1505.84			
44.75	491.84	1384.81			
47.75	492.02	1245.91			
50.75	493.25	1159.23			
53.75	495.84	1061.39			
56.75	496.61	996.77			
59.75	497.86	926.60			
62.75	499.98	904.34			
65.75	501.67	872.49			
68.75	503.80	853.37			
71.75	504.47	829.59			
74.75	506.22	830.02			
77.75	506.89	817.70			
80.75	506.62	809.50			
83.75	507.84	782.44			
86.75	507.39	813.42			
89.75	508.31	732.90			
92.75	507.61	747.64			
95.75	507.40	782.66			
98.75	505.94	810.48			
101.75	503.92	765.09			
104.75	502.69	791.62			
107.75	502.92	803.60			
110.75	502.18	732.74			
113.75	501.22	765.41			
116.75	500.72	789.75			
119.75	499.48	817.46			
122.75	498.41	793.36			
125.75	499.14	766.62			

Temperature: 260 °C, Sample: Donut sample  
 Shear rate:  $\dot{\gamma} = 6 \text{ s}^{-1}$

Time (s)	$\eta^+$ (Pa.s)	$N_1^+$ (Pa)
0.00	0.00	0.00
2.25	601.00	2569.31
4.65	645.31	4593.83
7.05	657.13	6062.06
9.45	643.95	6776.02
11.85	622.24	6918.92
14.25	598.16	6789.89
16.65	574.72	6370.26
19.05	555.41	5962.78
21.45	536.39	5498.57
23.85	520.76	4962.17
26.25	510.35	4592.98
28.65	502.80	4290.87
31.05	493.88	3916.35
33.45	488.13	3602.93
35.85	482.44	3195.40
38.25	478.25	2904.54
40.65	475.39	2609.89
43.05	473.90	2379.87
45.45	471.88	2204.81
47.85	469.64	2110.12
50.25	470.76	1982.63
52.65	470.09	1884.84
55.05	470.16	1776.17
57.45	471.21	1665.29
59.85	473.08	1605.49
62.25	474.28	1552.68
64.65	473.60	1486.78
67.05	473.01	1446.17
69.45	473.75	1417.14
71.85	476.00	1414.98
74.25	476.52	1391.81
76.65	479.29	1303.01
79.05	481.84	1304.10
81.45	483.26	1291.89
83.85	483.33	1256.08
86.25	482.51	1262.16
88.65	481.77	1274.61
91.05	483.19	1212.42
93.45	481.84	1178.18
95.85	481.46	1213.75
98.25	480.94	1272.88
100.65	481.54	1249.53

Temperature: 260 °C, Sample: Donut sample  
Shear rate:  $\dot{\gamma} = 8 \text{ s}^{-1}$

Time (s)	$\eta^+$ (Pa.s)	$N_1^+$ (Pa)
0.00	0.00	0.00
2.20	596.82	2655.96
4.60	626.01	4643.12
7.00	619.50	6639.14
9.40	597.72	8222.44
11.80	571.00	8909.45
14.20	544.61	9280.46
16.60	522.61	9074.91
19.00	503.42	8656.36
21.40	487.58	8176.76
23.80	474.56	7499.30
26.20	463.45	6903.64
28.60	454.68	6367.06
31.00	447.67	5859.96
33.40	441.27	5339.57
35.80	437.96	4937.10
38.20	436.61	4554.56
40.60	434.93	4190.20
43.00	433.64	3798.22
45.40	432.01	3474.64
47.80	429.93	3184.44
50.20	430.44	2909.74
52.60	431.56	2679.84
55.00	433.52	2460.43
57.40	436.17	2290.66
59.80	439.86	2136.09
62.20	442.96	2021.20
64.60	446.04	1918.67
67.00	449.41	1825.65
69.40	453.23	1769.84
71.80	457.04	1605.28
74.20	459.63	1518.97
76.60	461.76	1454.09
79.00	462.89	1425.49
81.40	467.48	1291.72
83.80	470.75	1197.28
86.20	471.08	1249.74
88.60	471.08	1297.20
91.00	471.19	1296.96
93.40	471.75	1249.25
95.80	470.17	1277.39
98.20	470.08	1376.37
100.60	470.41	1357.76

Temperature: 260 °C, Sample: Donut sample  
Shear rate:  $\dot{\gamma} = 10 \text{ s}^{-1}$

Time (s)	$\eta^+$ (Pa.s)	$M_1^+$ (Pa)
0.00	0.00	0.00
1.88	483.08	2309.50
4.38	514.57	4917.25
6.88	521.39	8108.50
9.38	510.54	10486.89
11.88	494.14	11846.54
14.38	476.04	12302.00
16.88	459.25	12094.95
19.38	444.37	11424.30
21.88	432.71	10528.49
24.38	422.23	9492.54
26.88	412.50	8539.09
29.38	404.26	7653.97
31.88	397.36	6852.26
34.38	392.21	6123.99
36.88	389.97	5479.95
39.38	389.26	4902.49
41.88	389.57	4460.39
44.38	389.96	3971.35
46.88	391.18	3541.57
49.38	395.74	3307.74
51.88	398.08	3076.52
54.38	400.50	2861.22
56.88	402.20	2617.22
59.38	404.35	2512.13
61.88	404.80	2320.94
64.38	406.46	2168.50
66.88	408.20	2077.00
69.38	411.11	1990.62
71.88	412.55	1967.32
74.38	414.26	1974.70
76.88	415.50	2033.43
79.38	415.15	2067.71
81.88	414.93	2126.67
84.38	414.70	2116.16
86.88	414.87	2060.10
89.38	413.72	2157.35
91.88	412.19	2175.41
94.38	411.69	2270.98
96.88	412.37	2158.51
99.38	413.49	2142.36
101.88	412.73	2106.28

## A.7.2 Interrupted flow

Temperature: 260 °C, Sample: Donut sample

Test conditions:  $\dot{\gamma} = 1 \text{ s}^{-1}$  for 100 s,  $\dot{\gamma} = 0 \text{ s}^{-1}$  for 50 s,  $\dot{\gamma} = 1 \text{ s}^{-1}$  for 100 s

Time (s)	$\sigma^+$ (Pa)	$N_1^+$ (Pa)	Time (s)	$\sigma^+$ (Pa)	$N_1^+$ (Pa)	Time (s)	$\sigma^+$ (Pa)	$N_1^+$ (Pa)
0.00	0.00	0.00	41.88	575.39	505.68	83.88	546.90	228.90
0.88	664.19	566.89	42.88	572.87	486.05	84.88	545.31	205.75
1.88	733.53	720.91	43.88	570.06	460.57	85.88	544.63	194.26
2.88	788.41	938.45	44.88	568.30	426.71	86.88	543.66	205.91
3.88	832.16	1217.85	45.88	566.46	407.86	87.88	543.44	206.47
4.88	862.00	1471.34	46.88	563.61	391.62	88.88	542.92	209.96
5.88	882.30	1693.45	47.88	560.93	376.44	89.88	542.11	203.46
6.88	886.92	1842.05	48.88	559.21	370.86	90.88	541.83	192.05
7.88	885.26	1939.26	49.88	557.90	357.55	91.88	542.34	199.08
8.88	878.77	2029.10	50.88	556.64	337.69	92.88	540.74	202.00
9.88	867.19	2084.29	51.88	557.45	322.04	93.88	539.67	202.03
10.88	852.60	2105.71	52.88	557.10	326.51	94.88	540.12	204.74
11.88	837.74	2103.17	53.88	557.95	318.85	95.88	540.40	203.25
12.88	821.18	2071.58	54.88	557.73	307.28	96.88	539.93	196.02
13.88	806.65	2018.46	55.88	557.90	295.49	97.88	541.08	198.62
14.88	792.14	1974.69	56.88	558.93	280.97	98.88	541.37	194.82
15.88	777.37	1914.62	57.88	560.02	276.02	99.88	541.56	182.36
16.88	762.53	1850.98	58.88	560.52	254.76	100.44	8.21	64.86
17.88	747.08	1782.40	59.88	560.91	242.18	100.94	4.67	26.75
18.88	731.36	1693.42	60.88	561.74	248.91	101.44	3.45	10.86
19.88	716.63	1620.36	61.88	561.96	238.13	101.94	2.81	4.40
20.88	706.19	1545.20	62.88	561.74	224.32	102.44	2.48	4.39
21.88	696.54	1490.22	63.88	561.11	224.41	102.94	2.16	-0.21
22.88	686.14	1420.61	64.88	560.80	226.19	103.44	1.94	-2.99
23.88	674.93	1335.44	65.88	561.04	238.55	103.94	1.87	-1.65
24.88	664.64	1263.05	66.88	561.72	242.41	104.44	1.77	-3.72
25.88	656.12	1221.76	67.88	560.93	229.43	104.94	1.62	-3.46
26.88	646.97	1161.49	68.88	560.58	236.22	105.44	1.59	-3.35
27.88	637.50	1073.49	69.88	559.49	242.28	105.94	1.57	-3.54
28.88	630.28	1014.44	70.88	559.62	246.65	106.44	1.46	-2.93
29.88	625.46	968.38	71.88	557.62	211.92	106.94	1.39	-1.83
30.88	620.78	915.39	72.88	557.16	223.53	107.44	1.33	-1.44
31.88	615.01	855.12	73.88	556.35	217.38	107.94	1.32	-1.99
32.88	609.23	802.55	74.88	555.55	226.19	108.44	1.27	-2.88
33.88	603.40	779.73	75.88	553.90	212.83	108.94	1.20	-2.92
34.88	600.71	738.65	76.88	551.89	207.08	109.44	1.18	-2.87
35.88	595.64	712.65	77.88	551.32	203.01	109.94	1.18	-3.18
36.88	591.45	676.70	78.88	550.93	226.21	110.44	1.14	-2.31
37.88	589.17	640.56	79.88	550.06	213.25	110.94	1.12	-1.21
38.88	585.34	596.18	80.88	549.84	214.26	111.44	1.12	-0.51
39.88	580.87	567.79	81.88	550.17	228.48	111.94	1.11	-2.99
40.88	578.49	558.77	82.88	548.01	226.40	112.44	0.98	-0.84

Continued

Time (s)	$\sigma^+$ (Pa)	$N_1^+$ (Pa)	Time (s)	$\sigma^+$ (Pa)	$N_1^+$ (Pa)	Time (s)	$\sigma^+$ (Pa)	$N_1^+$ (Pa)
112.94	1.07	-0.26	133.94	0.69	-3.12	159.88	536.40	213.20
113.44	1.06	-0.50	134.44	0.68	-6.61	160.88	532.85	224.41
113.94	1.06	2.45	134.94	0.69	-6.72	161.88	531.54	226.93
114.44	1.00	0.30	135.44	0.69	-6.93	162.88	528.52	211.68
114.94	1.02	1.16	135.94	0.59	-7.45	163.88	525.99	195.70
115.44	0.94	0.23	136.44	0.70	-7.06	164.88	523.08	221.29
115.94	1.00	2.04	136.94	0.69	-5.50	165.88	520.67	221.46
116.44	0.92	-0.43	137.44	0.62	-6.49	166.88	519.14	207.08
116.94	0.92	-1.15	137.94	0.71	-5.84	167.88	517.35	212.83
117.44	0.98	-0.22	138.44	0.70	-4.82	168.88	515.02	209.42
117.94	0.94	-0.21	138.94	0.58	-4.21	169.88	514.63	193.88
118.44	0.91	-1.05	139.44	0.63	-6.51	170.88	513.47	184.57
118.94	0.89	-2.24	139.94	0.65	-6.96	171.88	512.74	195.46
119.44	0.85	0.11	140.44	0.63	-9.12	172.88	510.78	187.10
119.94	0.82	0.84	140.94	0.64	-9.53	173.88	508.95	178.78
120.44	0.84	-0.24	141.44	0.63	-10.55	174.88	507.81	173.01
120.94	0.81	1.07	141.94	0.60	-8.38	175.88	506.51	165.42
121.44	0.77	1.06	142.44	0.62	-6.67	176.88	506.73	161.89
121.94	0.83	-2.30	142.94	0.61	-5.61	177.88	507.88	174.04
122.44	0.79	-0.23	143.44	0.64	-6.63	178.88	507.36	175.05
122.94	0.75	-0.55	143.94	0.60	-6.35	179.88	509.30	152.98
123.44	0.82	-0.13	144.44	0.61	-5.52	180.88	510.67	157.66
123.94	0.71	-2.91	144.94	0.53	-6.11	181.88	511.87	174.12
124.44	0.79	-3.72	145.44	0.57	-7.47	182.88	512.04	163.33
124.94	0.77	-3.82	145.94	0.57	-7.98	183.88	511.08	167.91
125.44	0.70	-4.08	146.44	0.55	-8.48	184.88	510.55	168.32
125.94	0.76	-0.72	146.94	0.53	-5.35	185.88	510.23	173.39
126.44	0.80	-0.65	147.44	0.51	-7.82	186.88	510.50	177.08
126.94	0.75	-2.00	147.94	0.51	-7.71	187.88	511.41	186.06
127.44	0.76	-0.38	148.44	0.53	-7.80	188.88	511.24	196.23
127.94	0.76	-0.42	148.94	0.49	-7.90	189.88	512.00	192.05
128.44	0.80	-0.03	149.44	0.51	-6.23	190.88	512.73	195.51
128.94	0.78	-1.10	149.94	0.55	-7.12	191.88	514.00	181.03
129.44	0.76	-1.32	150.88	542.23	178.90	192.88	515.48	194.92
129.94	0.75	-4.21	151.88	549.60	194.82	193.88	515.07	187.02
130.44	0.76	-2.69	152.88	550.63	187.68	194.88	514.96	187.55
130.94	0.72	-2.59	153.88	549.89	183.86	195.88	515.41	189.15
131.44	0.68	-1.74	154.88	548.76	176.08	196.88	517.29	181.71
131.94	0.73	-4.50	155.88	546.85	195.99	197.88	516.90	186.99
132.44	0.68	-5.33	156.88	545.49	198.57	198.88	517.70	191.52
132.94	0.71	-2.46	157.88	542.06	195.33	199.88	518.51	184.20
133.44	0.66	-2.86	158.88	540.98	198.62	200.88	518.80	176.51

Continued

Time (s)	$\sigma^+$ (Pa)	$N_1^+$ (Pa)	Time (s)	$\sigma^+$ (Pa)	$N_1^+$ (Pa)	Time (s)	$\sigma^+$ (Pa)	$N_1^+$ (Pa)
201.88	518.75	174.87	243.88	512.56	172.40	267.94	0.56	1.21
202.88	519.43	182.98	244.88	511.76	166.80	268.44	0.60	2.89
203.88	520.00	178.27	245.88	511.36	179.17	268.94	0.52	3.87
204.88	520.73	163.76	246.88	510.91	175.64	269.44	0.54	3.35
205.88	520.79	174.89	247.88	511.02	164.34	269.94	0.57	4.11
206.88	521.36	181.22	248.88	510.73	165.84	270.44	0.51	3.17
207.88	521.41	172.68	249.88	510.85	171.71	270.94	0.52	2.27
208.88	522.56	194.52	250.44	6.21	47.26	271.44	0.55	2.85
209.88	521.48	186.92	250.94	3.38	20.42	271.94	0.49	2.37
210.88	520.95	188.46	251.44	2.41	9.33	272.44	0.54	3.16
211.88	521.25	171.26	251.94	2.00	3.96	272.94	0.50	2.22
212.88	521.58	174.04	252.44	1.69	1.54	273.44	0.50	1.97
213.88	523.09	191.33	252.94	1.45	0.78	273.94	0.53	3.41
214.88	523.03	189.68	253.44	1.38	0.16	274.44	0.43	2.17
215.88	522.39	182.26	253.94	1.21	0.30	274.94	0.52	0.57
216.88	522.85	180.24	254.44	1.16	-0.33	275.44	0.51	3.01
217.88	523.77	173.80	254.94	1.12	0.70	275.94	0.55	2.05
218.88	522.56	185.13	255.44	1.07	-0.83	276.44	0.42	1.73
219.88	522.63	187.85	255.94	1.02	0.85	276.94	0.46	2.43
220.88	523.13	197.50	256.44	0.97	1.23	277.44	0.44	2.14
221.88	522.80	195.59	256.94	0.92	0.86	277.94	0.40	3.42
222.88	523.08	184.28	257.44	0.88	-0.51	278.44	0.42	2.89
223.88	523.03	182.53	257.94	0.81	0.59	278.94	0.50	3.54
224.88	522.67	189.82	258.44	0.85	-1.91	279.44	0.41	0.83
225.88	522.11	196.76	258.94	0.79	0.84	279.94	0.44	2.44
226.88	521.82	189.31	259.44	0.82	-0.78	280.44	0.43	2.53
227.88	522.96	189.39	259.94	0.72	0.35	280.94	0.41	3.55
228.88	523.26	189.77	260.44	0.76	-0.69	281.44	0.50	4.21
229.88	522.50	191.55	260.94	0.74	0.94	281.94	0.45	4.56
230.88	522.34	198.76	261.44	0.76	0.57	282.44	0.43	5.24
231.88	522.45	198.81	261.94	0.66	1.97	282.94	0.47	4.06
232.88	521.25	186.01	262.44	0.68	2.47	283.44	0.47	4.94
233.88	520.17	188.38	262.94	0.62	1.62	283.94	0.40	3.75
234.88	519.58	176.75	263.44	0.70	1.76	284.44	0.47	4.31
235.88	519.82	188.06	263.94	0.66	1.34	284.94	0.46	4.60
236.88	517.94	170.32	264.44	0.61	0.48	285.44	0.44	3.97
237.88	517.64	196.70	264.94	0.61	2.26	285.94	0.42	5.35
238.88	517.75	183.13	265.44	0.71	1.67	286.44	0.43	3.13
239.88	517.25	183.05	265.94	0.59	2.45	286.94	0.41	4.76
240.88	515.98	174.03	266.44	0.61	3.29	287.44	0.44	5.20
241.88	514.74	172.62	266.94	0.64	4.19	287.94	0.38	5.42
242.88	513.76	176.78	267.44	0.56	2.36	288.44	0.37	4.31

Temperature: 260 °C, Sample: Donut sample

Test conditions:  $\dot{\gamma} = 1 \text{ s}^{-1}$  for 100 s,  $\dot{\gamma} = 0 \text{ s}^{-1}$  for 200 s,  $\dot{\gamma} = 1 \text{ s}^{-1}$  for 50 s

Time (s)	$\sigma^+$ (Pa)	$N_1^+$ (Pa)	Time (s)	$\sigma^+$ (Pa)	$N_1^+$ (Pa)	Time (s)	$\sigma^+$ (Pa)	$N_1^+$ (Pa)
0.00	0.00	0.00	41.88	533.03	582.46	83.88	267.12	532.11
0.88	509.33	620.13	42.88	520.53	580.98	84.88	273.86	531.81
1.88	652.67	685.88	43.88	507.11	578.72	85.88	279.61	530.80
2.88	760.93	734.87	44.88	475.11	577.22	86.88	270.81	530.67
3.88	951.28	774.32	45.88	472.19	574.54	87.88	248.16	529.65
4.88	1143.69	799.54	46.88	469.09	571.25	88.88	258.33	531.22
5.88	1389.03	815.98	47.88	467.47	569.00	89.88	259.80	531.57
6.88	1626.24	821.00	48.88	471.14	568.05	90.88	251.49	533.67
7.88	1779.37	819.98	49.88	458.77	564.34	91.88	262.67	533.61
8.88	1884.81	817.54	50.88	436.24	564.23	92.88	262.78	534.49
9.88	1941.94	806.32	51.88	419.30	562.52	93.88	263.51	534.54
10.88	1961.52	794.94	52.88	405.00	560.19	94.88	250.68	533.77
11.88	1941.10	782.21	53.88	395.32	559.47	95.88	270.30	532.59
12.88	1913.16	769.02	54.88	405.60	557.80	96.88	273.23	532.88
13.88	1848.83	757.88	55.88	393.79	555.35	97.88	264.21	532.77
14.88	1776.30	747.44	56.88	379.45	551.84	98.88	260.64	532.17
15.88	1684.28	736.77	57.88	363.59	549.40	99.88	276.40	534.56
16.88	1594.18	724.38	58.88	361.75	547.84	101.75	14.52	1.73
17.88	1521.02	712.16	59.88	349.14	546.53	103.75	9.59	0.52
18.88	1448.70	703.04	60.88	349.37	544.87	105.75	5.96	0.08
19.88	1364.45	692.37	61.88	355.91	542.95	107.75	8.96	-0.15
20.88	1285.92	681.64	62.88	339.03	542.60	109.75	9.94	-0.28
21.88	1225.98	673.54	63.88	339.61	543.18	111.75	7.91	-0.34
22.88	1183.44	663.23	64.88	339.00	542.71	113.75	13.20	-0.43
23.88	1124.62	656.20	65.88	333.28	542.06	115.75	12.91	-0.57
24.88	1086.29	650.42	66.88	327.80	542.12	117.75	15.51	-0.55
25.88	1039.10	645.41	67.88	315.99	539.98	119.75	20.10	-0.64
26.88	986.57	639.99	68.88	314.13	538.24	121.75	20.16	-0.62
27.88	933.87	636.46	69.88	302.69	536.04	123.75	19.68	-0.67
28.88	895.23	631.40	70.88	290.62	535.87	125.75	21.45	-0.69
29.88	851.99	623.31	71.88	292.74	535.33	127.75	22.45	-0.76
30.88	826.97	616.32	72.88	291.14	537.05	129.75	21.04	-0.79
31.88	783.68	610.89	73.88	297.68	538.85	131.75	21.83	-0.87
32.88	743.95	606.01	74.88	274.09	538.26	133.75	19.79	-0.88
33.88	709.83	601.77	75.88	267.01	537.70	135.75	21.47	-0.90
34.88	688.96	599.15	76.88	276.63	536.52	137.75	21.78	-0.93
35.88	670.71	596.78	77.88	269.32	536.34	139.75	26.11	-1.03
36.88	656.25	593.87	78.88	282.86	535.81	141.75	23.09	-0.99
37.88	638.93	591.83	79.88	281.34	535.68	143.75	23.62	-0.98
38.88	609.04	588.01	80.88	285.89	535.45	145.75	29.68	-1.01
39.88	578.78	586.28	81.88	281.31	533.66	147.75	28.19	-0.95
40.88	547.66	584.37	82.88	275.13	533.42	149.75	27.58	-1.00

Continued

Time (s)	$\sigma^+$ (Pa)	$N_1^+$ (Pa)	Time (s)	$\sigma^+$ (Pa)	$N_1^+$ (Pa)	Time (s)	$\sigma^+$ (Pa)	$N_1^+$ (Pa)
151.75	28.91	-1.00	235.75	35.51	-1.41	309.88	252.25	541.27
153.75	27.35	-1.02	237.75	34.73	-1.36	310.88	265.55	537.30
155.75	27.19	-0.96	239.75	29.53	-1.44	311.88	278.93	533.60
157.75	28.33	-0.99	241.75	39.08	-1.37	312.88	272.20	529.08
159.75	29.60	-1.00	243.75	34.06	-1.42	313.88	264.60	526.39
161.75	26.78	-0.98	245.75	31.90	-1.42	314.88	265.85	522.81
163.75	26.83	-0.97	247.75	24.40	-1.35	315.88	272.20	520.84
165.75	28.17	-1.03	249.75	27.66	-1.36	316.88	286.25	519.30
167.75	28.16	-1.08	251.75	21.68	-1.38	317.88	284.57	517.93
169.75	29.16	-1.05	253.75	29.45	-1.44	318.88	267.18	518.41
171.75	29.08	-1.10	255.75	29.49	-1.35	319.88	259.74	518.82
173.75	29.13	-1.12	257.75	26.96	-1.32	320.88	246.53	519.47
175.75	29.16	-1.13	259.75	27.76	-1.28	321.88	243.35	518.69
177.75	28.53	-1.09	261.75	28.04	-1.34	322.88	239.28	517.80
179.75	28.02	-1.18	263.75	28.08	-1.36	323.88	236.05	517.09
181.75	29.62	-1.15	265.75	35.11	-1.36	324.88	246.50	516.91
183.75	30.17	-1.17	267.75	30.82	-1.31	325.88	229.21	515.95
185.75	28.94	-1.21	269.75	29.36	-1.36	326.88	230.30	517.09
187.75	30.31	-1.19	271.75	29.90	-1.33	327.88	255.35	517.57
189.75	34.10	-1.22	273.75	24.42	-1.40	328.88	258.63	517.86
191.75	31.90	-1.19	275.75	24.61	-1.41	329.88	241.45	518.47
193.75	31.68	-1.23	277.75	21.18	-1.43	330.88	257.33	519.47
195.75	32.81	-1.23	279.75	24.13	-1.45	331.88	269.11	518.45
197.75	33.54	-1.20	281.75	25.38	-1.44	332.88	283.13	518.45
199.75	34.82	-1.21	283.75	24.50	-1.42	333.88	285.11	518.82
201.75	34.57	-1.25	285.75	31.31	-1.41	334.88	287.20	518.99
203.75	32.85	-1.19	287.75	22.75	-1.49	335.88	287.28	518.88
205.75	34.53	-1.23	289.75	26.55	-1.45	336.88	282.40	518.82
207.75	36.32	-1.15	291.75	25.63	-1.47	337.88	287.32	517.74
209.75	35.38	-1.20	293.75	26.54	-1.44	338.88	271.44	519.47
211.75	35.08	-1.22	295.75	27.17	-1.43	339.88	264.87	518.93
213.75	34.86	-1.23	297.75	25.32	-1.49	340.88	249.15	517.99
215.75	34.03	-1.24	299.75	25.54	-1.47	341.88	267.69	518.05
217.75	35.80	-1.29	300.88	258.39	541.34	342.88	278.84	517.99
219.75	33.88	-1.31	301.88	235.10	551.30	343.88	287.64	516.98
221.75	36.03	-1.30	302.88	217.77	556.37	344.88	287.04	517.22
223.75	34.65	-1.26	303.88	228.87	558.51	345.88	287.45	516.84
225.75	33.80	-1.27	304.88	232.45	557.73	346.88	276.41	516.12
227.75	36.15	-1.27	305.88	231.61	556.07	347.88	283.92	516.49
229.75	35.46	-1.30	306.88	240.07	554.52	348.88	290.79	514.95
231.75	34.78	-1.29	307.88	263.14	550.47	349.88	281.18	513.94
233.75	35.83	-1.35	308.88	268.42	547.01	350.88	272.65	512.69

Temperature: 260 °C, Sample: Donut sample

Test conditions:  $\dot{\gamma} = 1 \text{ s}^{-1}$  for 10 s,  $\dot{\gamma} = 0 \text{ s}^{-1}$  for 20 s,  $\dot{\gamma} = 1 \text{ s}^{-1}$  for 70 s

Time (s)	$\sigma^+$ (Pa)	$N_1^+$ (Pa)	Time (s)	$\sigma^+$ (Pa)	$N_1^+$ (Pa)	Time (s)	$\sigma^+$ (Pa)	$N_1^+$ (Pa)
0.00	0.00	0.00	20.53	8.02	9.30	50.81	661.24	1091.27
0.49	630.69	368.54	21.03	7.74	6.34	51.71	657.48	1049.61
0.99	677.39	512.10	21.53	7.50	3.97	52.61	656.76	1016.94
1.49	711.73	611.85	22.03	7.30	1.59	53.51	653.46	1007.02
1.99	744.33	693.56	22.53	6.94	2.13	54.41	649.00	984.71
2.49	775.17	792.33	23.03	6.82	1.12	55.31	645.74	954.99
2.99	797.77	897.99	23.53	6.67	0.21	56.21	644.57	926.87
3.49	818.04	1011.53	24.03	6.49	-0.22	57.11	640.60	897.01
3.99	836.25	1113.58	24.53	6.34	1.08	58.01	639.05	874.28
4.49	848.59	1216.61	25.03	6.06	-3.55	58.91	637.24	856.74
4.99	856.50	1328.17	25.53	6.00	1.98	59.81	634.22	827.62
5.49	863.57	1440.40	26.03	5.91	-0.22	60.71	630.31	811.03
5.99	868.26	1534.24	26.53	5.76	-4.19	61.61	628.34	772.73
6.49	867.66	1616.93	27.03	5.61	2.27	62.51	626.07	754.43
6.99	865.90	1698.34	27.53	5.41	-1.59	63.41	624.16	747.71
7.49	866.78	1775.10	28.03	5.51	1.59	64.31	622.24	725.39
7.99	861.21	1840.72	28.53	5.31	3.01	65.21	621.31	708.33
8.49	856.52	1903.73	29.03	5.20	5.99	66.11	617.85	682.26
8.99	853.28	1939.85	29.53	5.02	5.17	67.01	615.21	670.59
9.49	850.64	1964.78	30.11	539.50	779.90	67.91	611.61	638.60
9.99	843.59	1998.89	31.01	809.75	1876.47	68.81	610.36	602.66
10.03	578.30	1872.23	31.91	812.77	1976.92	69.71	608.74	588.23
10.53	58.41	470.58	32.81	806.37	1994.16	70.61	607.93	581.10
11.03	39.59	298.80	33.71	798.37	1976.12	71.51	605.52	581.59
11.53	30.91	214.59	34.61	785.96	1948.02	72.41	603.38	577.56
12.03	25.57	164.88	35.51	775.69	1931.63	73.31	602.95	573.70
12.53	22.14	122.73	36.41	764.81	1879.68	74.21	602.57	560.17
13.03	19.48	95.51	37.31	754.10	1836.83	75.11	600.97	550.82
13.53	17.48	77.70	38.21	746.26	1796.63	76.01	600.88	542.62
14.03	15.87	62.02	39.11	737.09	1742.80	76.91	599.71	539.01
14.53	14.61	54.22	40.01	728.47	1694.57	77.81	599.40	521.82
15.03	13.58	46.08	40.91	721.08	1642.43	78.71	597.73	510.54
15.53	12.75	41.41	41.81	715.20	1577.41	79.61	596.47	506.07
16.03	12.03	37.32	42.71	708.95	1513.28	80.51	595.83	503.40
16.53	11.36	31.92	43.61	701.32	1455.47	81.41	596.62	482.03
17.03	10.74	27.97	44.51	695.80	1396.11	82.31	595.83	450.04
17.53	10.18	24.37	45.41	691.41	1352.46	83.21	595.07	447.90
18.03	9.67	20.18	46.31	686.27	1313.30	84.11	593.99	436.51
18.53	9.27	19.03	47.21	680.25	1262.87	85.01	594.35	421.82
19.03	8.96	11.33	48.11	675.11	1217.28	85.91	592.00	423.14
19.53	8.61	11.79	49.01	670.63	1181.66	86.81	591.13	417.87
20.03	8.37	7.86	49.91	665.58	1138.99	87.71	592.52	422.96

Continued

Time (s)	$\sigma^+$ (Pa)	$N_1^+$ (Pa)
88.61	592.09	427.60
89.51	590.02	439.75
90.41	589.87	424.08
91.31	589.37	407.01
92.21	591.04	406.52
93.11	589.44	393.81
94.01	589.07	390.65
94.91	587.72	382.57
95.81	586.91	384.78
96.71	586.22	378.02
97.61	586.51	375.39
98.51	585.67	368.70
99.41	586.36	382.41
100.31	585.60	387.25

### A.7.3 Flow reversal, following startup of flow

Temperature: 260 °C, Sample: Donut sample

Shear rate:  $\dot{\gamma} = 1 \text{ s}^{-1}$

Time (s)	$\eta^+$ (Pa.s)	$N_1^+$ (Pa)	Time (s)	$\eta^+$ (Pa.s)	$N_1^+$ (Pa)
0.00	0.00	0.00	80.31	513.29	306.90
1.56	431.80	-241.57	82.19	512.12	289.21
3.44	487.03	-269.82	84.06	510.96	283.33
5.31	547.31	-318.64	85.94	512.42	273.34
7.19	605.41	-304.25	87.81	512.24	267.16
9.06	652.38	-256.72	89.69	512.24	283.36
10.94	683.97	-175.29	91.56	511.78	275.68
12.81	698.51	-72.78	93.44	510.74	260.76
14.69	702.01	6.27	95.31	510.50	244.19
16.56	694.91	112.51	97.19	510.21	263.21
18.44	685.76	196.61	99.06	509.99	264.00
20.31	673.00	268.48	100.94	508.60	260.73
22.19	660.07	296.92			
24.06	646.10	321.17			
25.94	632.01	386.59			
27.81	620.30	390.42			
29.69	607.45	412.35			
31.56	597.39	409.19			
33.44	587.96	406.57			
35.31	580.41	406.46			
37.19	572.48	434.29			
39.06	566.69	413.49			
40.94	559.73	381.25			
42.81	554.86	392.49			
44.69	548.88	390.25			
46.56	545.58	365.42			
48.44	542.04	344.59			
50.31	537.29	349.06			
52.19	533.21	347.53			
54.06	530.50	327.88			
55.94	528.07	326.40			
57.81	526.56	326.22			
59.69	523.65	316.28			
61.56	522.51	299.24			
63.44	521.18	315.62			
65.31	520.41	313.79			
67.19	520.76	293.04			
69.06	519.90	298.31			
70.94	519.66	293.78			
72.81	517.75	290.19			
74.69	516.54	261.66			
76.56	515.27	283.03			
78.44	515.03	284.37			

Temperature: 260 °C, Sample: Donut sample  
 Shear rate:  $\dot{\gamma} = 2 \text{ s}^{-1}$

Time (s)	$\eta^+$ (Pa.s)	$N_1^+$ (Pa)	Time (s)	$\eta^+$ (Pa.s)	$N_1^+$ (Pa)
0.00	0.00	0.00	64.25	505.60	624.48
1.25	423.01	-349.47	65.75	503.85	606.70
2.75	452.94	-502.07	67.25	502.01	611.87
4.25	491.50	-620.40	68.75	501.44	610.51
5.75	533.20	-686.16	70.25	501.26	594.14
7.25	575.30	-686.37	71.75	500.99	607.83
8.75	611.97	-614.58	73.25	501.44	601.79
10.25	641.44	-547.85	74.75	499.97	573.96
11.75	662.76	-451.50	76.25	498.75	550.87
13.25	676.08	-323.28	77.75	497.35	550.87
14.75	683.65	-149.40	79.25	495.66	587.61
16.25	684.03	63.91	80.75	494.64	600.65
17.75	680.88	221.31	82.25	494.47	605.06
19.25	673.60	306.99	83.75	493.74	575.71
20.75	664.89	409.83	85.25	493.07	556.00
22.25	653.62	529.92	86.75	493.30	556.82
23.75	642.33	596.14	88.25	492.52	537.68
25.25	631.44	629.89	89.75	492.56	548.97
26.75	620.61	692.62	91.25	491.60	549.30
28.25	609.28	745.17	92.75	491.39	524.20
29.75	599.78	807.37	94.25	490.50	510.83
31.25	591.03	819.26	95.75	489.94	508.92
32.75	581.82	819.37	97.25	490.05	491.83
34.25	573.63	810.98	98.75	489.36	508.26
35.75	566.78	831.82	100.25	489.21	537.13
37.25	560.39	851.15			
38.75	554.60	831.15			
40.25	549.55	837.82			
41.75	544.44	779.88			
43.25	540.01	767.09			
44.75	535.35	757.17			
46.25	531.24	759.14			
47.75	528.32	779.86			
49.25	525.52	793.85			
50.75	523.15	762.53			
52.25	521.26	752.26			
53.75	518.78	742.23			
55.25	516.65	726.24			
56.75	513.96	702.73			
58.25	511.71	676.59			
59.75	510.08	687.72			
61.25	508.29	661.25			
62.75	506.94	639.97			

Temperature: 260 °C, Sample: Donut sample  
 Shear rate:  $\dot{\gamma} = 4 \text{ s}^{-1}$

Time (s)	$\eta^+$ (Pa.s)	$N_1^+$ (Pa)	Time (s)	$\eta^+$ (Pa.s)	$N_1^+$ (Pa)
0.00	0.00	0.00	64.25	472.20	1163.40
1.25	425.41	-433.14	65.75	471.70	1145.65
2.75	451.48	-647.66	67.25	470.86	1125.97
4.25	483.93	-862.15	68.75	469.67	1097.53
5.75	517.78	-1000.74	70.25	469.45	1104.59
7.25	551.56	-1046.67	71.75	469.33	1103.15
8.75	581.06	-990.93	73.25	468.67	1102.54
10.25	603.85	-896.10	74.75	467.42	1105.04
11.75	620.68	-732.51	76.25	467.09	1089.31
13.25	630.50	-528.15	77.75	465.91	1055.91
14.75	633.14	-271.81	79.25	466.02	1026.26
16.25	631.61	-34.21	80.75	465.29	1028.18
17.75	626.44	159.81	82.25	465.07	1016.64
19.25	619.48	418.96	83.75	464.45	1002.22
20.75	610.78	592.75	85.25	462.99	1026.24
22.25	601.49	801.56	86.75	462.37	1060.95
23.75	591.44	996.78	88.25	463.27	1013.92
25.25	581.48	1121.73	89.75	462.99	995.15
26.75	571.33	1238.16	91.25	462.88	1022.53
28.25	562.11	1331.79	92.75	463.56	1009.12
29.75	553.25	1394.55	94.25	464.56	965.90
31.25	545.90	1446.35	95.75	464.17	964.49
32.75	538.72	1434.70	97.25	464.45	974.20
34.25	532.15	1461.01	98.75	464.74	952.71
35.75	525.76	1478.45	100.25	464.72	946.15
37.25	519.62	1521.88			
38.75	515.03	1529.50			
40.25	509.59	1546.56			
41.75	505.09	1574.05			
43.25	500.66	1550.70			
44.75	496.95	1474.10			
46.25	493.03	1448.11			
47.75	489.65	1463.62			
49.25	487.30	1476.26			
50.75	484.84	1455.55			
52.25	483.08	1405.02			
53.75	481.11	1378.50			
55.25	479.22	1384.82			
56.75	477.30	1339.55			
58.25	476.41	1300.46			
59.75	475.34	1272.63			
61.25	474.28	1223.44			
62.75	473.32	1184.70			

Temperature: 260 °C, Sample: Donut sample  
 Shear rate:  $\dot{\gamma} = 6 \text{ s}^{-1}$

Time (s)	$\eta^+$ (Pa.s)	$N_1^+$ (Pa)	Time (s)	$\eta^+$ (Pa.s)	$N_1^+$ (Pa)
0.00	0.00	0.00	51.45	484.84	2101.78
1.05	440.32	-570.90	52.65	484.25	2032.41
2.25	456.86	-807.47	53.85	483.51	2012.74
3.45	479.77	-1056.28	55.05	482.23	1999.25
4.65	504.53	-1223.89	56.25	480.66	2022.34
5.85	528.93	-1312.29	57.45	481.03	2010.13
7.05	552.44	-1364.23	58.65	479.61	1994.88
8.25	573.17	-1320.56	59.85	477.51	1986.13
9.45	590.15	-1256.20	61.05	476.61	1948.59
10.65	603.64	-1078.54	62.25	475.42	1900.13
11.85	612.60	-860.30	63.45	474.82	1906.26
13.05	616.36	-606.25	64.65	473.77	1898.42
14.25	618.45	-264.63	65.85	473.85	1866.53
15.45	617.55	40.48	67.05	472.79	1796.68
16.65	613.06	298.72	68.25	472.34	1777.49
17.85	609.47	590.30	69.45	471.53	1834.22
19.05	602.28	827.64	70.65	470.55	1862.59
20.25	593.83	1110.50	71.85	469.73	1837.26
21.45	587.17	1261.75	73.05	468.90	1784.47
22.65	578.85	1481.53	74.25	466.96	1811.08
23.85	571.75	1653.95	75.45	465.70	1792.74
25.05	564.41	1782.29	76.65	465.02	1748.64
26.25	558.04	1946.41	77.85	463.30	1724.65
27.45	552.36	2102.21	79.05	461.73	1724.22
28.65	545.40	2204.37	80.25	460.53	1725.96
29.85	539.64	2287.71	81.45	460.90	1692.76
31.05	534.31	2356.23	82.65	461.42	1677.06
32.25	530.06	2331.81	83.85	461.42	1638.22
33.45	525.11	2322.21	85.05	460.67	1583.67
34.65	520.93	2384.22	86.25	460.98	1563.57
35.85	517.71	2367.64	87.45	461.95	1524.72
37.05	514.49	2375.48	88.65	461.34	1518.17
38.25	510.37	2324.40	89.85	460.53	1528.64
39.45	507.31	2299.50	91.05	459.78	1578.84
40.65	504.24	2284.73	92.25	457.30	1541.31
41.85	502.97	2239.72	93.45	456.56	1536.08
43.05	501.99	2242.34	94.65	457.30	1485.91
44.25	498.02	2263.72	95.85	457.01	1487.64
45.45	495.55	2284.67	97.05	456.71	1476.71
46.65	492.86	2223.14	98.25	456.48	1426.29
47.85	490.01	2143.69	99.45	453.86	1451.41
49.05	486.87	2182.14	100.65	453.12	1476.28
50.25	485.07	2188.22			

Temperature: 260 °C, Sample: Donut sample  
 Shear rate:  $\dot{\gamma} = 8 \text{ s}^{-1}$

Time (s)	$\eta^+$ (Pa.s)	$N_1^+$ (Pa)	Time (s)	$\eta^+$ (Pa.s)	$N_1^+$ (Pa)
0.00	0.00	0.00	51.40	438.41	2283.12
1.00	411.35	-759.70	52.60	438.13	2312.82
2.20	423.20	-1033.84	53.80	437.01	2292.71
3.40	441.50	-1248.59	55.00	435.89	2268.29
4.60	461.87	-1428.86	56.20	434.65	2209.80
5.80	484.10	-1517.93	57.40	433.42	2170.08
7.00	505.10	-1565.04	58.60	432.97	2107.64
8.20	523.74	-1520.09	59.80	432.57	2076.66
9.40	539.46	-1412.49	61.00	432.35	1992.84
10.60	551.68	-1266.50	62.20	432.52	1907.31
11.80	561.13	-1097.34	63.40	431.45	1886.79
13.00	565.72	-853.78	64.60	430.11	1844.45
14.20	566.06	-505.23	65.80	429.26	1818.70
15.40	564.72	-175.76	67.00	427.97	1818.70
16.60	560.56	162.52	68.20	426.62	1799.93
17.80	554.50	462.60	69.40	426.29	1766.76
19.00	549.11	774.26	70.60	425.44	1767.61
20.20	540.70	1072.72	71.80	424.88	1751.03
21.40	533.84	1396.16	73.00	424.15	1777.21
22.60	526.88	1607.84	74.20	422.13	1745.78
23.80	521.14	1781.58	75.40	419.99	1686.43
25.00	516.77	1919.10	76.60	418.65	1715.68
26.20	510.71	2081.03	77.80	418.25	1709.55
27.40	505.21	2202.82	79.00	417.25	1698.67
28.60	499.83	2207.61	80.20	417.08	1721.79
29.80	494.21	2261.73	81.40	417.19	1737.06
31.00	489.82	2317.19	82.60	417.30	1728.74
32.20	484.78	2402.29	83.80	416.01	1629.67
33.40	480.85	2454.65	85.00	415.62	1572.06
34.60	477.26	2500.50	86.20	414.73	1544.58
35.80	472.56	2527.59	87.40	414.33	1571.64
37.00	469.28	2604.85	88.60	414.44	1535.83
38.20	465.36	2677.31	89.80	412.42	1511.81
39.40	463.22	2678.17	91.00	412.09	1527.97
40.60	460.87	2643.67	92.20	411.86	1515.30
41.80	457.72	2573.39	93.40	411.13	1539.78
43.00	454.13	2531.91	94.60	409.89	1524.93
44.20	450.76	2552.86	95.80	408.83	1547.61
45.40	447.50	2472.56	97.00	407.43	1608.75
46.60	444.70	2443.72	98.20	406.58	1615.70
47.80	443.07	2398.39	99.40	405.85	1637.54
49.00	440.27	2351.63	100.60	405.68	1635.78
50.20	438.69	2313.67			

Temperature: 260 °C, Sample: Donut sample  
 Shear rate:  $\dot{\gamma} = 10 \text{ s}^{-1}$

Time (s)	$\eta^+$ (Pa.s)	$N_1^+$ (Pa)	Time (s)	$\eta^+$ (Pa.s)	$N_1^+$ (Pa)
0.00	0.00	0.00	64.25	420.83	2308.06
1.25	379.93	-928.08	65.75	420.39	2232.21
2.75	402.72	-1486.47	67.25	419.65	2270.69
4.25	431.08	-1847.67	68.75	418.62	2094.06
5.75	460.67	-2171.44	70.25	418.43	2187.40
7.25	490.20	-2186.84	71.75	418.32	2145.03
8.75	515.98	-2190.73	73.25	417.74	2222.61
10.25	535.90	-1917.33	74.75	416.65	2109.49
11.75	550.61	-1621.13	76.25	416.36	2156.06
13.25	559.19	-1123.00	77.75	415.33	2048.10
14.75	561.50	-715.34	79.25	415.42	2066.12
16.25	560.17	-149.03	80.75	414.79	1951.80
17.75	555.65	209.60	82.25	414.59	2006.95
19.25	549.57	820.15	83.75	414.05	1937.94
20.75	541.96	1058.45	85.25	412.78	2066.07
22.25	533.84	1565.68	86.75	412.24	2019.02
23.75	525.05	1926.78	88.25	413.02	2001.38
25.25	516.35	2261.99	89.75	412.78	1923.45
26.75	507.48	2382.59	91.25	412.68	2058.46
28.25	499.42	2653.54	92.75	413.27	1912.69
29.75	491.68	2742.87	94.25	414.15	1902.86
31.25	485.25	2927.99	95.75	413.81	1860.54
32.75	478.97	2785.83	97.25	414.05	1959.30
34.25	473.23	2918.65	98.75	414.31	1796.95
35.75	467.64	2915.01	100.25	414.29	1862.33
37.25	462.28	3082.95			
38.75	458.27	2980.33			
40.25	453.51	3094.18			
41.75	449.58	3111.15			
43.25	445.71	3142.08			
44.75	442.46	2866.67			
46.25	439.04	2892.18			
47.75	436.08	2884.59			
49.25	434.03	2989.36			
50.75	431.88	2828.60			
52.25	430.34	2803.79			
53.75	428.62	2709.94			
55.25	426.96	2801.75			
56.75	425.29	2590.61			
58.25	424.51	2589.27			
59.75	423.57	2492.74			
61.25	422.65	2470.67			
62.75	421.80	2272.93			

A.7.4 Steady state  $\eta$  and  $N_1$  in startup of flow (CW) and flow reversal (CCW)

Temperature: 260 °C, Sample: Donut sample

$\dot{\gamma}$	$\eta$ (Pa)-CW	$\eta$ (Pa.s)-CCW	$N_1$ (Pa)-CW	$N_1$ (Pa)-CCW
1	550.3	510.19	250.10	268.78
2	562.8	489.43	438.00	520.50
4	498.9	471.42	781.60	970.33
6	481.6	463.91	1208.50	1463.00
8	457.4	412.38	1656.10	1616.03
10	402.9	403.99	2009.40	1971.07

### A.8 Steady state $\eta$ and $N_1$ as a function of concentration for PBT

Temperature: 260 °C, Sample: Donut sample

$\phi$	$\eta$ (Pa.s)-CW	$N_1$ (Pa)-CW
0.3000	550.30	250.10
0.2500	461.28	215.38
0.2000	398.81	135.19
0.1500	411.69	97.62
0.0842	399.36	15.17
0.0407	387.59	2.18
0.0000	385.12	90.98

## **Appendix B. Fiber Orientation Analysis and Data**

## **Appendix B. Fiber Orientation Analysis and Data**

### B.1 Orientation analysis

The imaging program used to determine the orientation of each fiber, and the average orientation of the sample was written by Gregorio M. Vélez-García. The only contribution of the author to the program was in the form of discussion of format, and validation and as a result is not included in this dissertation. However, it will be published in the final dissertation of Gregorio M. Vélez-García upon completion of his PhD which is scheduled for 2009.

B.2.1 Fiber orientation data, parallel plate sample,  $\gamma = 0$

Position	$A_{11}$	$A_{22}$	$A_{33}$	$A_{12}$	$A_{13}$	$A_{23}$	$A_{1212}$	$A_{1211}$	$A_{1222}$	$A_{1233}$
1	0.4408	0.0472	0.5121	0.0895	-0.0172	-0.0215	0.0198	0.0559	0.0144	0.0191
2	0.5416	0.0494	0.4089	0.0890	-0.0549	-0.0221	0.0235	0.0553	0.0161	0.0176
3	0.4579	0.0911	0.4510	0.1075	0.0023	-0.0415	0.0301	0.0709	0.0263	0.0102
Average	0.4811	0.0618	0.4570	0.0950	-0.0241	-0.0280	0.0243	0.0604	0.0188	0.0158

B.3.1 Fiber orientation data, donut sample,  $\gamma = 0$

Position	A11	A22	A33	A12	A13	A23	A1212	A1211	A1222	A1233
1	0.5140	0.0441	0.4419	0.1106	0.0130	0.0113	0.0227	0.0680	0.0105	0.0321
2	0.4044	0.0415	0.5541	0.0581	0.1170	0.0545	0.0179	0.0290	0.0075	0.0216
3	0.3808	0.0261	0.5931	0.0596	0.0562	0.0306	0.0103	0.0360	0.0020	0.0217
4	0.7375	0.0272	0.2354	0.0686	0.0529	0.0440	0.0156	0.0609	0.0042	0.0036
Average 1-3	0.4371	0.0377	0.5252	0.0777	0.0604	0.0314	0.0173	0.0454	0.0069	0.0255
Average 1-4	0.5167	0.0349	0.4484	0.0753	0.0584	0.0347	0.0169	0.0495	0.0062	0.0197

B.3.2 Fiber orientation data, donut sample,  $\gamma = 4$

Position	$A_{11}$	$A_{22}$	$A_{33}$	$A_{12}$	$A_{13}$	$A_{23}$	$A_{1212}$	$A_{1211}$	$A_{1222}$	$A_{1233}$
1	0.6159	0.1442	0.2399	0.2174	0.0150	0.0189	0.0750	0.1405	0.0495	0.0274
4	0.5367	0.0419	0.4214	0.0307	0.1026	0.0893	0.0119	0.0185	0.0031	0.0091
Average 1&4	0.5803	0.0982	0.3215	0.1335	0.0544	0.0505	0.0466	0.0857	0.0286	0.0192

B.3.3 Fiber orientation data, donut sample,  $\gamma = 7$

Position	A11	A22	A33	A12	A13	A23	A1212	A1211	A1222	A1233
1	0.6657	0.0690	0.2653	0.1628	0.0951	0.0763	0.0355	0.1086	0.0159	0.0383
2	0.4564	0.1549	0.3887	0.1520	-0.1624	-0.0964	0.0345	0.0752	0.0399	0.0369
3	0.6801	0.0509	0.2690	0.1402	-0.1160	-0.0165	0.0353	0.1056	0.0165	0.0182
4	0.4235	0.0502	0.5262	0.1055	-0.0098	0.0035	0.0310	0.0645	0.0190	0.0220
Average 1-3	0.6010	0.0918	0.3071	0.1524	-0.0537	-0.0087	0.0351	0.0967	0.0240	0.0318
Average 1-4	0.5457	0.0789	0.3754	0.1378	-0.0400	-0.0049	0.0338	0.0866	0.0224	0.0287

B.3.4 Fiber orientation data, donut sample,  $\gamma = 9$

Position	A11	A22	A33	A12	A13	A23	A1212	A1211	A1222	A1233
1	0.6800	0.0893	0.2306	0.1440	-0.0338	-0.0207	0.0478	0.1008	0.0239	0.0193
2	0.6481	0.0990	0.2529	0.1786	-0.0207	-0.0128	0.0532	0.1248	0.0304	0.0234
3	0.4896	0.0716	0.4388	0.1009	0.0414	0.0399	0.0348	0.0608	0.0168	0.0233
4	0.4249	0.0585	0.5166	0.0415	0.0711	0.0997	0.0126	0.0289	0.0038	0.0088
Average 1-3	0.6128	0.0872	0.2999	0.1426	-0.0071	-0.0001	0.0457	0.0968	0.0239	0.0218
Average 1-4	0.5645	0.0798	0.3557	0.1166	0.0130	0.0256	0.0372	0.0794	0.0188	0.0185

B.3.5 Fiber orientation data, donut sample,  $\gamma = 12$

Position	A11	A22	A33	A12	A13	A23	A1212	A1211	A1222	A1233
1	0.4931	0.0922	0.4147	0.1024	-0.0611	-0.0454	0.0315	0.0562	0.0233	0.0228
2	0.5429	0.0740	0.3831	0.1140	0.0039	0.0045	0.0311	0.0669	0.0176	0.0296
3	0.6326	0.0823	0.2851	0.1540	0.0798	0.0269	0.0391	0.1047	0.0233	0.0260
4	0.7446	0.0681	0.1874	0.0371	0.0705	0.0391	0.0311	0.0392	-0.0086	0.0065
Average 1-3	0.5510	0.0831	0.3658	0.1215	0.0023	-0.0073	0.0336	0.0741	0.0214	0.0260
Average 1-4	0.6077	0.0787	0.3136	0.0968	0.0223	0.0063	0.0329	0.0639	0.0126	0.0203

B.3.6 Fiber orientation data, donut sample,  $\gamma = 25$

Position	$A_{11}$	$A_{22}$	$A_{33}$	$A_{12}$	$A_{13}$	$A_{23}$	$A_{1212}$	$A_{1211}$	$A_{1222}$	$A_{1233}$
1	0.6109	0.0871	0.3021	0.1464	-0.0401	-0.0227	0.0405	0.0948	0.0275	0.024
4	0.8377	0.0131	0.1492	0.0151	-0.0245	0.015	0.0097	0.0184	-0.0001	-0.0032
Average 1&4	0.6985	0.0585	0.2431	0.0957	-0.0341	-0.0081	0.0286	0.0653	0.0168	0.0135

B.3.7 Fiber orientation data, donut sample,  $\gamma = 50$

Position	A11	A22	A33	A12	A13	A23	A1212	A1211	A1222	A1233
1	0.6882	0.0524	0.2594	0.0721	-0.0345	-0.0038	0.0406	0.0554	0.0063	0.0104
2	0.7741	0.0605	0.1654	0.1530	-0.0765	-0.0136	0.0444	0.1186	0.0189	0.0154
3	0.7736	0.0560	0.1704	0.1497	-0.0227	-0.0013	0.0406	0.1175	0.0184	0.0138
4	0.8102	0.0373	0.1525	0.0449	0.1209	0.0355	0.0178	0.0400	-0.0018	0.0067
Average 1-3	0.7372	0.0558	0.2070	0.1175	-0.0441	-0.0061	0.0418	0.0913	0.0134	0.0128
Average 1-4	0.7515	0.0522	0.1963	0.1033	-0.0118	0.0020	0.0371	0.0812	0.0104	0.0116

### B.3.8 Fiber orientation data, donut sample, $\gamma = 100$

Position	$A_{11}$	$A_{22}$	$A_{33}$	$A_{12}$	$A_{13}$	$A_{23}$	$A_{1212}$	$A_{1211}$	$A_{1222}$	$A_{1233}$
1	0.7348	0.0913	0.1739	0.1866	-0.0002	0.0005	0.0561	0.1408	0.0319	0.0139
4	0.8122	0.0182	0.1696	0.0058	-0.0014	0.0262	0.0110	0.0049	0.0005	0.0004
Average 1&4	0.7722	0.0560	0.1718	0.0993	-0.0008	0.0129	0.0343	0.0751	0.0167	0.0074

B.3.9 Fiber orientation data, donut sample,  $\gamma = 200$

Position	$A_{11}$	$A_{22}$	$A_{33}$	$A_{12}$	$A_{13}$	$A_{23}$	$A_{1212}$	$A_{1211}$	$A_{1222}$	$A_{1233}$
1	0.7801	0.0826	0.1373	0.1775	0.0142	0.0155	0.0496	0.1335	0.0283	0.0158
4	0.8362	0.0385	0.1253	0.0559	0.0601	0.0324	0.0197	0.0536	0.0015	0.0009
Average 1&4	0.8152	0.0550	0.1298	0.1015	0.0429	0.0261	0.0309	0.0836	0.0115	0.0065

B.4.1 Fiber orientation data, donut sample, flow reversal  $\gamma = 4$

Position	A11	A22	A33	A12	A13	A23	A1212	A1211	A1222	A1233
1	0.6921	0.09	0.2179	0.178	-0.0162	-0.0126	0.053	0.1308	0.0292	0.018
2	0.7123	0.0924	0.1953	0.1788	-0.051	0.0121	0.0543	0.1327	0.0294	0.0167
3	0.6992	0.1097	0.1912	0.1803	-0.0101	0.0239	0.0489	0.1333	0.027	0.0201
4	0.8643	0.0217	0.1140	0.0314	0.0365	0.0297	0.0136	0.0257	0.0026	0.0031
Average 1-3	0.7008	0.0966	0.2026	0.1789	-0.0258	0.0062	0.0522	0.1322	0.0286	0.0182
Average 1-4	0.7526	0.0729	0.1746	0.1322	-0.0061	0.0137	0.0400	0.0985	0.0204	0.0134

B.4.2 Fiber orientation data, donut sample, flow reversal  $\gamma = 14$

Position	A11	A22	A33	A12	A13	A23	A1212	A1211	A1222	A1233
1	0.7296	0.0906	0.1798	0.188	-0.0659	-0.0224	0.0492	0.134	0.0279	0.0262
2	0.6395	0.096	0.2645	0.1807	0.0176	0.0226	0.0528	0.1237	0.0303	0.0268
3	0.7145	0.0532	0.2323	0.1513	-0.0647	-0.0107	0.0357	0.1131	0.0152	0.0229
4	0.9025	0.0292	0.0683	-0.0156	-0.0302	0.0173	0.0188	-0.0212	0.0062	-0.0006
Average 1-3	0.6897	0.0830	0.2273	0.1755	-0.0322	-0.0014	0.0471	0.1245	0.0256	0.0256
Average 1-4	0.7673	0.0634	0.1693	0.1058	-0.0315	0.0054	0.0368	0.0713	0.0185	0.0160

## **Appendix C. Numerical Method: Matlab Code**



```

extra_term_constant=0;
%stress_total = TERM1 (2*eta*D)+ (from suspending medium)
%      TERM2 (2*phi*eta*stress_C*D*A4)+ (hydrodynamic drag)
%      TERM3 (2*phi*eta*D) (extra term fiber diameter)
stress_form = 2; %stress_form = 1 only terms 1 and 2
%      stress_form = 2 terms 1, 2 and 3
stress_closure = 0 ; %if closure = 0 then quadratic closure
%      %if closure = 2 then hybrid
%      %if closure = 3 then H&L1
%      %if closure = 4 then IBOF
%%%%%%%%%%%%%%%%%%%%%%%%%%%%%%%%%%%%%%%%%%%%%%%%%%%%%%%%%%%%%%%%%%%%%%%%
%%%%%%%%%%%%%%%%%%%%%%%%%%%%%%%%%%%%%%%%%%%%%%%%%%%%%%%%%%%%%%%%%%%%%%%%

%if closure == 2 | closure ==4
tspan=timespan;
%else
%tspan=[0:t_step:timespan];
%end

if closure ==2 | closure == 0 |closure == 1 | closure ==3
final_matrix_count=0;%final_matrix_count counts the number of time steps
for ii=0:t_step:tspan
final_matrix_count=final_matrix_count+1;
t_span=[ii ii+t_step]; % for ODE solver

if closure == 2 | slip_function ==1
DET_A=( Azero(1)*Azero(2)*Azero(3)+Azero(4)*Azero(6)*Azero(5)+Azero(5)*Azero(4)*Azero(6) ) -
( Azero(2)*(Azero(5)^2)+Azero(1)*(Azero(6)^2)+Azero(3)*(Azero(4)^2) );
FF=1-27*DET_A;
end

if slip_function==1
orientation_SR=(1-slip_constant*27*DET_A)*stress_SR;
else
orientation_SR=orientation_SR;
end

[t,A]=ode15s(@JEFFERYwTUCKERorientation,t_span,Azero);
BB=size(A);
for i=1:6
Azero(i,1)=A(BB(1,1),i);
A_final(final_matrix_count,i)=A(BB(1,1),i);
t_final(final_matrix_count,1)=t(BB(1,1),1);
end

end %end for t_span
end %end for if

if closure ==4 %%for IBOF
final_matrix_count=0;%final_matrix_count counts the number of time steps
for ii=0:t_step:tspan

final_matrix_count=final_matrix_count+1;
t_span=[ii ii+t_step]; % for ODE solver

```

```

if slip_function==1

    DET_A=( Azero(1)*Azero(2)*Azero(3)+Azero(4)*Azero(6)*Azero(5)+Azero(5)*Azero(4)*Azero(6)
) - ( Azero(2)*(Azero(5)^2)+Azero(1)*(Azero(6)^2)+Azero(3)*(Azero(4)^2) );
    %FF=1-27*DET_A, beda+slip_constant*27*DET_A
    orientation_SR=(1-slip_constant*27*DET_A)*stress_SR;
else
    orientation_SR=orientation_SR;
end
orientation_SR;
IBOF_constants;% calls file that contains IBOF_c (21,3)

%I_1 = Azero(1)+Azero(2)+Azero(3);
I_2 = Azero(1)*Azero(2)+Azero(1)*Azero(3)+Azero(2)*Azero(3) - (Azero(4)^2) - (Azero(5)^2) -
(Azero(6)^2);
I_3 = Azero(1)*Azero(2)*Azero(3) + 2*Azero(4)*Azero(5)*Azero(6) - Azero(1)*(Azero(6)^2) -
Azero(3)*(Azero(4)^2)-Azero(2)*(Azero(5)^2);

IBOF_B =zeros(6,1);
%IBOF_c( #, i=1,2,3)
IBOF_B_(3,1) = IBOF_c(1,1) + IBOF_c(2,1)*I_2 + IBOF_c(3,1)*(I_2^2) + IBOF_c(4,1)*I_3 +
IBOF_c(5,1)*(I_3^2) +...
IBOF_c(6,1)*I_2*I_3 + IBOF_c(7,1)*(I_2^2)*I_3 + IBOF_c(8,1)*I_2*(I_3^2) +
IBOF_c(9,1)*(I_2^3) +...
IBOF_c(10,1)*(I_3^3) + IBOF_c(11,1)*(I_2^3)*I_3 + IBOF_c(12,1)*(I_2^2)*(I_3^2) +...
IBOF_c(13,1)*I_2*(I_3^3) + IBOF_c(14,1)*(I_2^4) + IBOF_c(15,1)*(I_3^4) +
IBOF_c(16,1)*(I_2^4)*I_3 +...
IBOF_c(17,1)*(I_2^3)*(I_3^2) + IBOF_c(18,1)*(I_2^2)*(I_3^3) +
IBOF_c(19,1)*(I_2)*(I_3^4) +...
IBOF_c(20,1)*(I_2^5) + IBOF_c(21,1)*(I_3^5);

IBOF_B_(4,1) = IBOF_c(1,2) + IBOF_c(2,2)*I_2 + IBOF_c(3,2)*(I_2^2) + IBOF_c(4,2)*I_3 +
IBOF_c(5,2)*(I_3^2) +...
IBOF_c(6,2)*I_2*I_3 + IBOF_c(7,2)*(I_2^2)*I_3 + IBOF_c(8,2)*I_2*(I_3^2) +
IBOF_c(9,2)*(I_2^3) +...
IBOF_c(10,2)*(I_3^3) + IBOF_c(11,2)*(I_2^3)*I_3 + IBOF_c(12,2)*(I_2^2)*(I_3^2) +...
IBOF_c(13,2)*I_2*(I_3^3) + IBOF_c(14,2)*(I_2^4) + IBOF_c(15,2)*(I_3^4) +
IBOF_c(16,2)*(I_2^4)*I_3 +...
IBOF_c(17,2)*(I_2^3)*(I_3^2) + IBOF_c(18,2)*(I_2^2)*(I_3^3) +
IBOF_c(19,2)*(I_2)*(I_3^4) +...
IBOF_c(20,2)*(I_2^5) + IBOF_c(21,2)*(I_3^5);

IBOF_B_(6,1) = IBOF_c(1,3) + IBOF_c(2,3)*I_2 + IBOF_c(3,3)*(I_2^2) + IBOF_c(4,3)*I_3 +
IBOF_c(5,3)*(I_3^2) +...
IBOF_c(6,3)*I_2*I_3 + IBOF_c(7,3)*(I_2^2)*I_3 + IBOF_c(8,3)*I_2*(I_3^2) +
IBOF_c(9,3)*(I_2^3) +...
IBOF_c(10,3)*(I_3^3) + IBOF_c(11,3)*(I_2^3)*I_3 + IBOF_c(12,3)*(I_2^2)*(I_3^2) +...
IBOF_c(13,3)*I_2*(I_3^3) + IBOF_c(14,3)*(I_2^4) + IBOF_c(15,3)*(I_3^4) +
IBOF_c(16,3)*(I_2^4)*I_3 +...
IBOF_c(17,3)*(I_2^3)*(I_3^2) + IBOF_c(18,3)*(I_2^2)*(I_3^3) +
IBOF_c(19,3)*(I_2)*(I_3^4) +...
IBOF_c(20,3)*(I_2^5) + IBOF_c(21,3)*(I_3^5);

IBOF_B_(1,1) = (3/5)*( - (1/7) + (1/5)*IBOF_B_(3,1)*((1/7) + (4/7)*I_2 + (8/3)*I_3 ) -
IBOF_B_(4,1))*((1/5) - ...

```

```

(8/15)*I_2 - (14/15)*I_3) - IBOF_B_(6,1)*((1/35) - (24/105)*I_3 - (4/35)*I_2 + (16/15)*I_2*I_3
+ ...
(8/35)*(I_2^2) );

```

```

IBOF_B_(2,1) = (6/7)* ( 1 - (1/5)*IBOF_B_(3,1)*(1+4*I_2) + (7/5)*IBOF_B_(4,1)*((1/6)-I_2) - ...
IBOF_B_(6,1)*((-1/5)+(2/3)*I_3+(4/5)*I_2-(8/5)*(I_2^2) ) );

```

```

IBOF_B_(5,1) = -(4/5)*IBOF_B_(3,1) - (7/5)*IBOF_B_(4,1) - (6/5)*IBOF_B_(6,1)*(1-(4/3)*I_2);

```

```

[t,A]=ode15s(@JEFFERYwTUCKERorientation,t_span,Azero);
BB=size(A);

```

```

for i=1:6
    Azero(i,1)=A(BB(1,1),i);
    A_final(final_matrix_count+1,i)=A(BB(1,1),i);
    t_final(final_matrix_count+1,1)=t(BB(1,1),1);
end

```

```

end %end for t_span
end %end for if

```

```

%
%
% %

```

```

%%%%%%%%%%%%%%%%%%%%%%%%%%%%%%%%%%%%%%%%%%%%%%%%%%%%%%%%%%%%%%%%%%%%%%%%%calculate stresses

```

```

size_t_final = size(t_final);

```

```

for ii=1:size_t_final(1,1)%%begining of loop to calculate stresses

```

```

%%%%%%%%%%%%%%%%%%%%%%%%%%%%%%%%%%%%%%%%%%%%%%%%%%%%%%%%%%%%%%%%%%%%%%%%%stress closure
if stress_closure == 0 %for quadratic

```

```

A4_11=2*stress_SR*A_final(ii,4)*A_final(ii,1);
A4_22=2*stress_SR*A_final(ii,4)*A_final(ii,2);
A4_33=2*stress_SR*A_final(ii,4)*A_final(ii,3);
A4_12=2*stress_SR*(A_final(ii,4)^2);

```

```

end

```

```

if stress_closure == 1 %then linear closure
A4_11=(6*A_final(ii,4)/7)*stress_SR;
A4_22=(6*A_final(ii,4)/7)*stress_SR;
A4_33=(2*A_final(ii,4)/7)*stress_SR;
A4_12=2*((A_final(ii,1)/7)+(A_final(ii,2)/7)-(1/35))*stress_SR;

```

```

end

```

```

if stress_closure ==2 %then hybrid

```

```

    DET_A=(
A_final(ii,1)*A_final(ii,2)*A_final(ii,3)+A_final(ii,4)*A_final(ii,6)*A_final(ii,5)+A_final(ii,5)*A_final(ii,

```

```

4)*A_final(ii,6) ) - (
A_final(ii,2)*(A_final(ii,5)^2)+A_final(ii,1)*(A_final(ii,6)^2)+A_final(ii,3)*(A_final(ii,4)^2) );
FF=1-27*DET_A;
A4_11= FF * 2*stress_SR*A_final(ii,4)*A_final(ii,1) + (1-FF)* (6*A_final(ii,4)/7)*stress_SR;
A4_22= FF * 2*stress_SR*A_final(ii,4)*A_final(ii,2) + (1-FF)* (6*A_final(ii,4)/7)*stress_SR;
A4_33= FF * 2*stress_SR*A_final(ii,4)*A_final(ii,3) + (1-FF)* (2*A_final(ii,4)/7)*stress_SR;
A4_12= FF * 2*stress_SR*(A_final(ii,4)^2) + (1-FF)* 2*((A_final(ii,1)/7)+(A_final(ii,2)/7)-
(1/35))*stress_SR;

end
if stress_closure == 3 %then H&L1
A4_11= 2*A_final(ii,1)*A_final(ii,4)*stress_SR - (4/5)*stress_SR*( A_final(ii,1)*A_final(ii,4) -
A_final(ii,4) + A_final(ii,4)*A_final(ii,2) + A_final(ii,5)*A_final(ii,6) );
A4_22= 2*A_final(ii,2)*A_final(ii,4)*stress_SR - (4/5)*stress_SR*( A_final(ii,1)*A_final(ii,4) -
A_final(ii,4) + A_final(ii,4)*A_final(ii,2) + A_final(ii,5)*A_final(ii,6) );
A4_33= (12/5)*stress_SR*A_final(ii,5)*A_final(ii,6) - (2/5)*stress_SR*A_final(ii,3)*A_final(ii,4) -
(4/5)*stress_SR*( A_final(ii,1)*A_final(ii,4)- A_final(ii,4) + A_final(ii,4)*A_final(ii,2) +
A_final(ii,5)*A_final(ii,6) );
A4_12= (4/5)*stress_SR*(A_final(ii,4)^2)+(6/5)*stress_SR*A_final(ii,1)*A_final(ii,2);

end

if stress_closure == 4 %then IBOF
IBOF_constants;% calls file that contains IBOF_c (21,3)
I_2 = A_final(ii,1)*A_final(ii,2)+A_final(ii,1)*A_final(ii,3)+A_final(ii,2)*A_final(ii,3) -
(A_final(ii,4)^2) - (A_final(ii,5)^2) - (A_final(ii,6)^2);
I_3 = A_final(ii,1)*A_final(ii,2)*A_final(ii,3) + 2*A_final(ii,4)*A_final(ii,5)*A_final(ii,6) -
A_final(ii,1)*(A_final(ii,6)^2) - A_final(ii,3)*(A_final(ii,4)^2)-A_final(ii,2)*(A_final(ii,5)^2);

IBOF_B =zeros(6,1);
%IBOF_c( #, i=1,2,3)
IBOF_B_(3,1) = IBOF_c(1,1) + IBOF_c(2,1)*I_2 + IBOF_c(3,1)*(I_2^2) + IBOF_c(4,1)*I_3 +
IBOF_c(5,1)*(I_3^2) +...
IBOF_c(6,1)*I_2*I_3 + IBOF_c(7,1)*(I_2^2)*I_3 + IBOF_c(8,1)*I_2*(I_3^2) +
IBOF_c(9,1)*(I_2^3) +...
IBOF_c(10,1)*(I_3^3) + IBOF_c(11,1)*(I_2^3)*I_3 + IBOF_c(12,1)*(I_2^2)*(I_3^2) +...
IBOF_c(13,1)*I_2*(I_3^3) + IBOF_c(14,1)*(I_2^4) + IBOF_c(15,1)*(I_3^4) +
IBOF_c(16,1)*(I_2^4)*I_3 +...
IBOF_c(17,1)*(I_2^3)*(I_3^2) + IBOF_c(18,1)*(I_2^2)*(I_3^3) +
IBOF_c(19,1)*(I_2)*(I_3^4) +...
IBOF_c(20,1)*(I_2^5) + IBOF_c(21,1)*(I_3^5);

IBOF_B_(4,1) = IBOF_c(1,2) + IBOF_c(2,2)*I_2 + IBOF_c(3,2)*(I_2^2) + IBOF_c(4,2)*I_3 +
IBOF_c(5,2)*(I_3^2) +...
IBOF_c(6,2)*I_2*I_3 + IBOF_c(7,2)*(I_2^2)*I_3 + IBOF_c(8,2)*I_2*(I_3^2) +
IBOF_c(9,2)*(I_2^3) +...
IBOF_c(10,2)*(I_3^3) + IBOF_c(11,2)*(I_2^3)*I_3 + IBOF_c(12,2)*(I_2^2)*(I_3^2) +...
IBOF_c(13,2)*I_2*(I_3^3) + IBOF_c(14,2)*(I_2^4) + IBOF_c(15,2)*(I_3^4) +
IBOF_c(16,2)*(I_2^4)*I_3 +...
IBOF_c(17,2)*(I_2^3)*(I_3^2) + IBOF_c(18,2)*(I_2^2)*(I_3^3) +
IBOF_c(19,2)*(I_2)*(I_3^4) +...
IBOF_c(20,2)*(I_2^5) + IBOF_c(21,2)*(I_3^5);

IBOF_B_(6,1) = IBOF_c(1,3) + IBOF_c(2,3)*I_2 + IBOF_c(3,3)*(I_2^2) + IBOF_c(4,3)*I_3 +
IBOF_c(5,3)*(I_3^2) +...

```

$$\begin{aligned}
& \text{IBOF\_c}(6,3)*I_2*I_3 + \text{IBOF\_c}(7,3)*(I_2^2)*I_3 + \text{IBOF\_c}(8,3)*I_2*(I_3^2) + \\
& \text{IBOF\_c}(9,3)*(I_2^3) + \dots \\
& \text{IBOF\_c}(10,3)*(I_3^3) + \text{IBOF\_c}(11,3)*(I_2^3)*I_3 + \text{IBOF\_c}(12,3)*(I_2^2)*(I_3^2) + \dots \\
& \text{IBOF\_c}(13,3)*I_2*(I_3^3) + \text{IBOF\_c}(14,3)*(I_2^4) + \text{IBOF\_c}(15,3)*(I_3^4) + \\
& \text{IBOF\_c}(16,3)*(I_2^4)*I_3 + \dots \\
& \text{IBOF\_c}(17,3)*(I_2^3)*(I_3^2) + \text{IBOF\_c}(18,3)*(I_2^2)*(I_3^3) + \\
& \text{IBOF\_c}(19,3)*(I_2)*(I_3^4) + \dots \\
& \text{IBOF\_c}(20,3)*(I_2^5) + \text{IBOF\_c}(21,3)*(I_3^5);
\end{aligned}$$

$$\begin{aligned}
& \text{IBOF\_B}(1,1) = (3/5)*(-1/7) + (1/5)*\text{IBOF\_B}(3,1)*(1/7) + (4/7)*I_2 + (8/3)*I_3 - \\
& \text{IBOF\_B}(4,1)*(1/5) - \dots \\
& (8/15)*I_2 - (14/15)*I_3 - \text{IBOF\_B}(6,1)*(1/35) - (24/105)*I_3 - (4/35)*I_2 + (16/15)*I_2*I_3 \\
& + \dots \\
& (8/35)*(I_2^2) \quad );
\end{aligned}$$

$$\begin{aligned}
& \text{IBOF\_B}(2,1) = (6/7)*(1 - (1/5)*\text{IBOF\_B}(3,1)*(1+4*I_2) + (7/5)*\text{IBOF\_B}(4,1)*((1/6)-I_2) - \dots \\
& \text{IBOF\_B}(6,1)*((-1/5)+(2/3)*I_3+(4/5)*I_2-(8/5)*(I_2^2)) \quad );
\end{aligned}$$

$$\text{IBOF\_B}(5,1) = -(4/5)*\text{IBOF\_B}(3,1) - (7/5)*\text{IBOF\_B}(4,1) - (6/5)*\text{IBOF\_B}(6,1)*(1-(4/3)*I_2);$$

%IBOF\_B(i,1)

$$\begin{aligned}
& \text{func\_a} = A\_final(ii,1)*A\_final(ii,4)+A\_final(ii,4)*A\_final(ii,2)+A\_final(ii,5)*A\_final(ii,6); \\
& \text{func\_b} = (A\_final(ii,5)^2)+A\_final(ii,1)*A\_final(ii,4)+A\_final(ii,4)*A\_final(ii,2); \\
& \text{func\_c} = (A\_final(ii,1)^2)+(A\_final(ii,4)^2)+(A\_final(ii,5)^2); \\
& \text{func\_d} = (A\_final(ii,4)^2)+(A\_final(ii,2)^2)+A\_final(ii,5)*A\_final(ii,6); \\
& \text{func\_e} = ((A\_final(ii,5)^2)/4) + ((A\_final(ii,5)*A\_final(ii,6))/4) + ((A\_final(ii,1)*A\_final(ii,4))/2) + \\
& ((A\_final(ii,4)*A\_final(ii,2))/2); \\
& \text{func\_f} = A\_final(ii,1)*A\_final(ii,5)+A\_final(ii,4)*A\_final(ii,5)+A\_final(ii,5)*A\_final(ii,3); \\
& \text{func\_g} = A\_final(ii,1)*A\_final(ii,5)+A\_final(ii,4)*A\_final(ii,6)+A\_final(ii,5)*A\_final(ii,3); \\
& \text{func\_h} = A\_final(ii,4)*A\_final(ii,5)+A\_final(ii,2)*A\_final(ii,5)+A\_final(ii,5)*A\_final(ii,3); \\
& \text{func\_i} = A\_final(ii,4)*A\_final(ii,5)+A\_final(ii,2)*A\_final(ii,6)+A\_final(ii,6)*A\_final(ii,3); \\
& \text{func\_j} = (A\_final(ii,5)^2)+A\_final(ii,5)*A\_final(ii,6)+(A\_final(ii,3)^2); \\
& \text{func\_k} = (A\_final(ii,5)^2)+A\_final(ii,1)*A\_final(ii,4)+A\_final(ii,2)*A\_final(ii,4); \\
& \text{func\_L} = ((A\_final(ii,5)^2)/3) + ((A\_final(ii,5)*A\_final(ii,6))/3) + ((A\_final(ii,4)*A\_final(ii,3))/3);
\end{aligned}$$

$$\begin{aligned}
& A4\_11=2*stress\_SR* ( \text{IBOF\_B}(6,1)*( \text{func\_b}*func\_c/2) + (\text{func\_c}*func\_a/2) ) + \text{IBOF\_B}(4,1)*( \\
& \text{func\_e} ) + \dots \\
& \text{IBOF\_B}(2,1)*(A\_final(ii,4)/2)+ \text{IBOF\_B}(5,1)*( \\
& (A\_final(ii,4)*func\_c/2)+(A\_final(ii,1)*func\_a/4)+(A\_final(ii,1)*func\_b/4) ) + \\
& \text{IBOF\_B}(3,1)*A\_final(ii,1)*A\_final(ii,4) );
\end{aligned}$$

$$\begin{aligned}
& A4\_22=2*stress\_SR* ( \text{IBOF\_B}(6,1)*( (\text{func\_d}*func\_a/2) + (\text{func\_b}*func\_d/2) ) + \dots \\
& \text{IBOF\_B}(5,1)*( (A\_final(ii,2)*func\_a/4)+(A\_final(ii,4)*func\_d/2)+(A\_final(ii,2)*func\_b/4) ) + \dots \\
& \text{IBOF\_B}(4,1)*(func\_e) + (\text{IBOF\_B}(2,1)*A\_final(ii,4)/2) + \text{IBOF\_B}(3,1)*A\_final(ii,2)*A\_final(ii,4) \\
& );
\end{aligned}$$

$$\begin{aligned}
& A4\_33=2*stress\_SR* ( \text{IBOF\_B}(5,1)*( (A\_final(ii,5)/12)*func\_f + (A\_final(ii,3)/12)*func\_a + \\
& (A\_final(ii,5)/12)*func\_g + (A\_final(ii,6)/12)*func\_f + \dots \\
& (A\_final(ii,5)/6)*func\_h + (A\_final(ii,6)/12)*func\_g + (A\_final(ii,5)/6)*func\_i + \\
& (A\_final(ii,4)/6)*func\_j + (A\_final(ii,3)/12)*func\_k ) + \dots \\
& \text{IBOF\_B}(3,1)*(func\_L) + \text{IBOF\_B}(4,1)*(func\_e/3) + \dots \\
& \text{IBOF\_B}(6,1)*( (\text{func\_a}*func\_j/6) + (\text{func\_b}*func\_j/6) + (\text{func\_f}*func\_h/6) + (\text{func\_g}*func\_h/6) + \dots \\
& (\text{func\_i}*func\_i/6) + (\text{func\_g}*func\_i/6) ) + (\text{IBOF\_B}(2,1)*A\_final(ii,4)/6) );
\end{aligned}$$

```

A4_12=2*stress_SR* ( IBOF_B_(5,1)*( (A_final(ii,2)*func_c/6) + (A_final(ii,4)*func_a/3) +
(A_final(ii,1)*func_d/6) + (A_final(ii,4)*func_b/3) ) +...
    IBOF_B_(4,1)*(((A_final(ii,1)^2)/6) + ((A_final(ii,4)^2)/3) + ((A_final(ii,5)^2)/6) +
((A_final(ii,5)*A_final(ii,6))/6) + ((A_final(ii,2)^2)/6) ) +...
    IBOF_B_(6,1)*( (func_c*func_d/3) + (func_b*func_a/3) + ((func_b^2)/6) + ((func_a^2)/6) ) +...
    IBOF_B_(3,1)*(((A_final(ii,4)^2)*2/3) + (A_final(ii,1)*A_final(ii,2)/3) ) + IBOF_B_(2,1)*(
(A_final(ii,1)/6) + (A_final(ii,2)/6) ) + (IBOF_B_(1,1)/3) );

end
%%%%%%%%%%%%%%%%%%%%%%%%%%%%%%%%%%%%%%%%%%%%%%%%%%%%%%%%%end of defining closure
for stress
% the 2 is in the closure approximation
if stress_form ==1 % suspending medium and hydrodrag

    const=hydro_stress_constant*vol_fraction*sus_viscosity;
    stress_12(ii,1)=sus_viscosity*stress_SR + const*A4_12;
    stress_N1(ii,1)=const*(A4_11-A4_22);

end
if stress_form ==2 % suspending medium, hydrodrag and extra term

    const=hydro_stress_constant*vol_fraction*sus_viscosity;
    stress_12(ii,1)=sus_viscosity*stress_SR + const*A4_12
+extra_term_constant*stress_SR*vol_fraction*sus_viscosity;
    stress_N1(ii,1)=const*(A4_11-A4_22);

end

end % end for the for loop to calculate stresses
%%%%%%%%%%%%%%%%%%%%%%%%%%%%%%%%%%%%%%%%%%%%%%%%%%%%%%%%%end of stress
calculation
%out put arguments  A_final, t_final, stress_12(ii,1), stress_N1(ii,1)
[t_final A_final];
strain=stress_SR.*t_final;
%[strain stress_12 stress_N1]
%EXPdonutPBT30; %experimental data at sr = 1, CP_D_strain, CP_D_N1, CP_D_eta
EXPfiberOrientation;%exp_A11 exp_A22 exp_A33 exp_A12 exp_A23 exp_A13 exp_strain
%experimentalDONUTpbt;%experimental data at sr = 4
EXPdonutPBT30_6; %experimental data for shear rate 6
%figure(3);

%experimental sr 6, EXP_strain_6, EXP_stress_6 EXP_N1_6
% EXP_strain_rev_6 EXP_stress_rev_6 EXP_N1_rev_6

%plot(EXP_strain,exp_A11,'b-');hold on
%plot(EXP_strain,exp_A22,'b-');hold on
%plot(EXP_strain,exp_A33,'b-');hold on
%plot(EXP_strain,exp_A12,'b-');hold on
plot(strain,A_final(:,1),'r-');hold on
plot(strain,A_final(:,2),'r-');hold on
plot(strain,A_final(:,3),'r-');hold on
plot(strain,A_final(:,4),'r-');hold on

%plot(CP_D_strain,CP_D_N1,'b-');hold on %sr1
%plot(CP_D_strain,CP_D_eta,'b-');hold on

```

```

%plot(exp_strain,exp_N1,'b-');hold on sr4
%plot(exp_strain,exp_shear_stress,'r-');hold on
%plot(EXP_strain_6,EXP_stress_6,'b-');hold on %sr6 forward
%plot(EXP_strain_6,EXP_N1_6,'b-');hold on

%plot(EXP_strain_rev_6,EXP_stress_rev_6,'b-');hold on %sr6 reverse
%plot(EXP_strain_rev_6,EXP_N1_rev_6,'b-');hold on
%
%plot(strain,stress_12,'r-');hold on
%plot(strain,stress_N1,'r-');hold on

%for i=1:200
%extract=[strain(i*50-50,1) A_final(i*50-50,:)]
%end

%find the max and min
%max(stress_12)
%min(stress_12)
%max(stress_N1)
%min(stress_N1)
toc

```

### Sub Programs

```

JEFFERYwTUCKERorientation
% This is the subprogram that solves the differential equations

% A(1)=A11, A(2)=A22, A(3)=A33, A(4)=A21, A(5)=A13, A(6)=A23

% Name our function
function Aprime = JEFFERYwTUCKERorientation(t,A)

global orientation_SR addTUCKER C1 alpha relaxation_time closure FF IBOF_B_BBB

if t <= relaxation_time
orientation_SR = orientation_SR; % Shear Rate
else
orientation_SR=0;
end

%Define A components based on closure

if closure ==0 %for quadratic

A4_11=2* orientation_SR*A(4)*A(1);
A4_22=2* orientation_SR*A(4)*A(2);
A4_33=2* orientation_SR*A(4)*A(3);
A4_12=2* orientation_SR*(A(4)^2);
A4_13=2* orientation_SR*A(4)*A(5);
A4_23=2* orientation_SR*A(4)*A(6);

end

if closure ==1 %then linear closure

```

```

A4_11=(6*A(4)/7)*orientation_SR;
A4_22=(6*A(4)/7)*orientation_SR;
A4_33=(2*A(4)/7)*orientation_SR;
A4_12=2*((A(1)/7)+(A(2)/7)-(1/35))*orientation_SR;
A4_13=(2*A(6)/7)*orientation_SR;
A4_23=(2*A(5)/7)*orientation_SR;

end

if closure ==2 %then hybrid

A4_11= FF * 2*orientation_SR*A(4)*A(1) + (1-FF)* (6*A(4)/7)*orientation_SR;
A4_22= FF * 2*orientation_SR*A(4)*A(2) + (1-FF)* (6*A(4)/7)*orientation_SR;
A4_33= FF * 2*orientation_SR*A(4)*A(3) + (1-FF)* (2*A(4)/7)*orientation_SR;
A4_12= FF * 2*orientation_SR*(A(4)^2) + (1-FF)* 2*((A(1)/7)+(A(2)/7)-(1/35))*orientation_SR;
A4_13= FF * 2*orientation_SR*A(4)*A(5) + (1-FF)* (2*A(6)/7)*orientation_SR;
A4_23= FF * 2*orientation_SR*A(4)*A(6) + (1-FF)* (2*A(5)/7)*orientation_SR;

end

if closure == 3 %then H&L1

A4_11= 2*A(1)*A(4)*orientation_SR - (4/5)*orientation_SR*( A(1)*A(4) - A(4) + A(4)*A(2) +
A(5)*A(6) );
A4_22= 2*A(2)*A(4)*orientation_SR - (4/5)*orientation_SR*( A(1)*A(4) - A(4) + A(4)*A(2) +
A(5)*A(6) );
A4_33= (12/5)*orientation_SR*A(5)*A(6) - (2/5)*orientation_SR*A(3)*A(4) - (4/5)*orientation_SR*(
A(1)*A(4)- A(4) + A(4)*A(2) + A(5)*A(6) );
A4_12= (4/5)*orientation_SR*(A(4)^2)+(6/5)*orientation_SR*A(1)*A(2);
A4_13= (6/5)*orientation_SR*A(1)*A(6) + (4/5)*orientation_SR*A(4)*A(5);
A4_23= (4/5)*orientation_SR*A(4)*A(6) + (6/5)*orientation_SR*A(5)*A(2);

end

if closure == 4 %then IBOF
%IBOF_B_(i,1)
func_a = A(1)*A(4)+A(4)*A(2)+A(5)*A(6);
func_b = (A(5)^2)+A(1)*A(4)+A(4)*A(2);
func_c = (A(1)^2)+(A(4)^2)+(A(5)^2);
func_d = (A(4)^2)+(A(2)^2)+A(5)*A(6);
func_e = ((A(5)^2)/4) + ((A(5)*A(6))/4) + ((A(1)*A(4))/2) + ((A(4)*A(2))/2);
func_f = A(1)*A(5)+A(4)*A(5)+A(5)*A(3);
func_g = A(1)*A(5)+A(4)*A(6)+A(5)*A(3);
func_h = A(4)*A(5)+A(2)*A(5)+A(5)*A(3);
func_i = A(4)*A(5)+A(2)*A(6)+A(6)*A(3);
func_j = (A(5)^2)+A(5)*A(6)+(A(3)^2);
func_k = (A(5)^2)+A(1)*A(4)+A(2)*A(4);
func_L = ((A(5)^2)/3) + ((A(5)*A(6))/3) + ((A(4)*A(3))/3);

A4_11=2*orientation_SR*( IBOF_B_(6,1)*( (func_b*func_c/2) + (func_c*func_a/2) ) + IBOF_B_(4,1)*(
func_e ) +...
IBOF_B_(2,1)*(A(4)/2) + IBOF_B_(5,1)*( (A(4)*func_c/2)+(A(1)*func_a/4)+(A(1)*func_b/4) ) +
IBOF_B_(3,1)*A(1)*A(4) );

A4_22=2*orientation_SR*( IBOF_B_(6,1)*( (func_d*func_a/2) + (func_b*func_d/2) ) +...
IBOF_B_(5,1)*( (A(2)*func_a/4)+(A(4)*func_d/2)+(A(2)*func_b/4) ) +...

```

```

IBOF_B_(4,1)*(func_e) + (IBOF_B_(2,1)*A(4)/2) + IBOF_B_(3,1)*A(2)*A(4) );

A4_33=2*orientation_SR*( IBOF_B_(5,1)*( (A(5)/12)*func_f + (A(3)/12)*func_a + (A(5)/12)*func_g +
(A(6)/12)*func_f +...
(A(5)/6)*func_h + (A(6)/12)*func_g + (A(5)/6)*func_i + (A(4)/6)*func_j + (A(3)/12)*func_k ) +...
IBOF_B_(3,1)*(func_L) + IBOF_B_(4,1)*(func_e/3) +...
IBOF_B_(6,1)*( (func_a*func_j/6) + (func_b*func_j/6) + (func_f*func_h/6) + (func_g*func_h/6) +...
(func_f*func_i/6) + (func_g*func_i/6) ) + (IBOF_B_(2,1)*A(4)/6) );

A4_12=2*orientation_SR*( IBOF_B_(5,1)*( (A(2)*func_c/6) + (A(4)*func_a/3) + (A(1)*func_d/6) +
(A(4)*func_b/3) ) +...
IBOF_B_(4,1)*( ((A(1)^2)/6) + ((A(4)^2)/3) + ((A(5)^2)/6) + ((A(5)*A(6))/6) + ((A(2)^2)/6) ) +...
IBOF_B_(6,1)*( (func_c*func_d/3) + (func_b*func_a/3) + ((func_b^2)/6) + ((func_a^2)/6) ) +...
IBOF_B_(3,1)*( ((A(4)^2)*2/3) + (A(1)*A(2)/3) ) + IBOF_B_(2,1)*( (A(1)/6) + (A(2)/6) ) +
(IBOF_B_(1,1)/3) );

A4_13= 2*orientation_SR*( IBOF_B_(5,1)*( (A(5)*func_c/12) + (A(6)*func_c/12) + (A(5)*func_a/6) +
(A(4)*func_f/6) +...
(A(1)*func_h/12) + (A(4)*func_g/6) + (A(1)*func_i/12) + (A(5)*func_k/6) ) +...
IBOF_B_(3,1)*( ((A(1)*A(5))/6) + ((A(1)*A(6))/6) + ((A(4)*A(5))*2/3) ) +
IBOF_B_(2,1)*((A(5)/12)+(A(6)/12)) +...
IBOF_B_(4,1)*( ((A(4)*A(5))/6) + ((A(5)*A(2))/12) + ((A(2)*A(6))/12) + ((A(5)*A(3))/12) +
((A(6)*A(3))/12) ) +...
IBOF_B_(6,1)*( (func_b*func_f/6) + (func_b*func_g/6) + (func_c*func_h/6) + (func_c*func_i/6) +...
(func_a*func_f/6) + (func_a*func_g/6) ) );

A4_23= 2*orientation_SR*( IBOF_B_(3,1)*( (A(4)*A(5)/3) + (A(4)*A(6)/3) + (A(5)*A(2)/3) ) +...
IBOF_B_(4,1)*( (A(1)*A(5)/6) + (A(4)*A(5)/12) + (A(4)*A(6)/12) + (A(5)*A(3)/6) ) +...
IBOF_B_(6,1)*( (func_d*func_f/6) + (func_d*func_g/6) + (func_b*func_h/6) + (func_b*func_i/6) +...
(func_a*func_h/6) + (func_a*func_i/6) ) + IBOF_B_(5,1)*( (A(5)*func_a/12) + (A(6)*func_a/12) +...
(A(2)*func_f/12) + (A(4)*func_h/6) + (A(2)*func_g/12) + (A(4)*func_i/6) + (A(5)*func_d/6) +
(A(5)*func_b/12) +...
(A(6)*func_b/12) ) + (IBOF_B_(2,1)*A(5)/6) );

```

end

```

J1=2*orientation_SR*A(4)-A4_11;
J2=-A4_22;
J3=-A4_33;
J4=orientation_SR*A(2)-A4_12;
J5=orientation_SR*A(6)-A4_13;
J6=-A4_23;

```

```

Tucker1=2*C1*orientation_SR*(1-(alpha*A(1)));
Tucker2=2*C1*orientation_SR*(1-(alpha*A(2)));
Tucker3=2*C1*orientation_SR*(1-(alpha*A(3)));
Tucker4=-2*alpha*C1*orientation_SR*A(4);
Tucker5=-2*alpha*C1*orientation_SR*A(5);
Tucker6=-2*alpha*C1*orientation_SR*A(6);

```

```

if addTUCKER ==0
  Aprime = [J1;
            J2;
            J3;

```

```

        J4;
        J5;
        J6];

end

if addTUCKER ==1
    Aprime = [J1+Tucker1;
             J2+Tucker2;
             J3+Tucker3;
             J4+Tucker4;
             J5+Tucker5;
             J6+Tucker6];
end

```

## C.2 Jeffery or Folgar-Tucker, Inhomogeneous Shear Field as in PP Rheometer

The following code solves Jeffery's equation or the F-T model for the case where the velocity gradient varies linearly as found in the PP rheometer using any one of the five programmed closure approximations, quadratic, linear, hybrid, H&L1, and the IBOF.

File name: parallelPlateMain.m

```

% This is the main body of the Program
% solves the generalized jeffery equation in terms of A
% Also can incorporate the Folgar-Tucker constant
%only dinh armstrong

clc
clear all
%format long e
%format long e
format short e
tic
%always keep at a shear rate of 1
global SR addTUCKER C1 alpha relaxation_time closure FF RSR IBOF_B_
slip_constant=1;
RSR=1; %Real Shear Rate To put in front of tucker term, different that shear rate
SR=slip_constant*RSR; % shear rate can vary for slip
final_strain=100;
strain_step=.5;
pp_steps=100; %number of steps I want to take from the center of the plate to the outside

eta_s=372;%suspending medium viscosity
Np=41; %stress constant
N1_SR=1; %shear rate to go in front of normal stress calculation

```

```

eta_calc_final(1,1)=0; % I always like to start from zero
eta_integral_counter=1;
eta_strain(1,1)=0;
for ijk = strain_step:strain_step:final_strain %beginning loop to calculate the viscosity at each strain

    eta_integral_counter=eta_integral_counter+1;
    eta_strain(eta_integral_counter,1)=ijk;

    integral_step=ijk/pp_steps; %the number of steps between center to rim strain
    %now I want to solve Jeffery's equation for those strain steps
    t_step=integral_step;
    timespan=ijk;% the time span now is the rim strain
    relaxation_time=1000000000; %time at which stress relaxation occurs
    %%%%%%%%%%%
    closure = 0; %if closure = 0 then quadratic closure
        %if closure = 1 then linear
        %if closure = 2 then hybrid
        %if closure = 3 then H&L1
        %if closure = 4 then IBOF
    %%%%%%%%%%%Tucker constants
    addTUCKER= 0;% if add Tucker = 0 then plain Jefferys equation
        % if add Tucker = 1 then adds the folgar tucker term
    alpha = 3;%if alpha = 3 then 3D, if 2 then 2D
    C1 =.0112; %0.0154% 0.000417; %0.01;%0.000417; %, best .8583 0.0199, the constant in front of Tucker
    term, they say 0.003-0.016
    %%%%%%%%%%%
    % Define initial conditions
    Azero=[.481; .0618; .457; .095; -.0241; -.028];%real new
    %Azero=[1/3; 1/3; 1/3; 0; 0; 0];% for completely random orientation
    %Azero=[.76783; .0798; .1542; .0896; .0; .0];%tucker flow reversal IC
    %Azero=[.424; .1704; .4056; .1302; .2674; .1635];%real
    %%%%%%%%%%%
    %%%%%%%%%%%other constants
    stress_closure = 0 ; %if closure = 0 then quadratic closure
        %if closure = 2 then hybrid
        %if closure = 3 then H&L1
        %if closure = 4 then IBOF

    if closure == 2 | closure ==4
        tspan=timespan;
    else
        tspan=[0:t_step:timespan];
    end

    if closure ==2 %%%for hybrid closure
        final_matrix_count=0;%final_matrix_count counts the number of time steps
        for ii=0:t_step:tspan
            final_matrix_count=final_matrix_count+1;
            t_span=[ii ii+t_step]; % for ODE solver

            DET_A=( Azero(1)*Azero(2)*Azero(3)+Azero(4)*Azero(6)*Azero(5)+Azero(5)*Azero(4)*Azero(6) ) -
            ( Azero(2)*(Azero(5)^2)+Azero(1)*(Azero(6)^2)+Azero(3)*(Azero(4)^2) );
            FF=1-27*DET_A;

```

```

[t,A]=ode15s(@JEFFERYwTUCKER,t_span,Azero);
BB=size(A);
for i=1:6
    Azero(i,1)=A(BB(1,1),i);
    A_final(final_matrix_count,i)=A(BB(1,1),i);
    t_final(final_matrix_count,1)=t(BB(1,1),1);
end

end %end for t_span
end %end for if

if closure ==4 %%%for IBOF
final_matrix_count=0;%final_matrix_count counts the number of time steps
for ii=0:t_step:tspan

final_matrix_count=final_matrix_count+1;
t_span=[ii t_step]; % for ODE solver

IBOF_constants;% calls file that contains IBOF_c (21,3)

%I_1 = Azero(1)+Azero(2)+Azero(3);
I_2 = Azero(1)*Azero(2)+Azero(1)*Azero(3)+Azero(2)*Azero(3) - (Azero(4)^2) - (Azero(5)^2) -
(Azero(6)^2);
I_3 = Azero(1)*Azero(2)*Azero(3) + 2*Azero(4)*Azero(5)*Azero(6) - Azero(1)*(Azero(6)^2) -
Azero(3)*(Azero(4)^2)-Azero(2)*(Azero(5)^2);

IBOF_B_ =zeros(6,1);
%IBOF_c (#, i=1,2,3)
IBOF_B_(3,1) = IBOF_c(1,1) + IBOF_c(2,1)*I_2 + IBOF_c(3,1)*(I_2^2) + IBOF_c(4,1)*I_3 +
IBOF_c(5,1)*(I_3^2) +...
IBOF_c(6,1)*I_2*I_3 + IBOF_c(7,1)*(I_2^2)*I_3 + IBOF_c(8,1)*I_2*(I_3^2) +
IBOF_c(9,1)*(I_2^3) +...
IBOF_c(10,1)*(I_3^3) + IBOF_c(11,1)*(I_2^3)*I_3 + IBOF_c(12,1)*(I_2^2)*(I_3^2) +...
IBOF_c(13,1)*I_2*(I_3^3) + IBOF_c(14,1)*(I_2^4) + IBOF_c(15,1)*(I_3^4) +
IBOF_c(16,1)*(I_2^4)*I_3 +...
IBOF_c(17,1)*(I_2^3)*(I_3^2) + IBOF_c(18,1)*(I_2^2)*(I_3^3) +
IBOF_c(19,1)*(I_2)*(I_3^4) +...
IBOF_c(20,1)*(I_2^5) + IBOF_c(21,1)*(I_3^5);

IBOF_B_(4,1) = IBOF_c(1,2) + IBOF_c(2,2)*I_2 + IBOF_c(3,2)*(I_2^2) + IBOF_c(4,2)*I_3 +
IBOF_c(5,2)*(I_3^2) +...
IBOF_c(6,2)*I_2*I_3 + IBOF_c(7,2)*(I_2^2)*I_3 + IBOF_c(8,2)*I_2*(I_3^2) +
IBOF_c(9,2)*(I_2^3) +...
IBOF_c(10,2)*(I_3^3) + IBOF_c(11,2)*(I_2^3)*I_3 + IBOF_c(12,2)*(I_2^2)*(I_3^2) +...
IBOF_c(13,2)*I_2*(I_3^3) + IBOF_c(14,2)*(I_2^4) + IBOF_c(15,2)*(I_3^4) +
IBOF_c(16,2)*(I_2^4)*I_3 +...
IBOF_c(17,2)*(I_2^3)*(I_3^2) + IBOF_c(18,2)*(I_2^2)*(I_3^3) +
IBOF_c(19,2)*(I_2)*(I_3^4) +...
IBOF_c(20,2)*(I_2^5) + IBOF_c(21,2)*(I_3^5);

IBOF_B_(6,1) = IBOF_c(1,3) + IBOF_c(2,3)*I_2 + IBOF_c(3,3)*(I_2^2) + IBOF_c(4,3)*I_3 +
IBOF_c(5,3)*(I_3^2) +...

```

```

        IBOF_c(6,3)*I_2*I_3 + IBOF_c(7,3)*(I_2^2)*I_3 + IBOF_c(8,3)*I_2*(I_3^2) +
IBOF_c(9,3)*(I_2^3) +...
        IBOF_c(10,3)*(I_3^3) + IBOF_c(11,3)*(I_2^3)*I_3 + IBOF_c(12,3)*(I_2^2)*(I_3^2) +...
        IBOF_c(13,3)*I_2*(I_3^3) + IBOF_c(14,3)*(I_2^4) + IBOF_c(15,3)*(I_3^4) +
IBOF_c(16,3)*(I_2^4)*I_3 +...
        IBOF_c(17,3)*(I_2^3)*(I_3^2) + IBOF_c(18,3)*(I_2^2)*(I_3^3) +
IBOF_c(19,3)*(I_2)*(I_3^4) +...
        IBOF_c(20,3)*(I_2^5) + IBOF_c(21,3)*(I_3^5);

```

```

        IBOF_B_(1,1) = (3/5)*(      -(1/7) + (1/5)*IBOF_B_(3,1)*( (1/7) + (4/7)*I_2 + (8/3)*I_3 ) -
IBOF_B_(4,1)*( (1/5) - ...
        (8/15)*I_2 -(14/15)*I_3 ) - IBOF_B_(6,1)*( (1/35) - (24/105)*I_3 - (4/35)*I_2 + (16/15)*I_2*I_3
+ ...
        (8/35)*(I_2^2) ) );

```

```

IBOF_B_(2,1) = (6/7)*(      1 - (1/5)*IBOF_B_(3,1)*(1+4*I_2) + (7/5)*IBOF_B_(4,1)*((1/6)-I_2) - ...
        IBOF_B_(6,1)*((-1/5)+(2/3)*I_3+(4/5)*I_2-(8/5)*(I_2^2) ) );

```

```

IBOF_B_(5,1) = -(4/5)*IBOF_B_(3,1) - (7/5)*IBOF_B_(4,1) - (6/5)*IBOF_B_(6,1)*(1-(4/3)*I_2);

```

```

[t,A]=ode15s(@parallelPlateSupport,t_span,Azero);
BB=size(A);
for i=1:6
    Azero(i,1)=A(BB(1,1),i);
    A_final(final_matrix_count,i)=A(BB(1,1),i);
    t_final(final_matrix_count,1)=t(BB(1,1),1);
end

```

```

end %end for t_span
end %end for if

```

```

if closure ==0 | closure ==1 | closure == 3

```

```

[t,A]=ode15s(@parallelPlateSupport,tspan,Azero);
A_final = A;
t_final = t;
%Solution matrix is [t A] where column 1=time 2=A11 3=A22 4=A33 5=A12 6=A13
%7=A23
end %end for if

```

```

%%%%%%%%%%%%%%%%%%%%%%%%%%%%%%%%%%%%%%%%%%%%%%%%%%%%%%%%%%%%%%%%%%%%%%%%%calculate stresses

```

```

size_t_final = size(t_final); %goes from zero to how many you tell it to
%so for 100 steps it has 101 data points

```

```

eta_calc=0;%starts the new eta_calc for the new strain
N1_N2_calc=0;
N1_calc=0;
for ii=1:size_t_final%%begining of loop to calculate stresses

```

```

%I think I have to get rid of the 2*SR in the stress decoupling

```

```

%%%%%%%%%%%%%%%%%%%%%%%%%%%%%%%%%%%%%%%%%%%%%%%%%%%%%%%%%stress closure
if stress_closure == 0 %for quadratic

```

```

A4_11=A_final(ii,4)*A_final(ii,1);
A4_22=A_final(ii,4)*A_final(ii,2);
A4_33=A_final(ii,4)*A_final(ii,3);
A4_12=(A_final(ii,4)^2);

```

```
end
```

```

if stress_closure == 1 %then linear closure
A4_11=(1/2)*(6*A_final(ii,4)/7)*RSR;
A4_22=(1/2)*(6*A_final(ii,4)/7)*RSR;
A4_33=(1/2)*(2*A_final(ii,4)/7)*RSR;
A4_12=(1/2)*2*((A_final(ii,1)/7)+(A_final(ii,2)/7)-(1/35))*RSR;

```

```
end
```

```

if stress_closure ==2 %then hybrid
    DET_A=(
A_final(ii,1)*A_final(ii,2)*A_final(ii,3)+A_final(ii,4)*A_final(ii,6)*A_final(ii,5)+A_final(ii,5)*A_final(ii,
4)*A_final(ii,6) ) - (
A_final(ii,2)*(A_final(ii,5)^2)+A_final(ii,1)*(A_final(ii,6)^2)+A_final(ii,3)*(A_final(ii,4)^2) );
    FF=1-27*DET_A;
A4_11=(1/2)* FF * 2*RSR*A_final(ii,4)*A_final(ii,1) + (1-FF)* (6*A_final(ii,4)/7)*RSR;
A4_22=(1/2)*FF * 2*RSR*A_final(ii,4)*A_final(ii,2) + (1-FF)* (6*A_final(ii,4)/7)*RSR;
A4_33=(1/2)*FF * 2*RSR*A_final(ii,4)*A_final(ii,3) + (1-FF)* (2*A_final(ii,4)/7)*RSR;
A4_12=(1/2)* FF * 2*RSR*(A_final(ii,4)^2) + (1-FF)* 2*((A_final(ii,1)/7)+(A_final(ii,2)/7)-
(1/35))*RSR;

```

```
end
```

```

if stress_closure == 3 %then H&L1
A4_11=(1/2)* 2*A_final(ii,1)*A_final(ii,4)*RSR - (4/5)*RSR*( A_final(ii,1)*A_final(ii,4) - A_final(ii,4)
+ A_final(ii,4)*A_final(ii,2) + A_final(ii,5)*A_final(ii,6) );
A4_22=(1/2)* 2*A_final(ii,2)*A_final(ii,4)*RSR - (4/5)*RSR*( A_final(ii,1)*A_final(ii,4) - A_final(ii,4)
+ A_final(ii,4)*A_final(ii,2) + A_final(ii,5)*A_final(ii,6) );
A4_33=(1/2)* (12/5)*RSR*A_final(ii,5)*A_final(ii,6) - (2/5)*RSR*A_final(ii,3)*A_final(ii,4) -
(4/5)*RSR*( A_final(ii,1)*A_final(ii,4)- A_final(ii,4) + A_final(ii,4)*A_final(ii,2) +
A_final(ii,5)*A_final(ii,6) );
A4_12=(1/2)* (4/5)*RSR*(A_final(ii,4)^2)+(6/5)*RSR*A_final(ii,1)*A_final(ii,2);

```

```
end
```

```
if stress_closure == 4 %then IBOF
```

```

    IBOF_constants;% calls file that contains IBOF_c (21,3)
    I_2 = A_final(ii,1)*A_final(ii,2)+A_final(ii,1)*A_final(ii,3)+A_final(ii,2)*A_final(ii,3) -
(A_final(ii,4)^2) - (A_final(ii,5)^2) - (A_final(ii,6)^2);
    I_3 = A_final(ii,1)*A_final(ii,2)*A_final(ii,3) + 2*A_final(ii,4)*A_final(ii,5)*A_final(ii,6) -
A_final(ii,1)*(A_final(ii,6)^2) - A_final(ii,3)*(A_final(ii,4)^2)-A_final(ii,2)*(A_final(ii,5)^2);

    IBOF_B =zeros(6,1);
    %IBOF_c (#, i=1,2,3)
    IBOF_B(3,1) = IBOF_c(1,1) + IBOF_c(2,1)*I_2 + IBOF_c(3,1)*(I_2^2) + IBOF_c(4,1)*I_3 +
IBOF_c(5,1)*(I_3^2) +...

```

$$\begin{aligned} & \text{IBOF\_c}(6,1)*I_2*I_3 + \text{IBOF\_c}(7,1)*(I_2^2)*I_3 + \text{IBOF\_c}(8,1)*I_2*(I_3^2) + \\ & \text{IBOF\_c}(9,1)*(I_2^3) + \dots \\ & \text{IBOF\_c}(10,1)*(I_3^3) + \text{IBOF\_c}(11,1)*(I_2^3)*I_3 + \text{IBOF\_c}(12,1)*(I_2^2)*(I_3^2) + \dots \\ & \text{IBOF\_c}(13,1)*I_2*(I_3^3) + \text{IBOF\_c}(14,1)*(I_2^4) + \text{IBOF\_c}(15,1)*(I_3^4) + \\ & \text{IBOF\_c}(16,1)*(I_2^4)*I_3 + \dots \\ & \text{IBOF\_c}(17,1)*(I_2^3)*(I_3^2) + \text{IBOF\_c}(18,1)*(I_2^2)*(I_3^3) + \\ & \text{IBOF\_c}(19,1)*(I_2)*(I_3^4) + \dots \\ & \text{IBOF\_c}(20,1)*(I_2^5) + \text{IBOF\_c}(21,1)*(I_3^5); \end{aligned}$$

$$\begin{aligned} \text{IBOF\_B\_}(4,1) &= \text{IBOF\_c}(1,2) + \text{IBOF\_c}(2,2)*I_2 + \text{IBOF\_c}(3,2)*(I_2^2) + \text{IBOF\_c}(4,2)*I_3 + \\ & \text{IBOF\_c}(5,2)*(I_3^2) + \dots \\ & \text{IBOF\_c}(6,2)*I_2*I_3 + \text{IBOF\_c}(7,2)*(I_2^2)*I_3 + \text{IBOF\_c}(8,2)*I_2*(I_3^2) + \\ & \text{IBOF\_c}(9,2)*(I_2^3) + \dots \\ & \text{IBOF\_c}(10,2)*(I_3^3) + \text{IBOF\_c}(11,2)*(I_2^3)*I_3 + \text{IBOF\_c}(12,2)*(I_2^2)*(I_3^2) + \dots \\ & \text{IBOF\_c}(13,2)*I_2*(I_3^3) + \text{IBOF\_c}(14,2)*(I_2^4) + \text{IBOF\_c}(15,2)*(I_3^4) + \\ & \text{IBOF\_c}(16,2)*(I_2^4)*I_3 + \dots \\ & \text{IBOF\_c}(17,2)*(I_2^3)*(I_3^2) + \text{IBOF\_c}(18,2)*(I_2^2)*(I_3^3) + \\ & \text{IBOF\_c}(19,2)*(I_2)*(I_3^4) + \dots \\ & \text{IBOF\_c}(20,2)*(I_2^5) + \text{IBOF\_c}(21,2)*(I_3^5); \end{aligned}$$

$$\begin{aligned} \text{IBOF\_B\_}(6,1) &= \text{IBOF\_c}(1,3) + \text{IBOF\_c}(2,3)*I_2 + \text{IBOF\_c}(3,3)*(I_2^2) + \text{IBOF\_c}(4,3)*I_3 + \\ & \text{IBOF\_c}(5,3)*(I_3^2) + \dots \\ & \text{IBOF\_c}(6,3)*I_2*I_3 + \text{IBOF\_c}(7,3)*(I_2^2)*I_3 + \text{IBOF\_c}(8,3)*I_2*(I_3^2) + \\ & \text{IBOF\_c}(9,3)*(I_2^3) + \dots \\ & \text{IBOF\_c}(10,3)*(I_3^3) + \text{IBOF\_c}(11,3)*(I_2^3)*I_3 + \text{IBOF\_c}(12,3)*(I_2^2)*(I_3^2) + \dots \\ & \text{IBOF\_c}(13,3)*I_2*(I_3^3) + \text{IBOF\_c}(14,3)*(I_2^4) + \text{IBOF\_c}(15,3)*(I_3^4) + \\ & \text{IBOF\_c}(16,3)*(I_2^4)*I_3 + \dots \\ & \text{IBOF\_c}(17,3)*(I_2^3)*(I_3^2) + \text{IBOF\_c}(18,3)*(I_2^2)*(I_3^3) + \\ & \text{IBOF\_c}(19,3)*(I_2)*(I_3^4) + \dots \\ & \text{IBOF\_c}(20,3)*(I_2^5) + \text{IBOF\_c}(21,3)*(I_3^5); \end{aligned}$$

$$\begin{aligned} \text{IBOF\_B\_}(1,1) &= (3/5)*(-1/7) + (1/5)*\text{IBOF\_B\_}(3,1)*(1/7) + (4/7)*I_2 + (8/3)*I_3 - \\ & \text{IBOF\_B\_}(4,1)*(1/5) - \dots \\ & (8/15)*I_2 - (14/15)*I_3 - \text{IBOF\_B\_}(6,1)*(1/35) - (24/105)*I_3 - (4/35)*I_2 + (16/15)*I_2*I_3 \\ & + \dots \\ & (8/35)*(I_2^2) \quad ); \end{aligned}$$

$$\begin{aligned} \text{IBOF\_B\_}(2,1) &= (6/7)*(1 - (1/5)*\text{IBOF\_B\_}(3,1)*(1+4*I_2) + (7/5)*\text{IBOF\_B\_}(4,1)*((1/6)-I_2) - \dots \\ & \text{IBOF\_B\_}(6,1)*((-1/5)+(2/3)*I_3+(4/5)*I_2-(8/5)*(I_2^2)) \quad ); \end{aligned}$$

$$\text{IBOF\_B\_}(5,1) = -(4/5)*\text{IBOF\_B\_}(3,1) - (7/5)*\text{IBOF\_B\_}(4,1) - (6/5)*\text{IBOF\_B\_}(6,1)*(1-(4/3)*I_2);$$

%IBOF\_B\_(i,1)

$$\begin{aligned} \text{func\_a} &= \text{A\_final}(ii,1)*\text{A\_final}(ii,4)+\text{A\_final}(ii,4)*\text{A\_final}(ii,2)+\text{A\_final}(ii,5)*\text{A\_final}(ii,6); \\ \text{func\_b} &= (\text{A\_final}(ii,5)^2)+\text{A\_final}(ii,1)*\text{A\_final}(ii,4)+\text{A\_final}(ii,4)*\text{A\_final}(ii,2); \\ \text{func\_c} &= (\text{A\_final}(ii,1)^2)+(\text{A\_final}(ii,4)^2)+(\text{A\_final}(ii,5)^2); \\ \text{func\_d} &= (\text{A\_final}(ii,4)^2)+(\text{A\_final}(ii,2)^2)+\text{A\_final}(ii,5)*\text{A\_final}(ii,6); \\ \text{func\_e} &= ((\text{A\_final}(ii,5)^2)/4) + ((\text{A\_final}(ii,5)*\text{A\_final}(ii,6))/4) + ((\text{A\_final}(ii,1)*\text{A\_final}(ii,4))/2) + \\ & ((\text{A\_final}(ii,4)*\text{A\_final}(ii,2))/2); \\ \text{func\_f} &= \text{A\_final}(ii,1)*\text{A\_final}(ii,5)+\text{A\_final}(ii,4)*\text{A\_final}(ii,5)+\text{A\_final}(ii,5)*\text{A\_final}(ii,3); \\ \text{func\_g} &= \text{A\_final}(ii,1)*\text{A\_final}(ii,5)+\text{A\_final}(ii,4)*\text{A\_final}(ii,6)+\text{A\_final}(ii,5)*\text{A\_final}(ii,3); \\ \text{func\_h} &= \text{A\_final}(ii,4)*\text{A\_final}(ii,5)+\text{A\_final}(ii,2)*\text{A\_final}(ii,5)+\text{A\_final}(ii,5)*\text{A\_final}(ii,3); \\ \text{func\_i} &= \text{A\_final}(ii,4)*\text{A\_final}(ii,5)+\text{A\_final}(ii,2)*\text{A\_final}(ii,6)+\text{A\_final}(ii,6)*\text{A\_final}(ii,3); \end{aligned}$$

```

func_j = (A_final(ii,5)^2)+A_final(ii,5)*A_final(ii,6)+(A_final(ii,3)^2);
func_k = (A_final(ii,5)^2)+A_final(ii,1)*A_final(ii,4)+A_final(ii,2)*A_final(ii,4);
func_L = ((A_final(ii,5)^2)/3) + ((A_final(ii,5)*A_final(ii,6))/3) + ((A_final(ii,4)*A_final(ii,3))/3);

A4_11=(1/2)*2*RSR* ( IBOF_B_(6,1)*( (func_b*func_c/2) + (func_c*func_a/2) ) + IBOF_B_(4,1)*(
func_e ) +...
IBOF_B_(2,1)*(A_final(ii,4)/2)+ IBOF_B_(5,1)*(
(A_final(ii,4)*func_c/2)+(A_final(ii,1)*func_a/4)+(A_final(ii,1)*func_b/4)) +
IBOF_B_(3,1)*A_final(ii,1)*A_final(ii,4) );

A4_22=(1/2)*2*RSR* ( IBOF_B_(6,1)*( (func_d*func_a/2) + (func_b*func_d/2) ) +...
IBOF_B_(5,1)*( (A_final(ii,2)*func_a/4)+(A_final(ii,4)*func_d/2)+(A_final(ii,2)*func_b/4) ) +...
IBOF_B_(4,1)*(func_e) + (IBOF_B_(2,1)*A_final(ii,4)/2) + IBOF_B_(3,1)*A_final(ii,2)*A_final(ii,4)
);

A4_33=(1/2)*2*RSR* ( IBOF_B_(5,1)*( (A_final(ii,5)/12)*func_f + (A_final(ii,3)/12)*func_a +
(A_final(ii,5)/12)*func_g + (A_final(ii,6)/12)*func_f +...
(A_final(ii,5)/6)*func_h + (A_final(ii,6)/12)*func_g + (A_final(ii,5)/6)*func_i +
(A_final(ii,4)/6)*func_j + (A_final(ii,3)/12)*func_k ) +...
IBOF_B_(3,1)*(func_L) + IBOF_B_(4,1)*(func_e/3) +...
IBOF_B_(6,1)*( (func_a*func_j/6) + (func_b*func_j/6) + (func_f*func_h/6) + (func_g*func_h/6) +...
(func_i*func_i/6) + (func_g*func_i/6) ) + (IBOF_B_(2,1)*A_final(ii,4)/6) );

A4_12=(1/2)*2*RSR* ( IBOF_B_(5,1)*( (A_final(ii,2)*func_c/6) + (A_final(ii,4)*func_a/3) +
(A_final(ii,1)*func_d/6) + (A_final(ii,4)*func_b/3) ) +...
IBOF_B_(4,1)*( ((A_final(ii,1)^2)/6) + ((A_final(ii,4)^2)/3) + ((A_final(ii,5)^2)/6) +
((A_final(ii,5)*A_final(ii,6))/6) + ((A_final(ii,2)^2)/6) ) +...
IBOF_B_(6,1)*( (func_c*func_d/3) + (func_b*func_a/3) + ((func_b^2)/6) + ((func_a^2)/6) ) +...
IBOF_B_(3,1)*( ((A_final(ii,4)^2)*2/3) + (A_final(ii,1)*A_final(ii,2)/3) ) + IBOF_B_(2,1)*(
(A_final(ii,1)/6) + (A_final(ii,2)/6) ) + (IBOF_B_(1,1)/3) );

end
%%%%%%%%%%%%%%%%%%%%%%%%%%%%%%%%%%%%%%%%%%%%%%%%%%%%%%%%%%%%%%%%%%%%%%%%%end of defining closure
for stress

%now trapedoidal rule real
if ii < size_t_final(1,1)
eta_calc=eta_calc+(integral_step)*(4*eta_s/(ijk^4))*(1+2*Np*(A4_12(1,1)))*(t_final(ii,1)^3);% this sums
up all the trapezoids
N1_N2_calc=N1_calc+(integral_step)*(6*eta_s*Np*N1_SR/(ijk^3))*(A4_11(1,1)-
A4_22(1,1)+A4_33(1,1)-A4_22(1,1))*(t_final(ii,1)^2); %really N1-N2
N1_calc=N1_calc+(integral_step)*(6*eta_s*Np*N1_SR/(ijk^3))*(A4_11(1,1)-
A4_22(1,1))*(t_final(ii,1)^2);
end %end real

end % end for the for loop to calculate stresses

%real
eta_calc_rim=(integral_step/2)*(4*eta_s/(ijk^4))*(1+2*Np*(A4_12(1,1)))*(t_final(ii,1)^3); %solves the
last value, the first value is always zero
eta_calc_final(eta_integral_counter,1)=eta_calc+eta_calc_rim;
N1_N2_calc_rim=(integral_step/2)*(6*eta_s*Np*N1_SR/(ijk^3))*(A4_11(1,1)-A4_22(1,1)+A4_33(1,1)-
A4_22(1,1))*(t_final(ii,1)^2);

```

```

N1_N2_calc_final(eta_integral_counter,1)=N1_N2_calc+N1_N2_calc_rim;
N1_calc_rim=(integral_step/2)*(6*eta_s*Np*N1_SR/(ijk^3))*(A4_11(1,1)-A4_22(1,1))*(t_final(ii,1)^2);
N1_calc_final(eta_integral_counter,1)=N1_calc+N1_calc_rim;
end % end for loop to calculate all the strains and viscositie sreal

```

```

eta_strain; %plot this vs. eta_calc_final

```

```

%%%%%%%%%%%%%%%%%%%%%%%%%%%%%%%%%%%%%%%%%%%%%%%%%%%%%%%%%end of stress
calculation

```

```

%out put arguments [eta_strain eta_calc_final N1_N2_calc_final N1_calc_final]

```

```

experimentalDONUTpbt;%experimental data at sr = 4

```

```

%figure(3);

```

```

%plot(exp_strain,exp_N1,'b-');hold on

```

```

[eta_strain eta_calc_final N1_N2_calc_final]

```

```

plot(eta_strain,eta_calc_final,'b-');hold on

```

```

%plot(exp_strain,exp_shear_stress,'r-');hold on

```

```

plot(eta_strain,N1_N2_calc_final,'b-');hold on

```

```

%plot(strain,A_final(:,4),'r-');hold on

```

```

%for i=1:200

```

```

%extract=[strain(i*50-50,1) A_final(i*50-50,:)]

```

```

%end

```

```

toc

```

## Subprogram

File name: parallelPlateSupport

% Aaron Eberle

%12/6/07

```

% A(1)=A11, A(2)=A22, A(3)=A33, A(4)=A21, A(5)=A13, A(6)=A23

```

```

% Name our function

```

```

function Aprime = parallelPlateSupport(t,A)

```

```

global SR addTUCKER C1 alpha relaxation_time closure FF RSR IBOF_B_BBB

```

```

if t <= relaxation_time

```

```

SR=SR; % Shear Rate

```

```

else

```

```

    SR=0;

```

```

end

```

```

%Define A components based on closure

```

```

if closure ==0 %for quadratic

```

```

A4_11=2*SR*A(4)*A(1);

```

```

A4_22=2*SR*A(4)*A(2);

```

```

A4_33=2*SR*A(4)*A(3);

```

```

A4_12=2*SR*(A(4)^2);

```

```
A4_13=2*SR*A(4)*A(5);
A4_23=2*SR*A(4)*A(6);
```

```
end
```

```
if closure ==1 %then linear closure
```

```
A4_11=(6*A(4)/7)*SR;
A4_22=(6*A(4)/7)*SR;
A4_33=(2*A(4)/7)*SR;
A4_12=2*((A(1)/7)+(A(2)/7)-(1/35))*SR;
A4_13=(2*A(6)/7)*SR;
A4_23=(2*A(5)/7)*SR;
```

```
end
```

```
if closure ==2 %then hybrid
```

```
A4_11= FF * 2*SR*A(4)*A(1) + (1-FF)* (6*A(4)/7)*SR;
A4_22= FF * 2*SR*A(4)*A(2) + (1-FF)* (6*A(4)/7)*SR;
A4_33= FF * 2*SR*A(4)*A(3) + (1-FF)* (2*A(4)/7)*SR;
A4_12= FF * 2*SR*(A(4)^2) + (1-FF)* 2*((A(1)/7)+(A(2)/7)-(1/35))*SR;
A4_13= FF * 2*SR*A(4)*A(5) + (1-FF)* (2*A(6)/7)*SR;
A4_23= FF * 2*SR*A(4)*A(6) + (1-FF)* (2*A(5)/7)*SR;
```

```
end
```

```
if closure == 3 %then H&L1
```

```
A4_11= 2*A(1)*A(4)*SR - (4/5)*SR*( A(1)*A(4) - A(4) + A(4)*A(2) + A(5)*A(6) );
A4_22= 2*A(2)*A(4)*SR - (4/5)*SR*( A(1)*A(4) - A(4) + A(4)*A(2) + A(5)*A(6) );
A4_33= (12/5)*SR*A(5)*A(6) - (2/5)*SR*A(3)*A(4) - (4/5)*SR*( A(1)*A(4)- A(4) + A(4)*A(2) +
A(5)*A(6) );
A4_12= (4/5)*SR*(A(4)^2)+(6/5)*SR*A(1)*A(2);
A4_13= (6/5)*SR*A(1)*A(6) + (4/5)*SR*A(4)*A(5);
A4_23= (4/5)*SR*A(4)*A(6) + (6/5)*SR*A(5)*A(2);
```

```
end
```

```
if closure == 4 %then IBOF
```

```
%IBOF_B_(i,1)
```

```
func_a = A(1)*A(4)+A(4)*A(2)+A(5)*A(6);
func_b = (A(5)^2)+A(1)*A(4)+A(4)*A(2);
func_c = (A(1)^2)+(A(4)^2)+(A(5)^2);
func_d = (A(4)^2)+(A(2)^2)+A(5)*A(6);
func_e = ((A(5)^2)/4) + ((A(5)*A(6))/4) + ((A(1)*A(4))/2) + ((A(4)*A(2))/2);
func_f = A(1)*A(5)+A(4)*A(5)+A(5)*A(3);
func_g = A(1)*A(5)+A(4)*A(6)+A(5)*A(3);
func_h = A(4)*A(5)+A(2)*A(5)+A(5)*A(3);
func_i = A(4)*A(5)+A(2)*A(6)+A(6)*A(3);
func_j = (A(5)^2)+A(5)*A(6)+(A(3)^2);
func_k = (A(5)^2)+A(1)*A(4)+A(2)*A(4);
func_L = ((A(5)^2)/3) + ((A(5)*A(6))/3) + ((A(4)*A(3))/3);
```

$$A4\_11=2*SR*( IBOF\_B_(6,1)*((func\_b*func\_c/2)+(func\_c*func\_a/2)) + IBOF\_B_(4,1)*(func\_e) + \dots \\ IBOF\_B_(2,1)*(A(4)/2)+ IBOF\_B_(5,1)*((A(4)*func\_c/2)+(A(1)*func\_a/4)+(A(1)*func\_b/4)) + \\ IBOF\_B_(3,1)*A(1)*A(4));$$

$$A4\_22=2*SR*( IBOF\_B_(6,1)*((func\_d*func\_a/2)+(func\_b*func\_d/2)) + \dots \\ IBOF\_B_(5,1)*((A(2)*func\_a/4)+(A(4)*func\_d/2)+(A(2)*func\_b/4)) + \dots \\ IBOF\_B_(4,1)*(func\_e) + (IBOF\_B_(2,1)*A(4)/2) + IBOF\_B_(3,1)*A(2)*A(4));$$

$$A4\_33=2*SR*( IBOF\_B_(5,1)*((A(5)/12)*func\_f + (A(3)/12)*func\_a + (A(5)/12)*func\_g + \\ (A(6)/12)*func\_f + \dots \\ (A(5)/6)*func\_h + (A(6)/12)*func\_g + (A(5)/6)*func\_i + (A(4)/6)*func\_j + (A(3)/12)*func\_k) + \dots \\ IBOF\_B_(3,1)*(func\_l) + IBOF\_B_(4,1)*(func\_e/3) + \dots \\ IBOF\_B_(6,1)*((func\_a*func\_j/6) + (func\_b*func\_j/6) + (func\_f*func\_h/6) + (func\_g*func\_h/6) + \dots \\ (func\_i*func\_i/6) + (func\_g*func\_i/6)) + (IBOF\_B_(2,1)*A(4)/6));$$

$$A4\_12=2*SR*( IBOF\_B_(5,1)*((A(2)*func\_c/6) + (A(4)*func\_a/3) + (A(1)*func\_d/6) + \\ (A(4)*func\_b/3)) + \dots \\ IBOF\_B_(4,1)*(((A(1)^2)/6) + ((A(4)^2)/3) + ((A(5)^2)/6) + ((A(5)*A(6))/6) + ((A(2)^2)/6)) + \dots \\ IBOF\_B_(6,1)*((func\_c*func\_d/3) + (func\_b*func\_a/3) + ((func\_b^2)/6) + ((func\_a^2)/6)) + \dots \\ IBOF\_B_(3,1)*(((A(4)^2)*2/3) + (A(1)*A(2)/3)) + IBOF\_B_(2,1)*((A(1)/6) + (A(2)/6)) + \\ (IBOF\_B_(1,1)/3));$$

$$A4\_13= 2*SR*( IBOF\_B_(5,1)*((A(5)*func\_c/12) + (A(6)*func\_c/12) + (A(5)*func\_a/6) + \\ (A(4)*func\_f/6)) + \dots \\ (A(1)*func\_h/12) + (A(4)*func\_g/6) + (A(1)*func\_i/12) + (A(5)*func\_k/6)) + \dots \\ IBOF\_B_(3,1)*(((A(1)*A(5))/6) + ((A(1)*A(6))/6) + ((A(4)*A(5))*2/3)) + \\ IBOF\_B_(2,1)*((A(5)/12)+(A(6)/12)) + \dots \\ IBOF\_B_(4,1)*(((A(4)*A(5))/6) + ((A(5)*A(2))/12) + ((A(2)*A(6))/12) + ((A(5)*A(3))/12) + \\ ((A(6)*A(3))/12)) + \dots \\ IBOF\_B_(6,1)*((func\_b*func\_f/6) + (func\_b*func\_g/6) + (func\_c*func\_h/6) + (func\_c*func\_i/6) + \dots \\ (func\_a*func\_f/6) + (func\_a*func\_g/6));$$

$$A4\_23= 2*SR*( IBOF\_B_(3,1)*((A(4)*A(5)/3) + (A(4)*A(6)/3) + (A(5)*A(2)/3)) + \dots \\ IBOF\_B_(4,1)*((A(1)*A(5)/6) + (A(4)*A(5)/12) + (A(4)*A(6)/12) + (A(5)*A(3)/6)) + \dots \\ IBOF\_B_(6,1)*((func\_d*func\_f/6) + (func\_d*func\_g/6) + (func\_b*func\_h/6) + (func\_b*func\_i/6) + \dots \\ (func\_a*func\_h/6) + (func\_a*func\_i/6)) + IBOF\_B_(5,1)*((A(5)*func\_a/12) + (A(6)*func\_a/12) + \dots \\ (A(2)*func\_f/12) + (A(4)*func\_h/6) + (A(2)*func\_g/12) + (A(4)*func\_i/6) + (A(5)*func\_d/6) + \\ (A(5)*func\_b/12) + \dots \\ (A(6)*func\_b/12)) + (IBOF\_B_(2,1)*A(5)/6));$$

end

$$J1=2*SR*A(4)-A4\_11; \\ J2=-A4\_22; \\ J3=-A4\_33; \\ J4=SR*A(2)-A4\_12; \\ J5=SR*A(6)-A4\_13; \\ J6=-A4\_23;$$

$$Tucker1=2*C1*RSR*(1-(alpha*A(1))); \\ Tucker2=2*C1*RSR*(1-(alpha*A(2)));$$

```
Tucker3=2*C1*RSR*(1-(alpha*A(3)));
Tucker4=-2*alpha*C1*RSR*A(4);
Tucker5=-2*alpha*C1*RSR*A(5);
Tucker6=-2*alpha*C1*RSR*A(6);
```

```
if addTUCKER ==0
    Aprime = [J1;
              J2;
              J3;
              J4;
              J5;
              J6];
```

```
end
```

```
if addTUCKER ==1
    Aprime = [J1+Tucker1;
              J2+Tucker2;
              J3+Tucker3;
              J4+Tucker4;
              J5+Tucker5;
              J6+Tucker6];
```

```
end
```

## IBOF Constants

```
%these are a list of the constants given the the Chung and Kwon paper
% Invariant-based optimal fitting closure approximation for the numerical
% prediction of flow-induced fiber orientation
```

```
IBOF_c = [ 0.24940908165786E2 -0.497217790110754E00 0.234146291570999E2;
           -0.435101153160329E3 0.234980797511405E2 -0.412048043372534E3;
           0.372389335663877E4 -0.391044251397838E3 0.319553200392089E4;
           0.703443657916476E4 0.153965820593506E3 0.573259594331015E4;
           0.823995187366106E6 0.152772950743819E6 -0.485212803064813E5;
           -0.133931929894245E6 -0.213755248785646E4 -0.605006113515592E5;
           0.880683515327916E6 -0.400138947092812E4 -0.477173740017567E5;
           -0.991630690741981E7 -0.185949305922308E7 0.599066486689836E7;
           -0.159392396237307E5 0.296004865275814E4 -0.110656935176569E5;
           0.800970026849796E7 0.247717810054366E7 -0.460543580680696E8;
           -0.237010458689252E7 0.101013983339062E6 0.203042960322874E7;
           0.379010599355267E8 0.732341494213578E7 -0.556606156734835E8;
           -0.337010820273821E8 -0.147919027644202E8 0.567424911007837E9;
           0.322219416256417E5 -0.104092072189767E5 0.128967058686204E5;
           -0.257258805870567E9 -0.635149929624336E8 -0.152752854956514E10;
           0.214419090344474E7 -0.247435106210237E6 -0.499321746092534E7;
           -0.449275591851490E8 -0.902980378929272E7 0.132124828143333E9;
           -0.213133920223355E8 0.724969796807399E7 -0.162359994620983E10;
           0.157076702372204E10 0.487093452892595E9 0.792526849882218E10;
           -0.232153488525298E5 0.138088690964946E5 0.466767581292985E4;
           -0.395769398304473E10 -0.160162178614234E10 -0.128050778279459E11];
```

### C.3 Hinch's Perfectly Flexible Fiber

The following code solves the Hinch equations for a perfectly flexible fiber give the initial fiber orientation in 3D.

```
File name: Hinch
%this program solves the Hinch equations for an infinitely extensible fiber
%in simple shear flow
%you have to input the initial values for x and z and it calculates...
%...the y values to give you a constant dS
%as a note it only gives you the positive root for y values

clear all
clc
format long

%%%%%%%% Evolution of flexible long glass fiber Hinch paper

tic%begin timer

% g stands for global
global SR g_x g_one_diff_T g_one_diff_x_s g_complete_T g_two_diff_x_s
global SR g_y g_one_diff_T g_one_diff_y_s g_complete_T g_two_diff_y_s
global SR g_z g_one_diff_T g_one_diff_z_s g_complete_T g_two_diff_z_s

tspan=6;
t_step=.025; %step size needs to be less than 0.05 and 0.025 works better
SR=1; %defines the shear rate

%%%%%%%%%%
L_f = 10; %fiber length
n = 31; % odd number of nodes along fiber,
Seg = n-1; % total number of arc segments, has to have even number of segments
S_1 = L_f/Seg; %arc length

%%%%%%%%%% Initial fiber orientation, have to define xi values and
x = [2 1.79 1.59 1.41 1.26 1.13 1.05 1.01 1.01 1.05 1.13 1.26 1.41 1.59 1.79 2 2.21 2.41 2.59 2.74 2.87 2.95
2.99 2.99 2.95 2.87 2.74 2.59 2.41 2.21 2]; %determine from a cosine function from -pi/2 to 3/2pi then
rotated
%x(1,1)=1/3
%for i=2:n
% x(i,1)=x(i-1,1)+(1/3);
%end
z=ones(31,1); %have to define the z points
y1 = 1; %have to define initial point for y
for i=1:n-1 %solve for y values to give constant delta_S only the positive root
y(1,1) = y1;
y(i+1,1) = (((S_1^2)-(( x(i+1,1)-x(i,1) )^2)-(( z(i+1,1)-z(i,1) )^2))^(1/2))+y(i,1);
end
%%%%%%%%%%
```

```

%%%%%%%%%% Setting a check to make sure number of nodes matches initial x
check_1=size(x);
check_2=size(z);
if check_1(1,1) ~= n | check_2(1,1) ~= n
    %disp('number of nodes does not match initial conditions for x');
    disp('number of nodes does not match initial conditions for x or z');
end
%%%%%%%%%%

%%%%%%%%%%plotting initial fiber orientation
%plot(x, y, '*-')
%for 3D%plot3(x, y, z, 'g-')
%%%%%%%%%%

%%%%%%%%%%check segment length
%for i=1:Seg
    %S_check(i)=(((x(1,i+1)-x(1,i))^2)+((y(1,i+1)-y(1,i))^2))^(1/2); %for 2D
    %S_check(i)=(((x(1,i+1)-x(1,i))^2)+((y(1,i+1)-y(1,i))^2)+((z(1,i+1)-z(1,i))^2))^(1/2); %for 3D%
%end
%S_check;
%%%%%%%%%%

%%%%%%%%%%begin time span loop
final_matrix_count=0;%final_matrix_count counts the number of time steps
for ii=0:t_step:tspan-t_step
    t_span=[ii ii+t_step]; % for ODE solver
    final_matrix_count=final_matrix_count+1;

    %now estimate the spatial derivatives
    %I used higher order estimates from taylor series expansion, I think ok

    %first order derivatives
    %XXXXXXXXXXXXXXXXXXXXXXXXXXXXX1
    %%%for the first and second node, higher order forward difference approximation
    for i=1:2
        one_diff_x_s(i,1)=(-x(i+2,1)+4*x(i+1,1)-3*x(i,1))/(2*S_1);
    end
    %%%error O(interp_step^2)
    %%%for the central nodes, higher order central difference approximation
    for i=3:n-2
        one_diff_x_s(i,1)=(-x(i+2,1)+8*x(i+1,1)-8*x(i-1,1)+x(i-2,1))/(12*S_1);
    end
    %%%error O(interp_step^4)
    %%%for last two nodes, higher order backward difference approximation
    for i=n-1:n
        one_diff_x_s(i,1)=(3*x(i,1)-4*x(i-1,1)+x(i-2,1))/(2*S_1);
    end
    %%%error O(interp_step^2)
    %XXXXXXXXXXXXXXXXXXXXXXXXXXXXX1

    %YYYYYYYYYYYYYYYYYYYYYYYYYYYYYY1
    %%%for the first and second node, higher order forward difference approximation
    for i=1:2
        one_diff_y_s(i,1)=(-y(i+2,1)+4*y(i+1,1)-3*y(i,1))/(2*S_1);
    end

```





```

row(1,1)=1;
row(2,1)=1;
column(1,1)=1;
column(2,1)=2;
row((n-2)*3-3,1)=n-2;
row((n-2)*3-2,1)=n-2;
column((n-2)*3-3,1)=n-3;
column((n-2)*3-2,1)=n-2;
%first and last row values for T
A(1,1)=-P(1,1);
A(2,1)=1;
A((n-2)*3-3,1)=1;
A((n-2)*3-2,1)=-P(n-2,1);
%all the middle coordinates
for i=2:n-3
    A((i-1)*3,1)=1;% 3 6 9.....
    A((i-1)*3+1,1)=-P(i,1);% 4 7 10...
    A((i-1)*3+2,1)=1;% 5 8 11.....

    for j=1:3
        sp_co=(i-2)*2+j+i;
        row(sp_co,1)=i;
        column(sp_co,1)=j+i-2;
    end
end
%put together sparse matrix
s_A=sparse(row,column,A);
T=s_A\b;%does not include T and ends of fiber
%%%%%%%%%%%%%%%%%%%%%%%%%%%%%%%%%%%%%%%%%%%%%%%%%%%%%%%%%%%%%%%%%%%%%%%%done solving for tension T

%
%Now estimate T', I am just going to do a rough estimate using nodes
%first node using forward difference
one_diff_T(1,1)=(T(1,1)-0)/(S_1);
%for the last node backward difference
one_diff_T(n,1)=0-T(n-2,1)/(S_1);
%second node using central difference
one_diff_T(2,1)=(T(2,1)-0)/(2*S_1);
%second from last node using central difference
one_diff_T(n-1,1)=0-T(n-3,1)/(2*S_1);
%for central nodes
for i=3:n-2
    one_diff_T(i,1)=(T(i,1)-T(i-2,1))/(2*S_1);
end

%put together the complete matrix for T
complete_T(1,1)=0;
complete_T(n,1)=0;
for i=2:n-1
    complete_T(i,1)=T(i-1,1);
end

%%%%%%%%%%%%%%%%%%%%%%%%%%%%%%%%%%%%%%%%%%%%%%%%%%%%%%%%%%%%%%%%%%%%%%%%done estimating T'
(one_diff_T)
%x
%y

```

```

%z
%SR
  %one_diff_T
  %one_diff_x_s
  %one_diff_y_s
  %one_diff_z_s
  %complete_T
  %two_diff_x_s
  %two_diff_y_s
  %two_diff_z_s
%%solve for dx/dt
%
for i=1:n %defines global variables to be solved using ode solver

  g_x=x(i,1);
  g_y=y(i,1);
  g_z=z(i,1);

  g_one_diff_T=one_diff_T(i,1);

  g_one_diff_x_s=one_diff_x_s(i,1);
  g_one_diff_y_s=one_diff_y_s(i,1);
  g_one_diff_z_s=one_diff_z_s(i,1);

  g_complete_T=complete_T(i,1);

  g_two_diff_x_s=two_diff_x_s(i,1);
  g_two_diff_y_s=two_diff_y_s(i,1);
  g_two_diff_z_s=two_diff_z_s(i,1);

  [tx_out,x_out_dot]=ode15s(@DxDt,t_span,x(i,1));%%t_span defines time span for ODE solver
  [ty_out,y_out_dot]=ode15s(@DyDt,t_span,y(i,1));
  [tz_out,z_out_dot]=ode15s(@DzDt,t_span,z(i,1));

  hx=size(x_out_dot);
  hy=size(y_out_dot);
  hz=size(z_out_dot);

  x(i,1)=x_out_dot(hx(1,1),1);%extract correct x from solution file
  y(i,1)=y_out_dot(hy(1,1),1);
  z(i,1)=z_out_dot(hz(1,1),1);

  tx=tx_out(hx(1,1),1);
  ty=ty_out(hx(1,1),1);
  tz=tz_out(hx(1,1),1);

end
%
%
%
%
%have to shrink fiber back to original size
%can linearly interpolate ds
new_S_l=zeros(Seg,1);
%[x y z];

```

```

%%%%
%Neeraj gets credit for this. I think that I shrink the nodes back to the

x_=0;
y_=0;
z_=0;
xp=zeros(n,1); % x',y'z' preserve original position of node points.
yp=zeros(n,1);
zp=zeros(n,1);

for i=1:n
    xp(i,1)=x(i,1);
    yp(i,1)=y(i,1);
    zp(i,1)=z(i,1);
end

for i=1:n-1
    %checks segment length
    new_S_l(i,1)=(((xp(i+1,1)-xp(i,1))^2)+((yp(i+1,1)-yp(i,1))^2)+((zp(i+1,1)-zp(i,1))^2))^(1/2);

    %calculates based on similar triangles, cos of angles are equal
    x(i+1,1)=xp(i,1)+(xp(i+1,1)-xp(i,1))*(S_l/new_S_l(i,1))-(x_);
    y(i+1,1)=yp(i,1)+(yp(i+1,1)-yp(i,1))*(S_l/new_S_l(i,1))-(y_);
    z(i+1,1)=zp(i,1)+(zp(i+1,1)-zp(i,1))*(S_l/new_S_l(i,1))-(z_);
    x_=xp(i+1,1)-x(i+1,1); % x distance between original and new node point i+1.
    y_=yp(i+1,1)-y(i+1,1); % y distance between original and new node point i+1.
    z_=zp(i+1,1)-z(i+1,1); % z distance between original and new node point i+1.
end

for i=1:Seg
    SSS_check(i)=(((x(i+1,1)-x(i,1))^2)+((y(i+1,1)-y(i,1))^2)+((z(i+1,1)-z(i,1))^2))^(1/2);
end
[x y z];
%
%construct output matrix
%final_matrix_count counts the number of time steps
%creates matrix of form [one_tx_step x one_ty_step y]
for i=1:n
    evolv_matrix(((final_matrix_count-1)*n)+i,1)=tx;
    evolv_matrix(((final_matrix_count-1)*n)+i,2)=x(i,1);
    evolv_matrix(((final_matrix_count-1)*n)+i,3)=ty;
    evolv_matrix(((final_matrix_count-1)*n)+i,4)=y(i,1);
    evolv_matrix(((final_matrix_count-1)*n)+i,5)=tz;
    evolv_matrix(((final_matrix_count-1)*n)+i,6)=z(i,1);
end

%to look at plot of output
if ii ==0 | ii ==1 |ii ==2 |ii ==3 |ii ==4 %so that I only extract data at integers
for i=1:n
    plot_x(i,1)=x(i,1);
    plot_y(i,1)=y(i,1);
    plot_z(i,1)=z(i,1);
end
%plot3(plot_x,plot_y,plot_z,-');hold on
plot(plot_x,plot_y,-');hold on

```

```

end %end for the if loop

end %end for the time loop ii

%output to file
fid = fopen('myoutputxy.txt','w');
fprintf(fid,'% -12f % -12f % -12f % -12f\n',evolv_matrix');
fclose(fid);
toc;

```

## Sub programs

### **DxDt.m**

```

%solve

function xdot = DxDt(tx_out,x_out_dot)

global SR g_x g_one_diff_T g_one_diff_x_s g_complete_T g_two_diff_x_s g_y

xdot = SR*g_y+g_one_diff_T*g_one_diff_x_s+(1/2)*g_complete_T*g_two_diff_x_s;

```

### **DyDt.m**

```

function ydot = DyDt(ty_out,y_out_dot)

global SR g_y g_one_diff_T g_one_diff_y_s g_complete_T g_two_diff_y_s

ydot=g_one_diff_T*g_one_diff_y_s+(1/2)*g_complete_T*g_two_diff_y_s;

```

### **DzDt.m**

```

function zdot = DzDt(tz_out,z_out_dot)

global SR g_z g_one_diff_T g_one_diff_z_s g_complete_T g_two_diff_z_s

zdot=g_one_diff_T*g_one_diff_z_s+(1/2)*g_complete_T*g_two_diff_z_s;

```

## **Appendix D. Nomenclature**

## Appendix D. Nomenclature

<b>A</b>	Second-order orientation tensor
<b>A<sub>4</sub></b>	Fourth-order orientation tensor
$a_r$	Aspect ratio: defined as the particles (major axis)/(minor axis)
$a_{re}$	Equivalent aspect ratio
$C$	Constant for the analytical solution of Jeffery's equation
$C''$	Shaqfeh and Fredrickson model constant
$C_1$	Folgar-Tucker constant
$c_1$	Fiber stress constant in Lipscomb model or Herman's orientation factor constant
$c_2$	Herman's orientation factor constant
<b>D</b>	Rate of strain tensor
$D$	Fiber diameter
$D/Dt$	Material derivative
$D_r$	Rotational diffusion constant
$E_f$	Flexural modulus
<b>E</b>	Cauchy strain tensor
$F_n$	Weighting factor for fiber orientation
$F_z^*$	Normal force
$G$	Complex modulus
$G'$	Storage modulus
$G''$	Loss modulus
$G_v$	Phan-Thien and Graham model function
$g$	Acceleration due to gravity
$h$	Spacing between fibers
$k$	Constant for the analytical solution of Jeffery's equation
$k_B$	Boltzmann's constant
$L$	Fiber length
$L_n$	Number average fiber length
$L_w$	Weight average fiber length
$L_{HA-avg}$	Huq and Azaiez average fiber length
$M$	Ellipsoid major axis or torque
<b>M</b>	Mobility tensor
$M_s$	Longitudinal component of the local filament mobility tensor <b>M</b>
$M_n$	Normal component of the local filament mobility tensor <b>M</b>
<b>M<sub>v</sub></b>	Transverse mobility tensor
$m$	Ellipsoid minor axis or extensional flow viscosity constant
$N$	Herman's orientation factor constant or hydrodynamic stress constant
$N_1$	First normal stress difference
$N_2$	Second normal stress difference
$N_1^+$	First normal stress difference growth function
$N_2^+$	Second normal stress difference growth function
$N_1^-$	First normal stress difference decay function
$N_2^-$	Second normal stress difference decay function
$N_1^{CP}$	Prediction for first normal stress difference in cone-and-plate

$N_2^{CP}$	Prediction for second normal stress difference in cone-and-plate
$N_1^{PP}$	Prediction for first normal stress difference in parallel plate
$N_2^{PP}$	Prediction for second normal stress difference in parallel plate
$n$	Number of fibers per unit volume
$R_i$	Inner radius of donut sample
$R_o$	Outer radius of donut sample
$r$	Radius
<b>S</b>	Deviatoric form of the orientation order parameter tensor <b>A</b>
$S_m$	Average spacing between fibers
$S$	Arc length
$T$	Temperature or period of rotation or tension in Hinch equations
$t$	Time
$t_s$	Sedimentation time scale
<b>u</b>	Unit vector used to represent fiber orientation
<b><math>\dot{\mathbf{u}}</math></b>	Material derivative of <b>u</b>
$v$	Velocity
<b>W</b>	Vorticity tensor
<b>x</b>	Position vector

### Greek Symbols

$\alpha$	Folgar-Tucker constant
$\alpha_c$	Correction factor
$\gamma$	Strain
$\gamma_o$	Strain amplitude
$\dot{\gamma}$	Shear rate
$\dot{\gamma}_R$	Shear rate at the rim of a parallel plate rheometer
$\dot{\gamma}_0$	Constant or initial shear rate
$\delta$	Out of phase angle with respect to strain
$\dot{\epsilon}$	Elongation rate
$\epsilon$	Tensile elongation strain
$\epsilon_B$	Biaxial elongation strain
$\xi_r$	Rotational friction factor
$\rho$	Density
$\eta$	Non-Newtonian steady-state shear viscosity
$\eta_B^+$	Biaxial elongation viscosity
$\eta_E^+$	Tensile elongation viscosity
$\eta_P^+$	Planar elongation viscosity
$\eta^{CP}$	Predicted viscosity for cone-and-plate
$\eta^{PP}$	Predicted viscosity for parallel plate
$\eta_s$	Suspending medium viscosity
$\eta^*$	Complex viscosity
$\eta'$	Real component of the complex viscosity
$\eta''$	Imaginary component of the complex viscosity

$\eta^+$	Shear stress growth coefficient
$\eta_0$	Zero shear viscosity
$\eta_r$	Reduced viscosity
$\eta_r^*$	Reduced complex viscosity
$\eta_{sp}$	Specific viscosity
$\eta_1^+$	General extensional flow viscosity
$\eta_2^+$	General extensional flow viscosity
$\theta$	Zenith angle
$\theta_0$	Zenith angle initial condition
$\sigma$	Total stress tensor
$\sigma^+$	Shear stress growth function
$\sigma^-$	Shear stress decay function
$\tau$	Extra stress tensor
$\tau_{critical}$	Shear stress at which a fiber buckles
$\varphi$	Azimuthal angle
$\varphi_0$	Azimuthal angle initial condition
$\phi$	Fiber volume fraction
$\psi$	Probability distribution function
$\omega$	Frequency

### **Operators**

$\nabla$	Gradient operator
----------	-------------------